

Scott Carey

From: Brent Wisner <brent.wisner@legalprivilege.ch>
Sent: Wednesday, November 2, 2022 8:35 PM
To: Scott Carey
Subject: NTRPA GB Meeting - Public Comment (November Third, Twenty Twenty-Two)
Attachments: Scenic_Roadway_Units.pdf; Creegan—Eagle Protect PBC.pdf; NATURE—Bitcoin emissions alone could push global warming above 2°C.pdf; NATURE—Policy assessments for the carbon emission flows and sustainability of Bitcoin.pdf; NATURE—Strategies in and outcomes of climate change litigation in the United States.pdf; NATURE—Filling the evidentiary gap in climate litigation.pdf; NATURE—Radiofrequency EMF irradiation effects on pre-B lymphocytes.pdf; NATURE—Whole-body exposures to radiofrequency-electromagnetic energy can cause DNA damage via an oxidative mechanism.pdf; NATURE—Anthropogenic electromagnetic noise disruptsmagnetic compass orientation in a migratory bird.pdf; NATURE—Exposure of Insects to Radio-Frequency Electromagnetic Fields from 2 to 120 GHz.pdf; NATURE—Radio-frequency electromagnetic field exposure of Western Honey Bees.pdf; NATURE—A magnetic compass aids monarch butterfly migration.pdf; Up in smoke—California's greenhouse gas reductions could be wiped out by 2020 wildfires.pdf

WARNING - This email originated from outside the State of Nevada. Exercise caution when opening attachments or clicking links, especially from unknown senders.

Good Afternoon NTRPA Governing Board,

We have the same old **corrupt** interests, using new surrogates to ratfuck our City! The Tahoe Chamber(s), [TRYP](#), South Tahoe Association of REALTORS, and Creegan's Cowork Tahoe, are all [astrourfing](#) our City to **destroy** [the only in-town section of the Hwy 50 scenic corridor](#) that has attained the scenic threshold. None of these stooges seem to appreciate Lake Tahoe's national scenic value, and selfishly just want a civic waterpark, to serve their own myopic material interests and private dealings. Let's unpack the dossier of offenders:

Amanda Adams, 1874 Colt Lane, Gardnerville, NV 89410.

Representing Tamra Wallace's Chamber of Commerce interests. She does not even live in our State.

Stephen Warne Ardagh, [2897 Lodgepole Trail, Meyers, CA](#).

**I'm the largest
microplastics polluter...**



**in the entire
Lake Tahoe basin!**

Representing Co-work Tahoe's (Cristy Creegan's) material conflict of interest. His "Eagle Protect" virtual company is all hype and primary sells single use plastics PPE. He is gouging off the pandemic. He helicoptered into the basin in 2018 from another country in a different hemisphere and does not live in town, and cannot even vote let alone run for office!

Marissa Chance Fox, 1060 Lamor Court, Meyers, CA.

Teleworks for a San Francisco law firm. Studied land planning law to help affluent developers skirt environmental protections akin to Lew Feldman. She inveigles and finagles watchdog agencies to get entitlements for multi-million dollar commercial projects. Does not live in town.

Sharon Kerrigan, 2187 Big Pine Avenue, SLT, CA.

Acts on express behalf of the President of South Tahoe Association of REALTORS. Would destroy Tahoe to churn real estate sales and flip a bunch of houses. This is the primary interest financing the Tahoe Daily Tribune. Masters of marketing PR; a truly

powerful and rotten bunch who have no scruples putting lipstick on a pig. The City of South Lake Tahoe's Recreation Facilities Department [placed a lien on her house in 2013](#) (recorded document # [2013-0023469](#))!

Nicholas Abelow, 115 Ponderosa Circle, Zephyr Cove, NV. Financial planner for the [ultra-wealthy](#). Young stooge of the Tahoe Chamber. This is the poster child of "spoiled by [trust funds](#)" and "old money."

Locals don't like the location and sitting of this hideous facility, just like they did not want VHR's, Cell Towers, or the Loop Road. These stooges will take you off a political cliff and then spit you back out! The League to "Save Tahoe" is captured by wily developers. **Watch out!**

These people don't care about the environment let alone locals, they are money hungry opportunists who manipulate their public image in false light to suppress well-deserved public opposition.

Thanks for considering.

Brent Wisner

SCHEDULE B

Attachment

CALIFORNIA FORM FAIR POLITICAL PRACTICES COM
Name Christi Creega

[ASSESSOR PARCEL NUMBER OR STREET ADDRESS : 3079 Harrison Avenue](#)

LIST OF SOURCES OF RENTAL INCOME OF \$10,000 OR MORE
Sierra Nevada Media Group
Eagle Protect PBC

P . S .

The ratfucking by exclusively **outside interests against City locals lives on against the Ski Run neighborhood:**

Chris McNamara: [259 Cheyenne Circle](#), & [466 Kent Way](#), both in Zephyr Cove, NV; and [2478 Alice Lake Road](#) in Meyers, CA (APNs: [1318-15-711-020](#), [1318-15-311-002](#), & [025-691-002](#)).

Cory Rich: [1944 Apalachee Drive](#) & [1952 Apalachee Drive](#), both in Meyers, CA (APNs: [033-703-010](#), & [033-693-007](#)).

Lincoln Else: [819 Lookout Point Circle](#) & [1913 Apalachee Drive](#), both in Meyers, CA (APNs: [033-275-004](#), & [033-705-005](#)).

Wynn Rujiraviriyapiny: [75 South Rubicon Circle # A](#), Zephyr Cove, NV; and [1200 Echo View Drive](#), Meyers, CA (APNs: [1318-23-218-013](#), & [033-333-008](#)).

Marissa Chance Fox: [1060 Lamor Court](#), Meyers, CA (APN: [033-623-015](#)).

Rachel Carlson: [3328 Ash Avenue](#) & [3100 Fresno Avenue](#) both properties are inside city limits, but **far from** Ski Run neighborhood (APN's: [027-225-005](#), [026-077-001](#)).

Jeff Cowen: [1362 Gilmore Lake Road](#), lives in City, but is a TRPA executive ready to rig deed restrictions! (APN: [025-224-010](#)).

These are publicly recorded records that can be found at the following government websites (<https://recorderclerkservice.edcgov.us/elweb/>) and (<http://assessor-search.douglasnv.us:1401/cgi-bin/asw100>).

Cory and Chris have been adversaries in the local's fight against VHR's and Cell Towers! These political hucksters aren't socially responsible; they're money-hungry, tax-dodging, environment-exploiting opportunists!

Brent Wisner

Contents lists available at [ScienceDirect](https://www.sciencedirect.com)

Environmental Pollution

journal homepage: www.elsevier.com/locate/envpol

Up in smoke: California's greenhouse gas reductions could be wiped out by 2020 wildfires[☆]

Michael Jerrett^{a,*}, Amir S. Jina^b, Miriam E. Marlier^a

^a Department of Environmental Health Sciences, Fielding School of Public Health, University of California, Los Angeles, 650 Charles E. Young Dr. S., 56-070 CHS Box 951772, Los Angeles, CA, 90095, USA

^b Harris School of Public Policy, University of Chicago, 1307 East 60th Street, Chicago, IL, 60637, USA

ARTICLE INFO

Keywords:

Climate change
Wildfires
Greenhouse gas emissions
Economic impacts

ABSTRACT

In this short communication, we estimate that California's wildfire carbon dioxide equivalent (CO₂e) emissions from 2020 are approximately two times higher than California's total greenhouse gas (GHG) emission reductions since 2003. Without considering future vegetation regrowth, CO₂e emissions from the 2020 wildfires could be the second most important source in the state above either industry or electrical power generation. Regrowth may partly or fully occur over a long period, but due to exigencies of the climate crisis most of the regrowth will not occur quickly enough to avert greater than 1.5 degrees of warming. Global monetized damages caused by CO₂e from in 2020 wildfire emissions amount to some \$7.1 billion USD. Our analysis suggests that significant societal benefits could accrue from larger investments in improved forest management and stricter controls on new development in fire-prone areas at the wildland-urban interface.

1. Introduction

Recent evidence suggests that climate change contributes to increased wildfire activity in the western United States (Abatzoglou and Williams, 2016). California's summer wildfire burned area increased eightfold from 1972 to 2018 (Williams et al., 2019), and statewide climate change projections predict an amplification of wildfire risk due to higher temperatures and drier conditions (Westerling, 2018). Climate change exacerbates fire risks already stoked by increasing development near the wildland-urban interface (WUI) that have made humans the main ignition source in California (Keeley and Syphard, 2018), as well as decades of fire suppression and underinvestment in preventive measures such as mechanical clearing or prescribed burns (Keeley and Syphard, 2021; Kolden, 2019; Radeloff et al., 2018). Wildfires, in turn, release GHG emissions that can contribute to climate change.

California experienced its most disastrous wildfire year on record in 2020. CalFire, the state agency responsible for leading California's wildfire prevention and suppression, reports that 1.7 million hectares burned in 2020 (CalFire, 2022). Many of the worst fire years in California's history have occurred in the past 20 years, with eighteen of the top 20 most destructive fires in terms of loss of life and property since

2000 and five in 2020 alone (CalFire, 2021). The 2020 fires have been followed by another extreme fire season with 1.0 million hectares burned in 2021.

In addition to the immediate loss of life and property, hospital admissions and premature deaths have likely happened because of the smoke exposure (Cascio, 2018; Fann et al., 2018; Reid et al., 2016; Wang et al., 2020), which blanketed large parts of the state with tens of millions of people with unhealthy air quality that persisted for months in some locations. Recent estimates put the economic costs of direct health costs at \$32 billion for 2018 (Wang et al., 2020). Future climate projections suggest that wildfires will become an increasingly important source of air pollution in the western U.S. (Ford et al., 2018; Liu et al., 2016).

When forests burn and are not balanced by vegetation regrowth, they shift from a natural sink to a source of carbon (van der Werf et al., 2017). This can represent a positive climate feedback loop in which increased GHG emissions contribute to climate change and further increase wildfire risk. Although wildfires are a natural feature of many ecosystems in California, the increase in severe and frequent wildfire events has raised the possibility of transformed post-fire ecosystems as new plant communities regrow following fire events that alter carbon

[☆] This paper has been recommended for acceptance by Pavlos Kassomenos.

* Corresponding author.

E-mail addresses: mjerrett@ucla.edu (M. Jerrett), mmarlier@ucla.edu (M.E. Marlier).

<https://doi.org/10.1016/j.envpol.2022.119888>

Received 10 April 2022; Received in revised form 1 July 2022; Accepted 31 July 2022

Available online 5 August 2022

0269-7491/© 2022 The Authors. Published by Elsevier Ltd. This is an open access article under the CC BY license (<http://creativecommons.org/licenses/by/4.0/>).

sequestration potential (Bowman et al., 2020). Regrowth relies on several factors including species burned, drought, and active replanting (Kibler, 2019). Even if long-term regrowth occurs, however, the carbon emissions occurring in the next 15–20 years will make it difficult to reach emission reduction targets needed to avert the 1.5 degree C increases in mean global temperature advocated by the Intergovernmental Panel on Climate Change (IPCC) (IPCC, 2018). Recent studies on the Australian wildfires have suggested that the magnitude of the fires in combination with the broadleaf species being burned likely places fires somewhere in between carbon neutrality and complete emissions (van der Velde et al., 2021).

In this short communication, we quantify the likely carbon emissions that occurred in 2020 from wildfire activity in California. We then situate these emissions in the context of other leading GHG emissions sectors in California. We conclude with policy recommendations for reporting of routine wildfire emissions and for increased investment in preventive measures.

1.1. Data and methods

Given substantial uncertainties among fire emissions inventories (Liu et al., 2020), we obtained multiple sources of fire emissions data for 2003–2020. First, we accessed satellite-based fire CO₂ emissions from the Global Fire Emissions Database version 4 with small fires (GFED4s) (1997–present; considered preliminary since 2017) and Global Fire Assimilation System version 1.2 (GFAS) using FIRECAM (Liu et al., 2020). These inventories represent “bottom-up” and “top-down” approaches to fire emissions estimation, respectively, and have shown the best correspondence with aerosol observations in North America (Carter et al., 2020). Although GFED and GFAS do not distinguish between wildfires and other landscape fires such as agricultural or prescribed burns, we expect this contribution to be minor in California. We also obtained wildfire-specific emissions estimates from the California Air Resources Board (CARB) (2000–2020), which combines individual fire perimeters with a wildland fire emissions model (CARB, 2020). The average across inventories is 127 mmt CO₂e for 2020 (ranging from 101 to 171 mmt CO₂e) and 18 mmt CO₂e for 2003–2019 (ranging from 15 to 22 mmt CO₂e).

We next compared wildfire emissions to sectoral GHG emissions for 2003–2020 to maintain consistency with availability for all three wildfire emissions inventories (CARB, 2021). In 2019, the CARB reported 418 mmt CO₂e emissions for all sources with the top 3 being transportation (166 mmt CO₂e), electrical power generation (59 mmt CO₂e), and industry (88 mmt CO₂e). For 2020, we assume constant emissions from the year 2019, as this was the last year where the CARB estimated sector-specific contributions to CO₂e, although this may be an underestimate due to potential emissions reductions during the COVID-19 pandemic (Liu et al., 2021).

Finally, to assess the socioeconomic benefits of reducing these CO₂ emissions, without considering the co-benefits of air pollution reductions, we apply the social cost of carbon (SC-CO₂). The SC-CO₂ is an estimate of the marginal damage caused by the emissions of an extra ton of CO₂ today in net present value. This value, adopted by the Biden administration in February 2021, is \$51 per ton with a 3% discount rate in 2020 USD (Interagency Working Group, 2016). We also apply a value of the SC-CO₂ where damages are restricted only to the United States. While this lower value of \$7.1 per ton in 2020 (Governmental Accountability Office, 2020) does not capture the global nature of emissions, it does allow us to attribute the local component of global damages caused by the fires.

2. Results

We first compared sectoral emissions to wildfire emissions, which indicate an approximate release of 127 mmtCO₂e in 2020, nearly seven times the 2003–2019 mean. From 2003 to 2019, California’s GHG

emissions declined by 65 mmt CO₂e (–13%), largely driven by reductions from the electric power generation sector. The 2020 fire season alone is two times higher than California’s total GHG emissions reductions and would comprise 49 percent of California’s 2030 total greenhouse emissions target of 260 mmtCO₂e (Fig. 1) (CARB, 2017).

Global monetized damages caused only by CO₂ from California’s fire emissions in 2020 is approximately \$7.09 billion in net present value when applying SC-CO₂ from the Biden Administration with a constant 3% discount rate. This value is reduced to approximately \$986.9 million in damage for the U.S. when considering only domestic damages. If we consider what this implies for California only, we calculate the median damages to California as a percent of U.S. damages in 2080–2099 implied by Hsiang et al. (2017). This gives values of 8.5%, 12.1%, 9.4% for Representative Concentration Pathways (RCPs) 2.6, 4.5, and 8.5 respectively. Scaling the previous U.S.-only value to the average of these percentages, this would imply that the carbon emissions-only damages for California would be approximately \$98.7 million in net present value.

3. Conclusions

In this short communication, we analyzed the likely CO₂e emissions from wildfires in California during 2020. Averaging three fire emissions estimates, we find that approximately 127 mmt CO₂e were emitted in 2020. We emphasize that our wildfire emissions estimates do not consider subsequent vegetation regrowth following fires so this is considered an upper bound for net wildfire GHG contributions to the atmosphere. This regrowth, however, could take decades or longer depending on the type of ecosystem that burned.

If we compare fire GHG emissions to total GHG emissions of 418 mmt CO₂e total in 2019, this amounts to a 30% increase in total emissions by all sectors. This makes the GHG emissions from wildfires the second most important source in the state, after transportation (166 mmtCO₂e), but above either industry or electrical power generation (88 and 59 mmt CO₂e, respectively). Viewed from the perspective of what this means for wildfire emission reductions from all other sectors combined, if we compare to reductions from 2003 to 2019 from 483 to 418 mmt CO₂e, the likely amount of increase from the fires is close to double all the emission reductions achieved in the state from 2003 to 2019.

The economic damages are informative for two key reasons. First, they represent a currently unquantified aspect of damages due to fires that are incurred globally, in the U.S., and in California itself. These damages should be counted in addition to fire control costs, damages from air pollution, and direct loss of life and property. Second, they provide a benchmark against which to compare the costs of prevention measures, based purely on climate change mitigation, and not including co-benefits of reduced pollution, lower property risk and loss, and other damages associated with fire risk. The Federal government and California recently signed a memorandum of understanding to increase to 1 million acres per year forest treatment to prevent wildfires in the State (State of California, 2020); in 2021, California invested \$1.5 billion in wildfire resilience programs, including prescribed burning (California Wildfire & Forest Resilience Task Force, 2022). If future treatments are moderately effective and reduce wildfire risk and subsequent CO₂e emissions by 20%, this would reduce 20% of the total \$7.09 billion in externality costs that we have calculated (i.e., \$1.42 billion in benefits). Including the carbon mitigation benefits further justifies the wildfire prevention costs.

Our analysis suggests several notable findings. First, wildfires in California have become a major and growing source of GHG emissions. Over the long to very long term, regrowth could alleviate some of the emissions, but this is unlikely to occur on the time scale necessary to meet near and medium-term emission targets needed to avert passing the 1.5 degree C threshold. Second, the magnitude of the emissions makes wildfires the second most important source of emissions in 2020 behind transportation emissions, and one that appears likely to grow

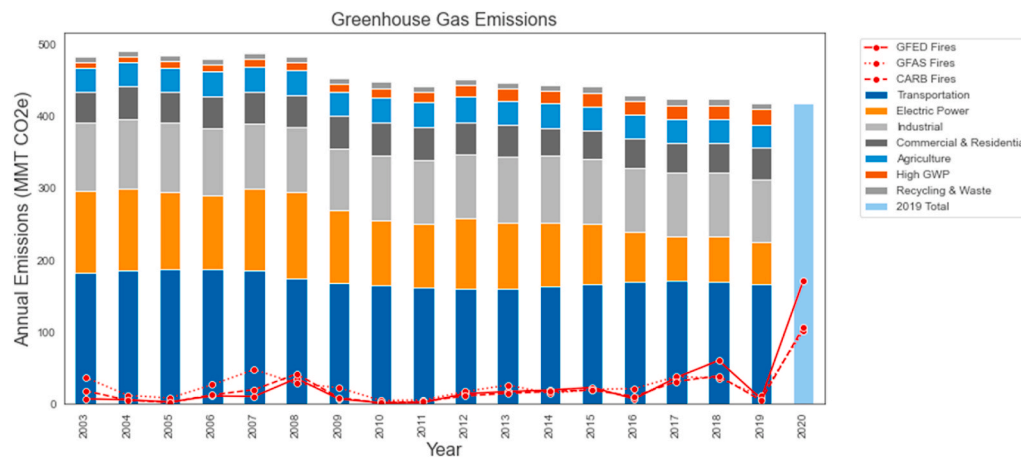


Fig. 1. Annual emissions from individual sectors and wildfire emissions. CARB, GFAS1.2, and GFED4s wildfire emissions shown as red lines (not considering vegetation regrowth). **Note:** Since data is not yet available, 2020 non-fire emissions are assumed to be equal to CARB 2019 estimates. (For interpretation of the references to colour in this figure legend, the reader is referred to the Web version of this article.)

with future climate change. Average wildfire emissions from the past five years (~46 mmt CO₂e from 2016 to 2020) ranks above the most recent individual contributions from the Commercial & Residential, Agriculture, Recycling & Waste, and High Global Warming Potential sectors. The latter includes fluorine-containing gases that destroy stratospheric ozone; sources include electricity transmission and distribution and semiconductor manufacturing. Third, wildfire emissions in 2020 essentially negate 18 years of reductions in GHG emissions from other sectors by a factor of two. Fourth, the additional global damages due only to the contribution of these emissions to climate change can be valued at \$7.09 billion.

The findings imply several research directions and policy actions. The externalities caused by fire emissions incurs damages globally and in California, and the economic value should be considered alongside other direct costs of fires (Feo et al., 2020), including prevention and suppression. Wildfire emissions are not routinely reported with other key emission sources such as transportation, industry, and power generation. While wildfire emissions tend to be more variable than other sectors, it is still important to track these emissions to ensure near and medium-term emission reduction targets are met. A likely consequence is that wildfire emissions have not received nearly the same level of societal investment or attention as emissions from other sectors. Although wildfires are to some extent natural occurrences, human activity contributes to making wildfires “unnatural disasters” through anthropogenic climate change and development at the WUI in fire prone areas. Moreover, forest management policies focused on fire suppression rather than on preventive measures such as mechanical clearing and prescribed burning activities also likely increases the risk of large, destructive wildfires. If fires are no longer in balance with ecosystem regrowth, we risk different vegetation communities regrowing with less potential for carbon sequestration. A need also exists to develop accessible quantitative tools for policymakers and the public to understand how wildfire risk can be reduced through better management, how much loss of life and property can be avoided, and how much it will cost to achieve these goals. This will allow for more accurate assessment of investments in improved forest management or prevention of development in fire prone areas at the wildland-urban interface.

Author statement

M. Jerrett: Conceptualization, Methodology, Writing – original draft, Reviewing & Editing. A. Jina: Methodology, Writing-Reviewing & Editing. M. Marlier: Conceptualization, Methodology, Writing – original draft, Reviewing & Editing.

Declaration of competing interest

The authors declare that they have no known competing financial interests or personal relationships that could have appeared to influence the work reported in this paper. Funding for Dr. Jerrett was supplied by the UCLA Center for Healthy Climate Solutions.

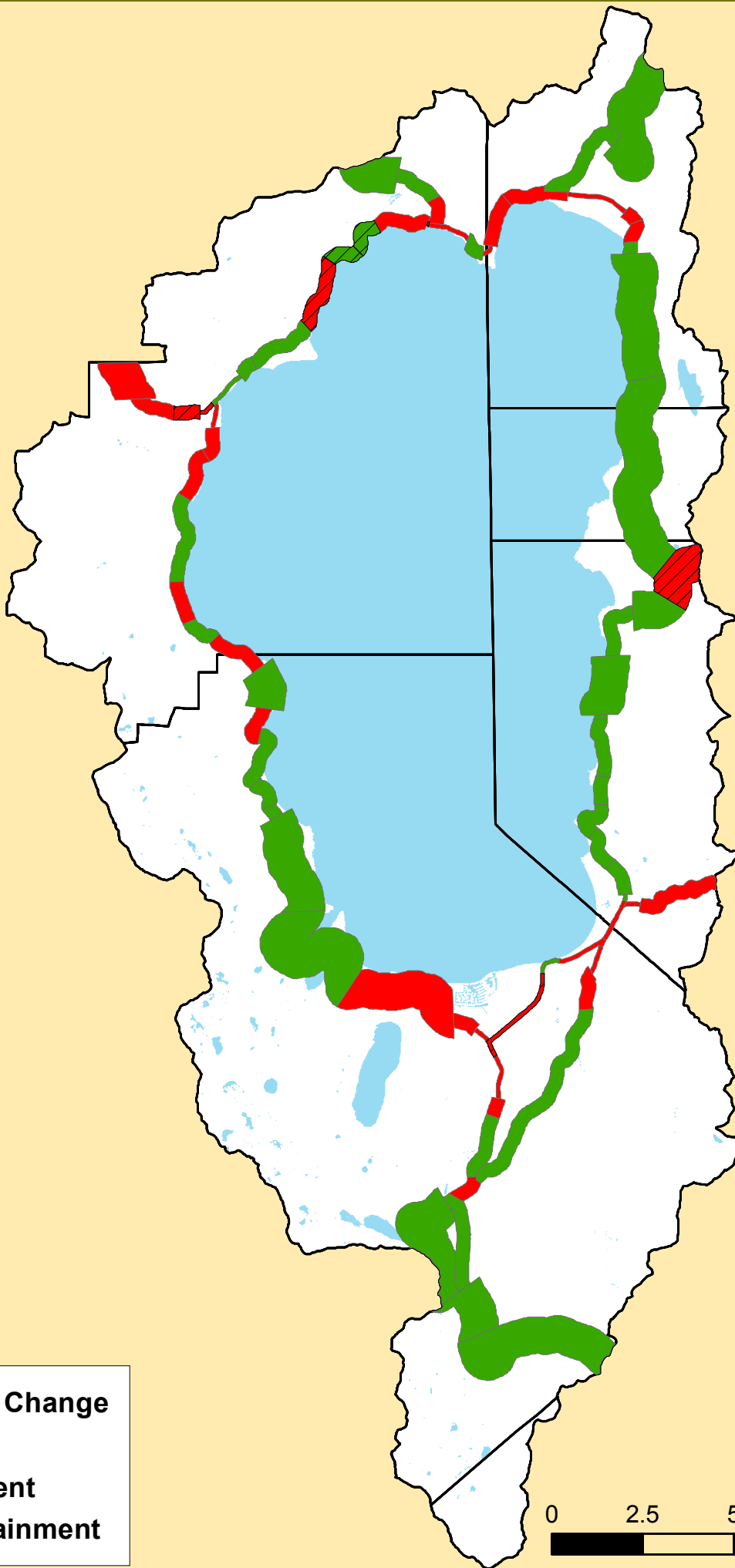
Data availability

Data will be made available on request.

References

- Abatzoglou, J.T., Williams, A.P., 2016. Impact of anthropogenic climate change on wildfire across western US forests. *Proc. Natl. Acad. Sci. USA* 113, 11770–11775. <https://doi.org/10.1073/pnas.1607171113>.
- Bowman, D.M.J.S., Kolden, C.A., Abatzoglou, J.T., Johnston, F.H., Werf, G.R. van der, Flannigan, M., 2020. Vegetation fires in the anthropocene. *Nat. Rev. Earth Environ.* 1–16. <https://doi.org/10.1038/s43017-020-0085-3>.
- CalFire, 2021. Top 20 most destructive California wildfire. URL, 8.13.21. https://www.fire.ca.gov/media/11417/top20_destruction.pdf.
- CalFire, 2022. Stats and events. URL, 6.9.22. <https://www.fire.ca.gov/stats-events/>.
- California Air Resources Board (CARB), 2017. California’s 2017 Climate Change Scoping Plan, pp. 1–132.
- California Air Resources Board (CARB), 2020. California Wildfire Burn Acreage and Preliminary Emissions Estimates.
- California Air Resources Board (CARB), 2021. California Greenhouse Gas Emission Inventory, 2021 Edition. Data available at: <https://ww3.arb.ca.gov/cc/inventory/data/data.htm>.
- California Wildfire & Forest Resilience Task Force, 2022. California’s Strategic Plan for Expanding the Use of Beneficial Fire. <https://fmr.fire.ca.gov/>.
- Carter, T.S., Heald, C.L., Jimenez, J.L., Campuzano-Jost, P., Kondo, Y., Moteki, N., Schwarz, J.P., Wiedinmyer, C., Darmenov, A.S., Silva, A.M. da, Kaiser, J.W., 2020. How emissions uncertainty influences the distribution and radiative impacts of smoke from fires in North America. *Atmos. Chem. Phys.* 20, 2073–2097. <https://doi.org/10.5194/acp-20-2073-2020>.
- Cascio, W.E., 2018. Wildland fire smoke and human health. *Sci. Total Environ.* 624, 586–595. <https://doi.org/10.1016/j.scitotenv.2017.12.086>.
- Fann, N., Alman, B., Broome, R.A., Morgan, G.G., Johnston, F.H., Pouliot, G., Rappold, A.G., 2018. The health impacts and economic value of wildland fire episodes in the U.S.: 2008–2012. *Sci. Total Environ.* 610–611, 802–809. <https://doi.org/10.1016/j.scitotenv.2017.08.024>.
- Feo, T.J., Evans, S., Mace, A.J., Brady, S.E., Lindsey, B., 2020. The Costs of Wildfire in California: an Independent Review of Scientific and Technical Information. California Council on Science and Technology. California Council on Science and Technology, pp. 1–248.
- Ford, B., Martin, M.V., Zelasky, S.E., Fischer, E.V., Anenberg, S.C., Heald, C.L., Pierce, J.R., 2018. Future fire impacts on smoke concentrations, visibility, and health in the contiguous United States. *GeoHealth* 2, 229–247. <https://doi.org/10.1029/2018gh000144>.
- Government Accountability Office, 2020. Social Cost of Carbon: Identifying a Federal Entity to Address the National Academies’ Recommendations Could Strengthen Regulatory Analysis. <https://www.gao.gov/assets/gao-20-254.pdf>.
- Hsiang, S., Kopp, R., Jina, A., Rising, J., Delgado, M., Mohan, S., Rasmussen, D.J., Muir-Wood, R., Wilson, P., Oppenheimer, M., Larsen, K., Houser, T., 2017. Estimating

- economic damage from climate change in the United States. *Science* 356, 1362–1369.
- Interagency Working Group, 2016. Technical Support Document: Technical Update of the Social Cost of Carbon for Regulatory Impact Analysis-Under Executive Order 12866. <https://www.whitehouse.gov/wp-content/uploads/2021/02/Technical-Support-Document-Social-Cost-of-Carbon-Methane-Nitrous-Oxide.pdf>.
- IPCC, 2018. Global Warming of 1.5°C. An IPCC Special Report on the impacts of global warming of 1.5°C above pre-industrial levels and related global greenhouse gas emission pathways. In: *The Context of Strengthening the Global Response to the Threat of Climate Change, Sustainable Development, and Efforts to Eradicate Poverty*. Cambridge University Press, Cambridge, UK and New York, NY, USA.
- Keeley, J.E., Syphard, A.D., 2018. Historical patterns of wildfire ignition sources in California ecosystems. *Int. J. Wildland Fire* 27, 781. <https://doi.org/10.1071/wf18026>.
- Keeley, J.E., Syphard, A.D., 2021. Large California wildfires: 2020 fires in historical context. *Fire Ecol* 17, 22. <https://doi.org/10.1186/s42408-021-00110-7>.
- Kibler, C.L., 2019. Multi-temporal Remote Sensing of Vegetation Regrowth after a Large Wildfire. Master of Arts Thesis. Department of Geography, University of California, Santa Barbara.
- Kolden, C.A., 2019. We're not doing enough prescribed fire in the western United States to mitigate wildfire risk. *Fire* 2, 30. <https://doi.org/10.3390/fire2020030>.
- Liu, J.C., Mickley, L.J., Sulprizio, M.P., Dominici, F., Yue, X., Ebisu, K., Anderson, G.B., Khan, R.F.A., Bravo, M.A., Bell, M.L., 2016. Particulate air pollution from wildfires in the Western US under climate change. *Clim. Change* 138, 655–666. <https://doi.org/10.1007/s10584-016-1762-6>.
- Liu, T., Mickley, L.J., Marlier, M.E., DeFries, R.S., Khan, M.F., Latif, M.T., Karambelas, A., 2020. Diagnosing spatial biases and uncertainties in global fire emissions inventories: Indonesia as regional case study. *Remote Sens. Environ.* 237, 111557 <https://doi.org/10.1016/j.rse.2019.111557>.
- Liu, J., Lipsitt, J., Jerrett, M., Zhu, Y., 2021. Decreases in near-road NO and NO₂ concentrations during the COVID-19 pandemic in California. *Environ. Sci. Technol. Lett.* 8, 161–167. <https://doi.org/10.1021/acs.estlett.0c00815>.
- Radeloff, V.C., Helmers, D.P., Kramer, H.A., Mockrin, M.H., Alexandre, P.M., Bar-Massada, A., Butsic, V., Hawbaker, T.J., Martinuzzi, S., Syphard, A.D., Stewart, S.I., 2018. Rapid growth of the US wildland-urban interface raises wildfire risk. *Proc. Natl. Acad. Sci. USA* 115, 3314–3319. <https://doi.org/10.1073/pnas.1718850115>.
- Reid, C.E., Brauer, M., Johnston, F.H., Jerrett, M., Balmes, J.R., Elliott, C.T., 2016. Critical review of health impacts of wildfire smoke exposure. *Environ. Health Perspect.* 124, 1334–1343. <https://doi.org/10.1289/ehp.1409277>.
- State of California, 2020. USDA Forest Service Pacific Southwest Region. *Agreement for Shared Stewardship of California's Forest and Rangelands*, pp. 1–9.
- van der Velde, I.R., van der Werf, G.R., Houweling, S., Maasakkers, J.D., Borsdorff, T., Landgraf, J., Tol, P., van Kempen, T.A., van Hees, R., Hoogeveen, R., Veefkind, J.P., Aben, I., 2021. Vast CO₂ release from Australian fires in 2019–2020 constrained by satellite. *Nature* 597, 366–369. <https://doi.org/10.1038/s41586-021-03712-y>.
- van der Werf, G.R., Randerson, J.T., Giglio, L., van Leeuwen, T.T., Chen, Y., Rogers, B.M., Mu, M., van Marle, M.J.E., Morton, D.C., Collatz, G.J., Yokelson, R.J., Kasibhatla, P. S., 2017. Global fire emissions estimates during 1997–2016. *Earth Syst. Sci. Data* 9, 697–720. <https://doi.org/10.5194/essd-9-697-2017>.
- Wang, D., Guan, D., Zhu, S., Kinnon, M.M., Geng, G., Zhang, Q., Zheng, H., Lei, T., Shao, S., Gong, P., Davis, S.J., 2020. Economic footprint of California wildfires in 2018. *Nat. Sustain.* 1–9 <https://doi.org/10.1038/s41893-020-00646-7>.
- Westerling, A.L., 2018. *Wildfire Simulations for California's Fourth Climate Change Assessment: Projecting Changes in Extreme Wildfire Events with a Warming Climate*. California's Fourth Climate Change Assessment, California Energy Commission. California's Fourth Climate Change Assessment. California Energy Commission.
- Williams, A.P., Abatzoglou, J.T., Gershunov, A., Guzman-Morales, J., Bishop, D.A., Balch, J.K., Lettenmaier, D.P., 2019. Observed impacts of anthropogenic climate change on wildfire in California. *Earth's Future* 7, 892–910. <https://doi.org/10.1029/2019ef001210>.



-  **Positive Change**
- Status**
-  **Attainment**
-  **Non-Attainment**

0 2.5 5 10 Miles



Strategies in and outcomes of climate change litigation in the United States

Sabrina McCormick^{1*}, Robert L. Glicksman², Samuel J. Simmens³, LeRoy Paddock⁴, Daniel Kim⁵ and Brittany Whited⁶

The courts have played a central role in climate policy, including the landmark Supreme Court case that led to the mandatory regulation of greenhouse gases by the United States. A wide variety of litigants have used the courts to affect policy outcomes at all scales. Therefore, to understand how the court addresses climate change is critical. Here we constructed and analysed a database of all the United State domestic climate lawsuits 1990–2016 (873), and collected qualitative data in the form of 78 in-depth interviews with litigants, involved scientists and advocates. We find proregulation litigants tend to win renewable energy and energy efficiency cases, and more frequently lose coal-fired power plant cases. Strategies such as the use of climate science and other science as well as collaboration in specific types of coalitions affect the outcomes of cases. Efforts to affect climate policy should consider these trends and outcomes.

Despite continuing concerns about the impacts of climate change, both the executive and legislative branches of the US government are moving to restrict their efforts to reduce greenhouse gas (GHG) emissions, including repealing or weakening emissions regulations and reducing funding for enforcement and climate research¹. Those seeking to minimize emissions and impacts, as well as to hold the government to account, are increasingly turning to the judicial branch to achieve their goals^{2–4}. At the same time, objectors to federal and state mitigation and adaptation actions have also litigated to preclude or reverse these actions.

There is an ongoing debate about the utility and outcomes of climate litigation^{5,6}. Although some claim that litigation has been an appropriate venue to force the government to address climate change or to bring lawsuits to prevent or limit government action with the potential to adversely affect or be adversely affected by climate change⁷, others contend that, at least to date, the courts have resisted litigants' attempts to make the courts a locus for climate decision-making⁸. Four typical goals of proregulatory plaintiffs and their constituents in climate-related lawsuits have been identified: force government regulators to take steps to reduce GHGs, change corporate behaviour, assign responsibility for impacts and change public debate about climate change issues⁹. Climate change cases raise challenges for litigants who pursue these goals that may not surface in other regulatory contexts. For instance, courts are reluctant to award compensation for climate-related harms due to difficulties in establishing a cause–effect link between the defendant's conduct and the plaintiff's harm^{10–13}. Issues of standing (whether or not a litigant has suffered the kind of harm that allows the case to be brought to the court with jurisdiction) may also pose significant obstacles to proregulatory litigants^{14,15}.

Cases have brought pro- and antiregulatory litigants face-to-face in a variety of litigation contexts^{16,17}. For example, a challenge by auto dealers to Vermont's GHG limits for motor vehicles resulted in the court upholding standards based on an exhaustive analysis of

the science that linked climate change to GHG emissions¹⁸. States and environmental groups convinced the US Supreme Court that carbon dioxide (CO₂) is a pollutant under the Clean Air Act (CAA), which requires the US Environmental Protection Agency (EPA) to make a determination as to whether emissions endanger public health and welfare. This ultimately led to the adoption of emission limits for motor vehicles¹⁹ and, later, the promulgation of limits on power plants under the Clean Power Plan²⁰. However, industry has challenged EPA's authority to enact the Clean Power Plan as a vehicle for restricting CO₂ emissions from existing coal-fired power plants (CFPPs)²¹. Environmental advocacy organizations have challenged environmental impact reviews based on the allegedly inadequate consideration of climate impacts²², whereas antiregulatory litigants have challenged agency decisions to list protected, endangered or threatened species based on the impacts of climate change²³.

These cases reflect some of the contexts in which courts are being asked to address climate impacts or to force executive branch officials to alter the manner in which they are doing so. The results turn on factors such as the roles courts think are appropriate for the judiciary in influencing important environmental, social and economic policy questions, how they react to scientific evidence that relates to climate change presented before agencies or during civil trials and what remedies they are willing to impose. Moreover, the answers will not be static, as science advances. Established legal theories and strategies, such as suits that force the consideration of climate impacts under the National Environmental Policy Act (NEPA), may receive a boost if uncertain or unforeseeable impacts are better substantiated. This may also strengthen proregulatory litigants' novel legal claims, such as efforts to compel governments to protect present and future generations from climate impacts in their role as trustees of their citizens' well-being^{24,25}. These public trust cases currently have had minimal success in the courts; however, developments in attribution science may make it easier for litigants to link the adverse effects of extreme events, such as storms or

¹Department of Environmental and Occupational Health, Milken Institute School of Public Health, The George Washington University, Washington, DC, USA. ²The George Washington University Law School, Washington, DC, USA. ³Department of Epidemiology and Biostatistics, Milken Institute School of Public Health, The George Washington University, Washington, DC, USA. ⁴The George Washington University Law School, Washington, DC, USA. ⁵Trachtenberg School of Public Policy & Public Administration, The George Washington University, Washington, DC, USA. ⁶New York University School of Law, Washington, DC, USA. *e-mail: sabmc@gwu.edu



OPEN

Radiofrequency EMF irradiation effects on pre-B lymphocytes undergoing somatic recombination

Elena Ioniță^{1,2}, Aurelian Marcu³, Mihaela Temelie¹, Diana Savu¹, Mihai Șerbănescu³ & Mihai Ciubotaru^{1,2}✉

Intense electromagnetic fields (EMFs) induce DNA double stranded breaks (DSBs) in exposed lymphocytes. We study developing pre-B lymphocytes following V(D)J recombination at their Immunoglobulin light chain loci (*IgL*). Recombination physiologically induces DNA DSBs, and we tested if low doses of EMF irradiation affect this developmental stage. Recombining pre-B cells, were exposed for 48 h to low intensity EMFs (maximal radiative power density flux S of $9.5 \mu\text{W}/\text{cm}^2$ and electric field intensity 3 V/m) from waves of frequencies ranging from 720 to 1224 MHz. Irradiated pre-B cells show decreased levels of recombination, reduction which is dependent upon the power dose and most remarkably upon the frequency of the applied EMF. Although 50% recombination reduction cannot be obtained even for an S of $9.5 \mu\text{W}/\text{cm}^2$ in cells irradiated at 720 MHz, such an effect is reached in cells exposed to only $0.45 \mu\text{W}/\text{cm}^2$ power with 950 and 1000 MHz waves. A maximal four-fold recombination reduction was measured in cells exposed to 1000 MHz waves with S from 0.2 to $4.5 \mu\text{W}/\text{cm}^2$ displaying normal levels of γH2AX phosphorylated histone. Our findings show that developing B cells exposure to low intensity EMFs can affect the levels of production and diversity of their antibodies repertoire.

Somatic or V(D)J recombination is the process that assembles in all jawed vertebrates the gene segments encoding the variable regions of the specific antigen immune receptors (T cell and Immunoglobulin IG) of the lymphoid T and B cells¹. This process occurs in lymphocyte precursors, is mediated by RAG (recombination activating gene proteins) recombinase a heterotetrameric complex made of a dimer of RAG1 and two monomers of RAG2^{2,3}. RAG1 a member of the DDE transposase/Integrase family is the key catalytic component of RAG. RAG binds specifically to recombination signal sequences (RSS) flanking germinal coding V, (D), J gene segments in the variable region at the IG and T cell receptor loci and catalyzes their rearrangement⁴. RAG recombination generates two DNA hairpins at the coding ends and two blunt double stranded DNA cuts at the signal ends. RAG maintains the paired cleaved ends in proximity and allows the ubiquitous set of non-homologous end-joining (NHEJ) DNA repair enzymes (Artemis, ATM, DNAPk, XRCC4, DNA Ligase IV) to resolve the hairpins and join the cleaved ends. For B and T lymphocytes recombination occurs at two stages during their differentiation⁵. We will discuss only the B lineage development in the bone marrow. First two rounds, D to J (in pre-pro stage) followed by V to DJ recombination (in late-pro stage) occur in pro-B cells at their Ig Heavy chain locus (*IgH*). Once *IgH* locus is rearranged, expressed *Ig μ* together with a surrogate light chain comprising $\lambda 5$ Vpre B proteins and two $\text{Ig}\alpha$, β signaling subunits assemble the pre-B cell receptor (pre-BCR)⁶, which marks the large pre-B cell stage. Stromal bone marrow cells secreted interleukin IL-7 binds to their receptor (IL-7R), a signal which is transduced as pro-survival and proliferative⁷. First, IL-7R signals through Janus Kinase 3-(JAK-3)⁸ phosphorylating and recruiting the signal transducer and activator of transcription 5A and B (STAT5A and B)^{9,10} which stimulate transcription of *Ccnd3* encoding Cyclin D3¹¹ and of the B cell lymphoma 2(*bcl2*) gene¹². Both Cyclin D3 and the anti-apoptotic BCL2 help pre-B cells through cell cycle G1 checkpoint allowing the replication of their DNA. Secondly, IL-7R signals in large pre-B cells through phosphoinositide 3-kinase (PI3K)¹³ and protein Kinase B (AKT) phosphorylating the forkhead box O 1, 3 (FOXO1,3) transcription factors, modification which exports them from nuclei and targets the proteins for degradation^{14–16}. FOXO1, 3 activate *e-rag* enhancer and *rag1*, 2 genes transcription^{14,17}. In large pre-B cells IL-7R also signals via the nuclear factor kappa light chain

¹Department of Physics of Life and Environmental Sciences, Horia Hulubei National Institute for R&D in Physics and Nuclear Engineering, 077125 Măgurele, Ilfov, Romania. ²Department of Immunology, Internal Medicine, Colentina Clinical Hospital, 72202 Bucharest, Romania. ³Center for Advanced Laser Technologies, National Institute for Laser Plasma and Radiation Physics, 077125 Măgurele, Ilfov, Romania. ✉email: mihai.ciubotaru@nipne.ro

enhancer of activated B cells (NF- κ B) stimulated by AKT phosphorylation of IKK α serine 23¹⁸. NF- κ B activates Cyclin D4 kinase which targets FOXO1 for phosphorylation and repression¹⁹. By inhibiting FOXO1, or phosphorylating STAT-5, IL-7R signals are transiently downregulating RAG proteins in large pre-B cells. After four to five rounds of replication the large pre-B lymphocytes get under the influence of cell surface pre-BCR receptor aggregation and stimulation (in absence of a bonified ligand), a signal which antagonizes that of IL-7R, induces cell cycle arrest and transitions cells towards small pre-B stage²⁰. Stimulation of pre-BCR cascades through RAS and extracellular signal- regulated kinase (ERK) upregulating the E2A transcription factor expression. E2A binds both Igk intronic and Igk 3' enhancers making the *Igk* light chain locus accessible for recombination²¹. Another effect of pre-BCR stimulation signals through spleen tyrosine kinase(SYK) and B cell-linker protein(BLNK) which together repress PI3K and AKT but stimulate mitogen activated p38 kinase which activates FOXO1 to express RAG^{13,20,22}. Consequently, in small pre-B cells subsequent V to J rearrangements occur at *Ig L k* or λ light chain loci. Upon completion of a successful V to J recombined allele, the cell develops into naïve immature B cell, exposing IgM B cell receptors (BCR).

Interference of V(D)J recombination with other concurrent exogenous factors favoring DNA DSBs, like ionizing or EM irradiation can induce DNA damage which may lead to oncogenic translocations such as those described in acute lymphoblastic leukemia (ALL)^{23,24}. Exposure of human blood lymphocytes from healthy donors to strong EMFs (2 h irradiation with sinusoidal pulses at 4×10^5 V/m 50 Hz with a carrier wave of 10 Hz²⁵) causes DNA DSBs and chromosomal lesions whose severity correlate with the intensity of the applied fields and the duration of exposure. However, less clear results come from studies with irradiated lymphocytes using low intensity, high radiofrequency(RF) EMFs (3 kHz–300 GHz)²⁶. Most of these studies have assessed the levels of EMF inflicted DNA single and DSBs on lymphocytes using the microgel electrophoresis technique or 'comet assay', which detects breaks with a sensitivity limit of 50 strand events per diploid cell²⁷. RF EM irradiation from cell phones was first studied by Phillips et al. in Molt-4 human lymphoblastoid cells exposed for 2–21 h to fields of 813.5 and 836.5 MHz with specific absorption rate (SAR) (2.4–26 μ W/g)²⁸. Variable degree of DNA damage is reported, mainly induced by high SAR values waves (increased at 24 or 26 μ W/g and decreased at 2.4 or 2.6 μ W/g) and longer exposures (21 h versus 2 h). Another study by Mashevich et al.²⁹ reveals that continuous 72 h exposure of human peripheral blood lymphocytes to EMFs of 830 MHz waves, with SAR ranging from 1.6 to 8.8 W/kg lead to SAR dependent aneuploidy with specific abnormalities on chromosome 17. However, in vitro exposure of human blood lymphocytes for only 2 h to short pulses of 2450 MHz, at an average power of 5 mW/cm²³⁰ showed no significant DNA damage as assessed by alkali comet assays. No signs of genotoxicity were found when total human blood leukocytes were in vitro exposed for 24 h either at a continuous or a pulsed-wave 1.9 GHz EMF with a SAR ranging between 0.1 and 10 W/Kg³¹. Absence of significant DNA damage response in human blood lymphocytes was also reported by a study by Stronati et al.³² in which blood specimens were continuously exposed for 24 h at a Global System Mobile Communication generated EMF of 935 MHz with a SAR of 1 or 2 W/Kg³². Similar negative results with respect to EMF induced DNA damage was reported in a study by Hook et al.³³ with cultured Molt-4 human lymphoblasts exposed for 24 h to four types of frequency mobile network modulations around 815–850 MHz with SAR values ranging from 2.4 to 3.2 W/Kg³³.

In our work we test the effects of in vitro irradiating V(D)J recombining pre-B cells with very low doses of RF EM waves. RAG stimulation is obtained either mimicking a pre-BCR stimulus with AKT inhibition, or with a stress inducible Abelson (Abl) kinase inhibitor response via STAT5 phosphorylation inhibition. For both stimuli, near 950–1000 MHz RF EMF cell irradiation, in the absence of detectable DNA DSBs, causes a four-fold reduction in recombination levels in exposed pre-Bs versus that assessed in non-irradiated cells.

Results

Design and specific experimental conditions used to assess *Ig k* locus rearrangements. Our study tests how gene recombination levels are influenced by exposure to EMFs with distinct emitted frequencies and power levels (dose–response). In vitro grown vAbl transformed murine pre-B cells stimulated to recombine V(D)J are exposed to a broadband (0.8–3 GHz) emission antenna which broadcasts an EMF from a RF generator (Fig. 1A upper region). For all experiments we standardized our cellular growing conditions to control irradiation parameters (see Supplemental Material section S1 and Fig. 1Sa and b). RAG expression and V(D)J recombination can be induced in vAbl transformed pre-B cells(differentiating them in small pre-B cells) upon stimulation either with an Abl tyrosine kinase inhibitor imatinib(mesylate of imatinib)(IMA)^{34,35}(Supplemental Material Fig. 1Sb growing dish wells 1, 2 and 3), or with an AKT inhibitor GSK-690693(GSK)¹⁹(wells 4, 5 and 6, Fig. 1Sb). Whereas IMA induces RAG by inhibiting vABL-1 tyrosine kinase via a stress-inducible GADD45 α action^{17,34,35}, GSK acts as AKT inhibitor, reducing NF- κ B and FOXO1 inhibitory phosphorylation (by CDK4) thus, mimicking a physiologic pre-BCR stimulation¹⁹ (see Supplemental material section S2). Time course experiments with RAG induction in vAbl pre-B cells using both drugs show maximal RAG1 levels after 36 h of stimulation (see Supplemental material S2 and Fig. 2Sa and b). Using this finding, after 48 h post drug induction (to allow recombination), all synchronized cultured cells were harvested and their genomic DNA extracted. A previously described two-steps nested PCR (polymerase chain reaction) which assesses the recombination extent taking place at *Igk* kappa light chain locus (chromosome 6, locus schematic and primer positions shown in Fig. 1B), is templated with the equivalent genomic DNA extracted from 2×10^6 cells from each tested culture set^{36,37}. In the absence of V(D)J recombination (control reactions with no stimulation Fig. 1C lane 2) the variable region V and J segments in germline configuration are too far apart on the chromosome to yield appropriate amplification products. The PCR amplification products obtained only from recombined templates (Fig. 1C lane 3) are separated after electrophoretic migration on 1.5% agarose gels and visualized after fluorescent staining with SYBR green (schematic lower drawing Fig. 1A, and gel scan Fig. 1C). This typical nested PCR reaction reports *k* locus recombination events with two detectable products; the predominant one Vk-Jk2 of 280 bp (95%) and Vk-Jk1 of

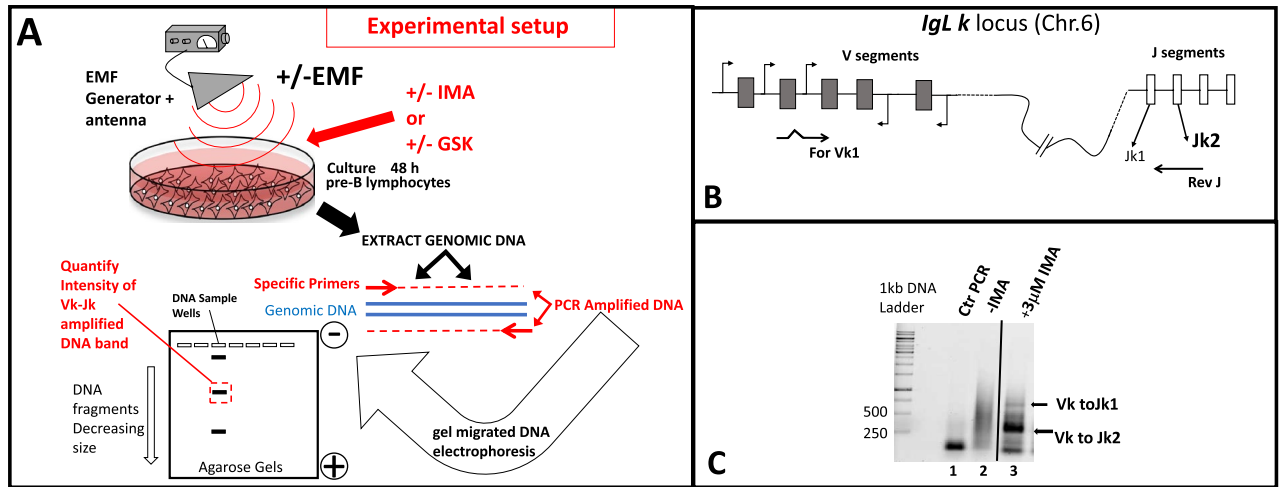


Figure 1. (A) Schematic depiction of the flow chart of the experimental design. Murine A-70 vAbl pre-B cells grown with or without exposure to Electromagnetic field influence(EMF), in the absence or presence of RAG stimulation either by Mesylate of Imatinib (IMA) or by GSK-690693(GSK), are harvested and their genomic DNA subjected to a two-steps PCR recombination assay identifying Vk to Jk rearrangements at their *IgL kappa* loci. The electrophoretically separated recombination products (Vk-Jk) are quantified by densitometry to assess the extent of locus rearrangements influenced by EMF. (B) Schematic configuration of *IgL kappa* locus on Mouse chromosome 6, and the positioning of the primers used in the assay. (C) PCR reactions electrophoretically separated in agarose gel stained with Sybr green identify the recombined products (arrows show Vk to Jk1 and Vk to Jk2) in lane 3 versus, control reactions lane 1 without genomic DNA, lane 2 templating genomic DNA from uninduced cells (in germline configuration). Such recombination amplified reactions are then used for densitometry quantifications. The entire gel from which (C) was cropped displaying amplifications (Vk to Jk response) from cells treated with a wide range of increasing IMA concentrations, is shown in Supplemental Material Fig. 3Sa.

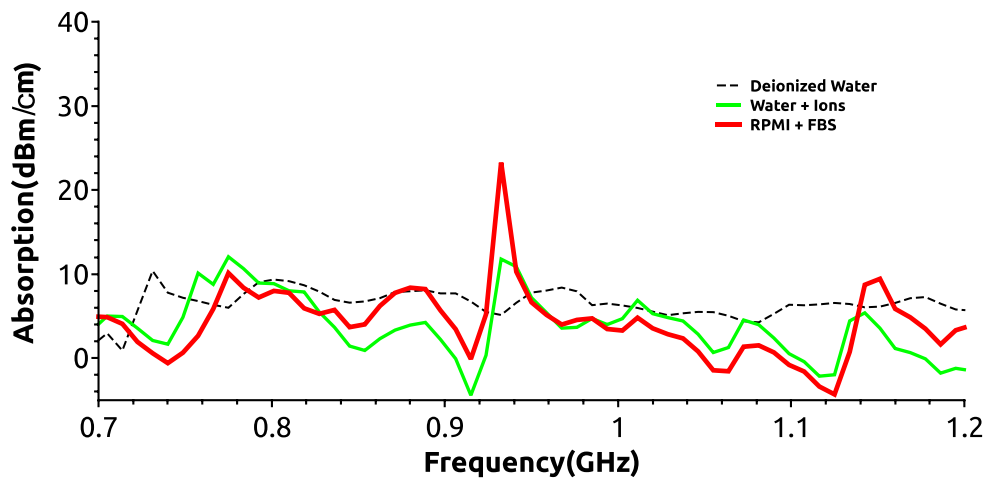


Figure 2. Absorption spectra measurements of filtered deionized water (dashed thin black line), tap water (green thick line Water + Ions) and RPMI cell culture medium with 10% fetal calf serum (FBS)(red thick line RPMI + FBS) All measurements were done using a Keysight-AGILENT-HP N9935A spectrum analyzer as described in “Methods” section.

700 bp (5%)³⁶ (Fig. 1C lane 3). Densitometric quantifications of the DNA Vk-Jk2 recombination products allow us to assess the EMF influence on recombination (Fig. 1A lower drawing). A dose-response (recombination) effect obtained with increasing IMA concentrations in 48 h stimulated pre-B cells is shown in supplementary Fig. 3Sa, gel and quantified data from three such experiments shown in Fig. 3Sb histograms. The lowest drug concentration (3 μM for IMA and of 10 μM for GSK,) for which maximal recombination effects are obtained, is used for each drug in our irradiation assays. For linear range quantifications of the image scans each reaction uses genomic DNA template at least at three distinct dilutions from the cellular extraction stock solution and the final result may be reported as an average of the three quantified products values corrected by the histone H1 band intensity of the corresponding sample. In Supplemental material in Fig. 3Sc an 3Sd a set of nested PCR

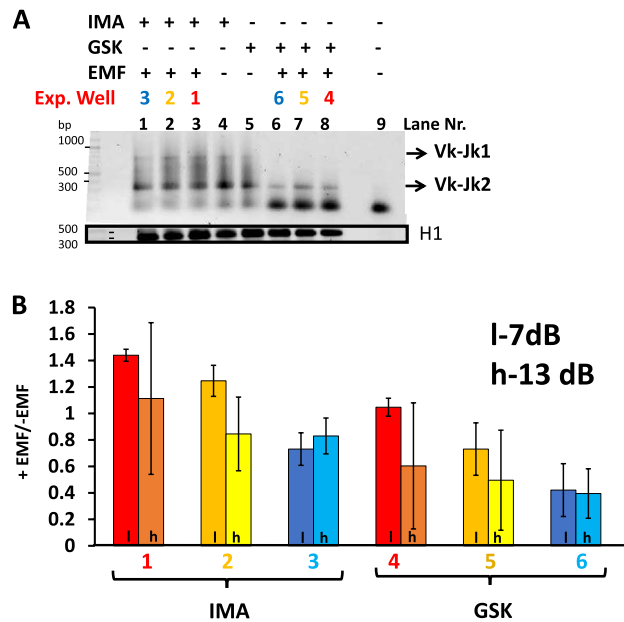


Figure 3. A two steps PCR recombination assay is used to identify Vk to Jk1 or Vk to Jk2 rearrangements from pre-B cells upon RAG induction with Imatinib or GSK. **(A)** A Sybr Green stained 1.5% Agarose TBE gel in which the recombination PCR reactions templated with initial 1:5 dilutions of genomic DNA extracted from each distinct cell treatment lot (2×10^6 cells) are electrophoretically resolved. The cells were either unexposed (gel reaction lanes 4 and 5) or subjected for 48 h to 1 GHz EMF irradiation (lanes 1 to 3 and 6 to 8) with the generator setting at 13 dBm. The color code designating the positions of exposed EMF (exp.Well) wells in the dish is the same with the one used in supplementary Fig. 1Sb. Last lane (9) of the gel, -DNA control reaction. The bottom black box (cropped from a distinct gel) displays Histone H1 PCR reactions templated with the same amount of genomic DNA as the recombination reactions above (control genomic DNA). **(B)** Identified Vk to Jk2 recombined products were quantified from scanned gels corresponding to PCR reactions from cells +/- Irradiation and the calculated ratios of band intensities expressed +EMF/-EMF (irradiated/nonexposed) for each well (color code consistent with that shown in Fig. 1S). The histograms represent the average values of three independent quantified experiments. EMF-Electromagnetic Field, Recombination pharmacological stimuli (Imatinib, IMA) versus (GSK-690693, GSK). H1, histone H1 control reaction PCR reactions. Darker font histograms correspond to lower 7 dBm (l) and brighter to higher 13 dBm (h) generator power settings.

reactions templated with serial dilutions of input genomic DNA from IMA stimulated cells, followed by quantification of the signal are shown to illustrate that the assay responds linearly in its amplified Vk-Jk2 band intensity.

EM wave absorption spectrum of the cell culture medium. We measured how the EM waves with frequencies ranging from 700 to 1224 MHz are absorbed by the fetal bovine calf serum supplemented cell culture medium (RPMI + FBS in Fig. 2) in which the pre-B cells are cultured. For comparison only absorption measurements were also performed for deionized water (conductivity $< 5 \mu\text{S}/\text{cm}$), and for ions containing unfiltered tap water samples (see Methods Water + ions, Fig. 2). The measurements were done using a setup in which an emission and a reception horn antenna were spaced 1 m apart with the liquid sample container positioned in the vicinity (1 cm) of the later (see Supplemental material Fig. 4S). The emission antenna was connected to a generator and signals from the receiver antenna were collected and recorded by a standard spectrum analyzer. In Fig. 2 are presented the background corrected absorption spectra per 1 cm width of each liquid sample measured. A well-defined absorption peak is observed at 938 MHz for the RPMI + FBS medium sample which is twice as large as the others measured at this frequency. All samples have similar absorption values for the rest of the tested spectral frequencies. This finding is important since the range of frequencies (720 MHz, 850 MHz, 950 MHz, 1 GHz and 1.2 GHz) to be used for cell irradiation centers our window of exposure between 950 MHz and 1 GHz, proximal to the maximal culture medium absorption peak.

To test how the cell growing medium affects the electric intensity of the exposing fields, EMF electric flux density (D displacement) measurements were made inside the incubator for each mentioned frequency, in the absence or presence of culture medium in the culture plate (Supplemental Material S3 and Fig. 5S). Values greater than one of the $D_m/D_{\text{air_inc}}$ (1.8–1.95) ratios measured between 750 and 1000 MHz (Supplemental material section S3 and Fig. 5Sc) show in this range, the complete RPMI + FBS cell growing medium selectively potentiates the developed fields.

EMF irradiation effects on V(D)J recombination in v-Abl pre-B cells. Murine vAbl pre-B cells were grown under normal conditions or stimulated either with 3 μM IMA or with 10 μM GSK in the presence/absence of an antenna which emits a generator controlled EMF from waves of 720 MHz, 850 MHz, 950 MHz,

1 GHz, 1.224 GHz each with 7 or 13 dBm output power setting. For all exposures, the antenna was held at 2.4 cm above the composite 6 wells plate as depicted in Supplemental material Fig. 1Sb (lower profile drawing) consistently keeping it in the same location with respect to the incubator walls (Supplemental material S1 and Fig. 1S). Cells were grown +/- EMF constant continuous exposure for 48 h with +/- IMA or +/- GSK. In Fig. 3A is shown a gel with resolved reactions either from nonexposed cells (lanes 4 and 5) or from cells continuously subjected for 48 h to the influence of 1 GHz fields (gel for generator set at 13dBm-h), with both RAG induction treatments (plate Exp. wells IMA 1, 2, 3 and GSK- 4, 5, 6 with color code shown in Supplemental material Fig. 1Sb). Visually one can see, a reduction of Vk to Jk2 recombination products obtained in reactions from irradiated cells versus those from similarly drug induced, non-irradiated cells (see Fig. 3A compare lane 4 non-irradiated to reactions in lanes 1–3 exposed for IMA, and lane 5 unexposed to lanes 6–8 from irradiated GSK stimulated cells). The irradiating effects are most pronounced in the plate wells closest to the actively emitting antenna elements ($\lambda/2$ for 1 GHz waves use as main element the 15 cm one located near wells 3 and 6 (Supplemental material Fig. 1Sb) hence, recombination reduction for plate Exp. wells 3, 6 > 2, 5 > 1, 4 or correspondingly gel lanes 1, 6 > 2, 7 > 3, 8). The value of the calculated ratios between recombination Vk-Jk2 PCR band intensities obtained from irradiated/non-irradiated(+EMF/-EMF) cells for all tissue culture wells are shown as histograms in Fig. 3B. Values less than one show specific Vk-Jk2 recombination reduction associated with EMF irradiation.

Similar experiments were performed with EMF exposures at 720, 850, 950, 1000 and 1224 MHz (each frequency centers on a different antenna element), generator setting either at 7 dBm or 13 dBm. To display a wider palette of EMF dose exposure values we summed up the data from all of the wells in Fig. 4 which displays cell Vk-Jk2 recombination Fractions(+EMF/-EMF -ordinates), against logarithm of measured irradiating power flux density S values ($\mu\text{W}/\text{cm}^2$ -abscissas) at each location. Each row of the two panels is for a distinct frequency with panels for each drug located on the same column: Fig. 4A(GSK- left) and B(IMA- right). Consistently all diagrams show power dependent reduction in cellular Vk-Jk2 recombination. S values into the emitting antenna were calculated from antenna recorded voltages, circuit impedance, and antenna constructive elements dimensions and reflect S in the air inside incubator, surrounding the involved culture well. In each panel with dotted black lines we pointed the EMF power dose required to induce a two-fold Vk-Jk2 recombination reduction from that of the non-irradiated lot (+EMF/-EMF 50% reduction shown as 0.5 ratio for Vk-Jk2, Cellular Recombination Fraction). In Fig. 4 when 50% recombination reduction (exposed versus non-irradiated cells) is not reached, the minimal recombination ratios obtained and their inducing S levels are shown in parenthesis. The most remarkable finding of our study is that even for such a small window of frequencies (between 720 and 1224 MHz), the power dose-response effect is dramatically influenced by the frequency of the irradiating EMF. If at 720 MHz one reaches a 0.56/0.70 maximal recombination reduction for 9.49 $\mu\text{W}/\text{cm}^2$ exposure, similar reduction in recombination effects are obtained at 950 MHz and 1 GHz with only 1/15th respectively 1/20th (0.63 or 0.43 $\mu\text{W}/\text{cm}^2$) the power used at 720 MHz. The power dose-cell recombination response curves at 950 MHz and 1 GHz EMFs show by far the most accentuated measured effects (for both drugs). For GSK at 1 GHz irradiation, an almost four-fold decrease in V(D)J recombination (from 0.90 to 0.22) is observed over a moderate increase in S exposure from 0.1 to 4.53 $\mu\text{W}/\text{cm}^2$ (see second from the bottom panel in Fig. 4A GSK 1000 MHz). Both curves in Fig. 4 for 1 GHz display an abrupt recombination decrease at a small increase in S (0.25–1 $\mu\text{W}/\text{cm}^2$) after which the cellular effect plateaus out over a larger window of higher exposure power S values (1–4.5 $\mu\text{W}/\text{cm}^2$). To emphasize the influence of EMF frequency Table 1 shows how recombination fractions (+EMF/-EMF) vary at a relatively constant $\approx 1.5 \mu\text{W}/\text{cm}^2$ irradiating power flux density S exposure level for all tested EMF frequencies. At this small irradiating power no effect is detectable at 720 MHz, whereas at 950 MHz a two-fold recombination reduction is measured reaching almost three-fold recombination inhibition at 1 GHz.

To circumvent the cellular growing medium polarization effects (which significantly change polarity at 720 MHz and above 1100 MHz, Supplemental material 3S and Fig. 5Sc) or its enhanced wave absorption at 938 MHz (Fig. 2), we intentionally represented in Fig. 5 the recombination fractions for two constant electric field intensity E exposure values, measured inside the medium; one of 0.4 V/m (Fig. 5A.) and the other of 0.6 V/m (Fig. 5B). The approximative intensity of the emitted electric field was calculated in the cell medium from the measured electric flux density (D_m displacement) values³⁸ described in the previous section, and averaged for the central plate well. For both E values and both pharmacological stimuli (IMA-red and GSK-blue) the most accentuated plots concavities (maximal irradiation induced recombination reduction effect), correspond to 950–1000 MHz. At both E values represented in Fig. 5 the recombination ratios are unaffected by EMFs at 720 MHz. In contrast, at 1000 MHz, a two-fold reduction is observed for the 0.4 V/m EMF intensity, and a three (IMA) to four-fold (GSK) decrease is measured at the stronger 0.6 V/m field exposure. The electric fields dose exposures -recombination reduction effects in Fig. 5 and those reported for EMFs power dose exposures in Fig. 4 are qualitatively similar. These data strongly suggest that exposure even to very low irradiation doses from specific 900–1000 MHz radiofrequency waves dramatically affect in irradiated pre-B cells the efficiency of V(D)J recombination at their Ig kappa locus.

Histone H2AX phosphorylation shows no detectable DNA DSB damage cell response in EMF exposed pre-B cells.

We asked whether the observed EMF irradiating effects on V(D)J recombination are due to DNA damage and presence of unrepaired DSBs. Impairment of DNA integrity can be assessed by the extent with which irradiation induces H2AX histone phosphorylation (γH2AX), a process associated with DNA DSBs and their intranuclear repair. The nuclear γH2AX repair foci are the fairest indication that the NHEJ DNA repair machinery acts properly in these cells repairing DSBs caused by any DNA lesion-causing agent^{39,40}. We grew cells under similar stimulation (+/- IMA, +/- GSK) and +/- EMF irradiation conditions (7 dBm or 13 dBm generator power settings at 950 MHz) with those described above but instead of extracting DNA, the harvested cells were fixed and doubly stained: (a) with Hoechst 33342 dye (for nuclear total DNA staining in

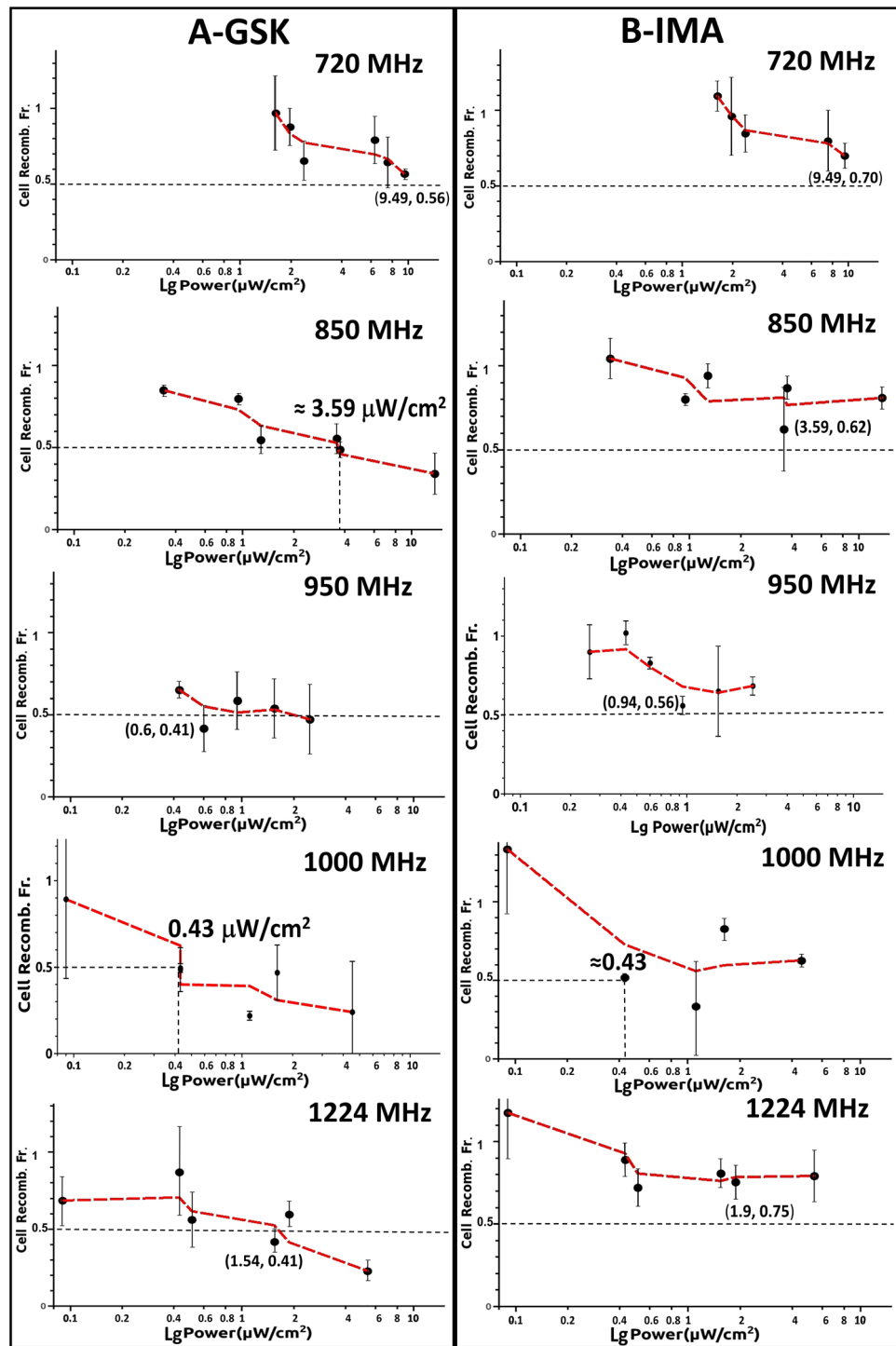


Figure 4. The EMF power dose-cell recombination response curves at 720, 850, 950, 1000 and 1224 MHz for both types of pharmacological agents stimulating RAG expression (A) (GSK-690693, GSK), and (B) (Imatinib, IMA). Cell Recomb. Fr. expresses the ratio values of measured Vk-Jk2 recombination quantified from cells grown in +EMF/-EMF (irradiated/non-exposed) conditions. Bottom abscissa displays logarithm of S power flux density values (Power $\mu\text{W}/\text{cm}^2$) measured around the emitting antenna inside the CO₂ 5 vol%, and 95% water humidity incubator air conditions, expressed as a single range in all panels (logarithmic scale). The black dotted line denote a level of EMF induced two-fold recombination reduction (Cell recomb. Fr. = 0.5), whereas when this level is not reached in the experiment the coordinates of the lowest obtained Cell Recomb. Fr. are given. The red dotted line connecting markers is just a Moving Window Average line which accounts for the average between successive data points displaying the trend of data variation. The error bars represent standard deviation (SD) values from three independent experiments.

Fraction recombination +EMF/-EMF (EMF at $S \approx 1.5 \mu\text{W}/\text{cm}^2$)		
Frequency (MHz)	Response stimulus	
	GSK	IMA
720	0.97 ± 0.2	1.09 ± 0.1
850	0.56 ± 0.1	0.8 ± 0.1
950	0.53 ± 0.2	0.65 ± 0.3
1000	0.38 ± 0.1	0.46 ± 0.3
1224	0.41 ± 0.1	0.8 ± 0.1

Table 1. Lists the measured cell recombination fraction (+EMF/-EMF) at a relative constant power flux density S value of $1.5 \mu\text{W}/\text{cm}^2$ for all tested frequencies.

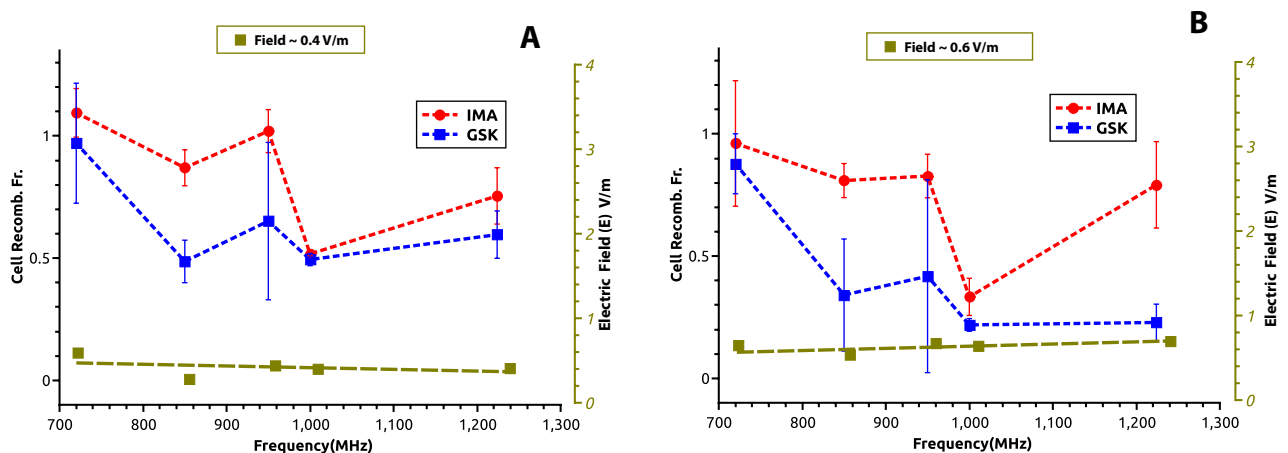


Figure 5. Variation of cell recombination fraction (+EMF/-EMF) with the field irradiation frequency shown in each panel for a constant receiver EMF electric intensity field E calculated in the cell culture medium. (A) EMF electric field intensity E 0.4 V/m, (B) EMF electric field intensity E 0.6 V/m. The pharmacological agents stimulating RAG expression GSK-690693, GSK-blue, and Imatinib, IMA-red. The pale green dotted line shows the relative constant distribution of measured electric field as a function of frequency. The error bars represent standard deviation (SD) values from three independent experiments.

blue) and (b) immunofluorescently with anti γH2AX antibodies yielding a Cy2 green fluorescence which identifies DNA DSBs repairing γH2AX foci⁴⁰(see Methods). As a DNA DSBs control an extra lot of cells were either noninduced or similarly drug treated but instead of EMF they were subjected to a quick 1 Gy, X ray irradiation dose prior to their harvest. Nine immunofluorescent images are shown in Fig. 6 A-I where blue contours show the cell nuclei and the green dots the DNA DSBs repairing γH2AX foci from: cells treated with +/- DMSO solvent control, +/- GSK, +/- IMA, +/- EMF set at 950 MHz, 7dBm exposure and the control lot of cells exposed to 1 Gy X ray. Such foci were also counted and their number reported per cell to a number of total 100 counted cells gathered from more than twenty successive field views for each experimental lot (shown as histograms in Fig. 6J) for both 7 dBm and 13 dBm generator power settings). 1 Gy dose X ray irradiated cells are shown in Fig. 6B control with DMSO solvent, E with IMA, H with GSK and in 6 J the corresponding foci/cell counted histograms. All images (Fig. 6B,E,H) and the quantified histograms from X ray irradiated cells show similar and considerable DNA DSB lesions with consequent accumulation of γH2AX repair foci, regardless of the chemical stimulus used. On the contrary, the long 48 h EMF exposure experiments do not show signs of detectable unrepaired DNA DSB damage (Fig. 6C DMSO solvent, F with IMA and I with GSK, and counted foci/cells in Fig. 6J), above the background level of non-irradiated control cultures (Fig. 6A,D,G and ctrl. histograms in Fig. 6J). Exposing for 48 h cells to EMF, regardless of drug treatment, does not seem to inflict significant/ cumulative unrepaired DNA DSB lesions, (unlike those caused even by mild quick irradiation with 1 Gy dose of X rays). Only such DNA injuries could have caused a detectable accumulation of repairing γH2AX foci at the time of their harvest. Indirectly, these results suggest that the significant EMF induced reduction in pre-B cells recombination reported in Figs. 3B, 4, 5 and Table 1 is probably not caused by an enhanced level of accumulated unrepaired DNA DSBs.

Discussion

V(D)J recombination the central process in lymphocyte development physiologically generates DNA DSBs during its course, when cells become susceptible to external sources of DNA damage⁵. Our work tests how pre-B lymphocytes exposure to low dose EMFs of frequencies ranging from 720 MHz to 1.2 GHz, used in utilitarian purpose telecommunication, affects the efficiency of their *Igk* loci rearrangements. First, we established a setup

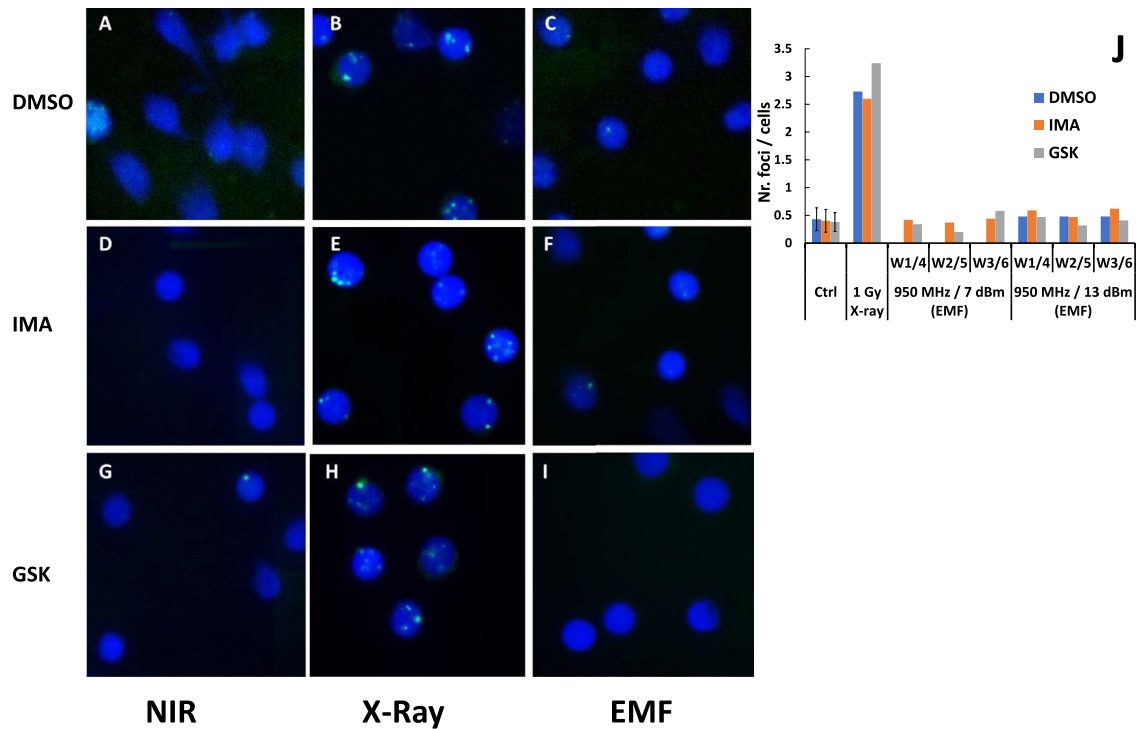


Figure 6. (A–I) Immunofluorescence detection of γ H2AX phosphorylated histone foci in pre-B cells exposed to EMF or X ray irradiation. The γ H2AX foci are shown in bright green— γ -H2AX, whereas DNA staining is in blue – nuclei. (A) Control solvent (DMSO) treated cells Nonirradiated (NIR); (B) Control (DMSO) treated 1 Gy X-ray irradiated cells(X-Ray); (C) Control (DMSO)treated EMF exposed (waves at 950 MHz, with emission generator power setting set at 7 dBm-EMF); (D) IMA treated NIR; (E) IMA, X-ray; (F) IMA, EMF; (G) GSK, NIR; (H) GSK, X-ray; (I) GSK, EMF. (J) Number of counted foci per /cell represented as histograms. W1/4 refers to growing plate wells 1 and 4, W2/5 wells 2 and 5 and W3/6 wells 3 and 6 equivalent positions with respect to which cells were EMF irradiated, with generator power setting set at 7 dBm and 13 dBm. GSK is cells treatment with 10 μ M GSK-690693, IMA their treatment with 3 μ M Imatinib. ANDOR camera assisted by IQ Live Cell Imaging software and foci analysis with Imaris for Cell Biologists software (both from OXFORD Instruments).

to control the EMF developed inside the cellular growing medium in a typical cell culture incubator. Cultured pre-B cells synchronously recombining V(D)J were EMF exposed during a 48 h window, which starts with RAG expression and ends with the NHEJ DSBs DNA repair⁵. A nested PCR assay is then used to study the cellular EMF irradiation gene effects.

The measured data in Figs. 3B, 4, 5 and Table 1 consistently show, EMFs cause a dose dependent reduction in V(D)J recombination in the irradiated pre-B cells, with similar effects for both RAG inducing stimuli (IMA or GSK) used. The magnitude of effects is tightly determined by the EMF frequency. A two-fold reduction in V κ -J κ 2 recombination at *Igk* locus narrowly can be obtained by an emitted S power value of 9.49 μ W/cm² at 720 MHz (Cell Recomb. Fr. 0.56 for GSK and 0.7 for IMA), whereas this effect may be achieved by a field developing one twentieth of that S dose at 1000 MHz (0.5 Cell Recomb. Fr. for both drugs at 0.43 μ W/cm²) (Fig. 4). The recombination reduction although observed for all EMFs tested, seems to be maximal for 950 and 1000 MHz waves, a small domain where the serum containing cell culture medium displays maximal EMF absorbance (Fig. 2), and augments by its molecular polarization the EMF electric intensity (supplementary Fig. 5Sc). We measured EMF local antenna emissive S values only in the incubator air surrounding the cell culture plate. Despite this limitation we measured and calculated the average irradiated electric field intensity E, inside the culture medium. The maximal effects were measured at 950 and 1000 MHz, where *Igk* recombination levels for an EMF of E 0.4 V/m are only half (Fig. 5A), or for one of 0.6 V/m E a quarter of those reported for same E values at 720 MHz (Fig. 5B). E dose effects parallel the frequency dependency described for the antenna emitted power dose S. However, the cell medium electric properties mentioned above, (increased absorbance and polarization between 900 and 1000 MHz), cannot account for the frequency results shown in Fig. 5 for irradiations at constant electric field E values. Besides such intrinsic medium properties there must be also a major EMF frequency direct influence on the cellular components linked to recombination.

Various wireless network service providers use for mobile phone communication frequencies ranging between 700 and 2100 MHz. At 1 cm distance, during outgoing calls the measured emitted field E intensities vary with \pm 5–15% from the 41.25 V/m (recommended ICNIRP value) with cell phone models, whereas their maximum output recorded power levels for a GSM1800 net varies between 0.25 and 1 W^{41,42}.

We assessed if the low dose 48 h EMF irradiations cause DNA DSBs and detectable γ H2AX repair foci in exposed cells. From the levels of detected γ H2AX repair foci of the EMF irradiated pre-B cells we could not reveal in exposed cells above background DNA DSBs repair activity (Fig. 6 compare panel A with C, G with I, and histograms in Fig. 6j). Using chromatin immunoprecipitation (ChIP) Savic et al.⁴³ show considerable γ H2AX accumulation near Jk5 in IgK locus after 24 h post STI571 (Imatinib) treatment of pre-Bs, but a dramatic more than two-fold decrease in γ H2AX detection as cells were kept from 24 to 48 h post STI571 treatment⁴³. We could not detect above background γ H2AX foci levels in IMA or GSK treated cells after 48 h culture growth. This could be due either to a considerable post RAG DSBs repair recovery, or to a reduced sensitivity of our immunofluorescence assay (less sensitive than ChIP in detecting γ H2AX). The onset of DNA DSBs either prior to or during pre-B cells maturation inhibits *rag1*, 2 transcription⁴⁴ and reduces the levels of *Igk* locus rearrangement events⁴⁵. These cellular stress effects are caused by ataxia teleangiectasia mutated (ATM) kinase either via NF- κ B, FOXO1 signaling^{44,46} or via GADD45a inhibition⁴⁵, both pathways directly targeting *rag* genes transcription levels. If very few EMF induced DSBs (below those detectable by γ H2AX foci assay), or breaks already repaired before our cell harvests could have reduced RAG expression in our experiments (via ATM kinase) this could explain our observed reduced recombination effects. We used in our experiments two RAG induction stimuli, IMA sensitive to ATM kinase via GADD45a inhibition^{44–46} and the second GSK690693 AKT-inhibitor insensitive to this signaling pathway¹⁹. If very few EMF induced DNA DSBs would have reduced RAG expression prior to, or during drug action, one would have expected experiments to show a more accentuated recombination reduction for IMA than that obtained for GSK treatment. Instead, the experimental data in Figs. 3B, 4, 5 and Table 1 show for both drugs very similar EMF induced reduction of *Igk* loci rearrangement levels (if not even slightly more pronounced reduction for GSK). IMA although a more potent RAG inducer than GSK has the disadvantage that post recombination blocks cells in Go phase preventing further their division^{36,47–49}. On the contrary, the AKT inhibitor GSK-690693 not only is a weaker RAG induction stimulus (closer to the one physiologically occurring in small pre-B cells)^{50,51} but also enables cells to divide prior to and after *Igk* loci rearrangements and protect their progress to the next stage of development¹⁹. Because our PCR assay intentionally uses the amount of templating genomic DNA from the same number of 2 millions harvested cells, replication would have “diminished the EMF recombination reduction” in GSK treated cells in contrast to those incubated with IMA (the later, on the contrary, “freezes” the EMF effect on BCL2 maintained survivors). As pointed earlier, in treated cells, both drugs show very similar EMF induced reduction of rearrangements in treated cells. Although we cannot fully refute that the observed EMF recombination effects may have been caused in irradiated pre-B cells by undetectable DNA DSBs via ATM, the line of evidence gathered from our experiments in Figs. 4, 5, 6 and the arguments presented above for the comparative IMA/GSK treatments make this mechanism a less likely candidate for their account.

Indirectly our work addresses the longstanding question of how innocuous low dose EMF irradiation from our telecommunication devices may be and whether it may affect the immunity of our organisms. It remains only to our speculation to extend the observed recombination effects induced by small EMFs from an in vitro culture system to the in vivo situation on the ability of irradiated B cells to elicit an unaltered antibody response to antigen challenge.

Methods

Materials. DNA oligonucleotides were purchased from Life Technologies and IDT DNA: Vk degenerate primer 5' GCTGCAGSTTCAGTGGCAGTGGCAGTGGRTCWGGRAC 3' where S is G or C, R is A or G, W is T or A, Jk2-1 primer 5' CAAAACCCTCCCTAGGTAGACAATTATCCCTC 3' and Jk2-2 primer 5' GGACAG TTTTCCCTCCTTAACACCTGATCTG 3'. For Histone H1 gene control amplifications the following primers were used: H1fw 5' GGCTGCTATCCAGGCAGAGAAGAACCG 3', H1rv: 5' GCTTTGGAGGCGCCTTCT TGGGCTTG 3'.

Murine pre B cells transformed with Abelson virus (v-Abl preB, A70 line, that harbor a μ -Bcl2 transgene) were a kind gift from Barry Sleckman Duke University⁴⁷. The cells were maintained in RPMI 1640 medium, supplemented with 10% FBS (both from GIBCO), 50 μ M 2-mercaptoethanol and induced at 0.5×10^6 cells/ml density either with 3 μ M Imatinib Mesylate (IMA) (SIGMA-ALDRICH) or with 10 μ M GSK-690693 (GSK) (GLAXOSMITHKLINE, SELLECK-chem) in solutions with 0.1% DMSO. After 48 h the cells were collected and analyzed using the nested PCR described below.

Pre-B Cells irradiation was performed with a 1 Hz–1.224 GHz, 13 dBm radiofrequency generator (Hameg Instruments 1 Hz–1.2 GHz programmable synthesizer HM8134-3, used throughout our study as emission generator) using a broadband irradiating 800 MHz–3 GHz LTE ATK-LOG ALP logarithmic antenna, in a regular CO₂ incubator (SANYO Electric Co. MCO-17AIC), with CO₂ 5 vol. %, and 95% purified water humidity. Cells were grown at 37 °C in 5 ml medium in standard six flat bottom wells (16.8 ml capacity) polystyrene lidded plates (Corning Costar), which were always positioned in the same place with respect to the incubator walls (in the center of the incubator, see Supplemental material Fig. 1Sa) and the emission antenna (antenna central guiding label positioned midway between wells 3 and 6 at 2.4 cm above the mid plane of the plate, see supplementary Fig. 1S). Two parallel sets of experiments were performed with wells 1, 2, 3 containing cells stimulated with 3 μ M IMA, whereas wells 4, 5 and 6 cells were stimulated with 10 μ M GSK (Fig. 1SB).

Two steps nested PCR reactions for K locus recombination. Template DNA was prepared for PCR using a modified technique developed by Schlissel³⁷. Pre-B A-70 v-Abl cells were harvested after 48 h incubation with IMA^{36,47}, GSK¹⁹ or unstimulated. Cultured cells (2×10^6 –2 millions) were pelleted for 15 s in a microfuge, washed once in PBS (phosphate saline buffer pH 7.2), resuspended in 200 μ l PCR lysis buffer (10 mM Tris pH 8.4, 2.5 mM MgCl₂, 50 mM KCl, 200 μ g/ml gelatin, 0.45% NP40, 0.45% Tween-20 (CALBIOCHEM), and 60 μ g/ml Proteinase K (Boehringer), and incubated at 56 °C for 3 h followed by 15 min at 95 °C. Dilution of templates

was done with PCR lysis buffer without Proteinase K. Two successive PCR amplifications were done in a final volume of 50 μ l containing 2 to 5 μ l template DNA, 10 mM Tris-HCl (pH 8.4; at room temperature), 50 mM KCl, 2.5 mM MgCl₂, 200 μ g/ml gelatin, 0.2 mM of all four dNTPs (all from ThermoFisher scientific), each oligonucleotide primer at 0.4 μ M (20 pmol each primer per reaction), and 1 U TAQ DNA polymerase (GoTaq PROMEGA) in nested reactions. First step PCR reactions for 25 cycles use Vk, and Jk2-1 primers. In the second step various dilutions (from 4 μ l 1:100 dilution of first PCR to 0.5 μ l of the first undiluted PCR) are individually used to template the second PCR reactions to which Vk and Jk2-2 primers are added and an additional round of 30 cycles amplification is performed. Cycling steps were: an initial 1 min denaturation at 94 °C, then repeated cycles each, 30 s at 94 °C, 0.5 min annealing at 50 °C, and 1.5 min polymerization at 72 °C. A final additional 5 min extension step was performed at 72 °C^{36,37}. PCR products were resolved on 1.5% agarose gel, stained either with ethidium bromide or Sybr Green (THERMOFISHER scientific) and visualized using the PharosFX system (BIORAD). The bands intensities were quantified using QuantityOne software.

Kappa locus amplification products analysis. Each Vk-Jk2 product band density of the gel scan image is quantified and the ratio between the densitometry value of the PCR product band detected from cells grown in the presence of EMF and the corresponding one without field exposure (EMF+/EMF-, Cell Recomb. Fr., Figs. 3, 4, 5) reports the changes in V(D)J recombination occurred upon each cell treatment (IMA/GSK). To normalize for DNA extraction levels we performed similar PCR amplifications from the same amount of template DNA using a pair of primers H1fw and H1rv to specifically detect the histone H1 gene.

γ H2AX foci analysis for irradiation induced DNA damage cellular response. Cells were grown under similar conditions with those described above for recombination assays. Additionally, a DNA DSBs control cell lot either uninduced or one for each RAG stimulus (IMA or GSK) was exposed to a quick 20 min X ray cumulative dose exposure of 1 Gray (X-ray irradiation with a slow rate 50-milligray /min with a Mevatron Primus 2D, 6MV, SIEMENS instrument) prior to their harvest. The samples were irradiated at 100 cm distance from the source axis, the field size being of 30 \times 30 cm. The dosimetry was performed using a water phantom (1 cm water depth). Symmetry and homogeneity were checked, the dose proved to be homogenous throughout the sample in the used plates. For all treatments, twenty minutes after harvest, instead of extracting DNA, the cells from each individual culture type were separately spread onto clean designated slide sets using a Cytospin Centrifuge. The cells were then fixed with paraformaldehyde, permeabilized with Triton X and then doubly stained with: (a) Hoechst 33342 dye (THERMO SCIENTIFIC) (for their nuclei-DNA total staining in blue) and (b) immunofluorescently with primary unlabeled anti γ H2AX antibodies of mouse antigen specificity complemented with secondary Cy2 labeled anti primary source antibodies (rat anti mouse IgG Cy2 detection antibodies-green)(both from SIGMA ALDRICH); to identify in green the DSB repairing γ H2AX foci⁴⁰. The slides were examined with a fluorescence microscope (OLYMPUS BX60) with adequate filter for the fluorophores, and images of the nuclei and γ H2AX foci recorded with a camera connected to the microscope. The images were analyzed using specific analysis software to quantify the number of foci per each cell treatment type, and morphologically to indicate their level of dispersion or nuclear positioning (see Fig. 6).

Western blot analysis for endogenous RAG time course induction in pre-B cells (Supplemental material Fig. 2S) following IMA/GSK treatment was performed as previously described in our work using anti RAG1 and anti RAG2 mouse monoclonal antibodies (gift from Dr. David G. Schatz, Yale University), and control sample purified murine core RAG1(384–1040) and coreRAG2 (1–387) fused to Maltose binding protein (MBP-40kD) which were transiently expressed in co-transfected HEK293T cells⁵² (source ATCC CRL-3216).

Absorption spectra measurements were made using two identical broadband (0.8–16 GHz) horn antennas facing each-other and placed at 1 m distance. The measurement subjected sample was placed in close proximity (1 cm) of the receiver whereas the emission antenna (supplementary Fig. 4S a and b), was coupled to the generator. The receiver antenna was connected to a commercial Spectrum Analyzer (Keysight-AGILENT-HP N9935A, 0.1- 9 GHz) on which the received signals were recorded and analyzed. The shown absorption spectra in Fig. 2 were obtained after subtraction of the background spectra with no liquid sample placed in the container in front of the receiver antenna. The deionized water used for measurement has the conductivity < 5 μ S/cm, whereas the used unfiltered tap water with ions has the following characteristic measured chemical parameters per liter (l) pH 6.5–9.5, Conductivity < 800 μ S/cm, ammonia < 0.5 mg/l, free residual Chlorine < 0.5 mg/l, Fe < 200 μ g/l, Mn < 50 μ g/l, Al < 200 μ g/l, nitrites < 0.5 mg/l, nitrates < 50 mg/l, Borate salts 1 mg/l, Chlorides 250 mg/l, Sulphates 250 mg/l, 65 mg/l calcium carbonate, Hardness < 5degrees (dGH).

Received: 29 November 2020; Accepted: 31 May 2021

Published online: 16 June 2021

References

1. Tonegawa, S. Somatic generation of antibody diversity. *Nature* **302**, 575–581 (1983).
2. Kim, M. S., Lapkouski, M., Yang, W. & Gellert, M. Crystal structure of the V(D)J recombinase RAG1-RAG2. *Nature* **518**, 507–511. <https://doi.org/10.1038/nature14174> (2015).
3. Sadofsky, M. J. The RAG proteins in V(D)J recombination: more than just a nuclease. *Nucleic Acids Res.* **29**, 1399–1409 (2001).
4. Schatz, D. G. & Ji, Y. Recombination centres and the orchestration of V(D)J recombination. *Nat. Rev. Immunol.* **11**, 251–263. <https://doi.org/10.1038/nri2941> (2011).
5. Schatz, D. G. & Swanson, P. C. V(D)J recombination: mechanisms of initiation. *Annu. Rev. Genet.* **45**, 167–202. <https://doi.org/10.1146/annurev-genet-110410-132552> (2011).

6. Herzog, S., Reth, M. & Jumaa, H. Regulation of B-cell proliferation and differentiation by pre-B-cell receptor signalling. *Nat. Rev. Immunol.* **9**, 195–205. <https://doi.org/10.1038/nri2491> (2009).
7. Peschon, J. J. *et al.* Early lymphocyte expansion is severely impaired in interleukin 7 receptor-deficient mice. *J. Exp. Med.* **180**, 1955–1960. <https://doi.org/10.1084/jem.180.5.1955> (1994).
8. O’Shea, J. J. & Plenge, R. JAK and STAT signaling molecules in immunoregulation and immune-mediated disease. *Immunity* **36**, 542–550. <https://doi.org/10.1016/j.immuni.2012.03.014> (2012).
9. Goetz, C. A., Harmon, I. R., O’Neil, J. J., Burchill, M. A. & Farrar, M. A. STAT5 activation underlies IL7 receptor-dependent B cell development. *J. Immunol.* **172**, 4770–4778. <https://doi.org/10.4049/jimmunol.172.8.4770> (2004).
10. Yao, Z. *et al.* Stat5a/b are essential for normal lymphoid development and differentiation. *Proc. Natl. Acad. Sci. U. S. A.* **103**, 1000–1005. <https://doi.org/10.1073/pnas.0507350103> (2006).
11. Cooper, A. B. *et al.* A unique function for cyclin D3 in early B cell development. *Nat. Immunol.* **7**, 489–497. <https://doi.org/10.1038/ni1324> (2006).
12. Jiang, Q. *et al.* Distinct regions of the interleukin-7 receptor regulate different Bcl2 family members. *Mol. Cell Biol.* **24**, 6501–6513. <https://doi.org/10.1128/MCB.24.14.6501-6513.2004> (2004).
13. Ramadani, F. *et al.* The PI3K isoforms p110alpha and p110delta are essential for pre-B cell receptor signaling and B cell development. *Sci Signal* **3**, ra60. <https://doi.org/10.1126/scisignal.2001104> (2010).
14. Amin, R. H. & Schlissel, M. S. Foxo1 directly regulates the transcription of recombination-activating genes during B cell development. *Nat. Immunol.* **9**, 613–622. <https://doi.org/10.1038/ni.1612> (2008).
15. Dengler, H. S. *et al.* Distinct functions for the transcription factor Foxo1 at various stages of B cell differentiation. *Nat. Immunol.* **9**, 1388–1398. <https://doi.org/10.1038/ni.1667> (2008).
16. Eijkelenboom, A. & Burgering, B. M. FOXOs: signalling integrators for homeostasis maintenance. *Nat. Rev. Mol. Cell Biol.* **14**, 83–97. <https://doi.org/10.1038/nrm3507> (2013).
17. Kuo, T. C. & Schlissel, M. S. Mechanisms controlling expression of the RAG locus during lymphocyte development. *Curr. Opin. Immunol.* **21**, 173–178. <https://doi.org/10.1016/j.coi.2009.03.008> (2009).
18. Ozes, O. N. *et al.* NF-kappaB activation by tumour necrosis factor requires the Akt serine-threonine kinase. *Nature* **401**, 82–85. <https://doi.org/10.1038/43466> (1999).
19. Ochodnicka-Mackovicova, K. *et al.* NF-kappaB and AKT signaling prevent DNA damage in transformed pre-B cells by suppressing RAG1/2 expression and activity. *Blood* **126**, 1324–1335. <https://doi.org/10.1182/blood-2015-01-621623> (2015).
20. Ochiai, K. *et al.* A self-reinforcing regulatory network triggered by limiting IL-7 activates pre-BCR signaling and differentiation. *Nat. Immunol.* **13**, 300–307. <https://doi.org/10.1038/ni.2210> (2012).
21. Inlay, M. A., Tian, H., Lin, T. & Xu, Y. Important roles for E protein binding sites within the immunoglobulin kappa chain intronic enhancer in activating V kappa J kappa rearrangement. *J. Exp. Med.* **200**, 1205–1211. <https://doi.org/10.1084/jem.20041135> (2004).
22. Herzog, S. *et al.* SLP-65 regulates immunoglobulin light chain gene recombination through the PI(3)K-PKB-Foxo pathway. *Nat. Immunol.* **9**, 623–631. <https://doi.org/10.1038/ni.1616> (2008).
23. Lieber, M. R., Yu, K. & Raghavan, S. C. Roles of nonhomologous DNA end joining, V(D)J recombination, and class switch recombination in chromosomal translocations. *DNA Repair (Amst)* **5**, 1234–1245. <https://doi.org/10.1016/j.dnarep.2006.05.013> (2006).
24. Marculescu, R., Le, T., Simon, P., Jaeger, U. & Nadel, B. V(D)J-mediated translocations in lymphoid neoplasms: a functional assessment of genomic instability by cryptic sites. *J. Exp. Med.* **195**, 85–98 (2002).
25. Delimaris, J., Tsilimigaki, S., Messini-Nicolaki, N., Ziros, E. & Piperakis, S. M. Effects of pulsed electric fields on DNA of human lymphocytes. *Cell Biol. Toxicol.* **22**, 409–415. <https://doi.org/10.1007/s10565-006-0105-1> (2006).
26. Phillips, J. L., Singh, N. P. & Lai, H. Electromagnetic fields and DNA damage. *Pathophysiology* **16**, 79–88. <https://doi.org/10.1016/j.pathophys.2008.11.005> (2009).
27. Olive, P. L. & Banath, J. P. The comet assay: a method to measure DNA damage in individual cells. *Nat. Protoc.* **1**, 23–29. <https://doi.org/10.1038/nprot.2006.5> (2006).
28. Phillips, J. L. *et al.* DNA damage in Molt-4 T-lymphoblastoid cells exposed to cellular telephone radiofrequency fields in vitro. *Bioelectrochem. Bioenerg.* **45**, 103–110. [https://doi.org/10.1016/s0302-4598\(98\)00074-9](https://doi.org/10.1016/s0302-4598(98)00074-9) (1998).
29. Mashevich, M. *et al.* Exposure of human peripheral blood lymphocytes to electromagnetic fields associated with cellular phones leads to chromosomal instability. *Bioelectromagnetics* **24**, 82–90. <https://doi.org/10.1002/bem.10086> (2003).
30. Leal, B. Z., Szilagyi, M., Prihoda, T. J. & Meltz, M. L. Primary DNA damage in human blood lymphocytes exposed in vitro to 2450 MHz radiofrequency radiation. *Radiat. Res.* **153**, 479–486. [https://doi.org/10.1667/0033-7587\(2000\)153\[0479:pddihb\]2.0.co;2](https://doi.org/10.1667/0033-7587(2000)153[0479:pddihb]2.0.co;2) (2000).
31. McNamee, J. P. *et al.* No evidence for genotoxic effects from 24 h exposure of human leukocytes to 1.9 GHz radiofrequency fields. *Radiat. Res.* **159**, 693–697. [https://doi.org/10.1667/0033-7587\(2003\)159\[0693:nfgef\]2.0.co;2](https://doi.org/10.1667/0033-7587(2003)159[0693:nfgef]2.0.co;2) (2003).
32. Stronati, L. *et al.* 935 MHz cellular phone radiation. An in vitro study of genotoxicity in human lymphocytes. *Int. J. Radiat. Biol.* **82**, 339–346. <https://doi.org/10.1080/09553000600739173> (2006).
33. Hook, G. J. *et al.* Measurement of DNA damage and apoptosis in Molt-4 cells after in vitro exposure to radiofrequency radiation. *Radiat. Res.* **161**, 193–200. <https://doi.org/10.1667/rr3127> (2004).
34. Muljo, S. A. & Schlissel, M. S. A small molecule Abl kinase inhibitor induces differentiation of Abelson virus-transformed pre-B cell lines. *Nat. Immunol.* **4**, 31–37. <https://doi.org/10.1038/ni870> (2003).
35. Wilson, M. K., McWhirter, S. M., Amin, R. H., Huang, D. & Schlissel, M. S. Abelson virus transformation prevents TRAIL expression by inhibiting FoxO3a and NF-kappaB. *Mol. Cells* **29**, 333–341. <https://doi.org/10.1007/s10059-010-0029-8> (2010).
36. Carmona, L. M., Fugmann, S. D. & Schatz, D. G. Collaboration of RAG2 with RAG1-like proteins during the evolution of V(D)J recombination. *Genes Dev.* **30**, 909–917. <https://doi.org/10.1101/gad.278432.116> (2016).
37. Schlissel, M. S. & Baltimore, D. Activation of immunoglobulin kappa gene rearrangement correlates with induction of germline kappa gene transcription. *Cell* **58**, 1001–1007. [https://doi.org/10.1016/0092-8674\(89\)90951-3](https://doi.org/10.1016/0092-8674(89)90951-3) (1989).
38. Gregson, S. M., McCormick, J. & Parini, C. *Principles of Planar Near-Field Antenna Measurements* 35–61 (The Institution of Engineering and Technology, London, 2007).
39. Helmink, B. A. *et al.* H2AX prevents CtIP-mediated DNA end resection and aberrant repair in G1-phase lymphocytes. *Nature* **469**, 245–249. <https://doi.org/10.1038/nature09585> (2011).
40. Huang, X. & Darzynkiewicz, Z. Cytometric assessment of histone H2AX phosphorylation: a reporter of DNA damage. *Methods Mol Biol* **314**, 73–80. <https://doi.org/10.1385/1-59259-973-7:073> (2006).
41. I. C. o. N.-I. R. P. Principles for non-ionizing radiation protection. *Health Phys.* **118**, 477–482. <https://doi.org/10.1097/hp.0000000000001252> (2020).
42. Isabona, J. & Srivastava, V. M. (2017) Cellular mobile phone—a technical assessment on electromagnetic radiation intensity on human safety. *IEEE*, 271–274. Doi: <https://doi.org/10.1109/NIGERCON.2017.8281899>
43. Savic, V. *et al.* Formation of dynamic gamma-H2AX domains along broken DNA strands is distinctly regulated by ATM and MDC1 and dependent upon H2AX densities in chromatin. *Mol. Cell* **34**, 298–310. <https://doi.org/10.1016/j.molcel.2009.04.012> (2009).
44. Fisher, M. R., Rivera-Reyes, A., Bloch, N. B., Schatz, D. G. & Bassing, C. H. Immature lymphocytes inhibit Rag1 and Rag2 transcription and V(D)J recombination in response to DNA double-strand breaks. *J. Immunol.* **198**, 2943–2956. <https://doi.org/10.4049/jimmunol.1601639> (2017).

45. Steinel, N. C. *et al.* The ataxia telangiectasia mutated kinase controls Iggkappa allelic exclusion by inhibiting secondary V kappa-to-J kappa rearrangements. *J. Exp. Med.* **210**, 233–239. <https://doi.org/10.1084/jem.20121605> (2013).
46. Ochodnicka-Mackovicova, K. *et al.* The DNA damage response regulates RAG1/2 expression in pre-B cells through ATM-FOXO1 signaling. *J. Immunol.* **197**, 2918–2929. <https://doi.org/10.4049/jimmunol.1501989> (2016).
47. Bredemeyer, A. L. *et al.* ATM stabilizes DNA double-strand-break complexes during V(D)J recombination. *Nature* **442**, 466–470. <https://doi.org/10.1038/nature04866> (2006).
48. Hantschel, O., Rix, U. & Superti-Furga, G. Target spectrum of the BCR-ABL inhibitors imatinib, nilotinib and dasatinib. *Leuk. Lymphoma* **49**, 615–619. <https://doi.org/10.1080/10428190801896103> (2008).
49. Marinelli Busilacchi, E. *et al.* Immunomodulatory effects of tyrosine kinase inhibitor in vitro and in vivo study. *Biol. Blood Marrow Transplant.* **24**, 267–275. <https://doi.org/10.1016/j.bbmt.2017.10.039> (2018).
50. Borghesi, L. *et al.* B lineage-specific regulation of V(D)J recombinase activity is established in common lymphoid progenitors. *J. Exp. Med.* **199**, 491–502. <https://doi.org/10.1084/jem.20031800> (2004).
51. Grawunder, U. *et al.* Down-regulation of RAG1 and RAG2 gene expression in preB cells after functional immunoglobulin heavy chain rearrangement. *Immunity* **3**, 601–608. [https://doi.org/10.1016/1074-7613\(95\)90131-0](https://doi.org/10.1016/1074-7613(95)90131-0) (1995).
52. Ciubotaru, M. *et al.* The architecture of the 12RSS in V(D)J recombination signal and synaptic complexes. *Nucleic Acids Res.* **43**, 917–931. <https://doi.org/10.1093/nar/gku1348> (2015).

Acknowledgements

This work was supported by the following projects: PN-III-P4-ID-PCE-2016-0502 Acronym V(D)JMYC contract 178/2017, 5/5.1/ELI-RO, RDI 2016 acronym "BIOSAFE" Contract Nr. 17/2016 and PN-III-P1-1.2-PCCDI-2017 acronym "ONCORAD" Contract Nr. 64/2018. We would also wish to acknowledge support from COMTEST srl. company from Dr. ing. Radu Mateescu in measuring probe absorption and discussions of the manuscript with Dr. Gabriel Banciu, D. Liviu Nedelcu and Dragos Geambasu.

Author contributions

E.I. has performed all the cell irradiation experiments, maintained the pre-B cells in culture, performed PCR from genomic DNA and quantified the amplification results. A.M. and M.S. have performed all the experiments to measure the EMF parameters used in irradiation, absorption spectra, power flux density and electric field intensity measurements. M.T. has performed the experiments to detect and quantify the γ H2AX foci whereas D.S. helped in interpreting the results of their foci/cell analysis. M.C. has designed the experiments, performed the analysis and interpretation of the cell irradiation experiments, supervised experiments and wrote the manuscript. All authors reviewed the manuscript.

Competing interests

The authors declare no competing interests.

Additional information

Supplementary Information The online version contains supplementary material available at <https://doi.org/10.1038/s41598-021-91790-3>.

Correspondence and requests for materials should be addressed to M.C.

Reprints and permissions information is available at www.nature.com/reprints.

Publisher's note Springer Nature remains neutral with regard to jurisdictional claims in published maps and institutional affiliations.



Open Access This article is licensed under a Creative Commons Attribution 4.0 International License, which permits use, sharing, adaptation, distribution and reproduction in any medium or format, as long as you give appropriate credit to the original author(s) and the source, provide a link to the Creative Commons licence, and indicate if changes were made. The images or other third party material in this article are included in the article's Creative Commons licence, unless indicated otherwise in a credit line to the material. If material is not included in the article's Creative Commons licence and your intended use is not permitted by statutory regulation or exceeds the permitted use, you will need to obtain permission directly from the copyright holder. To view a copy of this licence, visit <http://creativecommons.org/licenses/by/4.0/>.

© The Author(s) 2021

OPEN

Radio-Frequency Electromagnetic Field Exposure of Western Honey Bees

Arno Thielens^{1,2*}, Mark K. Greco³, Leen Verloock¹, Luc Martens¹ & Wout Joseph¹

Radio-frequency electromagnetic fields (RF-EMFs) can be absorbed in all living organisms, including Western Honey Bees (*Apis Mellifera*). This is an ecologically and economically important global insect species that is continuously exposed to environmental RF-EMFs. This exposure is studied numerically and experimentally in this manuscript. To this aim, numerical simulations using honey bee models, obtained using micro-CT scanning, were implemented to determine RF absorbed power as a function of frequency in the 0.6 to 120 GHz range. Five different models of honey bees were obtained and simulated: two workers, a drone, a larva, and a queen. The simulations were combined with *in-situ* measurements of environmental RF-EMF exposure near beehives in Belgium in order to estimate realistic exposure and absorbed power values for honey bees. Our analysis shows that a relatively small shift of 10% of environmental incident power density from frequencies below 3 GHz to higher frequencies will lead to a relative increase in absorbed power of a factor higher than 3.

Wireless communication is a widespread and growing technology. Most of the wireless networks and personal devices operate using Radio-Frequency (RF) electromagnetic fields (EMFs). The current networks rely on frequencies between 0.1 GHz and 6 GHz¹. These EMFs can be absorbed in dielectric media and can cause dielectric heating². This dielectric heating can occur in any living organism, including insects.

Absorption of RF EMFs in insects has been studied previously. Wang *et al.*³ studied absorption of RF EMFs in mashed codling moth larvae at 27 MHz and 915 MHz. Shrestha *et al.*⁴ studied dielectric heating of *Cryptolestes ferrugineus* S. in different stages (eggs, larvae, pupae, and adults) at 27 MHz. Shayesteh *et al.*⁵ exposed *Tribolium confusum* and *Plodia interpunctella* to RF EMFs at 2450 MHz^{6–8}. are reviews of RF heating of insects. Dielectric properties of insects are measured by Nelson *et al.*⁹ from 0.2 to 20 GHz through the determination of loss of RF EMF power in insect samples (rice weevil, red flour beetle, saw-toothed grain beetle, and lesser grain borer). Absorption of RF EMFs was studied by Halverson *et al.*¹⁰ in insects between 10–50 GHz. Thielens *et al.*¹¹ used numerical simulations to study absorption of RF EMFs from 2–120 GHz in four insect models. The main conclusions from the aforementioned studies are that (i) RF EMFs can be absorbed and can cause dielectric heating in insects and (ii) this absorption of RF-EMFs is frequency dependent. This frequency dependency is important since 5th generation (5G) networks are expected to partially operate at higher frequencies (up to 300 GHz)^{12,13}. This shift might induce a change in RF EMF absorption for insects¹¹.

Western Honey Bees (*Apis Mellifera*) are particularly important insects because of the environmental and economical importance of this species. Therefore, previous studies have focused on the potential effects of EMF exposure of Western Honey Bees. Low-frequency EM properties and exposure of honeybees was studied in¹⁴. The influence of Low-frequency magnetic fields on honey bee orientation has been studied in¹⁵. There have also been some studies on effects of RF EMF on honey bees. Potential effects of RF EMF exposure on reproduction of honey bee queens were investigated in¹⁶. Behavioral effects potentially caused by exposure to RF EMFs in honey bees have been investigated in^{17–19}. A disadvantage is that these studies are lacking a quantification of the amount of power that is absorbed in the studied honey bees, so called RF dosimetry²⁰. On the other hand, this absorption has been determined for a single honey bee worker in¹¹. However, Thielens *et al.*¹¹ do not provide any coupling of this absorption to a real RF-EMF exposure situation and only study a single honey bee, which provides no

¹Ghent University - imec, Department of Information Technology, Ghent, B-9052, Belgium. ²University of California Berkeley, Berkeley Wireless Research Center, Department of Electrical Engineering and Computer Sciences, Berkeley, CA, 94704, USA. ³Charles Sturt University, Medical Imaging, SDHS, Faculty of Science, Wagga Wagga, NSW, 2678, Australia. *email: arno.thielens@ugent.be

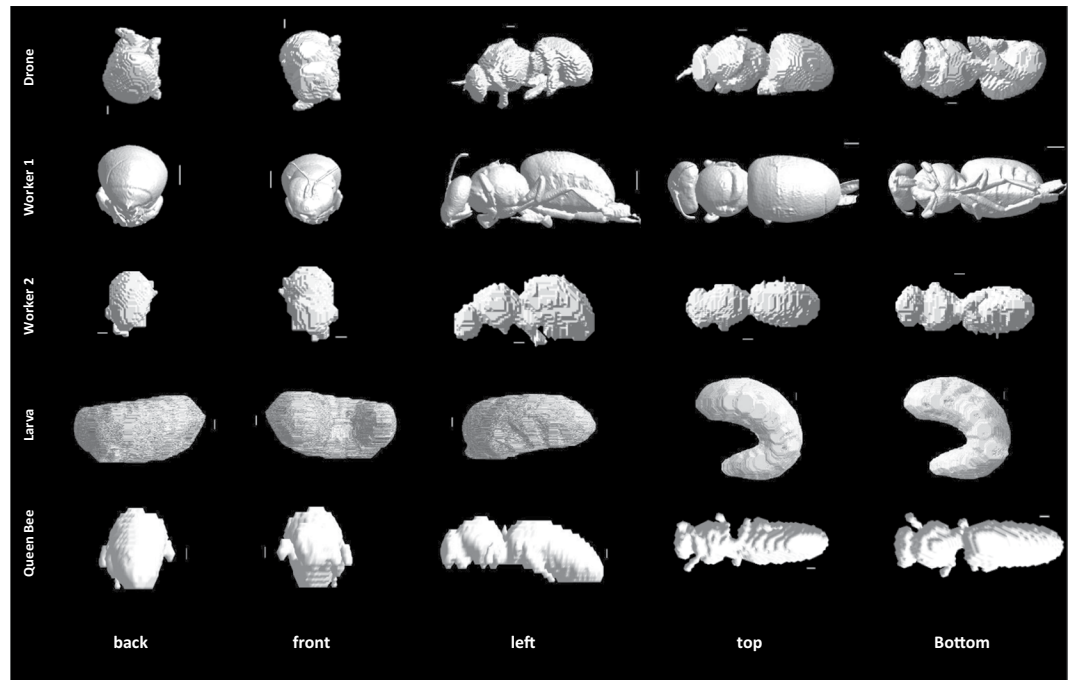


Figure 1. Studied Honey Bee Models, from top to bottom: Male Drone, Worker Bee 1, Worker Bee 2, Worker Larva and Queen Bee. Columns show different perspectives: back, front, left, top, and bottom view, respectively. The white lines show a 1 mm scale for reference.

information on the evolution of such absorption as a honey bee goes through different developmental stages. Nor is it clear whether this RF absorption is realistic for other castes, such as drones or queens, in a bee colony.

Therefore, the aims of this study were to numerically evaluate RF-EMF absorption in western honey bees and validate the frequency dependency of this absorption during various developmental stages and experimentally quantify real-life exposure of bees. To this aim, numerical simulations were executed to determine the absorption of RF-EMFs in five different honey bee models: a larva, a queen, two workers, and one drone, obtained using micro-CT imaging. These simulations were implemented as a function of frequency in a broad band, 0.6 GHz up to 120 GHz, that can be used to model both current and future telecommunication frequencies. In parallel, RF-EMF exposure measurements were executed near five bee hives in Belgium, in order to quantify the real exposure of such honey bees. Finally, these measured values were used to rescale the numerical simulations in order to quantify real honey bee absorption and assess a potential change in absorption in case a shift in operation frequencies in future telecommunication networks would occur.

Methods

Studied honey bees, imaging technique, and model development. Images of the studied insects are shown in Fig. 1. All studied insects are western honey bees (*Apis mellifera*), which is the most commonly used honey bee worldwide. Honey bees within a colony are subdivided into different castes. An active viable honeybee colony contains only one queen bee who spends most of her time laying 2,000 to 3,000 eggs per day. The queen is the only reproductive female within the colony and her health is vitally important to the survival of her colony. Damage to her ovaries has the potential to effect the function and survival of her progeny. A queen typically lives between approximately three and five years. From early spring time to mid-summer the queen lays unfertilized “haploid” eggs which develop into drone bees. All drones are males. Their specific role is to mate with a virgin queen so that she can initiate the propagation of a new colony. During this mating season, there are approximately 3,000 to 5,000 drones within any given colony. Drones typically live between one to two months.

A healthy honey bee colony can contain approximately 50,000 individuals. Most of these are sterile, female, worker bees. Worker bees perform all the tasks within a colony to keep it full of provisions and free from disease. This involves feeding and nursing larvae, foraging for nectar and pollen, storing nectar and pollen, guarding the entrance, tending to the hygiene of the queen-workers-drones and maintaining a clean hive environment. Workers live for three to four weeks during the active seasons (spring-summer-autumn) and approximately three months during the colder inactive season (winter). There are approximately 3,000 (winter) to 10,000 (summer) larvae present at any given time.

We chose representatives from all three castes within a honeybee colony, one queen bee, two worker bees, one drone bee and one worker larva. All honey bees were scanned at the Western Sydney University National Imaging Facility (Sydney, Australia) using a bench-top MicroCT scanner (Quantum GX MicroCT Imaging System, PerkinElmer, Hopkinton, MA, USA). The parameters used during this scanning depended on the scanned bee. Such scans are made using different projections, at different time intervals on the scanners settings.

The rotation between projections also depends on the scanner's settings and the studied honey bee (see below for full description).

Worker 1. The insect named 'Worker 1' is the same bee studied in¹¹, which had a full body length of approximately 11.0 mm long, is 5.0 mm wide, and had a mass of approximately 900 mg. During the scanning of Worker 1, the Micro-CT scanner was operated using the following parameters: 50 kVp, 80 mA, and a 2048×2048 pixels image matrix. This resulted in scans with a $20 \mu\text{m}$ isotropic voxel size. Each projection had a scanning time of 3.0 s, with 3.0 s rotation time in between projections. The total scan time for Worker 1 was approximately 18 min.

Worker 2. The second honey bee worker (Worker 2) has a full body length of 13 mm with cross sectional dimensions of 6.8 mm and 5.4 mm and a mass of approximately 900 mg. For Worker 2, the scanner was operated using the following parameters: 40 kVp, 70 mA, and a 2048×2048 pixels image matrix. The isotropic voxel size was $100 \mu\text{m}$. Each projection had a scanning time of 1.5 s. There was a 3.0 s rotation time in between each projection. The total scan time for the whole bee was approximately 10 min.

Larva. Larvae of this age (three weeks) are typically approximately 16 mm long with an approximate mass of 900 mg. The scanned larva was curled up, which made estimating its full body dimensions difficult, but the sample fitted within a $14 \times 7 \times 15 \text{ mm}^3$ box. This scanning of the larva was done using the following parameters: 50 kVp, 80 mA, and a 2048×2048 pixels image matrix. This resulted in scans with a $20 \mu\text{m}$ isotropic voxel size. Each projection had a scanning time of 3.0 s. and with a 3.0 s rotation time this resulted in a total scan time for the larva of 18 min.

Male drone. The drone has a full body length of 18 mm with cross sectional dimensions of 7.2 mm and 9.4 mm and an approximate mass of 1 g. During the scanning of the drone, the Micro-CT scanner was operated using the following parameters: 40 kVp, 70 mA, and a 2048×2048 pixels image matrix. The isotropic voxel size was $100 \mu\text{m}$. Each projection had a scanning time of 1.5 s. The full scan took 180 projections and there was a 3.0 s rotation time in between each projection. The total scan time for the whole bee was approximately 10 min.

Queen bee. The QB has a full body length of 19 mm and cross sectional dimensions of 7.5 times 7.1 mm^2 and an approximate mass of 1100 mg. The queen was scanned was using the following parameters: 40 kVp, 70 mA, and a 2048×2048 pixels image matrix. The isotropic voxel size was $250 \mu\text{m}$. Each projection had a scanning time of 1.5 s. There was a 1.5 s rotation time in between each projection. The total scan time for the queen bee was approximately 10 min.

Development of 3D models. The software running on the Quantum GX, bench-top MicroCT scanner was used for all honey bees to reconstruct the 180 projection images. Those were then converted into a 2D rendered image stack of 512, 16 bit bitmap images. Finally, the BeeView volume rendering software (DISECT Systems Ltd, Suffolk, UK) was used to acquire Bee volume data from the image stack. All 3D models of the insects were created using the software TomoMask (www.tomomask.com). We used the same approach as in¹¹. The image stack for each honey bee was imported into TomoMask, which also required the pixel and slice spacing. The software generated a 3D model using a marching cubes algorithm²¹. This model was then exported as an STL (STereo Lithography)²² file. This is a commonly used format to describe surface geometry. The models were also smoothed using the Taubin λ/μ smoothing scheme²³ implemented in MeshLab²⁴. The dimensions of the models and mesh integrity were checked (and corrected if necessary) before simulations using Netfabb (Autodesk, San Rafael, CA, USA).

Numerical simulations and RF EMF exposure conditions. Electromagnetic, numerical simulations were executed to estimate electromagnetic fields in and around the honey bees under far-field exposure. Far-field exposure is in this manuscript defined as RF-EMF sources being more than $2D^2/\lambda$ away from the insects, with D the largest dimension of the RF source and λ the wavelength of the RF-EMFs. This is often referred to as the Fraunhofer far-field limit²⁵. In general, far-field RF-EMF sources can be located in any direction from the honey bees. Therefore, different approaches exist to model such far-field exposure to RF-EMFs: a stochastic method where far-field exposure is decomposed in sets of plane waves according to certain statistics is used in^{26,27}, while a more limited set of plane-wave exposures coming from six predefined directions along the main axis of the exposed subject or animal are considered in^{11,28}. In this study, we have chosen to work with the latter method. We have modeled exposure of the studied honey bees by a set of 12 incident plane waves traveling along six directions defined by a Cartesian coordinate system, see Fig. 2. For each direction, two orthogonal incident electric field polarizations were chosen, since any other free-space E-field polarization can be obtained using a linear combination of both. All incident plane waves have a root-mean squared electric field strength of 1 V/m. This value is chosen to facilitate renormalization to any potential value of incident field strength.

Numerical simulations were executed using the Finite-Difference Time-Domain (FDTD) method implemented in Sim4life (ZMT, Zurich, Switzerland). This is a common technique used to determine RF-EMF in and near homogeneous and heterogeneous dielectric objects^{11,26,28}, such as the honey bees studied in this paper. In this method, the simulation domain is divided in cubes using a three-dimensional rectilinear grid. Depending on the wavelength, feature sizes of the objects in the simulations, and the desired spatial accuracy, a different spatial step is used to discretize the simulation. The FDTD algorithm requires a grid step smaller than one tenth of the smallest wavelength in the simulation domain in order to return stable solutions²⁹. Since this is a time-domain technique, it requires a predefined simulation time in order to reach a steady-state solution, which will again depend on the chosen spatial resolution, the wavelength, and the size of the simulation domain.

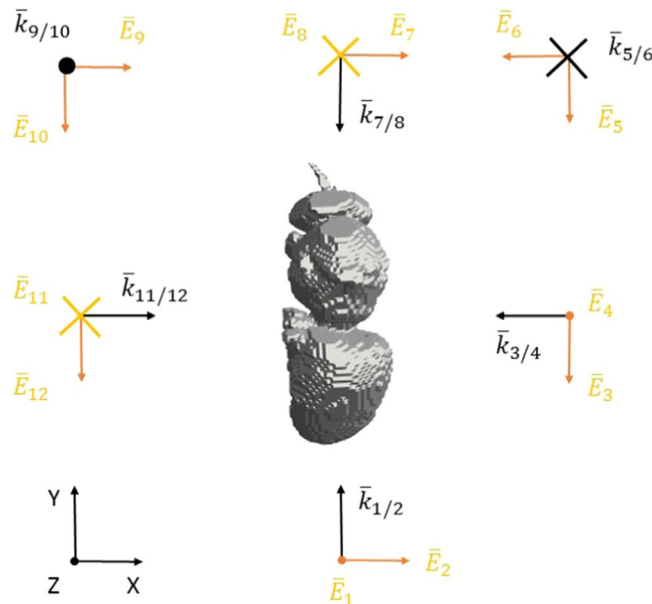


Figure 2. Configuration of the RF-EMF plane-wave simulations. Twelve potential RF plane waves incident from six directions are incident on the insect (honey bee drone shown here in grey, top view). Orange arrows indicate the electric field \bar{E}_i polarizations, while the black arrows indicate the direction of propagation with wave vector \bar{k}_{ij} of the plane waves. i and j indicate the simulations' configuration number, from 1 to 12.

	0.6 GHz	1.2 GHz	2 GHz	3 GHz	6 GHz	12 GHz	24 GHz	60 GHz	120 GHz
Maximal grid step (mm)									
Larva	0.2	0.2	0.2	0.2	0.2	0.1	0.1	0.1	0.1
Others	0.1	0.1	0.05	0.05	0.05	0.05	0.05	0.05	0.05
Simulated Periods									
Worker Bee 1	20	30	60	30	30	30	30	40	40
Others	10	20	20	30	30	30	30	30	30
ϵ_r	45.6	44.2	39.9	38.8	38.0	28.6	14.9	7.018	5.46
σ (S/m)	0.688	0.924	1.35	2.05	5.05	12.0	21.1	27.9	29.2

Table 1. Simulations Settings and Dielectric Properties of the Honey Bees.

We executed numerical simulations at nine harmonic frequencies from 0.6–120 GHz (sinusoidal waves at a single frequency). The lower and upper frequency limits were chosen because they correspond to the current limits in terms of simulation size and length that can realistically be supported by our simulation hardware. The simulated frequencies are listed in Table 1 alongside the chosen grid steps in the simulation domain and the number of periods used for every simulation. These settings were the same for each of the five studied honey bee models. The studied insects have certain dielectric properties, quantified using the relative permittivity (ϵ_r) and conductivity (σ). We did not measure the dielectric properties of the studied insects. Instead, we assigned dielectric parameters obtained from¹¹. The value at 1 GHz is obtained using the same literature database and interpolation presented in¹¹. Table 1 lists these properties. All insects were modeled as homogeneous objects. These configurations resulted in 12 (plane waves) \times 9 (frequencies) \times 5 (honey bees) = 540 simulation results.

After each simulation, the internal electric field in the insect model was extracted and used to calculate the total absorbed RF-EMF power (P_{abs}) in the honey bee. P_{abs} is calculated as the integrated product of the conductivity and the squared internal electric field strength (\bar{E}_{int}) over the total volume (V) of the insect:

$$P_{abs} = \int_V \sigma \times |\bar{E}_{int}|^2 \cdot dV \quad (1)$$

We report P_{abs} rather than specific absorption rate (SAR) values since we did not measure the mass and density of all the simulated honey bees. P_{abs} is an important quantity since dielectric heating of an insect is proportional to absorbed RF-EMF power².

In order to validate our simulations we tested the influence of four simulation settings on the RF-EMF P_{abs} : grid step size, dielectric parameters, angle of incidence, and number of simulated periods. The influence of the grid step is expected to be the most significant at the highest simulated frequency (120 GHz), since the chosen

maximal grid step of 0.05 mm is closest to the smallest wavelength in the simulation domain at that frequency in the tissue ($0.05 \text{ mm} = 0.045 \lambda$). Therefore the maximal grid step was set to $25 \mu\text{m}$ for exposure configuration number 2 in Fig. 2 for both the Larva and Worker 2 phantoms. In¹¹, it was demonstrated that the maximal uncertainty on the dielectric parameters occurs between 2 and 3 GHz, with maximal relative deviations of 40%. In order to test the dependency of our simulation results on the chosen dielectric parameters, we executed four additional FDTD simulations in exposure configuration number 2 shown in Fig. 2 using the Worker 2 phantom. In these simulations the dielectric parameters (ϵ, σ) were changed to: $(1.5.\epsilon, 1.5.\sigma)$, $(0.5.\epsilon, 1.5.\sigma)$, $(1.5.\epsilon, 0.5.\sigma)$, and $(0.5.\epsilon, 0.5.\sigma)$, respectively, allowing for a potential 50% deviation on the dielectric parameters, which should be larger than the uncertainty on the chosen dielectric parameters. We chose to model RF-EMF exposure of the studied honey bees using plane waves incident from 6 directions. However, it is uncertain whether this set of plane waves provides a complete overview of the full range in P_{abs} as function of the angle of incidence. In order to validate our exposure set up, we have executed 20 additional FDTD simulations at 6 GHz using the Worker 2 phantom, where the elevation, azimuth, and polarization angles were generated according to uniform distributions between $[0, \pi]$, $[0, 2\pi]$, and $[0, 2\pi]$, respectively. The settings of these FDTD simulations were the same as those shown in Table 1. Finally, the number of simulated periods was tested at 120 GHz for the Worker 2 phantom in exposure configuration number 2 shown in Fig. 2 by increasing the number of simulated periods to 120 instead of 30, see Table 1. After each of these validation simulations, the P_{abs} was extracted and compared to the one obtained in the original simulation set.

RF-EMF field measurements. In order to quantify current RF-EMF exposure of honey bees in real exposure scenarios, we executed RF-EMF exposure measurements at five sets of bee hives in Belgium at: Aalter, Merelbeke, Eeklo, Zomergem, and Drongen, see Fig. 3(a). At each measurement site, three different measurements were executed in order to quantify RF-EMF exposure.

First, a spectrum analyzer of the type FSL6 (R&S Belgium, Excelsiorlaan 31 1930 Zaventem Belgium) connected to a triaxial isotropic antenna was used to perform a broad-band RF overview measurement from 80 MHz to 6 GHz. These measurements were executed in two steps: first spectral overview measurements were executed from 0.08–3 GHz using a tri-axial antenna TS-EMF (Rhode and Schwartz, dynamic range of 1 mV/m–100 V/m for the frequency range of 80 MHz–3 GHz), followed by measurements from 3–6 GHz using a Clampco AT6000 antenna. At one out of five measurement sites, Drongen, a conical dipole antenna PCD 8250 (Seibersdorf Laboratories, Seibersdorf, Austria) was used for the 80 MHz - 3 GHz measurements. This antenna was rotated to obtain three orthogonal polarizations of the electric field. During these overview measurements, the spectrum analyzer measured in maximum-hold modus during 17 and 9 minutes in the lower and higher frequency bands, respectively. The antennas were supported by a plastic tripod and were placed at 1 m in front of the bee hive at a height of 1.5 m from the ground level. Figure 3 shows the studied bee hives and the measurement set up in the field. The 1.5 m height is a typical height at which such EM field measurements³⁰. Additionally, this height is mentioned in the ECC(02)04 standard³¹. The purpose of these measurements was to get an overview of which frequency bands were in use at the respective sites. These frequency bands were then investigated further in the second measurements.

Second, the same spectrum analyzer was connected to the tri-axial antenna TS-EMF which was again supported by the same tripod at a height of 1.5 m. The tripod was placed at two distances of 1 and 2 m from the central bee hive. The spectrum analyzer performed root-mean square electric field strength (E_{RMS}) measurements over a measurement period of 6 minutes² in each of the telecommunication frequency bands identified using the first measurement. Each of the three electric field components (E_x, E_y, E_z) were measured individually. E_{RMS} was then obtained as the square root of the sum of squares of the individual components.

$$E_{RMS} = \sqrt{E_x^2 + E_y^2 + E_z^2} \quad (2)$$

The spectrum analyzer measurements in terms of received power on the antenna were then recalculated using the known antenna factor of the tri-axial antenna to incident root-mean-squared electric field strength. The $E_{RMS,i}$ values in each frequency band (i) were then summed quadratically and the square root of that sum is listed as the total instantaneous electric field strength ($E_{RMS,tot}$).

$$E_{RMS,tot} = \sqrt{\sum_i E_{RMS,i}^2} \quad (3)$$

The measurement procedure and measurement settings for these RF-EMF exposure measurements are presented in³². The expanded measurement uncertainty (95% confidence interval) for electric field strength measurements using this set up is $\pm 3 \text{ dB}$ ³⁰. This measurement setup enables the most accurate assessment of *in situ* exposure from various RF-EMF sources³⁰.

Third, a broadband exposure measurement was executed using a Narda NBM-550 probe (Narda, Hauppauge, NY, USA) connected to an EF 0691 broad-band probe (Narda, Hauppauge, NY, USA) which has a frequency span from 100 kHz to 6 GHz, thus including so-called intermediate frequencies (IF). These IF fields are not considered in our numerical simulations. However, we measured those to provide a complete overview of the exposure to electromagnetic field below 6 GHz. The NMB probe was placed on top of the central bee hive and was left there during both RF measurements. The device measured and registered root-mean-squared electric field strengths with a period of 1 s. From those time series of measurements, we obtained the time average and the maximal value.

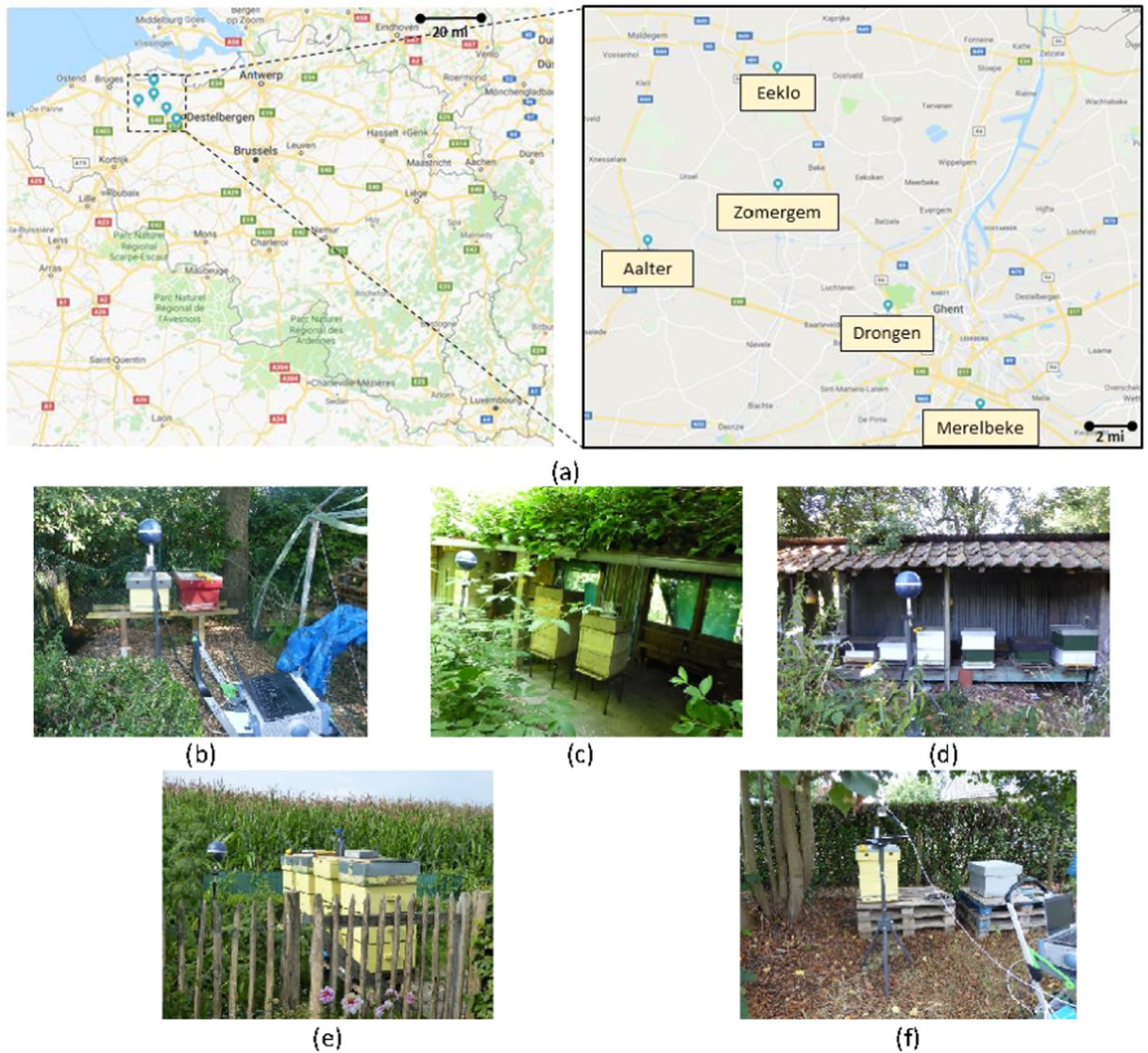


Figure 3. Five measurement locations near bee hives in Belgium: (a) Overview of the measurement locations (source: <https://www.google.com/maps>, Google Maps, Google, Alphabet inc., Mountain View, CA, USA) Map data: Google, GeoBasis-DE/BKG (b) Aalter, (c) Merelbeke, (d) Eeklo, (e) Zomergem, and (f) Drongen.

The researchers that executed the RF-EMF field measurements did not use personal devices during the measurements. All wireless devices brought to the measurement site by the researchers were operated in flight mode, i.e. any wireless transmissions by those devices were not allowed.

Estimation of realistic RF-EMF absorbed power in honey bees. Realistic P_{abs} absorbed in honey bees can be obtained by rescaling the simulated P_{abs} values using the measured incident field strengths. Therefore, we linearly averaged the total E_{RMS} values measured near the five bee hives at two different positions to obtain an average $E_{RMS,avg}$ value. In order to estimate exposure of honey bees in current wireless networks, we averaged the P_{abs} values using:

$$P_{abs,av}(f < 3 \text{ GHz}) = \frac{1}{4} \sum_{i=1}^4 P_{abs}(f_i) \tag{4}$$

with $f_i = 0.6, 1.2, 2, 3 \text{ GHz}$. We only considered P_{abs} values $< 3 \text{ GHz}$, since our measurements will show that there are only incident RF-EMFs below 3 GHz in the current environment of honey bees in Belgium. This value is then rescaled using:

$$P_{abs,real}(f < 3 \text{ GHz}) = \frac{E_{RMS,avg}^2}{1 \text{ V}^2/\text{m}^2} \times P_{abs,av}(f < 3 \text{ GHz}) \tag{5}$$

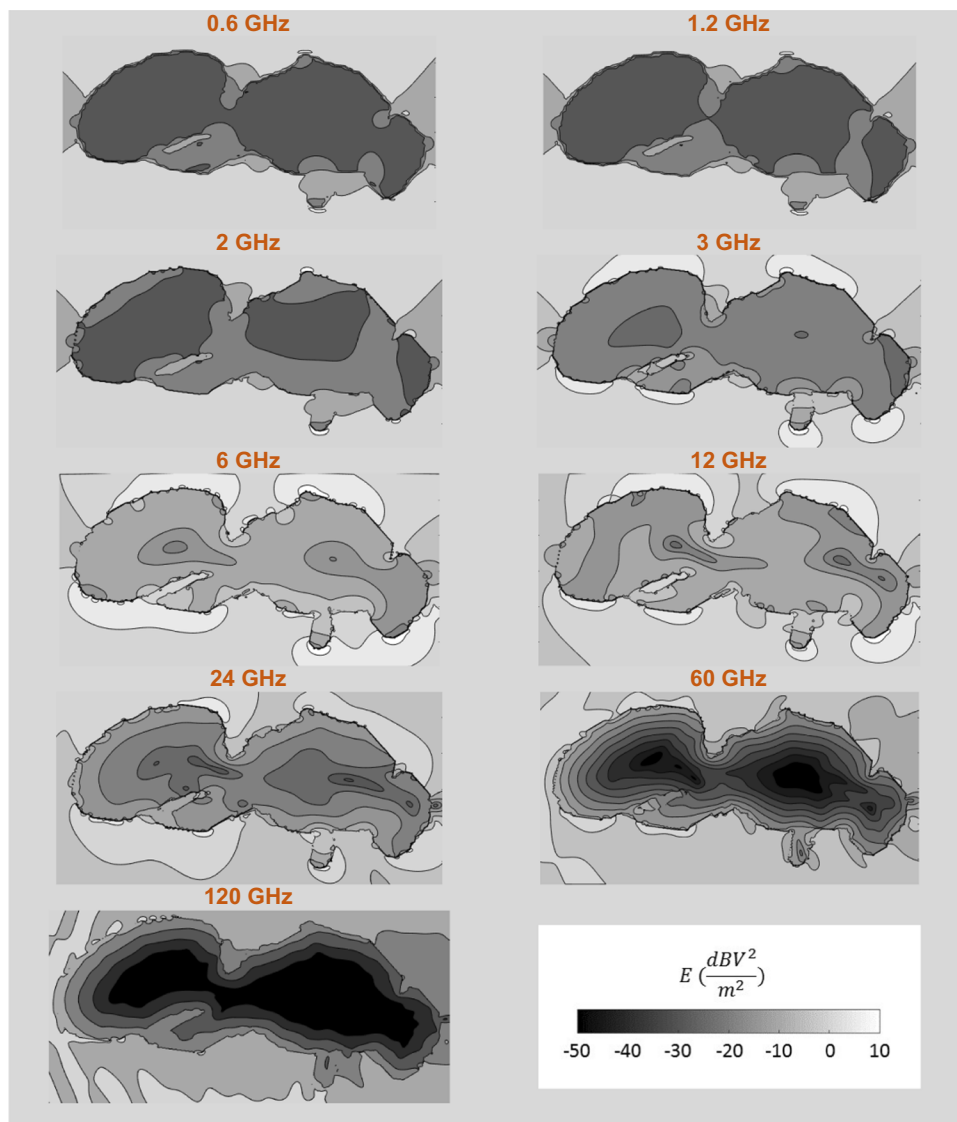


Figure 4. Relative electric field strength in and around a mid-sagittal plane of the Honey Bee Drone at the nine studied frequencies. Grey scale shows the electric field strengths relative to 1 V/m electric field strength.

In order to estimate the effect of a fraction ($p \in [0, 1]$) of the RF-EMF incident fields shifting to frequencies higher than 3 GHz we also determine the average P_{abs} for frequencies higher than 3 GHz, using:

$$P_{abs,av}(f > 3 \text{ GHz}) = \frac{1}{5} \sum_{j=1}^5 P_{abs}(f_j) \quad (6)$$

with $f_j = 6, 12, 24, 60, 120 \text{ GHz}$. The realistic $P_{abs,real}(p)$ for a fraction p of the power shifted to frequencies higher than 3 GHz is then calculated as:

$$P_{abs,real}(p) = p \times \frac{E_{RMS,avg}^2}{1 \text{ V}^2/\text{m}^2} \times P_{abs,av}(f > 3 \text{ GHz}) + (1 - p) \times \frac{E_{RMS,avg}^2}{1 \text{ V}^2/\text{m}^2} \times P_{abs,av}(f < 3 \text{ GHz}) \quad (7)$$

Results

Numerical simulations. Figure 4 shows the relative electric field strength (electric field strength divided by the maximum electric field strength in the simulation domain) in and around the studied drone in a mid-sagittal plane as function of frequency for exposure configuration number 1 shown in Fig. 2. The internal electric fields increase up to 12 GHz and shift towards the outside of the phantom at higher frequencies. At 120 GHz the electric

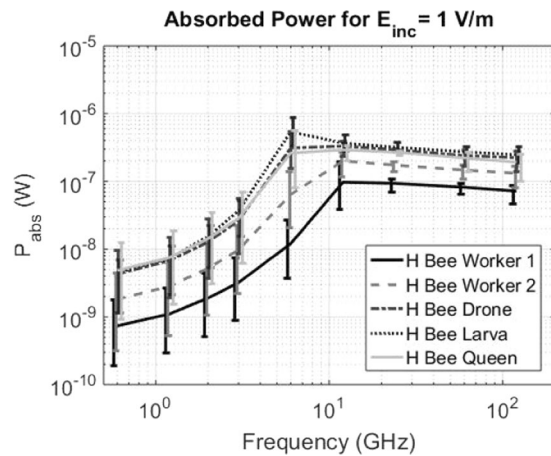


Figure 5. Total absorbed power (P_{abs}) in the five studied honey bees as function of frequency, normalized to an incident plane-wave field strength of 1 V/m at each frequency. The curves indicate the mean values over the twelve plane wave simulations, while the whiskers indicate the maximum and minimum values found at each frequency. The whiskers are slightly offset in order to avoid visual overlap but are all determined at the simulated frequencies described in the Methods Section.

field strengths decreases very rapidly within the phantom and electric fields are basically only present in the outer layers of the insect. This is caused by a decrease in skin depth that is driven by the increase in conductivity at higher frequencies, see Table 1. Note that the total RF-EMF absorbed power in the insect scales both with the internal electric field strength and the conductivity.

Figure 5 shows the normalized RF-EMF P_{abs} as a function of frequency for the five studied insects from 0.6 GHz up to 120 GHz. The curves connect the linear averages of the 12 P_{abs} values obtained for each honey bee at each simulated frequency, while the whiskers indicate the minimum and maximum P_{abs} values found at those frequencies. All P_{abs} values are normalized to an incident field strength of 1 V/m. Figure 5 shows an increase of P_{abs} over frequency for all studied phantoms up to 6 GHz. When comparing the average P_{abs} at 0.6 GHz and 6 GHz, we found relative increases of factors of 16, 35, 72, 121, and 54 for the Worker Bee 1, Worker Bee 2, Drone, Larva, and queen Bee, respectively. The P_{abs} slightly decreases over frequency beyond 12 GHz for all the studied honey bees. When comparing P_{abs} at 12 GHz and 120 GHz, we found relative decreases of 26%, 34%, 33%, 32%, and 34% for the Worker Bee 1, Worker Bee 2, Drone, Larva, and Queen Bee, respectively. The spread on the P_{abs} values obtained at each individual frequency reduces from up to a factor of 13 below 12 GHz to smaller than a factor 2.5 beyond 12 GHz. Figure 5 shows a general increase of P_{abs} with increasing volume and surface area of the studied insects. Previous studies on whole-body averaged absorbed RF power and specific absorption rate of humans have shown a dependency of these quantities on the absorption cross section, a quantity that scales with volume and/or surface area of an exposed subject. When the diagonals of the smallest rectangular brick that contain the insect phantoms are considered, the honey bee with the smallest diagonal, Worker Bee 1 with a diagonal of 13 mm has the overall lowest average P_{abs} . The Larva, Queen Bee, and Drone all have associated diagonals of 22 mm and have similar average P_{abs} values as function of frequency. The Worker Bee 2 has a diagonal that falls in between Worker 1 and the other insects of 16 mm and also has an average P_{abs} that falls in between the curve for the smaller worker and the other honey bee models, see Fig. 5. We attribute the differences between the two Worker Bee phantoms mainly to the difference in size of both phantoms. The larger Worker Bee 2 phantom has a larger diagonal, surface area, and volume. This leads to a higher absorption cross section³³ and higher P_{abs} .

The maximal P_{abs} for the five studied insect models occurs at those wavelengths that are close to the double of this diagonal, which suggests an absorption peak around half a wavelength. The maximum P_{abs} for the Larva model lies in between 3 and 12 GHz, i.e. in between 25 and 100 mm in terms of λ , while the diagonal of said bounding box is 22 mm for the phantom. For the other studied insect models the maximum P_{abs} lies in between 6 and 24 GHz, i.e. in between 23 and 50 mm in terms of λ , with associated phantom diagonals ranging from 16 mm to 22 mm.

As mentioned in the Methods section, the influence of dielectric parameters was studied with simulations using Worker 2 at 2 GHz with altered dielectric parameters. These resulted in P_{abs} values of 6.3×10^{-10} W, 6.3×10^{-9} W, 3.1×10^{-9} W, and 1.8×10^{-9} W, in comparison to 2.0×10^{-9} W for an incident field strength of 1 V/m. This corresponds to relative deviations of -69% , $+210\%$, $+50\%$, and -10% . These deviations are significant but smaller than the full range of a factor of 5 we observed for the larva at 2 GHz as a function of changing incident angle and polarization. These relative differences are small in comparison to the differences we observe over frequency for the same phantom: a factor of 121 over frequency from 0.6 to 6 GHz.

At 120 GHz we find a deviation on P_{abs} smaller than 0.1% when 120 simulation periods are executed in comparison to 30 simulation periods in configuration number 2 shown in Fig. 2 for the Worker 2 phantom. Indicating that the number of simulated periods is sufficient for these simulations. At the same frequency and in the same simulation configuration, a reduction of the grid step with a factor of 2 resulted in a P_{abs} of 8.6×10^{-8} W and 3.1×10^{-7} W for the Worker 2 and Larva phantoms, respectively, while the regular simulations with 0.1 mm

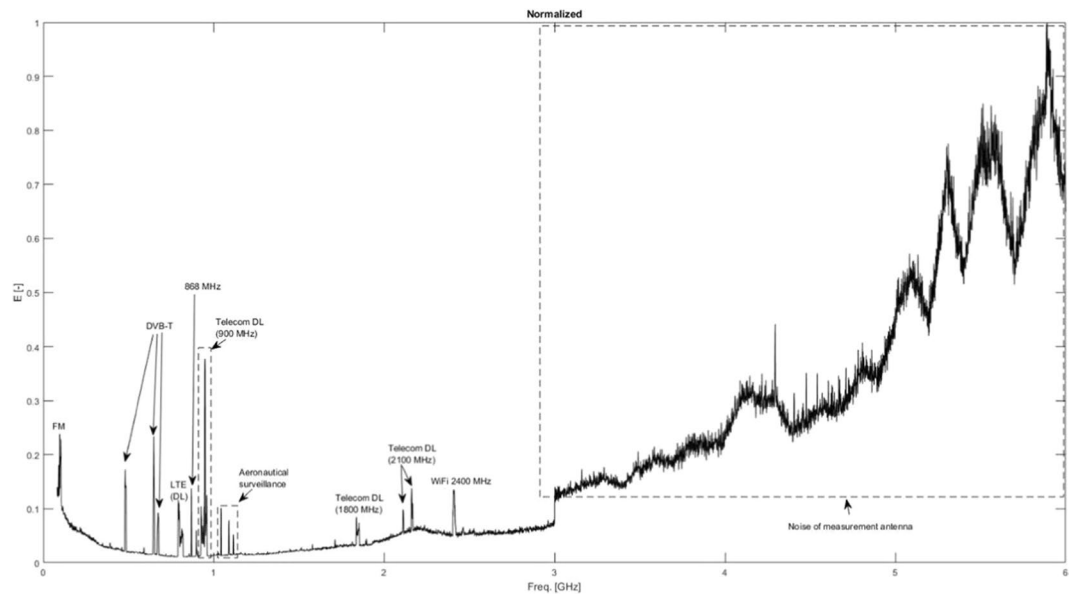


Figure 6. Overview measurement of electric field strength (normalized to maximally measured electric field strength), between 0.8 and 6 GHz, in Aalter. The wireless technologies associated with the different peaks are indicated in the figure as well.

and 0.05 mm grid steps, respectively, resulted in P_{abs} values of 8.4×10^{-8} W and 3.1×10^{-7} W for an incident field strength of 1 V/m. This corresponds to relative deviations of 0.3% and 0.5% for the Worker 2 and the Larva phantoms, respectively, indicating that the chosen grid step was small enough to result in stable numerical results.

The set of 20 incident plane waves with randomized angles of incidence and polarization at 6 GHz using the Worker 2 phantom resulted in an average P_{abs} of $4.5 \times 10^{-8} \pm 1.6 \times 10^{-8}$ W for an incident field strength of 1 V/m, while the set of 12 incident plane waves used to model far-field exposure results in an average P_{abs} of $6.5 \times 10^{-8} \pm 5.3 \times 10^{-8}$ W at the same frequency. The values are fairly close, which indicates that the set of 12 incident plane waves along the main axes is a good proxy for average exposure under a randomized angle of incidence and polarization. The set of twelve plane waves does seem to overestimate exposure at the higher percentiles, since they are significantly higher than those obtained using the random set of plane waves.

RF-EMF field measurements. Figure 6 shows an example of an RF-EMF overview measurement at one of the five studied bee hives (Aalter). Figure 6 shows the relative electric field strength, normalized to the maximally measured electric field strength. The different peaks correspond to several individual frequency bands that are used for telecommunication and broadcasting signals. These frequency bands were then measured individually using the same set-up with triaxial antenna and spectrum analyzer at two positions relative to the bee hive on each measurement site using the measurement procedure described in³².

Table 2 lists the measured E_{RMS} values at the five studied bee hives shown in Fig. 3. As all these measurement sites were rural, private areas, there were no uplink (emissions from a user device to the network) transmissions found. Downlink (DL, this is network to user communication) signals were found at all measurement sites. These signals were generated by three different mobile telecommunications providers in fourteen different frequency bands. The wireless technologies used by the telecommunication operators were: Long Term Evolution (LTE) in frequency bands close to 800 MHz and 1800 MHz, Global System for Mobile telecommunications (GSM) in frequency bands close to 900 MHz, and Universal Mobile Telecommunications Service (UMTS) in frequency bands close to 900 MHz and 2100 MHz. Four other telecommunication bands were identified: TETRA (Terrestrial Trunked Radio, 390–395 MHz) which is a technology used by public services (police, firefighters, etc.), an Industrial, Scientific, and/or Medical (ISM) application around 870 MHz, Digital Enhanced Cordless Telecommunications (DECT) close to 1900 MHz, and Wireless Fidelity (WiFi) at 2400 MHz. Additionally, several frequency bands with RF signals for broadcasting were measured: Frequency Modulated (FM) Radio around 100 MHz, Digital Audio Broadcasting (DAB) around 200 MHz, Digital Video Broadcasting (DVB) at 480–680 MHz. We found one unidentified RF wireless transmission at 592 MHz on two measurement sites: Merelbeke and Eeklo. The total E_{RMS} values ranged from 0.016 V/m on both positions in Merelbeke up to 0.226 V/m on position 1 in Drongen. The average E_{RMS} over the ten studied measurement sites was 0.06 V/m. FM Radio was the dominant source of RF exposure on 7/10 measurement positions. In Drongen and in Aalter, GSM 900 DL was the dominant contributor to the RF-EMF exposure. The field strength of WiFi signals depends strongly on the duty cycle used by the wireless technology³⁴. The measured E_{RMS} values can be extrapolated to peak values under the assumption of 100% duty cycle. In the case of Aalter, this would result in 0.027 V/m and 0.032 V/m on positions 1 and 2, respectively. In the case of Zomergem, this extrapolation would result in peak E_{RMS} values of 0.059 V/m and 0.016 V/m on positions 1 and 2, respectively. On both measurement sites, a theoretically maximal 90% duty cycle would make WiFi the dominant source of exposure. However, such a network load is unlikely in a rural

$E_{RMS}(V/m)$	Aalter		Merelbeke		Eeklo		Zomergem		Drongen	
Frequency Band	Pos 1	Pos 2	Pos 1	Pos 2	Pos 1	Pos 2	Pos 1	Pos 2	Pos 1	Pos 2
FM ^a radio	0.019	0.021	0.009	0.009	0.018	0.014	0.011	0.011	0.009	0.008
T-DAB	— ^b	—	—	—	—	—	0.004	0.005	0.005	0.004
TETRA (390 MHz-395 MHz)	0.001	0.001	0.002	0.001	0.001	0.001	—	—	0.001	0.002
DVB-T 482 MHz	0.009	0.006	—	—	0.003	0.003	0.008	0.006	0.004	0.002
Freq. 592 MHz	—	—	0.001	0.002	0.002	0.002	—	—	—	—
DVB-T 650 MHz	0.008	0.008	0.003	0.003	0.002	0.003	0.006	0.006	0.006	0.004
DVB-T 674 MHz	0.004	0.008	0.004	0.004	0.002	0.002	0.006	0.005	0.004	0.004
ISM 868 MHz (869.5 MHz)	0.001	0.001	—	—	—	—	—	—	—	—
LTE 800 DL Prov. 1 ^c	0.003	0.004	0.001	0.001	0.006	0.004	0.002	0.002	0.002	0.002
LTE 800 DL Prov. 2	0.002	0.002	0.004	0.004	0.002	0.002	0.002	0.002	0.047	0.031
LTE 800 DL Prov. 3	0.003	0.002	0.001	0.001	0.002	0.002	0.002	0.002	0.087	0.073
GSM 900 DL Prov. 1	0.005	0.004	0.001	0.002	0.005	0.007	0.003	0.004	0.004	0.004
GSM 900 DL Prov. 2	0.019	0.036	0.008	0.009	0.002	0.003	0.003	0.004	0.065	0.083
GSM 900 DL Prov. 3	0.004	0.004	0.003	0.002	0.002	0.003	0.003	0.004	0.180	0.137
UMTS 900 DL Prov. 1	0.001	0.002	0.001	0.001	0.003	0.003	0.002	0.002	0.002	0.001
UMTS 900 DL Prov. 2	0.001	0.001	0.005	0.006	0.001	0.001	0.001	0.001	—	—
UMTS 900 DL Prov. 3	0.002	0.002	0.001	0.001	0.001	0.001	0.002	0.001	0.055	0.055
LTE 1800 DL Prov. 1	—	—	—	—	0.004	0.005	—	—	—	—
LTE 1800 DL Prov. 3	0.004	0.004	—	—	—	—	—	—	—	—
DECT 1880 MHz	—	—	—	—	—	—	0.002	0.003	0.002	0.001
UMTS 2100 Prov. 1	—	—	—	—	0.006	0.007	—	—	—	—
UMTS 2100 DL Prov. 2	0.003	0.003	0.004	0.004	—	—	—	—	0.039	0.026
UMTS 2100 Prov. 3	0.005	0.006	—	—	—	—	—	—	—	—
WiFi 2400 MHz instantaneous ^d	0.007 ^e	0.008 ^e	—	—	—	—	0.006 ^f	0.002 ^f	—	—
Total instantaneous	0.032	0.046	0.016	0.016	0.022	0.020	0.019	0.018	0.226	0.189

Table 2. Measured root-mean squared electric field strengths (E_{RMS}) in the 80 MHz – 6 GHz frequency band in V/m. ^a‘FM’ = Frequency Modulated, ‘TETRA’ = Terrestrial Trunked Radio, ‘DVB-T’ = Digital Video Broadcasting - Terrestrial, ‘ISM’ = Industrial, Scientific, and Medical ‘LTE’ = Long Term Evolution, ‘GSM’ = Global System for Mobile Communication, ‘UMTS’ = Universal Mobile Telecommunications System, ‘DECT’ = Digital Enhanced Cordless Telecommunications, ‘WiFi’ = Wireless Fidelity. ^b‘—’ indicates that the frequency band was not present at the measurement site. ^cThree identified Providers are denoted as Prov. 1, 2, and 3. ^d E_{RMS} values for Wireless Fidelity (WiFi) depend on the used duty-cycle, which depends on the use of the network. ^eDuty cycle of 7%. ^fDuty cycle of 1%.

Location	Maximum E-field (1 s interval) (V/m)	Avg E-field (1 s interval) (V/m)
Aalter	0.430	0.272
Merelbeke	0.233	0.1675
Eeklo	0.652	0.532
Zomergem	0.665	0.346
Drongen	0.397	0.297
Average	0.503	0.344

Table 3. Measured maximum and time-averaged broadband incident electric field strengths (100 kHz – 6 GHz).

area. WiFi was not measured at three out of five measurement sites. Additionally, at all measurement sites, RF EMFs emitted by a pulsed radar or other wireless technologies used in aeronautical surveillance were observed. The E_{RMS} value of RF EMFs emitted by a radar cannot be accurately measured without having the specifications of the radar. Therefore, we can only measure the peak value over the 6 min measurement interval. These fields were the highest in Merelbeke, where at position 1 peak E-field values of 0.017 V/m and 2.2 V/m were measured at 1.09 GHz and 1.3 GHz, respectively, while at position 2 peak E-field values of 0.02 V/m and 2.9 V/m were measured at 1.09 GHz and 1.3 GHz, respectively.

In order to provide the readers with a complete overview of the exposure to EMF fields below 6 GHz at the chosen measurement sites, Table 3 lists measured values in the 100 kHz to 6 GHz range using a broadband field

Fraction < 3 GHz (1 - p) (%)	Fraction > 3 GHz p (%)	$P_{abs,real}(p)$ (nW)					$\frac{P_{abs,real}(p)}{P_{abs,real}(100\% < 3\text{ GHz})}$ (·)				
		Drone	Worker 1	Worker 2	Larva	Queen Bee	Drone	Worker 1	Worker 2	Larva	Queen Bee
100	0	0.63	0.010	0.26	0.73	0.71	1	1	1	1	1
90	10	2.5	0.57	1.2	3.0	2.3	3.9	5.7	4.6	4.2	3.3
80	20	4.3	1.0	2.1	5.3	3.9	6.8	10	8.2	7.4	5.6
70	30	6.2	1.5	3.1	7.6	5.6	9.7	15	12	11	7.8
60	40	8.0	2.0	4.0	9.9	7.2	13	20	15	14	10
50	50	9.8	2.4	5.0	12	8.8	16	25	19	17	12
40	60	12	2.9	5.9	15	10	18	29	23	20	15
30	70	14	3.4	6.9	17	12	21	34	26	23	17
20	80	15	3.9	7.8	19	14	24	39	30	26	19
10	90	17	4.3	8.8	22	15	27	43	33	30	21
0	100	19	4.8	9.7	24	17	30	48	37	33	24

Table 4. Absorbed power in the four studied insects for an incident electric field strength of 0.06 V/m, distributed uniformly over frequencies lower and higher than 3 GHz for different relative fractions.

probe. All the average values are higher than what is obtained from the frequency-selective measurements presented in Table 2, as should be the case since a broader band is considered.

Estimation of realistic RF-EMF absorbed power in honey bees. Using the results presented in Table 2, one can rescale the P_{abs} values shown in Fig. 5 in order to obtain a realistic estimate of the absorbed RF-EMF power in honey bees $P_{abs,real}$. The third to eighth columns of the top row of Table 4 list $P_{abs,real}$ assuming that all incident $E_{rms} = 0.06$ V/m is uniformly distributed over the simulated P_{abs} values lower than 3 GHz. These values range from 0.1 nW for Worker 1 until 0.7 nW for the Larva and Queen Bee. In each subsequent row, 10% of the incident power density is transferred to frequencies higher than 3 GHz. This causes an increase in the estimated $P_{abs,real}(p)$. In order to quantify this increase, the five columns to the right show the relative increase in $P_{abs,real}(p)$ as p increases from 0 to 1. A full shift of all RF-EMF power to frequencies higher than 3 GHz - without changing the incident field strength - would result in relative increases in absorbed power between a factors 24–48 for the studied honey bee models. Even a relatively small shift of 10% of the incident power density to higher frequencies will lead to a relative increase in P_{abs} of a factor higher than 3, see Table 4.

Discussion

This study investigates RF-EMF absorption in Western Honey Bees as a function of frequency in the 0.6 to 120 GHz range. To this aim, we used five different models of different honey bees: two workers, a drone, a larva, and a queen. These models were obtained using micro-CT imaging and used for FDTD simulations. These were used to evaluate far-field exposure of honey bees. This far-field exposure is modeled as a set of plane waves at harmonic frequencies between 0.6 and 120 GHz. The numerical simulations resulted in P_{abs} as a function of frequency for the different studied honey bees. These simulations were combined with real RF-EMF exposure measurements near bee hives in Belgium in order to estimate realistic exposure values for honey bees.

Micro-CT imaging is a technique that has previously been shown to accurately scan insects^{35,36}. The models used in this study have resolutions between 0.02 mm and 0.25 mm, which is larger than the resolution of the micro-CT models using in¹¹. Since the smallest grid step used in our simulations is 0.05 mm, the ideal resolution of the insect models would be smaller than that. The larger resolution of the scanning is not a problem for the stability of the FDTD algorithm, but more spatial resolution could be obtained with the same simulation settings. It is expected that the micro-CT models used in this study lead to a better estimation of P_{abs} and the spatial distribution of the electric fields than approximate models such as ellipsoids or cylinders³⁷.

The results of our numerical simulations, see Fig. 5, show an increase of P_{abs} with frequency up to 6–12 GHz. Figure 4 illustrates the mechanism behind this increase: as the frequency increases the EMFs are less likely to diffract around the honey bees, that are relatively small in comparison to the wavelengths <6 GHz, and can penetrate further in the models, generating higher internal electric fields and consequently higher P_{abs} values. Figure 4 also shows why the whole-body averaged P_{abs} does not increase beyond 12 GHz. As the conductivity increases, see Table 1, the electric fields will decay faster within the honey-bee phantoms, which leads to larger relative volumes within the insect with lower fields, see Fig. 4, which will also contribute to the whole-body averaged P_{abs} . This effect also causes the P_{abs} to have a smaller dependency (variation) on incident angle and polarization, see Fig. 5. We also observe that both the frequency-dependency of the P_{abs} , i.e. the transition point between sharp increase in P_{abs} over frequency and slight decrease over frequency, and the magnitude of the P_{abs} , i.e. the offset of the P_{abs} curve, depend on the honey bee's size. This effect was previously observed in¹¹. In general, the results presented in this manuscript are in excellent agreement with those presented in¹¹. The results in terms of P_{abs} obtained for the honey bees in this study fall right in between those obtained in¹¹ for the smaller Australian Stingless Bee and the larger Desert Locust, which confirms again the dependency of P_{abs} on phantom size. The same size-related effect was described for humans in^{28,33,38} and comparable frequency trends were observed in humans that have larger full-body sizes at MHz frequencies^{28,38}. It should be noted that this manuscript focused on exposure of individual insects in free space. In reality, honey bees might cluster, creating a larger absorption cross section and potentially higher absorption at lower frequencies.

The FDTD simulations presented in this manuscript use dielectric properties that were obtained from the literature survey executed in¹¹. Ideally, these dielectric parameters would be obtained for the honey bees studied in this manuscript. However, as shown in¹¹, most studies on dielectric properties of insects in literature^{3,39–41} show similar frequency dependencies of those dielectric parameters. We have executed additional numerical simulations to test for the uncertainty on the dielectric parameters and found deviations up to 210% on P_{abs} , which is significant but still smaller than the variations that exist due to changing angle of incidence and polarization at a fixed frequency, or changes in frequency. We modeled the insects as homogeneous dielectric objects, while in reality they have heterogeneous dielectric parameters. Even though the FDTD algorithm will always require an averaging of dielectric parameters over the cube size, further developments in honey bee and insect phantoms should be focused on the inclusion of multiple tissues in order to refine these models.

In-situ RF-EMF measurements were executed using a measurement set up consisting out of a spectrum analyzer connected to an isotropic, triaxial antenna according to the measurement procedure listed in³². We measured total incident E_{RMS} between 0.016 V/m and 0.226 V/m in five rural environments with a linear average of 0.06 V/m and a quadratic average of 0.1 V/m. Joseph *et al.*³² measured a median total E_{RMS} value of 0.09 V/m over several rural locations in Belgium, the Netherlands, and Sweden. Bhatt *et al.*¹ measured an average E_{RMS} value of 0.07 ± 0.04 V/m in rural environments in Belgium. Both previous studies of rural RF-EMF exposure are close to what we found in this manuscript and certainly within the measurement uncertainty of 3 dB on our measurements.

As our RF-EMF exposure measurements near bee hives demonstrate, see Table 2, most of the current RF-EMF exposure is located at frequencies ≤ 1 GHz. Additionally, Fig. 5 demonstrates that the P_{abs} in all studied Honey bee models is lowest at frequencies ≤ 1 GHz. This implies that in reality, potential shifts in telecommunication frequencies to higher frequencies might induce even larger increases than the ones estimated in Table 4 since in that analysis an average value over all P_{abs} values ≤ 3 GHz is assumed.

Strengths and limitations. This manuscript presents several contributions to the state of the art in the field of RF-EMF exposure assessment of insects. First, to the best of the authors' knowledge, this is the only paper where a numerical RF dosimetry is presented for different developmental stages of honey bees. Second, this is the only study that combined real, *in-situ* exposure measurements with numerical simulations of RF-EMF exposure of insects in order to estimate a realistic exposure of honey bees. In comparison to our previous study¹¹, we considered a broader frequency range from 0.6 GHz up to 120 GHz, which is more in line with the frequencies used in the current telecommunication networks (3 G and 4 G). Finally, this study presents a unique quantification of real-life exposure of honey bees and estimations of how this might change if future frequency shifts in that exposure might occur. A disadvantage of this study is that we did not execute dielectric and thermal measurements in order to obtain dielectric and thermal properties of the studied honey bees. We obtained dielectric properties from literature and were able to execute electromagnetic simulations. We did not perform thermal simulations in this study. Another disadvantage is that we modeled far-field exposure by a limited number of plane waves, while previous studies have shown that a large set of plane waves is necessary to properly model far-field exposure²⁶. We did execute a validation of our exposure set up by comparing it with a set of random plane wave exposures and found good correspondence, certainly close to the mean/median. Finally, we used FDTD simulations that are faced with uncertainties²⁹ and used models that have a limited spatial resolution. This is a disadvantage of any RF-EMF simulation study in comparison to a study that relies on measurements of real insects.

Future research. Our future research will focus on executing exposure measurements of insects in order to validate the RF-EMF P_{abs} values and the dielectric parameters. Additionally, we would like to execute thermal simulations of honey bees and other insects under RF-EMF exposure. Finally, we aim to work on the development of more insect phantoms, with more spatial accuracy and potentially several independently identified tissues.

Conclusions

Exposure of Western Honey Bees (*apis mellifera*) to radio-frequency (RF) electromagnetic fields was studied using a combination of *in-situ* exposure measurements near bee hives in Belgium and numerical simulations. The simulations use the finite-difference time-domain technique to determine the electromagnetic fields in and around five honey bee models exposed to plane waves at frequencies from 0.6 GHz up to 120 GHz. These simulations lead to a quantification of the whole-body averaged absorbed radio-frequency power (P_{abs}) as a function of frequency. The average P_{abs} increases by factors 16 to 121, depending on the considered phantom, when the frequency is increased from 0.6 GHz to 6 GHz for a fixed incident electric field strength. A relatively small decrease in P_{abs} is observed for all studied honey bees between 12 and 120 GHz. RF exposure measurements were executed on ten sites near five different locations with bee hives in Belgium. These measurements resulted in an average total incident RF field strength of 0.06 V/m, which was in excellent agreement with literature. This value was used to assess P_{abs} for those honey bees at those measurement sites. A realistic P_{abs} is estimated to be between 0.1 and 0.7 nW for the studied honey bee models. Assuming that 10% of the incident power density would shift to frequencies higher than 3 GHz would lead to an increase of this absorption between 390–570%. Such a shift in frequencies is expected in future networks.

Received: 1 October 2019; Accepted: 19 December 2019;

Published online: 16 January 2020

References

- Bhatt, C. R. R. *et al.* Assessment of personal exposure from radiofrequency-electromagnetic fields in Australia and Belgium using on-body calibrated exposimeters. *Environ. Res.* **151**, 547–563 (2016).
- International Commission on Non-Ionizing Radiation Protection, I. C. N. I. R. P. Guidelines for limiting exposure to time-varying electric, magnetic, and electromagnetic fields (up to 300 GHz). *Health Phys.* **74**, 494–522 (1998).
- Wang, S., Tang, J., Cavalieri, R. P. & Davis, D. C. Differential heating of insects in dried nuts and fruits associated with radio frequency and microwave treatments. *Transactions ASAE* **46**, 1175–1182 (2003).
- Shrestha, B., Yu, D. & Baik, O. D. Elimination of *Cryptolestes ferrugineus* s. in wheat by radio frequency dielectric heating at different moisture contents. *Prog. In Electromagn. Res.* **139**, 517–538 (2013).
- Shayesteh, N. & Barthakur, N. N. Mortality and behaviour of two stored-product insect species during microwave irradiation. *J. stored Prod. Res.* **32**, 239–246 (1996).
- Das, I., Kumar, G. & Shah, N. G. Microwave heating as an alternative quarantine method for disinfestation of stored food grains. *Int. J. Food Sci.* **2013**, 13 (2013).
- Hansen, J. D., Johnson, J. A. & Winter, D. A. History and use of heat in pest control: a review. *Int. J. Pest Manag.* **57**, 267–289 (2011).
- Wang, S. & Tang, J. Radio frequency and microwave alternative treatments for nut insect control: a review. *Int. Agric. Eng. J.* **10**, 105–120 (2001).
- Nelson, S. O. Review and assessment of radio-frequency and microwave energy for stored-grain insect control. *Transactions ASAE* **39**, 1475–1484 (1996).
- Halverson, S. L. *et al.* High-power microwave radiation as an alternative insect control method for stored products. *J. Econ. Entomol.* **89**, 1638–1648 (1996).
- Thielens, A. *et al.* Exposure of insects to radio-frequency electromagnetic fields from 2 to 120 GHz. *Sci. Reports* **8**, 3924 (2018).
- Colombi, D., Thors, B. & Tornevik, C. Implications of emf exposure limits on output power levels for 5G devices above 6 GHz. *IEEE Antennas Wirel. Propag. Lett.* **14**, 1247–1249 (2015).
- Pi, A. & Khan, F. An introduction to millimeter-wave mobile broadband systems. *IEEE Commun Mag* **49**, 101–107 (2011).
- Bindokas, V. P., Gauger, J. R. & Greenberg, B. Laboratory investigations of the electrical characteristics of honey bees and their exposure to intense electric fields. *Bioelectromagn.* **10**, 1–12 (1989).
- Ferrari, T. Magnets, magnetic field fluctuations and geomagnetic disturbances impair the homing ability of honey bees (*Apis mellifera*). *J. Apic. research* **53**, 452–465 (2014).
- Odemer, R. & Odemer, F. Effects of radiofrequency electromagnetic radiation (rf-emf) on honey bee queen development and mating success. *Sci. total environment* **661**, 553–562 (2019).
- Sharma, V. P. & Kumar, N. R. Changes in honeybee behaviour and biology under the influence of cellphone radiations. *Current Science* **98**, 1376–1378 (2010).
- Favre, D. Mobile phone-induced honeybee worker piping. *Adipologie* **42**, 270–279 (2011).
- Mixon, T. *et al.* Effects of GSM cellular phone radiation on the behaviour of honey bees. *Sci. Bee Cult.* **1**, 22–27 (2009).
- Chou, C. K. S. *et al.* Radio frequency electromagnetic exposure: tutorial review on experimental dosimetry. *Bioelectromagn.* **17**(3), 195–208 (1996).
- Lorensen, W. E. & Cline, H. E. Marching cubes: A high resolution 3D surface construction algorithm. *Comput. Graph.* **21**, 163–169 (1987).
- 3D systems. lithography interface specification. (1998).
- Taubin, G. A signal processing approach to fair surface design. *Proc. ACM SIGGRAPH* **95**, 351–358 (1995).
- Cignoni, P. *et al.* Meshlab: an open-source mesh processing tool. *Proc. Sixth Eurographics Italian Chapter Conf.* **6**, 129–136 (2008).
- Balanis, C. A. *Antenna theory: Analysis and design.* (2016).
- Vermeeren, G., Joseph, W. & Martens, L. Whole-body SAR in spheroidal adult and child phantoms in realistic exposure environment. *IET Electron. Lett.* **44**, 790–791 (2008).
- Thielens, A., Vermeeren, G., Joseph, W. & Martens, L. Stochastic method for determination of the organ-specific averaged SAR in realistic environments at 950 MHz. *Bioelectromagn.* **34**, 549–562 (2013).
- Bakker, J. F., Paulides, M. M., Christ, A., Kuster, N. & van Rhoon, G. C. Assessment of induced SAR in children exposed to electromagnetic plane waves between 10 MHz and 5.6 GHz. *Phys. Medicine Biol.* **55**, 3115–3130 (2010).
- Hand, J. W. Modelling the interaction of electromagnetic fields (10 MHz–10 GHz) with the human body: Methods and applications. *Phys. Medicine Biol.* **53**, R243–286 (2008).
- Cenelec European committee for electrotechnical standardisation. TC 106X WG1 EN 50492 *in situ*. basic standard for the *in-situ* measurement of electromagnetic field strength related to human exposure in the vicinity of base stations. (2008).
- Electronic communications committee (ECC) within the European conference of postal and telecommunications administrations (CEPT). ECC recommendation (02)04 (revised Bratislava 2003, Helsinki 2007) measuring non-ionising electromagnetic radiation (9 kHz – 300 GHz). <http://www.ero.dk>. (2004).
- Joseph, W., Verloock, L., Goeminne, F., Vermeeren, G. & Martens, L. Assessment of RF exposures from emerging wireless communication technologies in different environments. *Health Phys.* **102**, 161–172 (2012).
- Bamba, A. *et al.* A formula for human average whole-body SAR_{wb} under diffuse fields exposure in the GHz region. *Phys. Medicine Biol.* **59**, 7435–7456 (2014).
- Verloock, L., Joseph, W., Vermeeren, G. & Martens, L. Procedure for assessment of general public exposure from WLAN in offices and in wireless sensor network testbed. *Electromagn Biol Med* **33**, 21–28 (2014).
- Greco, M., Tong, J., Soleimani, M., Bell, G. D. & Schafer, M. O. Imaging live bee brains using minimally-invasive diagnostic radioentomology. *J. Insect Sci.* **12**, 1–7 (2012).
- Smith, D. B. *et al.* Exploring miniature insect brains using micro-CT scanning techniques. *Nat. Sci. Reports* **6**, 21768 (2016).
- Huang, Z., Chen, L. & Wang, S. Computer simulation of radio frequency selective heating of insects in soybeans. *Int. J. Heat Mass Transf.* **90**, 406–417 (2015).
- Hirata, A., Kodera, S., Wang, J. & Fujiwara, O. Dominant factors influencing whole-body average SAR due to far-field exposure in whole-body resonance frequency and GHz regions. *Bioelectromagn.* **28**, 484–487 (2007).
- Nelson, S. O., Bartley, P. G. & Lawrence, K. C. RF and microwave dielectric properties of stored-grain insects and their implications for potential insect control. *Transactions ASAE* **41**, 685–692 (1998).
- Colpitts, B., Pelletier, Y. & Cogswell, S. Complex permittivity measurements of the Colorado potato beetle using coaxial probe techniques. *J. Microw. Power Electromagn. Energy* **27**, 175–182 (1992).
- Massa, R. *et al.* Wide band permittivity measurements of palm (*Phoenix canariensis*) and *Rhynchophorus ferrugineus* (Coleoptera Curculionidae) for RF pest control. *J. Microw. Power Electromagn. Energy* **48**, 158–169 (2014).

Acknowledgements

This project has received funding from the European Union's Horizon 2020 research and innovation programme under the Marie Skłodowska-Curie grant agreement No 665501 with the research Foundation Flanders (FWO). A.T. is an FWO [PEGASUS]² Marie Skłodowska-Curie Fellow. The authors would like to thank the bee keepers who allowed us to perform measurements at their bee hives.

Author contributions

A.T. conducted the numerical simulations, analyzed the results, and drafted the manuscript. L.V. conducted the measurements. M.K.G. conducted the imaging and post processing of the imaging. W.J and L.M. contributed to analyzing the methodology and results. All authors reviewed the manuscript and provided input to the different sections.

Competing interests

The authors declare no competing interests.

Additional information

Correspondence and requests for materials should be addressed to A.T.

Reprints and permissions information is available at www.nature.com/reprints.

Publisher's note Springer Nature remains neutral with regard to jurisdictional claims in published maps and institutional affiliations.



Open Access This article is licensed under a Creative Commons Attribution 4.0 International License, which permits use, sharing, adaptation, distribution and reproduction in any medium or format, as long as you give appropriate credit to the original author(s) and the source, provide a link to the Creative Commons license, and indicate if changes were made. The images or other third party material in this article are included in the article's Creative Commons license, unless indicated otherwise in a credit line to the material. If material is not included in the article's Creative Commons license and your intended use is not permitted by statutory regulation or exceeds the permitted use, you will need to obtain permission directly from the copyright holder. To view a copy of this license, visit <http://creativecommons.org/licenses/by/4.0/>.

© The Author(s) 2020

Policy assessments for the carbon emission flows and sustainability of Bitcoin blockchain operation in China

Shangrong Jiang ^{1,7}, Yuze Li ^{1,2,7}, Quanying Lu², Yongmiao Hong^{2,3}, Dabo Guan^{4✉}, Yu Xiong⁵ & Shouyang Wang ^{1,2,6✉}

The growing energy consumption and associated carbon emission of Bitcoin mining could potentially undermine global sustainable efforts. By investigating carbon emission flows of Bitcoin blockchain operation in China with a simulation-based Bitcoin blockchain carbon emission model, we find that without any policy interventions, the annual energy consumption of the Bitcoin blockchain in China is expected to peak in 2024 at 296.59 Twh and generate 130.50 million metric tons of carbon emission correspondingly. Internationally, this emission output would exceed the total annualized greenhouse gas emission output of the Czech Republic and Qatar. Domestically, it ranks in the top 10 among 182 cities and 42 industrial sectors in China. In this work, we show that moving away from the current punitive carbon tax policy to a site regulation policy which induces changes in the energy consumption structure of the mining activities is more effective in limiting carbon emission of Bitcoin blockchain operation.

¹School of Economics and Management, University of Chinese Academy of Sciences, Beijing, China. ²Academy of Mathematics and Systems Science, Chinese Academy of Sciences, Beijing, China. ³Department of Economics and Department of Statistical Science, Cornell University, Ithaca, NY, USA. ⁴Department of Earth System Science, Tsinghua University, Beijing, China. ⁵Surrey Business School, University of Surrey, Guildford, UK. ⁶Center for Forecasting Science, Chinese Academy of Sciences, Beijing, China. ⁷These authors contributed equally: Shangrong Jiang, Yuze Li. ✉email: guandabo@tsinghua.edu.cn; sywang@amss.ac.cn

As Bitcoin attracted considerable amount of attention in recent years, its underlying core mechanism, namely blockchain technology, has also quickly gained popularity. Due to its key characteristics such as decentralization, auditability, and anonymity, blockchain is widely regarded as one of the most promising and attractive technologies for a variety of industries, such as supply chain finance, production operations management, logistics management, and the Internet of Things (IoT)^{1–3}. Despite its promises and attractiveness, its first application in the actual operation of the Bitcoin network indicates that there exists a non-negligible energy and carbon emission drawback with the current consensus algorithm. Therefore, there is an urgent need to address this issue. In this paper, we quantify the current and future carbon emission patterns of Bitcoin blockchain operation in China under different carbon policies. In recent years, the system dynamics (SD) based model is widely introduced for carbon emission flow estimation of a specific area or industry^{4,5}. In comparison to its counterparts, SD modeling has two main advantages in carbon emission flow assessment: first, by combining the feedback loops of stock and flow parameters, SD is able to capture and reproduce the endogenous dynamics of complex system elements, which enables the simulation and estimation of specific industry operations^{6–8}. In addition, since the SD-based model is focused on disequilibrium dynamics of the complex system^{9,10}, intended policies can be adjusted for scenario policy effectiveness evaluation. Consequently, based on system dynamics modeling, we develop the Bitcoin blockchain carbon emission model (BBCE) to assess the carbon emission flows of the Bitcoin network operation in China under different scenarios.

This paper uses the theory of carbon footprint to create a theoretical model for Bitcoin blockchain carbon emission assessment and policy evaluation^{11,12}. First, we establish the system boundary and feedback loops for the Bitcoin blockchain carbon emission system, which serve as the theoretical framework to investigate the carbon emission mechanism of the Bitcoin blockchain. The BBCE model consists of three interacting subsystems: Bitcoin blockchain mining and transaction subsystem, Bitcoin blockchain energy consumption subsystem, and Bitcoin blockchain carbon emission subsystem. Specifically, transactions packaged in the block are confirmed when the block is formally broadcasted to the Bitcoin blockchain. To increase the probability of mining a new block and getting rewarded, mining hardware will be updated continuously and invested by network participants for a higher hash rate, which would cause the overall hash rate of the whole network to rise. The network mining power is determined by two factors: first, the network hash rate (hashes computed per second) positively accounts for the mining power increase in the Bitcoin blockchain when high hash rate miners are mining; second, power usage efficiency (PUE) is introduced to illustrate the energy consumption efficiency of Bitcoin blockchain as suggested by Stoll¹³. The network energy cost of the Bitcoin mining process is determined by the network energy consumption and average electricity price, which further influences the dynamic behavior of Bitcoin miners. The BBCE model collects the carbon footprint of Bitcoin miners in both coal-based energy and hydro-based energy regions to formulate the overall carbon emission flows of the whole Bitcoin industry in China. The level variable GDP consists of Bitcoin miner's profit rate and total cost, which reflects the accumulated productivity of the Bitcoin blockchain. It also serves as an auxiliary factor to generate the carbon emission per GDP in our model, which provides guidance for policy makers in implementing the punitive carbon taxation on the Bitcoin mining industry. Bitcoin blockchain reward halving occurs every four years, which means that the reward of broadcasting a new block in Bitcoin blockchain will be zero in

2140. As a result, the Bitcoin market price increases periodically due to the halving mechanism of Bitcoin blockchain. Finally, by combining both carbon cost and energy cost, the total cost of the Bitcoin mining process provides a negative feedback for miner's profit rate and their investment strategies. Miners will gradually stop mining in China or relocate to elsewhere when the mining profit turns negative in our BBCE simulation. The comprehensive theoretical relationship of BBCE parameters is demonstrated in Supplementary Fig. 1.

We find that the annualized energy consumption of the Bitcoin industry in China will peak in 2024 at 296.59 Twh based on the Benchmark simulation of BBCE modeling. This exceeds the total energy consumption level of Italy and Saudi Arabia and ranks 12th among all countries in 2016. Correspondingly, the carbon emission flows of the Bitcoin operation would peak at 130.50 million metric tons per year in 2024. Internationally, this emission output surpasses the total greenhouse gas emission output of the Czech Republic and Qatar in 2016 reported by cia.gov under the Benchmark scenario without any policy intervention. Domestically, the emission output of the Bitcoin mining industry would rank in the top 10 among 182 prefecture-level cities and 42 major industrial sectors in China, accounting for approximately 5.41% of the emissions of the electricity generation in China according to the China Emission Accounts & Datasets (www.ceads.net). In addition, the maximized carbon emission per GDP of the Bitcoin industry would reach 10.77 kg/USD based on BBCE modeling. Through scenario analysis, we find that some commonly implemented carbon emission policies, such as carbon taxation, are relatively ineffective for the Bitcoin industry. On the contrary, site regulation policies for Bitcoin miners which induce changes in the energy consumption structure of the mining activities are able to provide effective negative feedbacks for the carbon emission of Bitcoin blockchain operation.

Results

The energy and carbon emission problem of Bitcoin mining in China. Although the Proof-of-Work (PoW) consensus algorithm has enabled Bitcoin blockchain to operate in a relatively stable manner, several unexpected behaviors of the Bitcoin blockchain have been detected: first, the attractive financial incentive of Bitcoin mining has caused an arms race in dedicated mining hardware¹⁴. The mining hardware has evolved through several generations. Initially, miners used the basic Central Processing Unit (CPU) on general-purpose computers. Then, a shift was made to the Graphic Processing Unit (GPU) that offered more power and higher hash rates than the CPU. Finally, the Application-Specific Integrated Circuits (ASICs) that are optimized to perform hashing calculations were introduced. Nevertheless, the rapid hardware development and fierce competition have significantly increased the capital expenditure for Bitcoin mining¹⁵; second, the Bitcoin mining activity and the constant-running mining hardware has led to large energy consumption volume. Previous literature has estimated that the Bitcoin blockchain could consume as much energy per year as a small to medium-sized country such as Denmark, Ireland, or Bangladesh¹⁶; finally, the large energy consumption of the Bitcoin blockchain has created considerable carbon emissions (see Supplementary Fig. 2 for details). It is estimated that between the period of January 1st, 2016 and June 30th, 2018, up to 13 million metric tons of CO₂ emissions can be attributed to the Bitcoin blockchain¹⁷. Although the estimate ranges vary considerably, they have indicated that energy consumption of network and its corresponding environmental impacts have become a non-negligible issue.

The growing energy consumption and the environmental impacts of the Bitcoin blockchain have posed problems for many

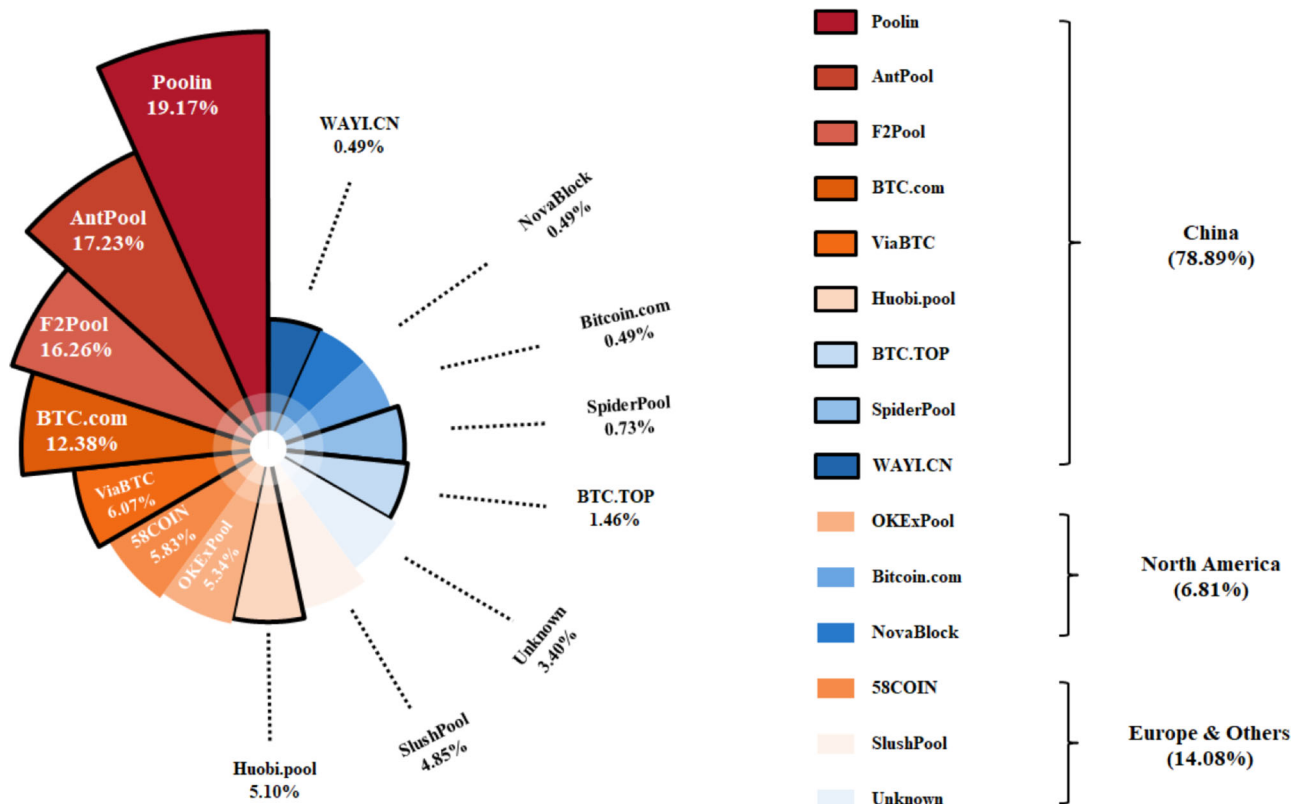


Fig. 1 Mining pool distributions of Bitcoin blockchain. As of April 2020, China accounts for more than 75% of Bitcoin blockchain operation around the world. Some rural areas in China are considered as the ideal destination for Bitcoin mining mainly due to the cheaper electricity price and large undeveloped land for pool construction. The mining pool statistics is obtained from <https://btc.com/stats>.

Table 1 Scenario parameter settings.

Scenarios	Measures	Market access (%)	Miner site selection (%)	Carbon tax
Benchmark (BM)	Baseline policy intervention	100	40	2
Market access (MA)	Raise the market access standards for Bitcoin miner efficiency	50	40	2
Site regulation (SR)	Strict regulation on Bitcoin industry in the coal-based energy region	100	20	2
Carbon tax (CT)	Extra punitive carbon tax on Bitcoin mining	100	40	4

Note: Exogenous auxiliary parameters are introduced to assess the carbon emission flows under different Bitcoin policy measures. In terms of variable settings, three main parameters are chosen as the scenario factors in the proposed BBCE model, including market access (MA), miner site regulation (SR), and carbon tax (CT).

countries, especially for China. Due to the proximity to manufacturers of specialized hardware and access to cheap electricity, majority of the mining process has been conducted in China as miners in the country account for more than 75% of the Bitcoin network’s hashing power, as shown in Fig. 1. As one of the largest energy consuming countries on the planet, China is a key signatory of the Paris Agreement^{18–20}. However, without appropriate interventions and feasible policies, the intensive Bitcoin blockchain operation in China can quickly grow as a threat that could potentially undermine the emission reduction effort taken place in the country¹⁰.

Suggested by the previous work²¹ and the subsystems of our proposed BBCE model, we consider three main Bitcoin policies conducted at different stages of the Bitcoin mining industry, which then formulates the four scenario assessments for Bitcoin blockchain carbon emission flows (in Table 1). In detail, Benchmark (BM) scenario is a baseline and current scenario of each policy factor, which suggests that the Bitcoin industry continues to operate under minimal policy intervention. In the

Benchmark scenario, market access is assumed to be 100%, which indicates that profitable Bitcoin miners of all efficiencies are allowed to operate in China. As suggested by the actual regional statistics of Bitcoin miners, we assume 40% of miners are located in the coal-based area in the Benchmark scenario. Moreover, the punitive carbon tax will be imposed if the carbon emission per GDP of the Bitcoin industry is greater than 2. In the other three scenarios, policies on different Bitcoin mining procedures are adjusted due to energy saving and emission reduction concerns. Specifically, in the Bitcoin mining and transaction subsystem, market access standard for efficiency is doubled, i.e., profitable miners with low efficiency are forbidden to enter the Chinese Bitcoin market in the market access (MA) scenario, and policy makers are forced to maintain the network stability of Bitcoin blockchain in an efficient manner. In the site regulation (SR) scenario, Bitcoin miners in the coal-based area are persuaded and suggested to relocate to the hydro-rich area to take advantage of the relatively lower cost of surplus energy availability in the area due to factors such as rain season, which results in only 20% of

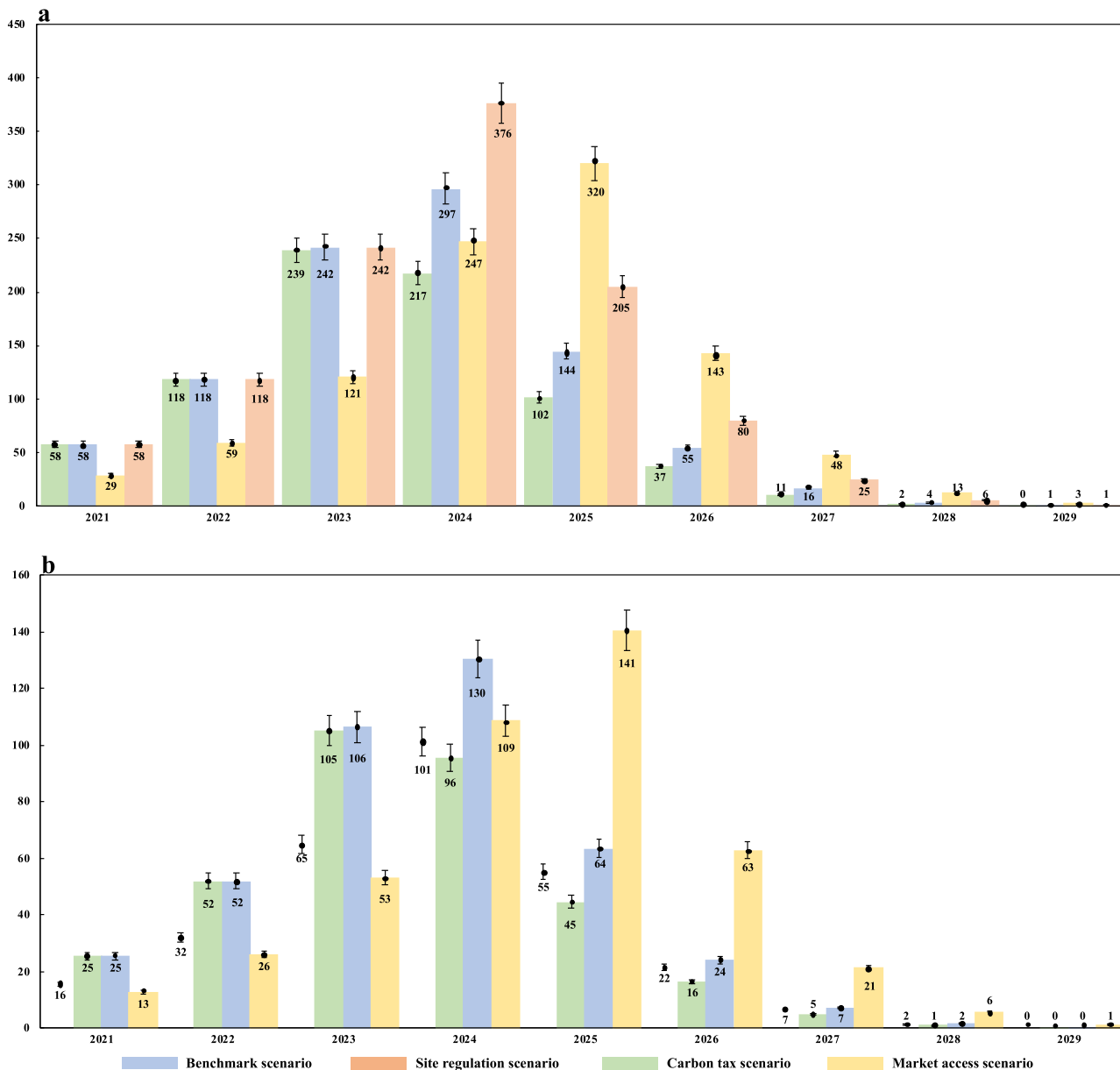


Fig. 2 Estimated annualized scenario simulation results. Estimated annualized energy consumption (a) and carbon emission flows (b) of Bitcoin operation in China are generated through monthly simulation results of BBCE modeling from 2021 to 2029. The blue, red, yellow, and green bars in a and b indicate the annual energy consumption and carbon emission flows of Chinese Bitcoin industry in benchmark, site regulation, market access, and carbon tax scenario, respectively. Each data is presented as mean values ± SEM based on 95% confidence intervals calculated by two-tailed t-tests ($p < 0.05$). $n = 204$ emission observations.

miners remaining in the coal-based area in the scenario. In the carbon tax (CT) scenario, carbon tax is increased to two-times the initial value to enforce more strict punishment for high carbon emission behaviors of Bitcoin blockchain. Utilizing the above scenarios, carbon emission flows and energy consumptions of Bitcoin blockchain are assessed, the carbon and energy reduction effectiveness of different policies are evaluated in BBCE simulations from the period of 2014–2030.

Carbon emission flows of Bitcoin blockchain operation.

Without any policy interventions, the carbon emission pattern of the Bitcoin blockchain will become a non-negligible barrier against the sustainability efforts of China. The peak annual energy consumption and carbon emission of the Bitcoin blockchain in

China are expected to exceed those of some developed countries such as Italy, the Netherlands, Spain, and Czech Republic. Figure 2 reports the estimated annualized energy consumption and carbon emission flows of Bitcoin blockchain in China. As the baseline assessment under minimal policy intervention, the Benchmark scenario simulates the natural operation results of the Bitcoin blockchain. In the BM scenario, the annual energy consumption of Bitcoin blockchain in China will gradually grow and eventually peak in 2024, at 296.59 Twh per year. This suggests that Bitcoin industry operation would follow an energy intensive pattern. In fact, energy consumed by Chinese Bitcoin blockchain in 2024 will exceed the energy consumption level of Italy and Saudi Arabia in 2016, ranking it 12th among all the countries. Regarding the carbon tax scenario, the highest energy demand of the Bitcoin industry slightly decreases due to carbon emission

penalties, at 217.37 Twh. However, the results of the market access and site regulation scenarios indicate that the total energy consumption of the Bitcoin industry will reach 350.11 Twh and 319.80 Twh, respectively, in 2024 and 2025.

It is clear that the carbon emission behavior of the Bitcoin industry is consistent with the Bitcoin blockchain energy consumption intensity. In the BM scenario, annual carbon emission of the Bitcoin industry is expected to reach its maximum in 2024, at 130.50 million metric tons. In essence, the carbon emission pattern of the Bitcoin industry would become an increasing threat to China's greenhouse emission reduction target. At the international level, the estimated Bitcoin carbon emission in China exceeds the total greenhouse emission of the Czech Republic and Qatar in 2016, ranking it 36th worldwide. At the domestic level, the emission output of the Bitcoin mining industry would rank in the top 10 among 182 Chinese prefecture-level cities and 42 major industrial sectors. In comparison, the carbon emissions generated by Bitcoin blockchain experienced a significant reduction in SR and CT scenarios, which illustrate the positive impact of these carbon-related policies. On the contrary, the MA scenario witnesses a considerable increase of Bitcoin carbon emission to 140.71 million metric tons in 2025.

Based on the scenario results of the BBCE model, the Benchmark scenario indicates that the energy consumed and the carbon emissions generated by Bitcoin industry operation are simulated to grow continuously as long as mining Bitcoin maintains its profitability in China. This is mainly due to the positive feedback loop of the PoW competitive mechanism, which requires advanced and high energy-consuming mining hardware for Bitcoin miners in order to increase the probability of earning block rewards. In addition, the flows and long-term trend of carbon emission simulated by the proposed system dynamics model are consistent with several previous estimations^{10,13}, which are devoted to precisely estimate the carbon footprint of Bitcoin blockchain.

The Paris Agreement is a worldwide agreement committed to limit the increase of global average temperature^{22,23}. Under the Paris Agreement, China is devoted to cut down 60% of the carbon emission per GDP by 2030 based on that of 2005. However, according to the simulation results of the BBCE model, we find that the carbon emission pattern of Bitcoin blockchain will become a potential barrier against the emission reduction target of China. As shown in Fig. 3, the peak annualized emission output of the Bitcoin mining industry would make it the 10th largest emitting sector out of a total of 42 major Chinese industrial sectors. In particular, it would account for approximately 5.41% of the emissions of the electricity generation in China according to the China Emission Accounts & Datasets (www.ceads.net). The peak carbon emission per GDP of Bitcoin industry is expected to sit at 10.77 kg per USD. In addition, in the current national economy and carbon emission accounting of China, the operation of the Bitcoin blockchain is not listed as an independent department for carbon emissions and productivity calculation. This adds difficulty for policy makers to monitor the actual behaviors of the Bitcoin industry and design well-directed policies. In fact, the energy consumption per transaction of Bitcoin network is larger than numerous mainstream financial transaction channels¹⁷. To address this issue, we suggest policy makers to set up separated accounts for the Bitcoin industry in order to better manage and control its carbon emission behaviors in China.

Carbon policy effectiveness evaluation. Policies that induce changes in the energy consumption structure of the mining activities may be more effective than intuitive punitive measures in limiting the total amount of energy consumption and carbon emission in the Bitcoin blockchain operation. Figure 4 presents the values of key parameters simulated by BBCE model. The

carbon emission per GDP of the BM scenario in China is larger than that of all other scenarios throughout the whole simulation period, reaching a maximum of 10.77 kg per USD in June 2026. However, we find that the policy effectiveness under the MA and CT scenario is rather limited on carbon emission intensity reduction, i.e., the policy effectiveness of Market access is expected to reduce in August 2027 and that of Carbon tax is expected to be effective until July 2024. Among all the intended policies, Site Regulation shows the best effectiveness, reducing the peak carbon emission per GDP of the Bitcoin industry to 6 kg per USD. Overall, the carbon emission per GDP of the Bitcoin industry far exceeds the average industrial carbon intensity of China, which indicates that Bitcoin blockchain operation is a highly carbon-intense industry.

In the BM scenario, Bitcoin miners' profit rate are expected to drop to zero in April 2024, which suggests that the Bitcoin miners will gradually stop mining in China and relocate their operation elsewhere. However, it is important to note that the entire relocation process does not occur immediately. Miners with higher sunk costs tend to stay in operation longer than those with lower sunk costs, hoping to eventually make a profit again. Consequently, the overall energy consumption associated with Bitcoin mining remains positive until the end of 2030, at which time almost all miners would have relocated elsewhere. Correspondingly, the network hash rate is computed to reach 1775 EH per second in the BM scenario and the miner total cost to reach a maximum of 1268 million dollars. Comparing the scenario results for the three policies, the profitability of mining Bitcoin in China is expected to deteriorate more quickly in the CT scenario. On the other hand, Bitcoin blockchain can maintain profitability for a longer period in MA and SR scenarios.

Some attractive conclusions can be drawn based on the results of BBCE simulation: although the MA scenario enhances the market access standard to increase Bitcoin miners' efficiencies, it actually raises, rather than reduces, the emission output based on the simulation outcome. In the MA scenario, we observe the phenomenon of incentive effects proposed by previous works, which is identified in other fields of industrial policies, such as monetary policies, transportation regulations, and firm investment strategies^{24–26}. In essence, the purpose of the market access policy is to limit the mining operations of low-efficiency Bitcoin miners in China. However, the surviving miners are all devoted to squeezing more proportion of the network hash rate, which enables them to stay profitable for a longer period. In addition, the Bitcoin industry in China generates more CO₂ emissions under the MA scenario, which can be mainly attributed to the Proof-of-Work (PoW) algorithm and profit-pursuit behaviors of Bitcoin miners. The results of the MA scenario indicate that market-related policy is likely to be less effective in dealing with high carbon emission behaviors of the Bitcoin blockchain operation.

The carbon taxation policy is widely acknowledged as the most effective and most commonly implemented policy on carbon emission reduction²⁷. However, the simulation results of the CT scenario indicate that carbon tax only provides limited effectiveness for the Bitcoin industry. The carbon emission patterns of the CT scenario are consistent with the BM scenario until Bitcoin miners are aware that their mining profits are affected by the punitive carbon tax on Bitcoin mining. On the contrary, the evidence from the SR scenario shows that it is able to provide a negative feedback for the carbon emissions of Bitcoin blockchain operation. In our simulation, the maximized carbon emission per GDP of the Bitcoin industry is halved in the SR scenario in comparison to that in the BM scenario. It is interesting to note that although the peak annualized energy consumption cost of the Bitcoin mining industry in the SR scenario is higher than that in the BM scenario, a significantly higher proportion of miners have

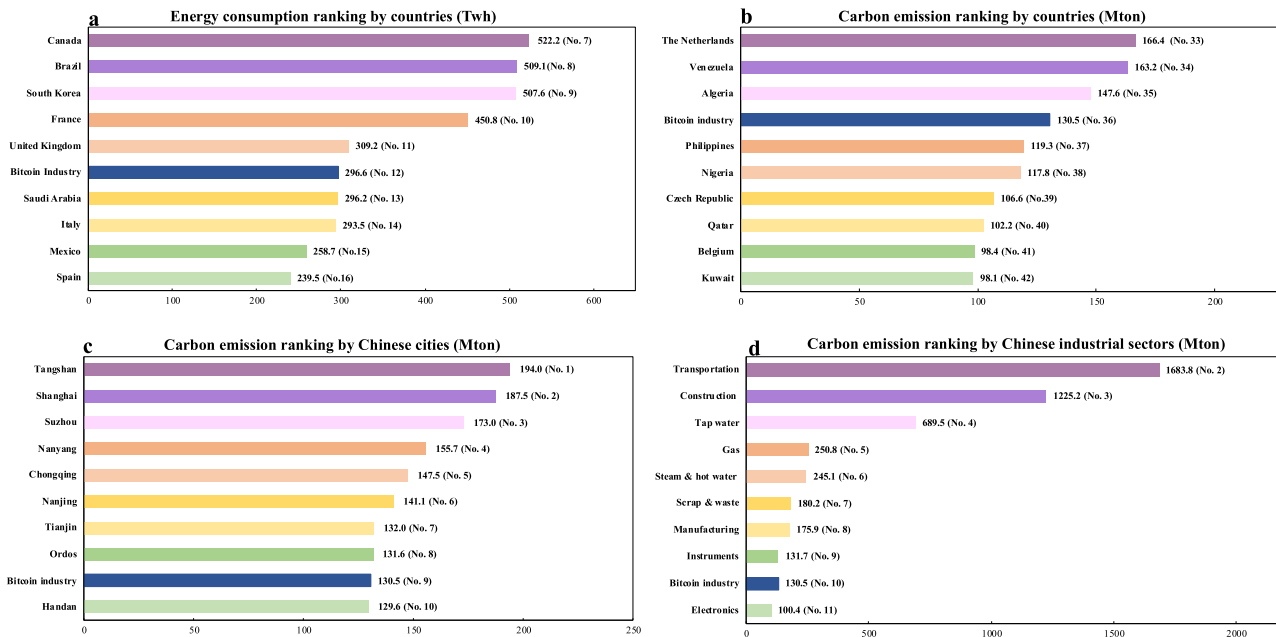


Fig. 3 Bitcoin industry energy consumption and carbon emission comparisons. In Fig. 3, the peak energy consumption and carbon emission of Bitcoin industry are compared to national level emissions of other countries as well as to the emissions of domestic cities and industrial sectors in China. Annual energy consumption and ranking by countries **a** are obtained from cia.gov (www.cia.gov), carbon emission and ranking by countries **b** are collected from global carbonatlas (www.globalcarbonatlas.org). The carbon emission by Chinese cities **(c)** and industrial sectors **(d)** are obtained from China Emission Accounts and Datasets (www.ceads.net). Due to the unreleased or missing data in some database, the above energy consumption and carbon emission data are obtained for 2016 level.

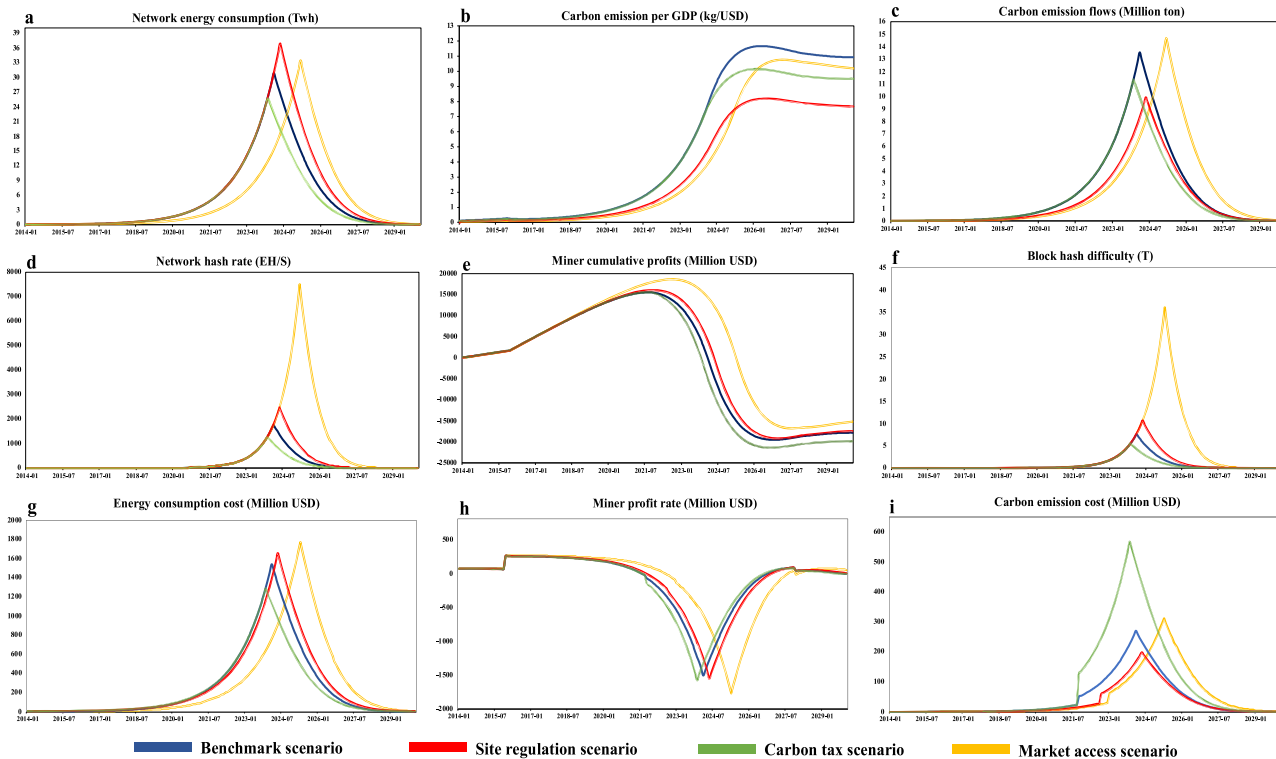


Fig. 4 BBCE scenario assessment comparisons. **a-i** Monthly network energy consumption **(a)**, carbon emission per GDP **(b)**, carbon emission flows **(c)**, network hash rate **(d)**, miner cumulative profits **(e)**, block hash difficulty **(f)**, energy consumption cost **(g)**, miner profit rate **(h)**, and carbon emission cost **(i)** under each intended policy are simulated and calculated by BBCE framework. Based on the regressed parameters of the BBCE model, the whole sample timesteps of network carbon emission assessment cover the period from January 2014 to January 2030.

relocated to conduct Bitcoin mining operation in the hydro-rich area in the SR scenario. Consequently, this naturally lowers the associated carbon emission cost in comparison to the BM scenario.

In general, the carbon emission intensity of the Bitcoin blockchain still far exceeds the average industrial emission intensity of China under different policy interventions, including limiting Bitcoin mining access, altering the miner energy consumption structure and implementing carbon emissions tax. This result indicates the stable high carbon emission property of Bitcoin blockchain operations. Nevertheless, it is rather surprising to arrive at the conclusion that the newly introduced cryptocurrency based on disruptive blockchain technology is expected to become an energy and carbon-intensive industry in the near future.

Discussion

The current Proof-of-Work consensus algorithm used in the Bitcoin blockchain can potentially undermine the wide implementation and the operational sustainability of the disruptive blockchain technology. Overall, Bitcoin is a typical and pioneering implementation of blockchain technology. Its decentralized transaction characteristics and consensus algorithm provide a novel solution for trust mechanism construction, which can be beneficial and innovative for a variety of industrial development and remote transactions. In recent years, blockchain technology has been introduced and adopted by abundant traditional industries which seek to optimize their operation process in the real world²⁸, such as supply chain finance²⁹, smart contract³⁰, international business and trade³¹, as well as manufacturing operations³². In addition, a national digital currency based on blockchain technology, namely Digital Currency Electronic Payment (DCEP), is scheduled and designed by The People's Bank of China, which is expected to replace the current paper-currency-based M0 supply in China.

However, the current consensus algorithm of Bitcoin, namely Proof-of-Work, gives rise to the hash rate competitions among Bitcoin miners for its potential block reward, which attracts an increasing number of miners to engage in an arms race and raise the energy consumption volumes of the whole Bitcoin blockchain. As a result, although PoW is designed to decentralize Bitcoin transactions and prevent inflation, we find that it would become an energy and carbon-intensive protocol, which eventually leads to the high carbon emission patterns of Bitcoin blockchain operation in China. The evidence of Bitcoin blockchain operation suggests that with the broaden usages and applications of blockchain technology, new protocols should be designed and scheduled in an environmentally friendly manner. This change is necessary to ensure the sustainability of the network—after all, no one wants to witness a disruptive and promising technique to become a carbon-intensive technology that hinders the carbon emission reduction efforts around the world. The auditable and decentralized transaction properties of blockchain provide a novel solution for trust mechanism construction, which can be beneficial and innovative for a variety of industrial development and remote transactions. However, the high GHG emission behavior of Bitcoin blockchain may pose a barrier to the worldwide effort on GHG emission management in the near future. As a result, the above tradeoff is worthy of future exploration and investigation.

Different from traditional industries, the carbon emission flows of emerging industries such as Bitcoin blockchain operation are unaccounted for in the current GDP and carbon emissions calculations. Without proper accounting and regulation, it is rather challenging to assess the carbon emission flows of these new industries using traditional tools such as input–output analysis. Through system dynamics modeling, our analysis constructs the emission feedback loops as well as captures the carbon emission

patterns. Furthermore, we are able to conduct emission assessment and evaluate the effectiveness of various potential implementable policies. Through scenario analysis, we show that moving away from the current punitive carbon tax policy consensus to a site regulation (SR) policy which induces changes in the energy consumption structure of the mining activities is more effective in limiting the total amount of carbon emission of Bitcoin blockchain operation. Overall, our results have demonstrated that system dynamics modeling is a promising approach to investigate the carbon flow mechanisms in emerging industries.

At the same time, we acknowledge there exists some limitations to our study and outline future directions for research. First, to reflect the true designed fundamental value of Bitcoin as intended by Nakamoto, our model assumes that the long-term Bitcoin price is primarily influenced by halving mechanism of Bitcoin mining rewards and is subjected to a linear increase every time a reward halving occurs. While the historical average Bitcoin price between each reward halving occurrence has generally followed this pattern since 2014, it is extremely volatile in real market operation and is subjected to the influence of other factors such as investor expectations. Therefore, a degree of uncertainty remains as to whether the linearity price assumption would hold, particularly as the Bitcoin market continues to grow into the future. Furthermore, our site regulation (SR) scenario assumes no cost on miners from relocating to clean-energy-based regions. In reality, there may be certain costs associated with this action, such as transportation. Therefore, although our results suggest that a site regulation (SR) policy may be more effective than the current punitive carbon tax policy consensus in limiting the total amount of carbon emission of Bitcoin blockchain operations, it is important to note that these are simulations arising from system dynamics modeling and are limited by the assumptions above.

Second, the projected carbon emissions of Bitcoin blockchain operation related to electricity production depends on the source which is used for its generation. In all of except for the Site Regulation (SR) scenario, we do not consider the potential changes of the Chinese energy sector in the future, which implies that miners would predominantly operate in the coal-based area. While this is certainly true as the current electricity mix in China is heavily dominated by coal, a series of efforts to incentivise electricity production on the basis of renewable energy sources (www.iea.org) and policies to increase the price for electricity generated on the basis of coal have been implemented. Consequently, these renewable energy-related efforts and policies can potentially affect the electricity consumption and subsequently, the amount of related carbon emission generated from Bitcoin blockchain operation.

Third, it is important to note that although our results suggest that with the broaden usage and application, blockchain technology could become a carbon-intensive technology that hinders the carbon emission reduction efforts around the world, as with any prediction model, many unforeseeable uncertainties could happen in the future that could cause the reality to deviate from the prediction. While it is true the blockchain technology, and Bitcoin as one of its applications, is, and increasingly will play a significant role in the economy, ultimately, the choice of adopting and using this technology lies in the hands of humans. Consequently, we should carefully evaluate the trade-offs before applying this promising technology to a variety of industries.

Methods

This paper constructs a BBCE model to investigate the feedback loops of Bitcoin blockchain and simulates the carbon emission flows of its operations in China. In view of the complexity of Bitcoin blockchain operation and carbon emission process, the BBCE modeling for Bitcoin carbon emission assessment is mainly based on the following assumptions: (1) The electricity consumption of the Bitcoin mining process mainly consists of two types of energy: coal-based energy and hydro-based energy. (2) Bitcoin price is extremely volatile in real market

operations, which is inappropriate for long-term assessment in the BBCE model. Referring to the historical Bitcoin price data, we assume that the long-term Bitcoin price is mainly affected by the halving mechanism of Bitcoin mining rewards. (3) Miners gradually stop or choose other destinations for mining if the Bitcoin mining process is no longer profitable in China. (4) Bitcoin policies are consistent with the overall carbon emission flows in China. In other words, policies such as market access of Bitcoin miners and carbon tax of the Bitcoin blockchain operations can be retriggered for different emission intensity levels. (5) Miners maintain full investment intensity while in operation, as any reduction in individual investment intensity would put miners in disadvantage and jeopardize their chances of mining new blocks and receiving the reward.

By investigating the inner feedback loops and causalities of the systems, BBCE modeling is able to capture the corresponding dynamic behaviors of system variables based on proposed scenarios^{33,34}. Supplementary Fig. 1 shows the complete structure of BBCE modeling. The whole quantitative relationships of BBCE parameters are demonstrated in Supplementary Methods. Utilizing the flow diagram of BBCE systems illustrated in Supplementary Fig. 1, detailed feedback loops and flows of Bitcoin blockchain subsystems are discussed and clarified. The types, definitions, units, and related references of each variable in Supplementary Fig. 1 are reported in Supplementary Table 1.

Bitcoin mining and transaction subsystem. The Bitcoin blockchain utilizes Proof-of-Work (PoW) consensus algorithm for generating new blocks and validating transactions. Bitcoin miners earn a reward if the hash value of target blocks computed by their hardware is validated by all network participants. On the other hand, transactions packaged in the block are confirmed when the block is formally broadcasted to the Bitcoin blockchain. To increase the probability of mining a new block and getting rewarded, the mining hardware will be updated continuously and invested by network participants for higher hash rate, which would cause the hash rate of the whole network to rise. In order to maintain the constant 10-minute per new block generation process, the difficulty of generating a new block is adjusted based on the current hash rate of the whole Bitcoin network.

The halving mechanism of block reward is designed to control the total Bitcoin circulation (maximum of 21 million Bitcoins) and prevent inflation. Reward halving occurs every four years, which means that the reward of broadcasting a new block in Bitcoin blockchain will be zero in 2140. As a result, the Bitcoin market price increases periodically due to the halving mechanism of Bitcoin blockchain. With the growing popularity and broadened transaction scope of Bitcoin, the total transactions and transaction fee per block may steadily grow, which drive the other source of Bitcoin miner's profit rate. Overall, the profit of Bitcoin mining can be calculated by subtracting the total cost of energy consumption and carbon emissions from block reward and transaction fees. Miners will stop investing and updating mining hardware in China when the total cost exceeds the profit rate. Consequently, the whole network hash rate receives a negative feedback due to the investment intensity reductions.

Bitcoin energy consumption subsystem. The network mining power is determined by two factors: first, the network hash rate (hashes computed per second) positively accounts for the mining power increase in Bitcoin network when high hash rate miners are invested. However, the updated Bitcoin miners also attempt to reduce the energy consumption per hash, i.e., improve the efficiency of Bitcoin mining process, which helps to reduce the network mining power consumption. In addition, policy makers may raise the market access standard and create barriers for the low-efficiency miners to participate in Bitcoin mining activities in China. In terms of the energy consumption of the whole network, the power usage effectiveness is introduced to illustrate the energy consumption efficiency of Bitcoin blockchain as suggested by Stoll¹³. Finally, the network energy cost of Bitcoin mining process is determined by the network energy consumption and average electricity price, which further influences the dynamics behaviors of Bitcoin miner's investment.

Bitcoin carbon emission subsystem. The site selection strategies directly determine the energy types consumed by miners. Although the electricity cost of distinctive energies is more or less the same, their carbon emission patterns may vary significantly according to their respective carbon intensity index. In comparison to miners located in hydro-rich regions, miners located in coal-based regions generate more carbon emission flows under the similar mining techniques and energy usage efficiency due to the higher carbon intensity of coal-based energy¹⁷. The proposed BBCE model collects the carbon footprint of Bitcoin miners in both coal-based and hydro-based energy regions to formulate the overall carbon emission flows of the whole Bitcoin blockchain in China.

The level variable GDP consists of Bitcoin miner's profit rate and total cost, which suggests the productivity of the Bitcoin blockchain. It also serves as an auxiliary factor to generate the carbon emission per GDP in our model, which provides guidance for policy makers to implement punitive carbon taxation on Bitcoin industry. Finally, by combining both carbon cost and energy cost, the total cost of Bitcoin mining process provides a negative feedback for miner's profit rate and their investment strategies.

BBCE model parameterizations and quantitative settings. Our BBCE model has been constructed in Vensim software (PLE version 8.2.1). The time-related Bitcoin blockchain time-series data are obtained from www.btc.com, including network hash rate, block size, transaction fee, and difficulty. In addition, the auxiliary parameters and macroenvironment variables for network carbon emission flows assessment are set and considered through various guidelines. For example, the carbon intensities of different energies are suggested by Cheng et al.³⁵. The average energy cost in China and carbon taxation are collected from the World Bank. The site proportion of Bitcoin miners in China are set based on the regional statistics of Bitcoin mining pools in www.btc.com. Moreover, the monthly historical data of Bitcoin blockchain are utilized for time-related parameter regression and simulation from the period of January 2014 to January 2020 through Stata software (version 14.1). Based on the regressed parameters, the whole sample timesteps of network carbon emission assessment cover the period from January 2014 to January 2030 in this study, which is available for scenario investigations under different Bitcoin policies. The initial value of static parameters in BBCE model are shown in Supplementary Table 2, the actual values of the parameterizations adopted are reported in Supplementary Methods, and the key quantitative settings of each subsystem are, respectively, run as follows:

According to the guidance of the Cambridge Bitcoin Electricity Consumption Index (<https://www.cbeci.org>) and Küfeoğlu and Özkuran¹⁶, Bitcoin mining equipment is required to update and invest for remaining profitability. It is clear that mining hardware in the Bitcoin network consists of various equipments and their specifications. As a result, the investment intensity in Bitcoin blockchain is computed by the average price of a profitable mining hardware portfolio. The quantitative relationship between investment intensity and time can be expressed as the following form:

$$\text{Investment intensity} = \alpha_1 \times \text{Time} \times \text{Proportion of Chinese miners} \quad (1)$$

In Eq. (1), the parameter α_1 serves as the investment intensity function coefficient on time and the proportion of Chinese miners, which is estimated and formulated by the historical data of Bitcoin blockchain operation from the period of January 2014–January 2020. Then the Bitcoin miner profits are accumulated by profit rate and investment intensity flows, which can be obtained as follows:

$$\text{Miner cumulative profits}_t = \int_0^t (\text{Miner profit rate} - \text{Investment intensity}) dt \quad (2)$$

As discussed above, the aim of Bitcoin mining hardware investment is to improve the miner's hash rate and the probability of broadcasting a new block. Utilizing the statistics of Bitcoin blockchain, the hash rate of the Bitcoin network is regressed, and the equation is:

$$\text{Mining hash rate} = e^{\beta_1 + \alpha_2 \text{Investment intensity}} \quad (3)$$

Where β_1 and α_2 represent the network hash rate constant function coefficient and coefficient on investment intensity, respectively. Similarly, the average block size of Bitcoin is consistent with time due to the growing popularity of Bitcoin transactions and investment. The block size is estimated by time and is illustrated as below:

$$\text{Block size} = e^{\beta_2 + \alpha_3 \text{Time}} \quad (4)$$

Where β_2 and α_3 indicate the block size function constant coefficient and coefficient on time, respectively. The proportion of Chinese miners in the Bitcoin mining process will gradually decrease if mining Bitcoin in China is not profitable. So, the proportion parameter in the BBCE model is set as follows:

$$\text{Proportion of Chinese miners} = \text{IF THEN ELSE}(\text{Miner cumulative Profits} < 0, 0.7 - 0.01 \times \text{Time}, 0.7) \quad (5)$$

Suggested by the mining pool statistics obtained from BTC.com, China accounts for approximately 70% of Bitcoin blockchain operation around the world. As a result, we set the initial proportion of Chinese Bitcoin miners as 70%. In addition, the proportion of Chinese Bitcoin miners will gradually decrease if the Bitcoin mining process is no longer profitable in China.

The energy consumed per hash will reduce, i.e., the mining efficiency of the Bitcoin blockchain will improve, when updated Bitcoin hardware is invested and introduced. Moreover, the market access standard for efficiency proposed by policy makers also affects network efficiency. Consequently, the mining efficiency can be calculated as follows:

$$\text{Mining efficiency} = e^{\beta_3 + \alpha_4 \times \text{Investment intensity} \times \text{Market assess standard for efficiency}} \quad (6)$$

Where β_3 and α_4 act as the mining efficiency function constant coefficient and coefficient on investment intensity and market access standard for efficiency, respectively. The above function coefficients of BBCE parameters are regressed and formulated based on the actual Bitcoin blockchain operation data from the period of January 2014 to January 2020, and the specific value of each parameter is reported in Supplementary Methods.

The mining power of the Bitcoin blockchain can be obtained by network hash rate and mining efficiency. The equation of mining power is shown as follows:

$$\text{Mining power} = \text{Mining hash rate} \times \text{Mining efficiency} \quad (7)$$

Finally, the energy consumed by the whole Bitcoin blockchain can be expressed by mining power and power usage effectiveness:

$$\text{Network energy consumption} = \text{Mining power} \times \text{Power usage effectiveness} \quad (8)$$

Employing the regional data of Bitcoin mining pools, coal-based and hydro-based energy is proportionally consumed by distinctive Bitcoin pools. The total carbon flows in Bitcoin blockchain are measured by the sum of both monthly coal-based and hydro-based energy carbon emission growth. The integration of total carbon emission is:

$$\text{Total carbon emission}_t = \int_0^t \text{Carbon emission flow} dt \quad (9)$$

In addition, carbon emissions per GDP are introduced to investigate the overall carbon intensity of the Bitcoin mining process in China, which is formulated by the following equation:

$$\text{Carbon emission per GDP} = \text{Carbon emission}/\text{GDP} \quad (10)$$

Suggested by the World Bank database, we introduce the average taxation percentage for industrial carbon emission (1%) as the initial carbon tax parameter in BBCE modeling. In addition, the punitive carbon taxation on the Bitcoin blockchain will be conducted by policy makers, i.e., the carbon taxation on the Bitcoin blockchain will be doubled, if the carbon emission per GDP of the Bitcoin blockchain is larger than average industrial carbon emission per GDP in China (2 kg/GDP). As a result, the carbon tax of Bitcoin blockchain is set as:

$$\text{Carbon tax} = 0.01 \times \text{IF THEN ELSE}(\text{carbon emission per GDP} > 2, 2, 1) \quad (11)$$

Validation and robustness tests. In order to test the suitability and robustness of BBCE modeling system structures and behaviors, three model validation experiments are introduced and conducted in our study, i.e., the structural suitability tests (see Supplementary Fig. 3), reality and statistical tests (see Supplementary Fig. 4), and sensitivity analysis (see Supplementary Fig. 5). The validation results of the three tests are reported in Supplementary Discussion. Overall, the model validation results indicate that the proposed BBCE model can effectively simulate the causal relationship and feedback loops of carbon emission system in Bitcoin industry, and the parameters in BBCE model have significant consistencies with actual Bitcoin operating time-series data. In addition, the sensitivity analysis of BBCE model also shows that a slight variation of the BBCE parameters does not lead to the remarkable changes in the model behaviors or the ranking of the intended carbon reduction policies, thus indicating that the proposed BBCE model has excellent behavioral robustness and stability.

Reporting summary. Further information on experimental design is available in the Nature Research Reporting Summary linked to this paper.

Data availability

All original datasets used and the generated data from the results of the study are available at CEADS database (<https://www.ceads.net/user/download-anonymous.php?id=1083>). All data are also available from the corresponding authors upon reasonable request.

Received: 25 August 2020; Accepted: 2 March 2021;

Published online: 06 April 2021

References

- Nakamoto, S. Bitcoin: A Peer-to-Peer Electronic Cash System. *Bitcoin.org* (2008).
- Zheng, Z., Xie, S., Dai, H. N., Chen, X. & Wang, H. Blockchain challenges and opportunities: a survey. *Int. J. Web Grid Serv.* **14**, 352–375 (2018).
- Li, L., Liu, J., Chang, X., Liu, T. & Liu, J. Toward conditionally anonymous Bitcoin transactions: a lightweight-script approach. *Inf. Sci.* **509**, 290–303 (2020).
- Gallagher, K. S., Zhang, F., Orvis, R., Rissman, J. & Liu, Q. Assessing the policy gaps for achieving China's climate targets in the Paris Agreement. *Nat. Commun.* **10**, 1–10 (2019).
- Jokar, Z. & Mokhtar, A. Policy making in the cement industry for CO₂ mitigation on the pathway of sustainable development-A system dynamics approach. *J. Clean. Prod.* **201**, 142–155 (2018).
- Beckage, B. et al. Linking models of human behaviour and climate alters projected climate change. *Nat. Clim. Chang.* **8**, 79–84 (2018).
- Wang, D., Nie, R., Long, R., Shi, R. & Zhao, Y. Scenario prediction of China's coal production capacity based on system dynamics model. *Resour. Conserv. Recycl.* **129**, 432–442 (2018).
- Hepburn, C. et al. The technological and economic prospects for CO₂ utilization and removal. *Nature* **575**, 87–97 (2019).
- Stave, K. A. A system dynamics model to facilitate public understanding of water management options in Las Vegas, Nevada. *J. Environ. Manag.* **67**, 303–313 (2003).
- Wu, S., Liu, L., Gao, J. & Wang, W. Integrate risk from climate change in China under global warming of 1.5 and 2.0 °C. *Earth's Futur.* **7**, 1307–1322 (2019).
- Magnani, F. et al. The human footprint in the carbon cycle of temperate and boreal forests. *Nature* **447**, 849–851 (2007).
- Lenzen, M. et al. The carbon footprint of global tourism. *Nat. Clim. Chang.* **8**, 522–528 (2018).
- Stoll, C., Klaaßen, L. & Gallersdörfer, U. The carbon footprint of bitcoin. *Joule* **3**, 1647–1661 (2019).
- Cheng, Y., Du, D., & Han, Q. A hashing power allocation game in cryptocurrencies. *Lect. Notes Comput. Sci.* **11059**, 226–238 (2018).
- Vranken, H. Sustainability of bitcoin and blockchains. *Curr. Opin. Environ. Sustain.* **28**, 1–9 (2017).
- Küfeoğlu, S. & Özkuran, M. Bitcoin mining: a global review of energy and power demand. *Energy Res. Soc. Sci.* **58**, 101273 (2019).
- Krause, M. J. & Tolaymat, T. Quantification of energy and carbon costs for mining cryptocurrencies. *Nat. Sustain.* **1**, 711–718 (2018).
- Liu, Z. et al. Reduced carbon emission estimates from fossil fuel combustion and cement production in China. *Nature* **524**, 335–338 (2015).
- Aldy, J. et al. Economic tools to promote transparency and comparability in the Paris Agreement. *Nat. Clim. Chang.* **6**, 1000–1004 (2016).
- du Pont, Y. R. et al. Equitable mitigation to achieve the Paris Agreement goals. *Nat. Clim. Chang.* **7**, 38–43 (2017).
- Tang, L., Wu, J., Yu, L. & Bao, Q. Carbon emissions trading scheme exploration in China: a multi-agent-based model. *Energy Policy* **81**, 152–169 (2015).
- Schleussner, C. F. et al. Science and policy characteristics of the Paris Agreement temperature goal. *Nat. Clim. Chang.* **6**, 827–835 (2016).
- Rogelj, J. et al. Paris Agreement climate proposals need a boost to keep warming well below 2 °C. *Nature* **534**, 631–639 (2016).
- Holt, C. A. & Laurry, S. K. Risk aversion and incentive effects: new data without order effects. *Am. Econ. Rev.* **95**, 902–912 (2005).
- Newell, R. G., Jaffe, A. B. & Stavins, R. N. The effects of economic and policy incentives on carbon mitigation technologies. *Energy Econ.* **28**, 563–578 (2006).
- Ioannou, I., Li, S. X. & Serafeim, G. The effect of target difficulty on target completion: the case of reducing carbon emissions. *Account. Rev.* **91**, 1467–1492 (2016).
- Hagmann, D., Ho, E. H. & Loewenstein, G. Nudging out support for a carbon tax. *Nat. Clim. Chang.* **9**, 484–489 (2019).
- van der Waal, M. B. et al. Blockchain-facilitated sharing to advance outbreak R&D. *Science* **368**, 719–721 (2020).
- Saberi, S., Kouhizadeh, M., Sarkis, J. & Shen, L. Blockchain technology and its relationships to sustainable supply chain management. *Int. J. Prod. Res.* **57**, 2117–2135 (2019).
- Karamitsos, I., Papadaki, M. & Al Barghuthi, N. B. Design of the blockchain smart contract: a use case for real estate. *J. Inf. Secur.* **9**, 177–190 (2018).
- Jessel, B. & DiCaprio, A. Can blockchain make trade finance more inclusive? *J. Financ. Transform.* **47**, 35–50 (2018).
- Leng, J. et al. Makerchain: a blockchain with chemical signature for self-organizing process in social manufacturing. *J. Clean. Prod.* **234**, 767–778 (2019).
- Lane, D. C. Diagramming conventions in system dynamics. *J. Oper. Res. Soc.* **51**, 241–245 (2000).
- Richardson, G. P. Reflections on the foundations of system dynamics. *Syst. Dyn. Rev.* **27**, 219–243 (2011).
- Cheng, Z., Li, L. & Liu, J. Industrial structure, technical progress and carbon intensity in China's provinces. *Renew. Sust. Energ. Rev.* **81**, 2935–2946 (2018).

Acknowledgements

This work was supported by grants from the National Natural Science Foundation of China (71988101 and 72022019).

Author contributions

S.J. and Y.L. contributed to conceptualizing and designing the work, acquiring the data, conducting the analysis, interpreting the data, writing, and revising of the paper. Q.L. interpreted the data. Y.H. revised the paper. D.G. revised the paper and supervised the work. Y.X. revised the paper. S.W. conceptualized the work, revised the paper, and supervised the work.

Competing interests

The authors declare no competing interests.

Additional information

Supplementary information The online version contains supplementary material available at <https://doi.org/10.1038/s41467-021-22256-3>.

Correspondence and requests for materials should be addressed to D.G. or S.W.

Peer review information *Nature Communications* thanks Hector F. Calvo-Pardo, Lea Diestelmeier and other anonymous, reviewers for their contributions to the peer review of this work. Peer review reports are available.

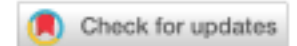
Reprints and permission information is available at <http://www.nature.com/reprints>

Publisher's note Springer Nature remains neutral with regard to jurisdictional claims in published maps and institutional affiliations.



Open Access This article is licensed under a Creative Commons Attribution 4.0 International License, which permits use, sharing, adaptation, distribution and reproduction in any medium or format, as long as you give appropriate credit to the original author(s) and the source, provide a link to the Creative Commons license, and indicate if changes were made. The images or other third party material in this article are included in the article's Creative Commons license, unless indicated otherwise in a credit line to the material. If material is not included in the article's Creative Commons license and your intended use is not permitted by statutory regulation or exceeds the permitted use, you will need to obtain permission directly from the copyright holder. To view a copy of this license, visit <http://creativecommons.org/licenses/by/4.0/>.

© The Author(s) 2021



Filling the evidentiary gap in climate litigation

Rupert F. Stuart-Smith^{1,2,3}✉, Friederike E. L. Otto^{1,2}, Aisha I. Saad^{1,4}, Gaia Lisi^{1,5},
Petra Minnerop⁶, Kristian Cedervall Lautau⁷, Kristin van Zwieten^{1,5} and Thom Wetzer^{1,3,5}

Lawsuits concerning the impacts of climate change make causal claims about the effect of defendants' greenhouse gas (GHG) emissions on plaintiffs and have proliferated around the world. Plaintiffs have sought, inter alia, compensation for climate-related losses and to compel governments to reduce their GHG emissions. So far, most of these claims have been unsuccessful. Here we assess the scientific and legal bases for establishing causation and evaluate judicial treatment of scientific evidence in 73 lawsuits. We find that the evidence submitted and referenced in these cases lags considerably behind the state of the art in climate science, impeding causation claims. We conclude that greater appreciation and exploitation of existing methodologies in attribution science could address obstacles to causation and improve the prospects of litigation as a route to compensation for losses, regulatory action and emission reductions by defendants seeking to limit legal liability.

Plaintiffs have brought over 1,500 climate-related lawsuits worldwide, and the number of claims filed continues to increase¹. Without effective non-judicial mechanisms providing compensation for climate-related loss and damage, plaintiffs have filed lawsuits seeking financial remedies from high-emitting corporations for losses suffered due to climate change². Robust scientific evidence is critical to the success of such claims^{3–5}. For example, claims for compensatory damages must demonstrate a causal link between the defendant's behaviour and the plaintiff's injury. Recognizing this, recent literature has drawn on analogous categories of case, such as toxic torts, in which modified causation tests reconcile legal causal analysis with scientific evidence that demonstrates multiple entities' contributions to the risk of harm⁵. However, despite developments in scientific⁶ and legal theory⁵ on causation and attribution of climate change damages, compensatory damages claims have been unsuccessful. Other lawsuits challenge inadequate state and corporate climate change mitigation targets and policies⁷. To establish admissibility, these claims may also rely on courts finding that emissions resulting from defendants' policies led to impacts affecting the plaintiffs.

A claim must first meet procedural requirements that render it admissible, including 'standing', which establishes that plaintiffs have legally protected interests that entitle them to bring the claim. Demonstrating a connection between defendants' actions and plaintiffs' injuries may contribute to meeting the standing requirement. So far, admissibility has been the primary outcome-determinative obstacle for climate litigation⁸. If claims pass procedural hurdles, more stringent causation standards for attributing losses to defendants' actions are applied to determine plaintiffs' entitlement to relief (remedies).

To establish causation, the court needs to receive scientific evidence, including through expert witness testimony, bounded by rules on the expert's independence and duties to the court, and amicus briefs submitted by third parties. Courts interpret this evidence through the lens of legal reasoning⁵. Such legal rules, encompassing both 'normative correctives' applied to evidence⁵ and the standard of proof, vary between jurisdictions (Supplementary Information, 'Standards of proof in law'). Across jurisdictions,

however, courts ascribe value to authoritative sources of evidence such as IPCC reports or peer-reviewed publications⁹. The a priori question motivating this research is whether the scientific evidence courts were provided with and have access to reflects the 'state of the art'.

Challenges to scientifically demonstrating causation

The fields of event attribution and trend detection and attribution evaluate the causal relationships at issue in climate litigation. Attribution science comprises methods that generally use counterfactual enquiry to link observed trends or changes in the probability or intensity of climate-related events to human influence. Existing methods can quantify the contribution of GHG emissions to specific events, including (1) extreme events, including storms¹⁰, droughts¹¹, heatwaves¹² or floods¹³, (2) long-term trends in glacier lengths¹⁴ or sea levels and (3) persistent changes, for instance in mean temperatures or precipitation¹⁵. Despite the clear relevance of attribution-science evidence, there is limited precedent for courts to base findings of causation on such evidence, partly due to its relative novelty. In common with most forms of scientific evidence, including regarding the health consequences of exposure to pharmaceutical substances, courts' use of climate change attribution evidence to assess causation is subject to several considerations.

First, GHG emissions are fungible and climate change impacts result from the cumulative emissions of multiple parties. This underlies use of 'market share theory'⁵, an approach that, following precedent in pharmaceutical and tobacco litigation, allocates damages among defendants according to the portion of emissions for which they are responsible⁵. Market share theory has been used to allocate damages in cases where losses derive linearly or nonlinearly from multiple entities' actions, to reduce evidentiary challenges in calculating defendants' exact contributions to losses. It is recognized that this simplistic allocation basis may not exactly reflect defendants' contributions to losses. Attribution-science evidence that directly quantifies individual defendants' contributions to plaintiffs' losses could be used instead of the market share approach. This may be helpful for impacts with nonlinear emissions–impact relationships¹⁶.

¹Oxford Sustainable Law Programme, University of Oxford, Oxford, UK. ²Environmental Change Institute, University of Oxford, Oxford, UK. ³Institute for New Economic Thinking at the Oxford Martin School, University of Oxford, Oxford, UK. ⁴Harvard Law School, Harvard University, Cambridge, MA, USA. ⁵Faculty of Law, University of Oxford, Oxford, UK. ⁶Durham Law School, Durham University, Durham, UK. ⁷Faculty of Law, University of Copenhagen, Copenhagen, Denmark. ✉e-mail: rupert.stuart-smith@ouce.ox.ac.uk

SCIENTIFIC REPORTS



OPEN

Exposure of Insects to Radio-Frequency Electromagnetic Fields from 2 to 120 GHz

Arno Thielens^{1,2}, Duncan Bell³, David B. Mortimore⁴, Mark K. Greco⁵, Luc Martens¹ & Wout Joseph¹

Insects are continually exposed to Radio-Frequency (RF) electromagnetic fields at different frequencies. The range of frequencies used for wireless telecommunication systems will increase in the near future from below 6 GHz (2G, 3G, 4G, and WiFi) to frequencies up to 120 GHz (5G). This paper is the first to report the absorbed RF electromagnetic power in four different types of insects as a function of frequency from 2 GHz to 120 GHz. A set of insect models was obtained using novel Micro-CT (computer tomography) imaging. These models were used for the first time in finite-difference time-domain electromagnetic simulations. All insects showed a dependence of the absorbed power on the frequency. All insects showed a general increase in absorbed RF power at and above 6 GHz, in comparison to the absorbed RF power below 6 GHz. Our simulations showed that a shift of 10% of the incident power density to frequencies above 6 GHz would lead to an increase in absorbed power between 3–370%.

Radio-Frequency (RF) electromagnetic fields (EMFs) enable wireless communication between billions of users worldwide. Presently, this mainly occurs at RF frequencies located between 100 MHz and 6 GHz¹. Wireless telecommunication base stations are the dominant sources of outdoor RF-EMFs¹. Humans and animals alike are exposed to these fields, which are partially absorbed by their bodies, e.g. reported for insects in². The absorbed dose depends on the frequency^{3,4}, and can be strongly enhanced when a full-body or partial-body resonance occurs³. This RF absorption has already been studied for particular insects at different individual frequencies: 27 MHz^{5,6}, 900–915 MHz^{6–8}, and 2450 MHz⁹.

This absorption may cause dielectric heating¹⁰. Heating affects insect behavior, physiology, and morphology¹¹. Reviews of studies that investigate RF heating of insects are presented in^{12–14}. Other authors focus on environmental RF exposure of insects^{15,16} or expose insects to RF radiation in order to investigate potential biological effects^{17,18}. Studies on non-thermal effects of exposure to RF-EMF exist:¹⁹ presents a review of potential mechanisms for non-thermal effects and a review of non-thermal effects of EMF exposure wildlife is presented in²⁰. Most existing studies focus on RF frequencies below 6 GHz. The same frequencies at which the current generations of telecommunication operate¹. However, due to an increased demand in bandwidth, the general expectation is that the next generation of telecommunication frequencies will operate at so-called millimeter-wavelengths: 30–300 GHz^{21,22}. Therefore, future wavelengths of the electromagnetic fields used for the wireless telecommunication systems will decrease and become comparable to the body size of insects and therefore, the absorption of RF-EMFs in insects is expected to increase. Absorption of RF energy was demonstrated in insects between 10–50 GHz²³, but no comparison was demonstrated with the RF absorption at frequencies below 10 GHz. The radar cross section of insects has been determined above 10 GHz, but this quantity includes both scattering and absorption²⁴. It is currently unknown how the total absorbed RF power in insects depends on the frequency to which they are exposed.

Most of the previously cited studies depend on measurements using RF equipment such as antennas, waveguides, and dielectric probes to determine the absorption of RF-EMFs in insects. An alternative approach would

¹Department of Information Technology, Ghent University - imec, Ghent, B-9052, Belgium. ²Department of Electrical Engineering and Computer Sciences, University of California Berkeley, Berkeley Wireless Research Center, Berkeley, CA, 94704, USA. ³Department of Science and Technology, Faculty of Health and Science, University of Suffolk, Ipswich, IP30AQ, United Kingdom. ⁴Newbourne Solutions Ltd, Newbourne, Woodbridge, IP12 4NR, United Kingdom. ⁵Charles Sturt University, Medical Imaging, SDHS, Faculty of Science, Wagga Wagga, NSW 2678, Australia. Correspondence and requests for materials should be addressed to A.T. (email: arno.thielens@berkeley.edu)

be to use numerical simulations. This approach was previously used to determine the absorption of RF-EMFs in humans and requires numerical models or phantoms^{25–28}.

Techniques for creating heterogeneous, three-dimensional insect models with micrometer resolution have previously been demonstrated in²⁹.

However, up to now, insect phantoms have not been used in electromagnetic simulations.

The aims of this study were to, for the first time, numerically evaluate RF-EMF absorption in real models of insects and to determine a potential difference in RF absorption in insects due to current and future telecommunication networks. To this aim, we studied the absorbed RF power in four different insect models obtained using micro-CT imaging as a function of frequency in a broad band, 2 GHz up to 120 GHz, that covers both the existing and the foreseen future wireless telecommunication bands. Voxel precision in the order of 5–20 μm is obtained, required for accurate electromagnetic simulations.

Methods

The Insects. *Australian Stingless Bee (Tetragonula carbonaria).* This bee (*Tetragonula carbonaria*) is native to Australia. The scanned insect was approximately 4.5 mm long, 3.0 mm wide, and has a mass of 2.5 mg.

Western Honeybee (Apis mellifera). This bee (*Apis mellifera*) originated in Europe. It is the most common honeybee. The studied specimen was approximately 11.0 mm long, 5.0 mm wide, and has a mass of 900 mg.

Desert Locust (Schistocerca gregaria). The studied locust (*Schistocerca gregaria*) was approximately 55.0 mm long, 18.0 mm wide, and has an approximate mass of 3.5 g.

Beetle (Geotrupes stercorarius). The studied beetle is a dor beetle (*Geotrupes stercorarius*). The beetle was found and scanned (see below) at Aberdeen University in Scotland. The beetle's length was 8.01 mm and its width is 4.5 mm. The insect's mass was not measured at the time of scanning. The average mass of a dor beetle is 220 mg³⁰.

Scanning Methods. *Australian Stingless Bee.* MicroCT scans were performed with a Skyscan 1172 high-resolution MicroCT system (Bruker MicroCT, Kontich, Belgium). This system has a sealed, microfocus x-ray tube with a 5 μm focal spot size. The x-rays were produced by exposing the anode to 40 kV at 100 μA . Prior to scanning, the sample containing the insect was placed on the pedestal between the x-ray source and the CCD detector. After positioning the sample, 600 2D x-ray images over 180° were captured by exposing the sample and then rotating it to the next exposure position with a slice-to-slice rotation distance of 2 μm , and a total acquisition time of approximately 60 min: each 2D image represents one slice. The scanner software then converted each slice to axial orientation and created 998 bitmap images (16 bit grey scale) which were stored for 2D viewing and 3D reconstruction as a 983 Mb dataset. The resulting isotropic voxel size was 5 μm .

Western Honeybee. A bench-top MicroCT scanner (Quantum GX MicroCT Imaging System, PerkinElmer, Hopkinton, MA, USA) at the Western Sydney University National Imaging Facility (Sydney, Australia) was used to scan the bee. The following parameters were used: 50 kVp, 80 μA , high resolution 2048 \times 2048 pixels image matrix, with 20 μm isotropic voxel size. Scanning time was 3.0 s for each of the 180 projections with 3.0 s rotation in between each projection. The total scan time was approximately 18 min per whole bee. The Quantum GX, bench-top MicroCT scanner's software was used to reconstruct the 180 projection images and then to convert them into a 2D rendered image stack of 512, 16 bit bitmap images. Bee volume data were then acquired by loading the image stack into BeeView volume rendering software (DISECT Systems Ltd, Suffolk, UK).

Desert Locust. The locust was suspended vertically in a 30-mm acrylic tube that was mounted tightly on the micro-CT's inclination stage. This stage was used to ensure that the rotation axis was at 90° to the x-ray source. Exposure factors were: 50 kVp and 198 μA . The data were isotropic 16 bit 2000 \times 2000 pixels with 1048 rows. Pixel size was 10.469 μm . Skyscan NRecon software version 1.5.1.4 (Bruker, Kontich, Belgium) was used to reconstruct the projection data³¹. Having obtained the projection data in the form of an image stack of 2-D TIFF files the data was viewed as a 3-D model using Disect software, DISECT Systems²⁹.

Beetle. The beetle was scanned at Aberdeen University on a Skyscan 1072 Micro-CT scanner (Bruker, Kontich, Belgium) using 50 kV and 197 μA , at 10.46 μm pixels isotropically. The images were then converted to axial slices using Skyscan's NRECON software (version 1.4). The produced axial image stack was further processed and analyzed using the Tomomask software (www.tomomask.com) before viewing in disect.

Development of 3D models. 3D models of the insects were created using the software TomoMask (www.tomomask.com). The image stack for each insect was firstly imported into the software together with details of the pixel and slice spacing. Regions to be converted into a 3D model are defined in TomoMask by drawing a mask of the wanted regions on each slice. This can be done automatically using the Luminance mask function which creates a mask based on the grey level of the pixels. The threshold values for the mask are set to include all of the insect tissue but will exclude air cavities and very fine structures, such as wings. The 3D model (generated by a marching cubes algorithm³²) is exported as an STL (STereo Lithography)³³ format file. STL files describe only the surface geometry of a three-dimensional object without any representation of colour or texture. Typically some smoothing of the models is required and this is realized using the Taubin λ/μ smoothing scheme³⁴ implemented in MeshLab³⁵. The Taubin method is good at removing noise whilst preserving shapes and features. Dimensions of the models and mesh integrity are finally checked (and corrected if necessary) using Netfabb (Autodesk, San Rafael, CA, USA).

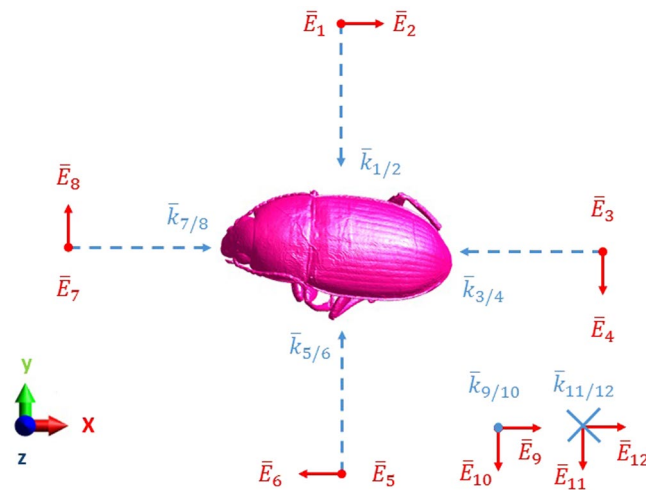


Figure 1. Illustration of the RF-EMF exposure set up. The insect (Beetle shown here in pink) is exposed to twelve RF plane waves incident from six directions along the positive and negative directions of the Cartesian axes shown on the bottom left with two orthogonal polarizations for each direction. The twelve wave vectors $\bar{k}_{i/j}$ are indicated in blue (dashed arrows), while the polarization of the incident electric fields \bar{E}_i are indicated in red. i and j indicate the configuration number, from 1 to 12.

Dielectric Properties. The propagation of EMFs inside and around the obtained 3D insect phantoms will depend on their dielectric properties: the relative permittivity (ϵ_r) and conductivity (σ). In this study, we have executed and relied on a literature review of previous measurements of dielectric properties of insects, predominantly using the coaxial-line probe method³⁶. There exist alternative methods. A toroidal resonator was used to determine the dielectric properties of two insects at 2370 MHz³⁷. Dielectric properties of Rice Weevils (*Sitophilus oryzae*) are obtained using the coaxial probe method for frequencies from 5×10^4 – 2×10^{10} Hz². The same technique was used on three other insects: the Red Flour Beetle (*Tribolium castaneum*), the Sawtooth Grain Beetle (*Oryzaephilus surinamensis*), and the Lesser Grain Borer (*Rhyzopertha dominica*), from 0.2–20 GHz³⁶. The same method was also used to measure dielectric properties of four insects: the Codling Moth (*Cydia pomonella*), the Indian Mealmoth (*Plodia interpunctella*), the Mexican fruit fly (*Anastrepha ludens*), and the Navel Orange Worm (*Amyelois transitella*) from 27–1800 MHz⁶. Coaxial measurements on a Colorado Beetle (*Leptinotarsa decemlineata*) were performed from 0.1–26.5 GHz and used to derive a fit to the measurement data³⁸.

We have pooled the data series, real and imaginary part of ϵ_r , as a function of frequency, obtained by^{6,36,38} and interpolated them from 2–120 GHz in steps of 0.1 GHz. We have then averaged over all available data at every frequency steps considered in the simulations.

Numerical Simulations. The Finite-Difference Time-Domain (FDTD) technique implemented in the commercial simulation software Sim4life (ZMT, Zurich, Switzerland) is used to evaluate absorption of RF-EMFs inside the insects as a function of frequency. This technique is commonly used to determine absorption of RF-EMF in heterogeneous human body models³. The FDTD method requires one to discretize the simulation domain using a three-dimensional grid. The simulation domain is divided in a number of cubes (discretized) with spatial extends that are defined by the spatial grid steps in the simulation domain. RF-EMFs can be incident from any direction. Therefore, we have chosen to work with 12 incident plane waves with a root-mean-squared electric field strength of 1 V/m, illustrated in Fig. 1, along 6 directions defined by Cartesian axes, with two orthogonal polarizations of the incident RF-EMFs along each axis.

The exposure was modeled using single frequency sinusoidal (harmonic) continuous plane waves. We did not take into account a potential modulation of the waves, which might be present in real telecommunication signals. This same technique has previously been used to evaluate the frequency dependence of RF absorption in the human body³. Simulations were executed for sinusoidal plane waves at 7 harmonic (single) frequencies: 2, 3, 6, 12, 24, 60, and 120 GHz. This resulted in a dataset of 4 (insects) \times 7 (frequencies) \times 12 (plane waves: 6 angles of incidence \times 2 polarizations) = 336 simulations.

The Australian Stingless Bee, the Western Honey Bee, and the Beetle were discretized with steps of 0.05 mm in each direction, while the larger Locust was discretized with steps of 0.2 mm in each direction at frequencies below 60 GHz and a step of 0.1 mm at 60 GHz and 120 GHz. These spatial steps provided a balance between simulation time (which depends on the number of grid steps and the relative grid step size in comparison to the wavelength) and spatial resolution of the insects' features. A stable FDTD simulation yields reproducible results that converge over time. The quantities determined using the FDTD algorithm should converge to a constant value as the simulation progresses in time. After a certain simulation time, these values will remain constant, this is referred to as a steady state. A grid step smaller than one tenth of the smallest wavelength in the simulation domain is necessary for a stable FDTD simulation³⁹. This is a requirement of the FDTD algorithm³⁹ and remains valid in all our

Insect	L (mm)	W (mm)	H (mm)	D (mm)	Range λ_{max} (mm)
Beetle	8.01	4.5	4.29	10.14	5–25
Australian Stingless Bee	4.89	3.39	3.99	7.16	2.5–12.5
Western Honey Bee	11	4.154	4.044	12.43	12.5–50
Locust	54.99	18.49	17.55	60.61	25–100

Table 1. Dimensions of the studied insect models along the different axes shown in Fig. 1. L, W, and H, are the dimensions in the X, Y, and Z, directions, respectively. D is the size of the diagonal of the brick with dimensions $L \times W \times H$. The final column lists the range in wavelengths where the maximal $P_{abs}(\lambda_{max})$ will be located.

simulations. The smallest wavelength in tissue ($\lambda/\sqrt{\epsilon_r}$) is 1.1 mm at 120 GHz. At this frequency we used grid steps of 0.05 mm ($\leq 0.045 \times \lambda/\sqrt{\epsilon_r}$) for all insects, except for the locust where we used 0.1 mm ($\leq 0.09 \times \lambda/\sqrt{\epsilon_r}$).

We ensured that the grid steps were small enough to prevent disconnections in the models. All insects were considered as consisting of homogeneous tissue with frequency-dependent dielectric parameters obtained as an average of the values we found in literature (previous section). This is an approximation, since real insects have heterogeneous tissue properties. Each simulation was executed until a steady state was reached. The number of periods necessary to reach a steady state solution depended on the studied insect and frequency and was between 20–80. This was controlled by temporal monitoring of the electric field strength along a line in the simulation domain until it reached a steady state. Additionally, the chosen number of simulation periods allowed for propagation of at least 3 times the length of the insects' diagonal (see Table 1).

After every simulation, the absorbed RF-EMF power (P_{abs}) in the insect was extracted. The P_{abs} is calculated as the product of the conductivity and the squared electric field strength integrated over the volume of the insect. The whole-body averaged specific absorption rate can be obtained by dividing P_{abs} by the insects' mass (assuming a homogeneous mass density). Absorbed RF-EMF power is generally used as a proxy for dielectric tissue heating¹⁰. We have not executed full thermal simulations due to uncertainties on the specific heat capacities of the insects and heat dissipation mechanisms.

Results

3D Models. Figure 2 shows the used 3D models obtained using micro-CT scanning of four insects.

Dielectric Properties. Figure 3 shows the imaginary and real parts of ϵ_r obtained by averaging those values that were available in^{6,36,38}. The real part is positive and decreases with frequency, while the imaginary part is negative (lossy media) and shows a minimum between 10–20 GHz. These are in line with the Debye dielectric curves proposed in³⁸. Figure 3 adds further perspective by showing the corresponding conductivity in (S/m) and the RF penetration depth.

Numerical Simulations. Figure 4 illustrates the frequency dependence of the absorption of RF-EMFs in the Western Honeybee in terms of the ratio of the electric field strength inside the insect to the maximum electric field in the simulation domain. At the currently used frequencies for telecommunication (<6 GHz), the wavelength is relatively large compared to the insects and the waves do not penetrate into the insects, which results in lower P_{abs} values. At 12–24 GHz, the fields penetrate more and more into the insect as the wavelength becomes comparable to the insects' size and the conductivity increases as well. At the highest studied frequencies, the fields penetrate less deep into the insect, but their amplitude is higher, resulting in a similar or slightly lower P_{abs} .

Figure 5 shows the P_{abs} linearly averaged over all twelve plane waves as a function of frequency for all studied insects. The absorbed power increases with increasing frequency from 2–6 GHz for all insects under exposure at a constant incident power density or incident electric field strength of 1 V/m. The absorbed power in the Locust, the largest studied insect, decreases slightly at the studied frequencies >6 GHz, but remains higher than at 2 and 3 GHz. The Western Honeybee shows an increase up to 12 GHz, followed by a slight decrease up to 120 GHz (P_{abs} remains more than $10 \times$ higher than <6 GHz). The smaller Australian Stingless Bee shows an increase of P_{abs} with frequency up to 60 GHz and a slight decrease at 120 GHz. The P_{abs} in the Beetle increases until 24 GHz and slightly decreases at higher frequencies.

Table 1 lists the dimensions of the different studied insects, compared to the wavelength λ -range in which the maximal P_{abs} will be located. The P_{abs} is simulated for discrete frequency steps. Therefore, the λ_{max} that corresponds to the maximum P_{abs} is located in between the wavelength steps right below and above the wavelength step that corresponds to the maximum simulated P_{abs} , see Fig. 4. The main diagonal of the insects' bounding box is within the range in which the wavelength of maximal absorption λ_{max} is located for three out of the four studied insects. This indicates that the absorption is (partly) determined by the size of the insects.

Numerical simulations are never the same as reality and there are always uncertainties associated with any EM simulation technique. We report the following sources of uncertainty: model variations and variation on dielectric properties.

The insect models are scanned with a resolution of 20 μm , 10.5 μm , 10.5 μm , and 5 μm , for the Honey Bee, the Locust, the Beetle, and the Australian Stingless Bee, respectively. These are 40%, 5–10%, 21%, and 10% of the spatial grid step used in the simulations of the Honey Bee (0.05 mm), the Locust (0.1–0.2 mm), the Beetle (0.05 mm), and the Australian Stingless Bee (0.05 mm), respectively. This indicates that the grid step is dominant

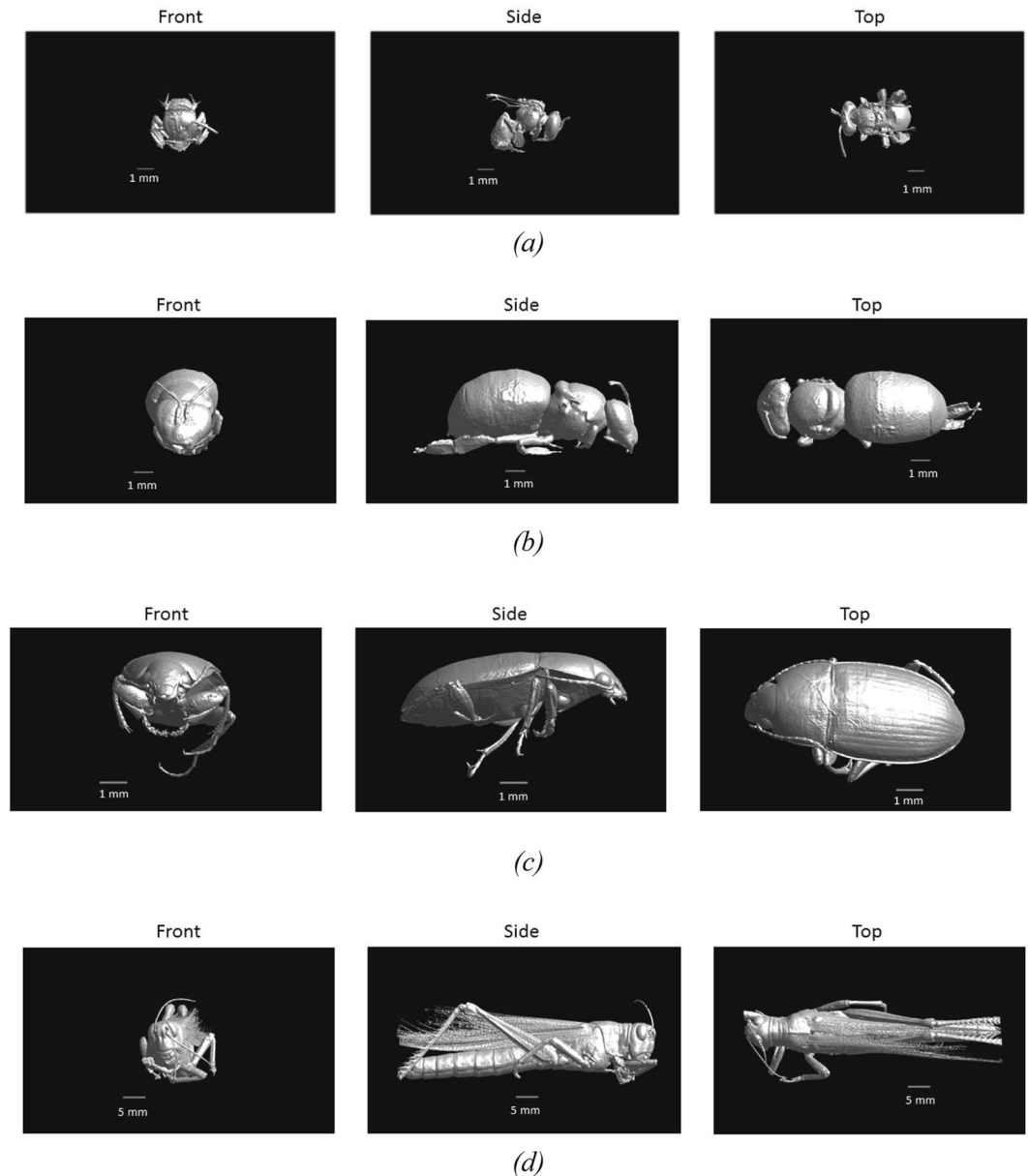


Figure 2. Frontal, side, and Top view of the four studied insects. (a) Australian Stingless Bee, (b) Western Honeybee, (c) Beetle, and (d) Locust.

in determining the spatial extends of the used models and not the resolution of the scanning method. In order to investigate the effect of the chosen grid step on the obtained P_{abs} values, we have executed the simulation with configuration 9 (Fig. 1) at 120 GHz with a maximal grid step that is half of the grid step used in our simulations using all four studied insects. We assume the largest effect of grid step size at the highest frequency. A 50% reduction in grid step (more accurate modelling) resulted in deviations of 1.1%, 2.5%, 0.32%, and 0.24%, for the Honey Bee, the Locust, the Beetle, and the Australian Stingless Bee, respectively. These deviations are small in comparison to the variations as a function of frequency, see Fig. 5, and the uncertainty caused by the dielectric parameters, see the next paragraph.

Deviations on ϵ_r will influence P_{abs} : the real part of ϵ_r will (partly) determine the magnitude of the internal electric fields, while P_{abs} scales linearly with conductivity. The maximal relative deviations on the real and imaginary part of ϵ_r are $(-13, +36)\%$ and $(-40, +36)\%$, respectively, which occur between 2–3 GHz. We have executed a simulation using configuration 1 at 2 GHz for the Beetle phantom, shown in Fig. 1, using five different sets of dielectric properties accounting for the deviations mentioned above: $[Re(\epsilon_r), Im(\epsilon_r)]$, $[1.36 \times Re(\epsilon_r), 1.36 \times Im(\epsilon_r)]$, $[1.36 \times Re(\epsilon_r), 0.6 \times Im(\epsilon_r)]$, $[0.87 \times Re(\epsilon_r), 1.36 \times Im(\epsilon_r)]$, and $[0.87 \times Re(\epsilon_r), 0.6 \times Im(\epsilon_r)]$, in order to determine the effect of the uncertainty of dielectric properties on P_{abs} . We found maximal relative deviations of $[-57, +59]\%$ relative to the value obtained using $[Re(\epsilon_r), Im(\epsilon_r)]$. These deviations are small in comparison to the variations as a function of frequency, see Fig. 5.

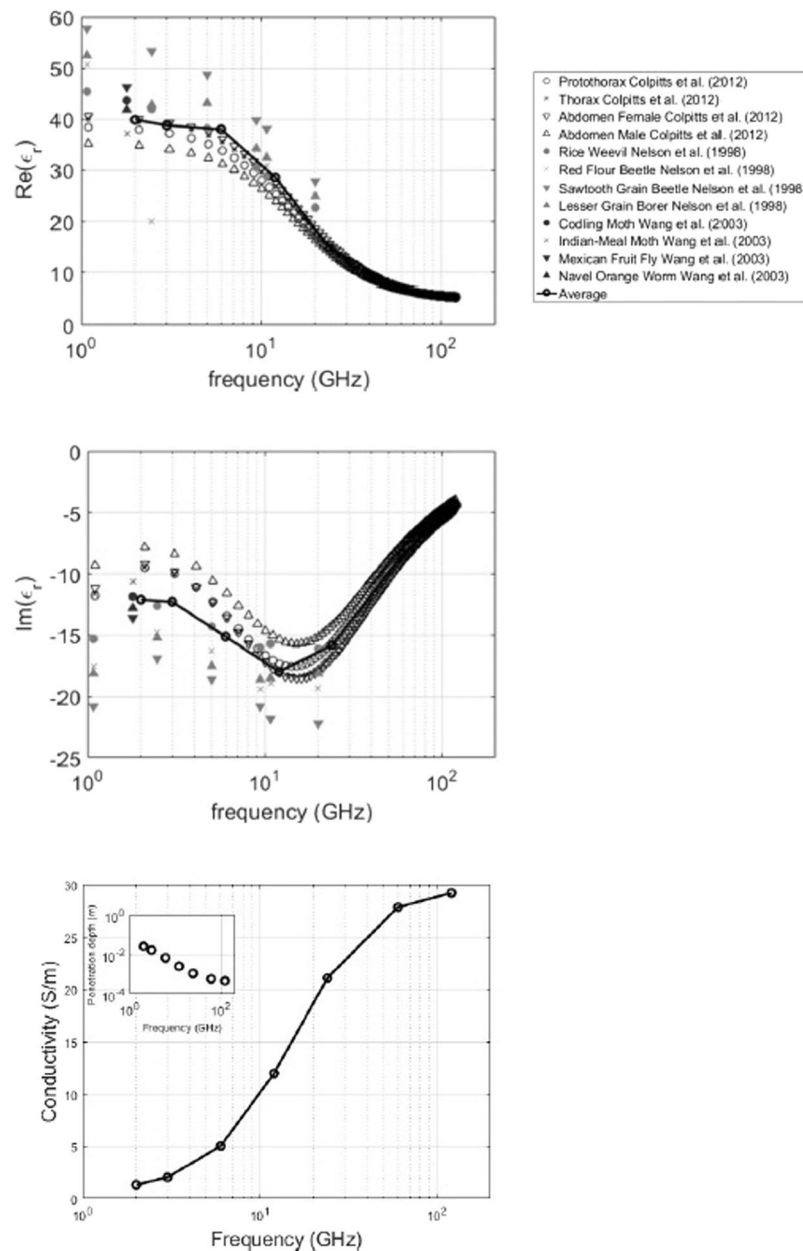


Figure 3. From top to bottom: Real part of the used dielectric permittivity, Imaginary part of the used dielectric permittivity, and conductivity with RF-EMF penetration depth as an inset. Markers show measurements obtained from literature. The black line with circular markers shows the average over the available data series at those frequencies.

Previous studies have indicated that large differences in dielectric properties might exist between adult insects and larvae⁴⁰. Worst-case deviations of $[Re(\epsilon_r)/7, Im(\epsilon_r)/5]$ at 5 GHz and $[Re(\epsilon_r)/6, Im(\epsilon_r)/8]$ at 15 GHz were observed in⁴⁰. We have executed simulations of configuration 1 using the beetle (shown in Fig. 1) at 6 GHz and 12 GHz where we have applied these reduced dielectric parameters. We found an increase in P_{abs} of 4% at 6 GHz and a decrease of 66% in P_{abs} at 12 GHz. Figure 5 shows that these variations are smaller than the variations we observed for varying angles of incidence at a fixed frequency.

Discussion

In this study, we have evaluated the absorption of RF-EMFs in insects as a function of frequency. To this aim, we obtained novel insect models using micro-CT imaging, which were used in FDTD simulations. In these simulations they were exposed to plane waves incident from six directions and two polarizations.

The frequency of the incident harmonic plane waves was varied from 2–120 GHz and resulted in P_{abs} as a function of frequency.

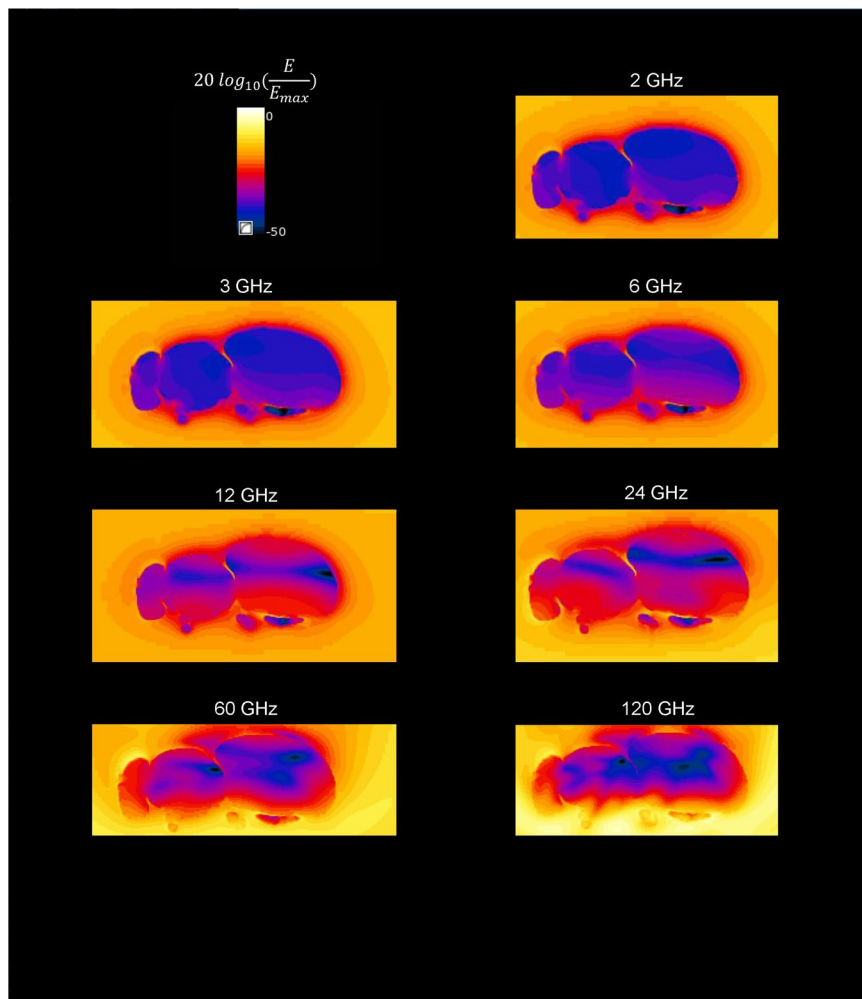


Figure 4. Normalized Electric field strength (dB) in a mid-transverse cross section of the Western Honey Bee as a function of frequency for a single plane wave incident from below with polarization orthogonal to the shown plane (No. 5 in Fig. 1). Normalization was executed for each simulation separately, i.e. E_{max} can be different in each subfigure.

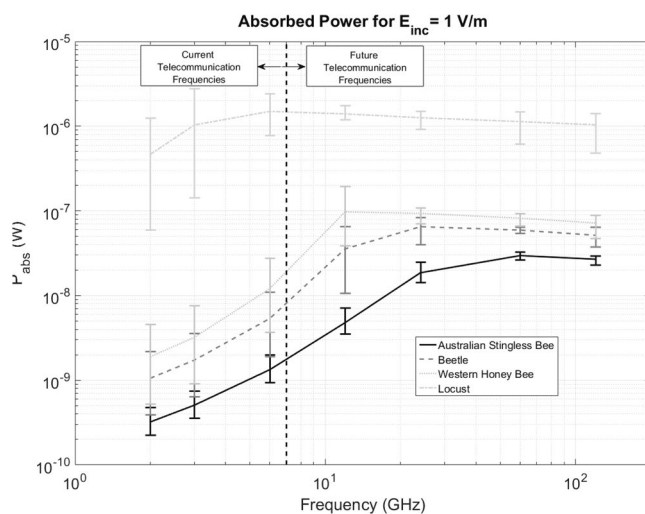


Figure 5. P_{abs} for an incident field strength of 1 V/m as a function of frequency for all studied insects. The markers indicate the average over all twelve plane waves at each of the simulated frequencies, while the whiskers indicate the minimal and maximal P_{abs} values obtained during the simulations.

Previous studies have shown that Micro-CT imaging can be successfully used as a non-invasive technique to accurately scan insects and develop 3D models with micrometer resolution^{29,41}. Models with micrometer resolution are necessary to obtain accurate results in FDTD simulations at 120 GHz ($\lambda = 2.5$ mm), since a discretization of $\lambda/10$ in the simulation domain is recommended to obtain stable results³⁹. It has been demonstrated for human body models that real anatomical models generally result in more accurate and realistic results than approximate models^{3,25,28}. Therefore, we also expect our real insect models to lead to more accurate results regarding absorbed RF power than, for example, cylindrical phantoms with different diameters and heights, which were used in previous studies of RF exposure of insects⁴².

The dielectric properties that were assigned to the studied insects were obtained from an interpolation of data found in literature. Ideally, the simulations should be executed with dielectric properties measured in the actual insects that were used to create the models. Figure 3 does show that most insects show a similar frequency behavior, which we have averaged by using an interpolation over values listed in literature.

Our numerical simulations show that the absorption of RF-EMFs in the insect models is frequency dependent. The P_{abs} is smallest at the lowest studied frequencies 2 GHz and 3 GHz, for all insects. P_{abs} shows a peak, which depends on the size and/or mass of the insects. The three smaller insects show their maximum at a frequency higher than 6 GHz: 60 GHz, 24 GHz, and 12 GHz for the Australian Stingless Bee, the Beetle, and the Honey Bee, respectively. The Locust shows a maximum at 6 GHz. We attribute this frequency behavior to two effects: first, the efficiency of RF-EMFs coupling into the models is maximal at frequencies comparable to the length of the insects, as Table 1 illustrates. Second, the interpolation of the imaginary part of the dielectric constant shows a minimum at 12 GHz, which means that RF-EMFs can cause the highest local SAR at these frequencies, see Fig. 3.

The difference between the maximal and minimal P_{abs} found at one frequency for different angles of incidence is smaller at the frequencies >6 GHz, than at the frequencies <6 GHz, in particular for the three smaller insects. This indicates that the angle of incidence is less important at these frequencies. This suggests that there is little difference in efficiency when depositing RF power in the studied insects with a single plane wave compared to depositing the same power using uncorrelated sources or reflections coming from all directions. In this study, we have only used single plane-wave simulations to determine P_{abs} . The averaging over P_{abs} does not include interference effects, which might result in lower (destructive interference) or higher (constructive interference) bounds on the P_{abs} values shown in Fig. 5.

A similar frequency behavior (increase, peak, decrease, and dependency on body size) is observed in human body models^{3,4}. However, at frequencies which are roughly a factor 100–1000 times lower, because the human body is approximately the same order of magnitude larger than that of the studied insects. For example, the heterogeneous adult human body model Duke shows an increase in P_{abs} from 10 MHz–80 MHz, a peak between 80 MHz–90 MHz, followed by a decrease in P_{abs} (and a second peak at higher frequencies)³. The smaller child phantom Thelonus shows an increase in P_{abs} from 10 MHz–100 MHz, a peak between 100 MHz–200 MHz, followed by a decrease in P_{abs} ³.

In order to quantify the effect of a shift to higher telecommunication frequencies on P_{abs} , one can use the data presented in Fig. 5. If we assume an incident $E_{rms} = 1$ V/m which is uniformly distributed over 2, 3, and 6 GHz, we find average P_{abs} values of 0.71 nW, 2.6 nW, 5.7 nW, and 990 nW, for the Australian Stingless Bee, the Beetle, the Honey Bee, and the Locust, respectively. If we assume that 10% of this incident field would be evenly distributed over the frequencies above 6 GHz, the P_{abs} increases to 2.6 nW, 7.7 nW, 14 nW, and 1.0 μ W, for the Australian Stingless Bee, the Beetle, the Honey Bee, and the Locust, respectively. These are increases of 370%, 290%, 240%, and 3%, respectively. Note that this is a conservative estimation of the increase in P_{abs} , since we assume a constant incident field and a uniform distribution of the currently used frequencies <6 GHz. Nowadays, most of the incident power density used for telecommunication is located at frequencies ≤ 2 GHz¹, where all insects show a minimal P_{abs} . In an isolated approximation (no convection or conduction) and under the assumption of unchanging mass and specific heat capacitance, the rate of temperature increase scales linearly with increasing P_{abs} . As an example, for the Australian Stingless Bee (mass = 2.5 mg) a P_{abs} of 3×10^{-8} W is estimated for an incident field strength of 1 V/m at 60 GHz. Under the assumption that the insect has a specific heat capacity equal to that of water (4179 J/K kg⁴³), this RF-EMF exposure would result in a temperature increase of 3×10^{-6} K/s, in an isolated approximation.

Strengths and Limitations

Our paper has several clear strengths and contributions to the state of the art in literature. To our knowledge, this is the only paper in which real insects are used to create models for numerical simulations. Moreover, this is the first paper that investigates the exposure of electric fields with RF frequencies associated with 5 G wireless communication and that shows that the absorbed power in insects is expected to increase in unchanged environmental conditions with respect to the one of current wireless communication systems (3 G and 4 G). A disadvantage of our study is the use of homogeneous models in the simulations, whereas real insects will have heterogeneous tissue parameters. Variations on dielectric parameters can exist on a scale that is smaller than the spatial resolution that any scanning method can currently obtain⁴⁴. The FDTD method requires a division of the simulation domain in a number of voxels, which each have to be assigned homogeneous dielectric properties³⁹. Any numerical simulation will be an approximation of reality. To our knowledge, the FDTD method, although faced with uncertainties^{3,39,44} is the best simulation method currently available to estimate the quantities studied in this manuscript. This paper is limited to electromagnetic dosimetry, which is focused on determining absorbed power values. These can be used as an input in thermal modelling of the insects. However, a full thermal analysis was outside the scope of this paper. Finally, we have included variations in angles and polarizations of incident waves. However, we have only looked at a limited number of plane waves, whereas real exposure is composed of plane waves from any direction.

Future Research

In our future research, we would like to model more insects to get a better understanding of the frequency dependence of the absorbed RF-EMF power as a function of insect size. We would also like to develop heterogeneous insect models with tissue-specific dielectric parameters. Finally, our goal is to determine the effect of absorption of RF-EMFs on the core temperature of insects as a function of frequency. To this aim, we want to use infrared temperature measurements of insects exposed to high electromagnetic fields as function of frequency.

Conclusions

We investigated the absorbed radio-frequency electromagnetic power in four different real insects as a function of frequency from 2–120 GHz. Micro-CT imaging was used to obtain realistic models of real insects. These models were assigned dielectric parameters obtained from literature and used in finite-difference time-domain simulations. All insects show a dependence of the absorbed power on the frequency with a peak frequency that depends on their size and dielectric properties. The insects show a maximum in absorbed radio frequency power at wavelengths that are comparable to their body size. They show a general increase in absorbed radio-frequency power above 6 GHz (until the frequencies where the wavelengths are comparable to their body size), which indicates that if the used power densities do not decrease, but shift (partly) to higher frequencies, the absorption in the studied insects will increase as well. A shift of 10% of the incident power density to frequencies above 6 GHz would lead to an increase in absorbed power between 3–370%. This could lead to changes in insect behaviour, physiology, and morphology over time due to an increase in body temperatures, from dielectric heating. The studied insects that are smaller than 1 cm show a peak in absorption at frequencies (above 6 GHz), which are currently not often used for telecommunication, but are planned to be used in the next generation of wireless telecommunication systems. At frequencies above the peak frequency (smaller wavelengths) the absorbed power decreases slightly.

References

- Bhatt, C. R. R. *et al.* Assessment of personal exposure from radiofrequency-electromagnetic fields in australia and belgium using on-body calibrated exposimeters. *Environ. Res.* **151**, 547–563 (2016).
- Nelson, S. O. Review and assessment of radio-frequency and microwave energy for stored-grain insect control. *Transactions ASAE* **39**, 1475–1484 (1996).
- Bakker, J. F., Paulides, M. M., Christ, A., Kuster, N. & van Rhooen, G. C. Assessment of induced SAR in children exposed to electromagnetic plane waves between 10 MHz and 5.6 GHz. *Phys. Medicine Biol.* **55**, 3115–3130 (2010).
- Hirata, A., Kodera, S., Wang, J. & Fujiwara, O. Dominant factors influencing whole-body average SAR due to far-field exposure in whole-body resonance frequency and GHz regions. *Bioelectromagn.* **28**, 484–487 (2007).
- Shrestha, B., Yu, D. & Baik, O. D. Elimination of cruptolestes ferrungineus s. in wheat by radio frequency dielectric heating at different moisture contents. *Prog. In Electromagn. Res.* **139**, 517–538 (2013).
- Wang, S., Tang, J., Cavalieri, R. P. & Davis, D. C. Differential heating of insects in dried nuts and fruits associated with radio frequency and microwave treatments. *Transactions ASAE* **46**, 1175–1182 (2003).
- Dubey, M. K., Janowiak, J., Mack, R., Elder, P. & Hoover, K. Comparative study of radio-frequency and microwave heating for phytosanitary treatment of wood. *Eur. J. Wood Prod.* **74**, 491–500 (2016).
- Tang, J. Unlocking potentials of microwaves for food safety and quality. *J. Food Sci.* **80**, E1776–E1793 (2015).
- Shayesteh, N. & Barthakur, N. N. Mortality and behaviour of two stored-product insect species during microwave irradiation. *J. stored Prod. Res.* **32**, 239–246 (1996).
- International Commission on Non-Ionizing Radiation Protection, I. C. N. I. R. P. Guidelines for limiting exposure to time-varying electric, magnetic, and electromagnetic fields (up to 300 GHz). *Heal. Phys.* **74**, 494–522 (1998).
- Sanborn, A. Thermoregulation in insects. encyclopedia of entomology (2008).
- Das, L., Kumar, G. & Shah, N. G. Microwave heating as an alternative quarantine method for disinfestation of stored food grains. *Int. J. Food Sci.* **2013**, 13 (2013).
- Hansen, J. D., Johnson, J. A. & Winter, D. A. History and use of heat in pest control: a review. *Int. J. Pest Manag.* **57**, 267–289 (2011).
- Wang, S. & Tang, J. Radio frequency and microwave alternative treatments for nut insect control: a review. *Int. Agric. Eng. J.* **10**, 105–120 (2001).
- Balmori, A. Anthropogenic radiofrequency electromagnetic fields as an emerging threat to wildlife orientation. *Sci. Total. Environ.* **518–519**, 58–60 (2015).
- Vijver, M. G. *et al.* Investigating short-term exposure to electromagnetic fields on reproductive capacity of invertebrates in the field situation. *Electromagn Biol Med* **33**, 21–28 (2014).
- Cammaerts, M. C., Vandenbosch, G. A. E. & Volski, V. Effect of short-term gsm radiation at representative levels in society on a biological model: The ant myrmica sabuleti. *J Insect Behav* **27**, 514–526 (2014).
- Marec, F. & Ondracek, B. V. J. The effect of repeated microwave irradiation on the frequency of sex-linked recessive lethal mutations in drosophila melanogaster. *Mutat. Res.* **157**, 163–167 (1985).
- Pall, M. L. Electromagnetic fields act via activation of voltage-gated calcium channels to produce beneficial or adverse effects. *J. Cell. Mol. Medicine* **17**, 958–965 (2013).
- Balmori, A. Electromog and species conservation. *Sci. Total. Environ.* **496**, 314–316 (2014).
- Colombi, D., Thors, B. & Tornevik, C. Implications of emf exposure limits on output power levels for 5 G devices above 6 Ghz. *IEEE Antennas Wirel. Propag. Lett.* **14**, 1247–1249 (2015).
- Pi, A. & Khan, F. An introduction to millimeter-wave mobile broadband systems. *IEEE Commun Mag* **49**, 101–107 (2011).
- Halverson, S. L., Burkholder, W. E., Bigelow, T. S., Nordheim, E. V. & Misenheimer, E. M. High-power microwave radiation as an alternative insect control method for stored products. *J. Econ. Entomol.* **89**, 1638–1648 (1996).
- Riley, J. R. Radar cross section of insects. *IEEE* **73**, 228–232 (1985).
- Findlay, R. P. & Dimbylow, P. F. Calculations of specific energy absorption rate in a seated voxel model of the human body from 10 MHz to 3 GHz. *Phys. Medicine Biol.* **51**, 2339–2352 (2006).
- Dimbylow, P., Bolch, W. & Lee, C. Sar calculations from 20 MHz to 6 GHz in the university of florida newborn voxel phantom and their implications for dosimetry. *Phys. Medicine Biol.* **55**, 1519–1530 (2010).
- Hand, J. W., Li, Y. & Hajnal, J. V. Numerical study of RF exposure and the resulting temperature rise in the foetus during a magnetic resonance procedure. *Phys. Medicine Biol.* **55**, 913–930 (2010).
- Christ, A. *et al.* The virtual family, development of surface-based anatomical models of two adults and two children for dosimetric simulations. *Phys. Medicine Biol.* **55**, N23–38 (2010).
- Greco, M., Tong, J., Soleimani, M., Bell, G. D. & Schafer, M. O. Imaging live bee brains using minimally-invasive diagnostic radioentomology. *J. Insect Sci.* **12**, 1–7 (2012).

30. Nervo, B., Tocco, C., Caprio, E., Palestini, C. & Rolando, A. The effects of body mass on dung removal efficiency in dung beetles. *PLoS One* **9**, e107699 (2014).
31. Tarplee, M. & Corps, N. Skyscan 1072 desktop X-Ray microtomograph – sample scanning, reconstruction, analysis and visualisation (2-D and 3-D) protocols, guidelines, notes, selected references and FAQ. available at: <http://www.geog.qmul.ac.uk/docs/staff/4952.pdf> (accessed may 2008) (2008).
32. Lorensen, W. E. & Cline, H. E. Marching cubes: A high resolution 3D surface construction algorithm. *Comput. Graph.* **21**, 163–169 (1987).
33. 3d systems. lithography interface specification (1998).
34. Taubin, G. A signal processing approach to fair surface design. *Proc. ACM SIGGRAPH* **95**, 351–358 (1995).
35. Cignoni, P. *et al.* Meshlab: an open-source mesh processing tool. *Proc. Sixth Eurographics Italian Chapter Conf.* **6**, 129–136 (2008).
36. Nelson, S. O., Bartley, P. G. & Lawrence, K. C. Rf and microwave dielectric properties of stored-grain insects and their implications for potential insect control. *Transactions ASAE* **41**, 685–692 (1998).
37. Ondracek, J. & Brunnhofer, V. Dielectric properties of insect tissues. *Gen Physiol Biophys* **3**, 251–257 (1984).
38. Colpitts, B., Pelletier, Y. & Cogswell, S. Complex permittivity measurements of the colorado potato beetle using coaxial probe techniques. *J. Microw. Power Electromagn. Energy* **27**, 175–182 (1992).
39. Hand, J. W. Modelling the interaction of electromagnetic fields (10 MHz–10 GHz) with the human body: Methods and applications. *Phys. Medicine Biol.* **53**, R243–286 (2008).
40. Massa, R. *et al.* Wide band permittivity measurements of palm (phoenix canariensis) and rhynchophorus ferrugineus (coleoptera curculionidae) for RF pest control. *J. Microw. Power Electromagn. Energy* **48**, 158–169 (2014).
41. Smith, D. B. *et al.* Exploring miniature insect brains using micro-CT scanning techniques. *Nat. Sci. Reports* **6**, 21768 (2016).
42. Huang, Z., Chen, L. & Wang, S. Computer simulation of radio frequency selective heating of insects in soybeans. *Int. J. Heat Mass Transf.* **90**, 406–417 (2015).
43. Osborne, N. S., Stimson, H. F. & Ginnings, D. C. Measurements of heat capacity and heat of vaporization of water in the range 0 to 100 degrees C. *J. Res. Natl. Bureau Standards* **23**, 197–260 (1939).
44. Panagopoulos, D. J., Johansson, O. & Carlo, G. L. Evaluation of specific absorption rate as a dosimetric quantity for electromagnetic fields bioeffects. *Plos One* **8** (2013).

Acknowledgements

This project has received funding from the European Union's Horizon 2020 research and innovation programme under the Marie Skłodowska-Curie grant agreement No 665501 with the research Foundation Flanders (FWO). A.T. is an FWO [PEGASUS]² Marie Skłodowska-Curie Fellow. The Eva Crane Trust (Charitable Incorporated Organisation Number: 1175343) has partly funded the insect data collection, which was used for this study by M.K.G.

Author Contributions

A.T. conducted the numerical simulations, analyzed the results, and drafted the manuscript, M.K.G., D.B., and D.B.M. conducted the imaging and post processing of the imaging. W.J. and L.M. contributed to analyzing the methodology and results. All authors reviewed the manuscript and provided input to the different sections.

Additional Information

Competing Interests: The authors declare no competing interests.

Publisher's note: Springer Nature remains neutral with regard to jurisdictional claims in published maps and institutional affiliations.



Open Access This article is licensed under a Creative Commons Attribution 4.0 International License, which permits use, sharing, adaptation, distribution and reproduction in any medium or format, as long as you give appropriate credit to the original author(s) and the source, provide a link to the Creative Commons license, and indicate if changes were made. The images or other third party material in this article are included in the article's Creative Commons license, unless indicated otherwise in a credit line to the material. If material is not included in the article's Creative Commons license and your intended use is not permitted by statutory regulation or exceeds the permitted use, you will need to obtain permission directly from the copyright holder. To view a copy of this license, visit <http://creativecommons.org/licenses/by/4.0/>.

© The Author(s) 2018

Bitcoin emissions alone could push global warming above 2°C

Bitcoin is a power-hungry cryptocurrency that is increasingly used as an investment and payment system. Here we show that projected Bitcoin usage, should it follow the rate of adoption of other broadly adopted technologies, could alone produce enough CO₂ emissions to push warming above 2 °C within less than three decades.

Camilo Mora, Randi L. Rollins, Katie Taladay, Michael B. Kantar, Mason K. Chock, Mio Shimada and Erik C. Franklin

Leaders from 176 countries have ratified the Paris Agreement, reached during the Twenty-first Conference of the Parties to the UNFCCC (COP 21), to mitigate GHG emissions and keep anthropogenic global warming within 2 °C to avoid the impacts of ever-more-catastrophic climate hazards such as drought, heatwaves, wildfire, storms, floods and sea-level rise, among others. From 1860 to 2014, humanity emitted ~584.4 GtC from fossil fuel combustion, industry processes and land-use change, which has been mirrored by ~0.9 °C of global warming (green line in Fig. 1a). Temperature projections from 42 Earth system models (ESMs) developed for the recent Coupled Model Intercomparison Project Phase 5 (CMIP5) under four alternative emission scenarios show that an additional 231.4 to 744.8 GtC would push global warming across the 2 °C threshold (Fig. 1a; the range represents the 5th and 95th percentiles among model projections, see Methods). Reducing emissions to keep warming below 2 °C is already regarded as a very difficult challenge given the increasing human population and consumption¹ as well as a lack of political will². Then came Bitcoin.

Bitcoin is a decentralized cashless payment system introduced in early 2009, and it is now accepted by over 100,000 merchants and vendors worldwide³. Each transaction paid for with Bitcoin is compiled into a 'block' that requires a computationally demanding proof-of-work to be resolved, which in turn uses large amounts of electricity⁴. Based on the assumptions that 60% of the economic return of the Bitcoin transaction verification process goes to electricity, at US\$5¢ per kWh and 0.7 kg of CO₂-equivalent (CO₂e) emitted per kWh, Digiconomist⁵ estimated that Bitcoin usage emits 33.5 MtCO₂e annually, as of May 2018. Foteinis⁶ repeated this approach using emissions adjusted by a

broader life cycle of electricity generation and found that for 2017, the global emissions from Bitcoin and Ethereum usage were 43.9 MtCO₂e. Compiling data on the electricity consumption of the various computing systems used for Bitcoin verification at present and the emissions from electricity production in the countries of the companies that performed such computing, we estimated that in 2017, Bitcoin usage emitted 69 MtCO₂e (s.d. = ±0.4; see Methods).

Globally, ~314.2 billion cashless transactions are carried out every year⁷, of which Bitcoin's share was ~0.033% in 2017⁵. The environmental concern regarding Bitcoin usage arises from the large carbon footprint for such a small share of global cashless transactions, and the potential for it to be more broadly used under current technologies. Bitcoin usage has experienced an accelerated growth (Supplementary Fig. 1), which is a common pattern during the early adoption of broadly used technologies⁸. Should Bitcoin follow the median growth trend observed in the adoption of several other technologies (Fig. 1b), it could equal the global total of cashless transactions in under 100 years. Yet, the cumulative emissions of such usage growth could fall within the range of emissions likely to warm the planet by 2 °C within only 16 years (red line in Fig. 1b). The cumulative emissions of Bitcoin usage will cross the 2 °C threshold within 22 years if the current rate is similar to some of the slowest broadly adopted technologies, or within 11 years if adopted at the fastest rate at which other technologies have been incorporated (that is, the red area in Fig. 1b). Projections in this analysis assume that the portfolio of fuel types used to generate electricity remains fixed at today's values (see Supplementary Table 3).

The future usage of Bitcoin is a topic of considerable discussion. There is currently considerable economic motivation for

companies to compute the proof-of-work for each Bitcoin block (for example, the latest block on 8 May 2018 (block 521819) gave a reward of 12.5 bitcoins plus 0.1 bitcoins for transaction fees, with a total monetary value of US\$116,041 on that date's exchange rate; <https://blockchain.info>) — the expected time needed to resolve that proof-of-work is around 10 minutes. However, Bitcoin is set up in such a way that rewards should halve every 210,000 blocks, or approximately every 4 years (for example, 50 bitcoins in 2008, 25 in 2012, and so on). Over time, this could reduce the motivation for companies to resolve the computationally demanding proof-of-work for each block, potentially overwhelming the system and reducing general interest in the use of Bitcoin. Alternatively, Bitcoin usage may generate sufficient transaction fees to support the system, which is how Bitcoin was originally conceived.

Although we are unable to predict the fate of Bitcoin, our analysis suggests that if its rate of adoption follows broadly used technologies, it could create an electricity demand capable of producing enough emissions to exceed 2 °C of global warming in just a few decades. Given the decentralized nature of Bitcoin and the need to maximize economic profits, its computing verification process is likely to migrate to places where electricity is cheaper, suggesting that electricity decarbonization could help to mitigate Bitcoin's carbon footprint — but only where the cost of electricity from renewable sources is cheaper than fossil fuels. Certainly, high electricity cost will push the development of more efficient hardware. However, reducing Bitcoin's carbon footprint should not rest solely on some yet-to-be-developed hardware but include simple modifications to the overall system, such as adding more transactions per block or reducing the difficulty or time required to resolve the proof-of-work — both of which could result in immediate electricity reductions for Bitcoin usage. Our analysis is

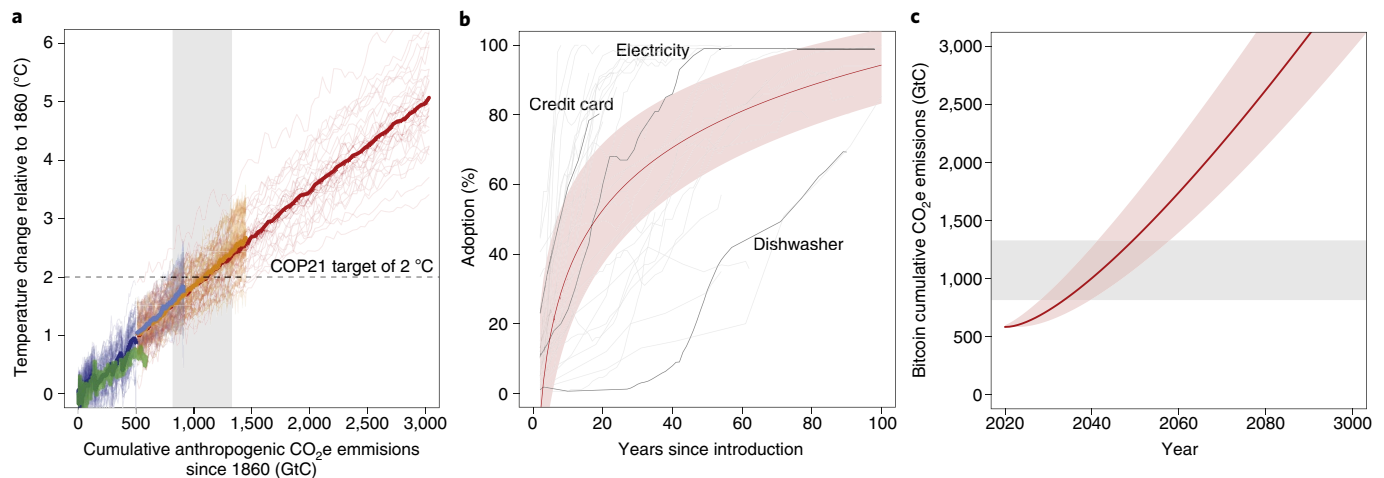


Fig. 1 | Carbon emissions from projected Bitcoin usage. **a**, Current and projected trends in global average temperature as a function of cumulative man-made carbon emissions. Narrow lines depict the projections of individual ESMs, while the thick lines indicate the multimodel median. The dashed line represents the COP 21 target of 2 °C global warming, and the grey shaded area represents the CO₂e emissions among ESMs at which such a threshold is crossed (values are for the 5th and 95th percentiles of all model projections). **b**, Trends in the adoption of broadly used technologies. Data are available for the United States, and used here as a reference. The red shaded area indicates the margins of the upper and lower quantiles, and the red line is the median tendency among technologies (see Methods). Grey lines indicate trends for each of the technologies (see Methods). **c**, Cumulative emissions from Bitcoin usage under the average growth rate of technologies that have been broadly adopted as shown in **b**. The grey shaded area indicates the carbon emissions above which warming exceeds 2 °C.

based on Bitcoin alone; however, the problem of high electricity consumption is common to several cryptocurrencies, suggesting that any further development of cryptocurrencies should critically aim to reduce electricity demand, if the potentially devastating consequences of 2 °C of global warming are to be avoided. □

Online content

Any methods, additional references, Nature Research reporting summaries, source data, statements of data availability and associated accession codes are available at <https://doi.org/10.1038/s41558-018-0321-8>.

Camilo Mora^{1*}, Randi L. Rollins^{2,3}, Katie Taladay¹, Michael B. Kantar⁴, Mason K. Chock⁵, Mio Shimada⁵ and Erik C. Franklin^{1,6}

¹Department of Geography and Environment, University of Hawai'i at Mānoa, Honolulu, HI, USA. ²Department of Biology, University of Hawai'i at Mānoa, Honolulu, HI, USA. ³Pacific Biosciences Research Center, School of Ocean and Earth Science and Technology, University of Hawai'i at Mānoa, Honolulu, HI, USA. ⁴Department of Tropical Plant and Soil Science, University of Hawai'i at Mānoa, Honolulu, HI, USA. ⁵Department of Botany, University of Hawai'i at Mānoa, Honolulu, HI, USA. ⁶Hawai'i Institute of Marine Biology, School of Ocean and Earth Science and Technology, University of Hawai'i at Mānoa, Kāne'ohe, HI, USA. *e-mail: cmora@hawaii.edu

Published online: 29 October 2018

<https://doi.org/10.1038/s41558-018-0321-8>

References

1. Raupach, M. R. et al. *Proc. Natl Acad. Sci. USA* **104**, 10288–10293 (2007).

2. Kemp, L. *Palgrave Commun.* **3**, 9 (2017).
3. Cuthbertson, A. Bitcoin now accepted by 100,000 merchants worldwide. *International Business Times* (4 February 2015); <https://go.nature.com/2CckFXs>
4. De Vries, A. *Joule* **2**, 801–805 (2018).
5. *Bitcoin Energy Consumption Index* (Digiconomist, 2017); <https://digiconomist.net/bitcoin-energy-consumption>
6. Foteinis, S. *Nature* **554**, 169 (2018).
7. *Global Payment Systems Survey 2016* (World Bank, 2016).
8. Bass, F. M. *Manag. Sci.* **50**, 1833–1840 (2004).

Acknowledgements

The authors wish to thank the numerous data providers named in the supplements of this paper for making their data freely available. We also thank SeaGrant Hawaii for providing funds to acquire the computers used in these analyses. This paper was developed as part of the graduate course on 'Methods for Large-Scale Analyses' in the Department of Geography and Environment at the University of Hawai'i at Mānoa.

Additional information

Supplementary information is available for this paper at <https://doi.org/10.1038/s41558-018-0321-8>.

Methods

Amount of CO₂e needed to surpass the 2 °C COP 21 target. The 2015 Paris Agreement set the goal to limit global warming to 2 °C. To quantify the amount of CO₂e emissions required to warm the planet by 2 °C (that is, CO₂ emissions plus the CO₂e emissions of other anthropogenic GHGs), we used temperature projections from ESMs and the driving CO₂e emissions of such models (see below). For each ESM, we estimated the CO₂e emissions at which 2 °C warming was reached (the *x* axis value at which each narrow line in Fig. 1a intercepted the 2 °C warming threshold) and grouped those results to estimate the 5th and 95th percentiles (grey box in Fig. 1a). We also collected data on 'observed' temperature change and CO₂e emissions from 1860 to 2014 as validation for model projections, to quantify current warming and cumulative emissions, and estimate the CO₂e emissions needed to surpass the COP 21 target. The observed temperature change and CO₂e emissions since 1860 are shown as a green line in Fig. 1a (temperature data from NOAA-CIRES 20th Century Reanalysis V2c⁹, CO₂e emissions data from the Carbon Dioxide Information Analysis Center¹⁰). The observed and projected cumulative CO₂e emissions are very similar over the time period for which they overlap (see blue and green lines in Fig. 1a), however, they used different methods and emission sources. Fossil fuel emissions, industrial processes and land-use change are the main anthropogenic GHG contributing to current warming (Supplementary Fig. 2), and are all in common to both databases used in this analysis.

Temperature projections. We analysed global annual average surface air temperature from 42 ESMs developed for CMIP5. We used the historical experiment, which for all models includes the period from 1860 to 2005 and Representative Concentration Pathways (RCPs) 2.6, 4.5 and 8.5, which include the period from 2006 to 2100. The historical experiment was designed to model recent climate (reflecting changes due to both anthropogenic and natural causes) whereas the RCP scenarios represent contrasting mitigation efforts between rapid GHG reductions (RCP 2.6) and a business-as-usual scenario (RCP 8.5). For each model, under each experiment, we calculated the difference in the global average temperature between every year in the time series and 1860. For any given experiment, global annual averages from all models at any given year were used to estimate the multimodel median temperature change for that year (thick lines in Fig. 1a). Temperature change for each model and the multimodel median are shown in Fig. 1a.

CO₂e projections. Although CO₂ is the primary GHG contributing to the total anthropogenic radiative forcing (changes in the Earth's energy balance due to human activities), other anthropogenic agents also contribute to the warming trends projected by ESMs (such as methane, aerosols and so on). During the timeframe of this study, volcanic and solar radiative forcings have remained reasonably constant and proportionally very small in relation to the anthropogenic forcing (Supplementary Fig. 2), indicating that they contribute minimally to the warming trends from ESMs, and thus were not considered in this analysis. For the purpose of standardization, we calculated the CO₂e emissions for the radiative forcing from all anthropogenic activities used by the historical and RCP experiments. For this purpose, we obtained CO₂ emissions, their radiative

forcing and the total anthropogenic radiative forcing under each experiment (data from Meinshausen et al.¹¹). We estimate the CO₂e emissions for the total anthropogenic radiative forcing as the amount of CO₂ required to achieve the total anthropogenic radiative forcing given the ratio of actual CO₂ emissions and the actual CO₂ radiative forcing. As an example, from 1860 until 2005 the historical experiment shows that the cumulative CO₂ emissions from fossil fuels, cement, gas flaring, bunker fuels and land-use amounted to 453.247 GtC and a resulting radiative forcing of 1.675 W m⁻², whereas the total anthropogenic radiative forcing was 1.840 W m⁻². Thus, the CO₂e emissions for that total anthropogenic radiative forcing were estimated at 497.984 GtC (1.840 × (453.247/1.675)). Projected anthropogenic CO₂e emissions under different experiments are plotted against temperature change from the different models in Fig. 1a. Note that CO₂e emissions are given in weight units of carbon, which can be converted to units of carbon dioxide (CO₂), simply multiply these estimates by 3.667.

Amount of CO₂e produced by Bitcoin usage. Any given transaction using Bitcoin is compiled into a block requiring a proof-of-work to be resolved, with the winning company/pool being awarded a certain amount of new bitcoins plus any extra transactions fees. The CO₂e emissions from this procedure emerge primarily from the electricity demands of the hardware used and the location where the electricity is generated. To assess the carbon footprint of the global Bitcoin Network, using as reference the year 2017, we used the following approach. We started by compiling a list of current hardware suitable for Bitcoin and their energy efficiencies (hashes per electricity consumed, Supplementary Table 1). To each block mined in 2017 (data from <https://blocktrail.com>), we assigned a random hardware from Supplementary Table 1 and multiplied the number of hashes required to solve the block by the energy efficiency of the random hardware; this returned the amount of electricity consumed to solve the given block. Note that the available data for mined blocks include their difficulty, which can be used to estimate the number of hashes as (hashes = difficulty × 2³²; equation from O'Dwyer and Malone¹²). For each block mined in 2017, we also collected data on the company claiming the given block, and searched for their country/countries of operation (Supplementary Table 2). For the resulting list of countries, we collected data on the types of fuels used for electricity generation (Supplementary Table 3), and using average standards of CO₂e emissions for the generation of electricity with those types of fuels (under a life-cycle carbon approach, Supplementary Table 4), we estimated the total carbon emission equivalents to produce electricity in those countries (Supplementary Table 2). By multiplying the electricity consumption of every block in 2017 by the electricity emissions in the country where the proof-of-work was likely to be resolved, we were able to estimate the total CO₂e emissions for computing every block in 2017. Summing the CO₂e emissions from all blocks in 2017 yielded the Bitcoin emissions in that year. This approach was repeated 1,000 times to capture the variability in the random selection of hardware, and this is described as the s.d.

Projected usage and carbon emissions from Bitcoin. The likely future of Bitcoin has been broadly discussed in online forums with opinions ranging from it being a case of boom and bust, or alternatively, an early stage

in a 'new industrial revolution'. We studied the carbon emissions of Bitcoin if it follows the adoption trends of other broadly used technologies. For this, we used the incorporation rate of 40 different technologies for which data are readily available: the automatic transmission, automobile, cable TV, cellular phone, central heating, colour TV, computer, credit card, dishwasher, disk brakes, dryer, e-book reader, electric power, electric range/burners, electronic ignition, flush toilet, freezer, home air conditioning, household refrigerator, Internet, landline phone, microcomputer, microwave, nitrogen oxides pollution controls (boilers), podcasting, power steering, radial tires, radio, refrigerator, Real Time Gross Settlement adoption, running water, shipping container port infrastructure, smartphone, social media, stove, tablet, vacuum, washer dryer, washing machine and water heater (data for the USA from ref.¹³, credit card data from ref.¹⁴). Data include the year and percentage of population using the given technology. The first year of usage for each technology was set to one, to allow comparison of trends among technologies (narrow grey lines in Fig. 1b). For each year, we calculated the average and lower and upper quantiles of per cent population using all technologies and applied a logistic model to such trends (the red line and red shading in Fig. 1b). The projected trends of technology usage adoption were used to estimate likely Bitcoin usage assuming a global total of ~314.2 billion cashless transactions. We used only cashless transactions that are likely to occur in places where infrastructure is already in place for the usage of Bitcoin as a reference (for example, we do not assume that Bitcoin will replace transactions using fiat currency). The CO₂e emissions of projected Bitcoin usage were estimated using the CO₂e emissions for Bitcoin transactions in 2017 as a reference. We randomly sampled blocks mined in 2017 until their total number of transactions were equal to the projected number of transactions, then we added the CO₂e emissions from computing such randomly selected blocks. The approach was repeated 1,000 times.

Code availability. Raw code used for this study are publicly available online at <https://github.com/moracamillo/Bitcoin/>.

Data availability

The authors declare that all data supporting the findings of this study are available within the article, its Supplementary Information files and at <https://github.com/moracamillo/Bitcoin/>.

References

- NOAA-CIRES 20th Century Reanalysis V2c (NOAA, accessed 28 February 2018); <https://go.nature.com/2CDGaXg>
- Global Carbon Budget (Global Carbon Project, accessed 28 February 2018); <http://www.globalcarbonproject.org/carbonbudget/17/data.htm>
- Meinshausen, M. et al. *Climatic Change* **109**, 213–241 (2011).
- O'Dwyer, K. J. & Malone, D. Bitcoin mining and its energy footprint. In *25th IET Irish Signals & Systems Conference 2014 and 2014 China-Ireland International Conference on Information and Communities Technologies* <http://doi.org/cvqm> (IEEE, 2014).
- Technology Adoption by Households in the United States* (Our World in Data, accessed 28 February 2018); <https://go.nature.com/2NCnUyj>
- Consumer Credit and Payment Statistics* (Federal Reserve Bank of Philadelphia, accessed 28 February 2018); <https://www.philadelphiafed.org/consumer-finance-institute/statistics>

Anthropogenic electromagnetic noise disrupts magnetic compass orientation in a migratory bird

Svenja Engels^{1,2*}, Nils-Lasse Schneider^{1,2*}, Nele Lefeldt^{1,2}, Christine Maira Hein^{1,2}, Manuela Zapka^{1,2}, Andreas Michalik^{1,2}, Dana Elbers^{1,2}, Achim Kittel³, P. J. Hore⁴ & Henrik Mouritsen^{1,2}

Electromagnetic noise is emitted everywhere humans use electronic devices. For decades, it has been hotly debated whether man-made electric and magnetic fields affect biological processes, including human health^{1–5}. So far, no putative effect of anthropogenic electromagnetic noise at intensities below the guidelines adopted by the World Health Organization^{1,2} has withstood the test of independent replication under truly blinded experimental conditions. No effect has therefore been widely accepted as scientifically proven^{1–6}. Here we show that migratory birds are unable to use their magnetic compass in the presence of urban electromagnetic noise. When European robins, *Erithacus rubecula*, were exposed to the background electromagnetic noise present in unscreened wooden huts at the University of Oldenburg campus, they could not orient using their magnetic compass. Their magnetic orientation capabilities reappeared in electrically grounded, aluminium-screened huts, which attenuated electromagnetic noise in the frequency range from 50 kHz to 5 MHz by approximately two orders of magnitude. When the grounding was removed or when broadband electromagnetic noise was deliberately generated inside the screened and grounded huts, the birds again lost their magnetic orientation capabilities. The disruptive effect of radiofrequency electromagnetic fields is not confined to a narrow frequency band and birds tested far from sources of electromagnetic noise required no screening to orient with their magnetic compass. These fully double-blinded tests document a reproducible effect of anthropogenic electromagnetic noise on the behaviour of an intact vertebrate.

For more than 50 years, it has been known that night-migratory songbirds can use the Earth's magnetic field to orient spontaneously in their migratory direction when placed in an orientation cage at night in spring and autumn^{7,8}. This basic experiment has been independently replicated many times in various locations⁹. We were therefore puzzled to find that night-migratory songbirds tested between autumn 2004 and autumn 2006 in wooden huts on the University of Oldenburg campus (53.1507° N, 8.1648° E) seemed unable to orient in the appropriate migratory direction. Typical data for European robins are shown in Fig. 1a.

Noting that Ritz *et al.*^{10,11} had reported the sensitivity of European robins to radiofrequency magnetic fields, in the winter of 2006/2007 we decided to reduce the electromagnetic noise in our test huts by screening them with electrically connected and grounded aluminium plates (Extended Data Fig. 1). The screening left static magnetic fields such as the Earth's completely unaffected, but attenuated the electromagnetic noise inside the huts in the frequency range from about 50 kHz to at least 20 MHz by about two orders of magnitude (Fig. 1c, d and Methods). The effect on the birds' orientation capabilities was profound: with the aluminium screens in place, the birds oriented in their normal migratory direction the following spring (2007; Fig. 1b) and in subsequent years (data in references 12–15). When the horizontal component of the static magnetic field was rotated 120° anticlockwise or when the vertical component was inverted, the birds changed their orientation as expected^{12–15}.

These observations suggested that, by chance, we could have discovered a biological system that is sensitive to man-made electromagnetic noise in the range up to 5 MHz with intensities well below the guidelines for human exposure proposed by the International Commission on Non-Ionizing Radiation Protection (ICNIRP) and adopted by the World Health Organization^{1,2}.

Any report of an effect of low-frequency electromagnetic fields on a biological system should be subjected to particular scrutiny for at least

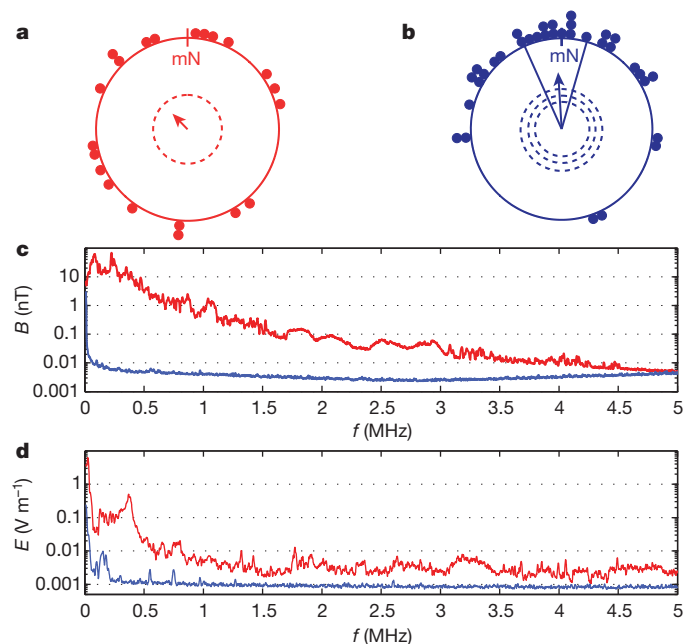


Figure 1 | Magnetic compass orientation of migratory European robins tested at the University of Oldenburg requires aluminium screening. In unscreened wooden huts, European robins were disoriented (a, spring 2005, $n = 21$, mean direction 316° , mean vector length $r = 0.19$, $P = 0.48$ (Rayleigh test)), but after installing grounded aluminium screens, the birds oriented highly significantly towards North in spring (b, spring 2007, $n = 34$, mean direction $356^\circ \pm 20^\circ$ (95% confidence interval), $r = 0.59$, $P < 0.001$). c, d, Anthropogenic electromagnetic noise in the huts before (red) and after (blue) installation of screens. Traces c and d show the magnetic (B) and electric (E) components of the measured electromagnetic fields, respectively, as a function of frequency (f). In a, b, each dot indicates the mean orientation of all the tests of one individual bird in the given condition. The dots are colour-coded as in c, d. The arrows show group mean vectors flanked by their 95% confidence interval limits (solid lines). The dashed circles indicate the minimum length of the group mean vector needed for significance according to the Rayleigh test (inner circle, $P = 0.05$; middle, $P = 0.01$; outer, $P = 0.001$). mN, magnetic North.

¹Institut für Biologie und Umweltwissenschaften, Universität Oldenburg, D-26111 Oldenburg, Germany. ²Research Centre for Neurosensory Sciences, University of Oldenburg, D-26111 Oldenburg, Germany. ³Institute of Physics, University of Oldenburg, D-26111 Oldenburg, Germany. ⁴Department of Chemistry, University of Oxford, Physical and Theoretical Chemistry Laboratory, Oxford OX1 3QZ, UK.

*These authors contributed equally to this work.

three reasons. First, such claims in the past have often proved difficult to reproduce^{1–6}. Second, animal studies are commonly used to evaluate human health risks and have contributed to guidelines for human exposures^{1–4}. Third, “seemingly implausible effects require stronger proof”¹⁶.

Therefore, we systematically conducted a large number of double-blind experiments over the last 7 years to test whether the restored orientation inside the aluminium-screened buildings was really attributable to the reduced exposure to anthropogenic electromagnetic noise. To ensure that our results were reliable, different generations of students independently replicated several key measurements. We also consulted with leading experts to ensure that we very carefully measured the electromagnetic fields experienced by the birds in each of the experimental conditions described below. Electromagnetic fields have magnetic and electric components, and, especially in the so-called ‘near-field’ (within a few wavelengths of the source), they must be measured separately.

First, we measured that the aluminium shielding lost its ability to screen anthropogenic electromagnetic noise when the grounding was disconnected (Fig. 2e, f). We therefore performed a series of experiments in which we tested a group of birds alternately in two different, aluminium-screened, wooden huts; one grounded and one left ungrounded. The experimenters were unaware which hut was which. The results were striking: on the days when the birds were tested in a grounded hut, they oriented in their mean northerly migratory direction as expected in spring (Fig. 2a, c). By contrast, the same birds were randomly oriented on the days when they were tested in an ungrounded hut (Fig. 2b, d). Thus, we could control the orientation of the birds inside the huts by connecting or disconnecting the grounding of the aluminium screens (Fig. 2).

Second, we assessed whether the electromagnetic noise was directly responsible for the disorientation. The birds were tested in the grounded aluminium-screened huts in which they normally orient very well (Figs 1b, 2a, c and data in references 12–15). The birds became disoriented (Fig. 3a)

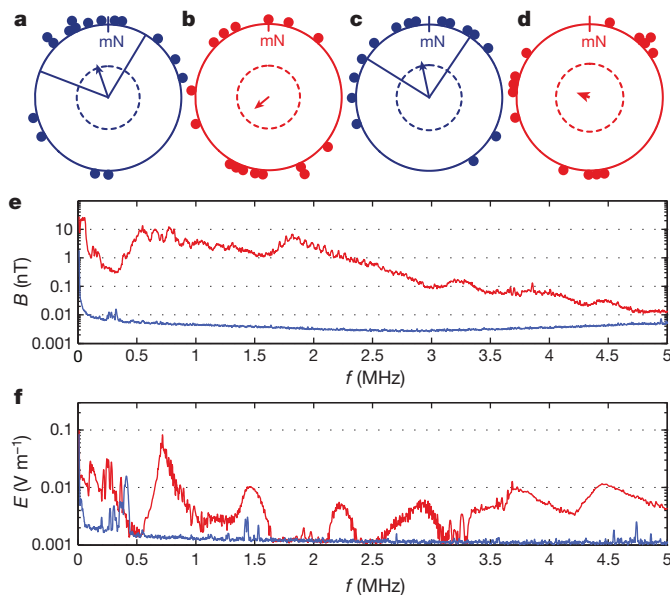


Figure 2 | Connecting and disconnecting the grounding of the screens turns on and off the birds’ magnetic compass orientation capabilities. When the screens were grounded, European robins oriented significantly in their migratory direction (a, spring 2008, $n = 16$, mean direction $341^\circ \pm 40^\circ$, $r = 0.45$, $P = 0.04$), whereas they were randomly oriented when the grounding was disconnected (b, spring 2008, $n = 16$, mean direction 230° , $r = 0.22$, $P = 0.47$). In another set of identical tests, this pattern repeated itself (c, grounded screens, spring 2008, $n = 15$, mean direction $348^\circ \pm 41^\circ$, $r = 0.48$, $P = 0.03$; d, grounding disconnected, spring 2008, $n = 14$, mean direction 290° , $r = 0.12$, $P = 0.82$). e, f, Magnetic and electric field intensities, respectively, as a function of frequency when the screens were grounded (blue) or ungrounded (red).

when we introduced broadband electromagnetic noise ranging from 2 kHz up to ca. 9 MHz (Fig. 3d, e and Extended Data Fig. 2) into the huts at magnetic field intensities similar to those measured for the background anthropogenic noise (Fig. 1c). To make sure that the observed effect was not simply due to the presence of the signal generator and associated electronics, we repeated these tests under identical conditions but with the output of the signal generator reduced to the lowest possible amplitude (Fig. 3d, e and Extended Data Fig. 2). In this condition, the birds oriented in their migratory direction in spring (Fig. 3b) and reoriented appropriately when the static magnetic field was rotated 120° anticlockwise (Fig. 3c). Thus, the disorientation appears to be caused by the electromagnetic noise, and not by the mere presence of the electronics.

Third, we assessed whether the effects are limited to a specific part of the radiofrequency spectrum. To answer this question, we tested European robins inside the grounded, aluminium-screened huts and in the presence of deliberately introduced broadband electromagnetic noise either in the frequency range from ca. 20 kHz to 450 kHz or from ca. 600 kHz to 3 MHz (Fig. 4f, g and Extended Data Fig. 2). As a control, we tested the same birds exposed to very-low-amplitude broadband noise ranging from ca. 2 kHz to 9 MHz (Figs 3d, e, 4f, g and Extended Data Fig. 2) in which we had observed that the birds could orient (Fig. 3b, c). As expected, the control birds again oriented appropriately (Fig. 4d, e). By contrast, broadband electromagnetic noise in both of the above non-overlapping frequency bands prevented the birds from orienting using their magnetic compass (Fig. 4a–c). Thus, the effects are not limited to one specific frequency or to one part of the radiofrequency spectrum.

The peak magnetic field intensity of the anthropogenic electromagnetic noise at any single frequency measured on typical days around the University of Oldenburg is on the order of 0.1–50 nT. The total time-dependent magnetic field, summed over the frequency range 10 kHz–5 MHz, is much stronger (on the order of at most 200–1,100 nT, see

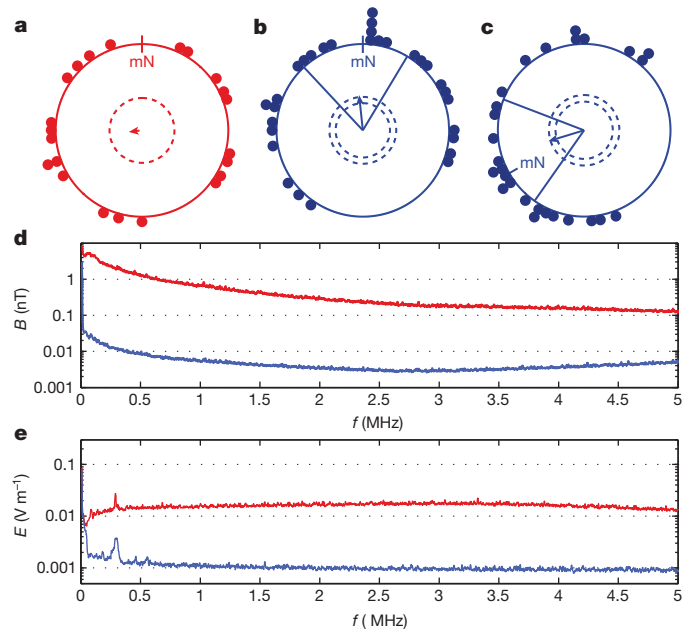


Figure 3 | Artificially produced broadband electromagnetic noise disrupts the magnetic compass orientation of birds tested inside the grounded aluminium-screened huts. Broadband, noise-modulated, electromagnetic fields between 2 kHz and 5 MHz (red traces in d, e and Extended Data Fig. 2) added inside the grounded screens resulted in disorientation of the birds (a, autumn 2010, $n = 22$, mean direction 278° , $r = 0.07$, $P = 0.91$). When the same equipment sent out the weakest possible broadband electromagnetic noise (blue traces in d, e and Extended Data Fig. 2), the birds oriented significantly towards North (b, spring 2011, $n = 30$, mean direction $354^\circ \pm 38^\circ$, $r = 0.39$, $P = 0.009$) and turned their orientation appropriately when the static magnetic field was rotated -120° (c, spring 2011, mN at 240° , $n = 27$, mean direction $253^\circ \pm 38^\circ$, $r = 0.41$, $P = 0.008$). d, Magnetic field intensity. e, Electric field intensity.

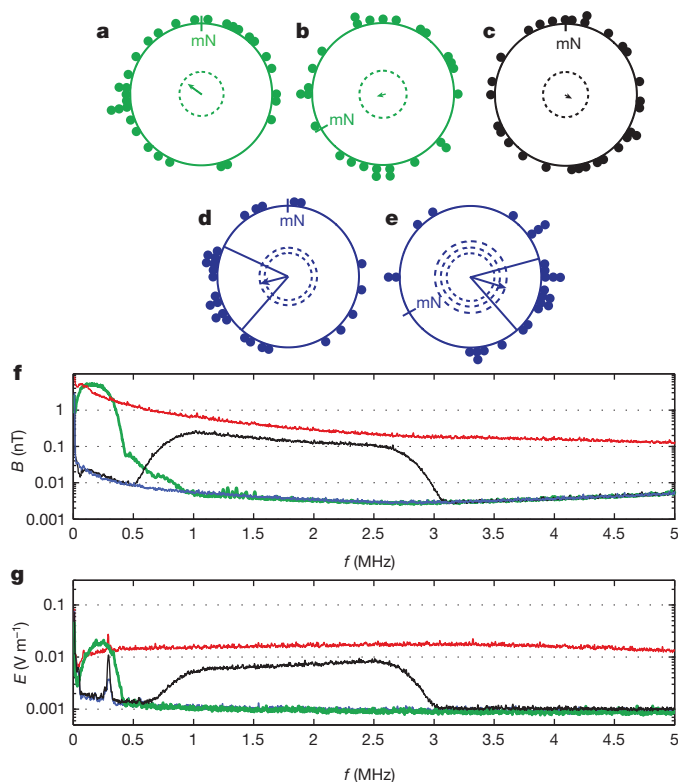


Figure 4 | The disruptive effect of broadband electromagnetic noise on magnetic compass orientation is not limited to a single narrow frequency range. Addition of broadband, noise-modulated, electromagnetic fields between ca. 20 kHz and 450 kHz (green traces in **f, g**) inside the grounded screens resulted in disorientation of the birds in the normal field (**a**, autumn 2011, $n = 31$, mean direction 306° , $r = 0.24$, $P = 0.17$) and in a field turned -120° horizontally (**b**, autumn 2011, $n = 27$, mean direction 235° , $r = 0.03$, $P = 0.96$). Broadband fields between ca. 600 kHz and 3 MHz (black traces in **f, g**) also disoriented the birds (**c**, autumn 2011, $n = 30$, mean direction 108° , $r = 0.11$, $P = 0.70$). When the same equipment sent out the weakest possible broadband electromagnetic noise (blue traces in **f, g**), the birds showed appropriately directed magnetic compass orientation (**d**, autumn 2011, $n = 27$, mean direction $258^\circ \pm 37^\circ$, $r = 0.42$, $P = 0.008$), and responded to a -120° horizontal rotation of the static field (**e**, autumn 2011, $n = 26$, mean direction $107^\circ \pm 32^\circ$, $r = 0.51$, $P < 0.001$). For comparison, the red traces in **f, g** show the intensity of the strong 2 kHz–9 MHz broadband noise used for the experiments presented in Fig. 3. **f**, Magnetic field intensity. **g**, Electric field intensity.

Extended Data Table 1), but still much weaker than the Earth's magnetic field (ca. 49,000 nT in Oldenburg). Ritz *et al.*¹¹ reported that the magnetic orientation capabilities of European robins in Frankfurt were disabled by highly directional, monochromatic radiofrequency fields with magnetic field intensities of 15 nT or more, but not at 5 nT under otherwise identical conditions. Their birds were only disoriented at magnetic intensities below ca. 100 nT when the radiofrequency matched the electron Larmor frequency (1.315 MHz in Frankfurt; 1.363 MHz in Oldenburg), that is, the resonance frequency of the spin of a free electron interacting with the Earth's magnetic field. Electromagnetic fields similar to those used by Ritz *et al.*^{10,11} never occur in natural or urban environments. The anthropogenic electromagnetic noise birds and other living beings experience is not monochromatic, nor is it spatially or temporally coherent (Fig. 1c, d). It has rapidly varying phases and directions and many different frequencies are present simultaneously. The electromagnetic noise we investigated is therefore fundamentally different from the conditions used previously¹¹. Furthermore, our birds were never exposed to magnetic fields stronger than 1 nT at 1.315 MHz or 1.363 MHz (Figs 1–5), and two non-overlapping frequency ranges interfere with the birds' ability to use their magnetic compass (Fig. 4). Thus, the disruptive effect on

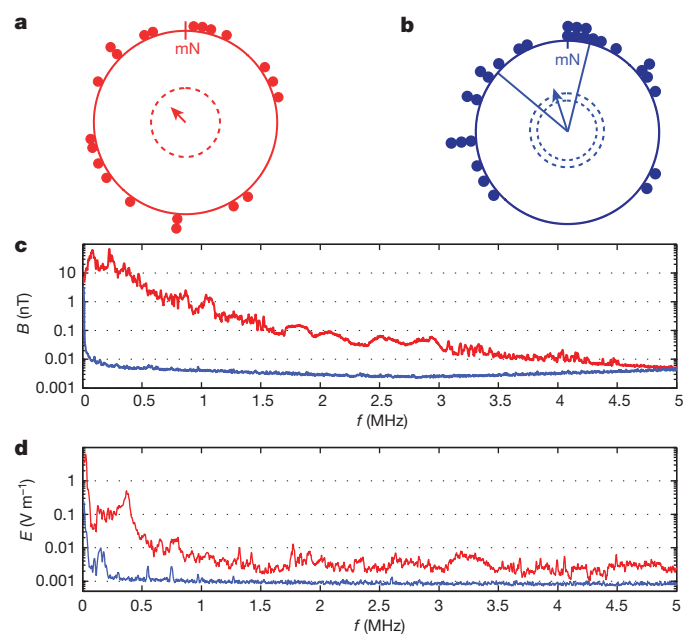


Figure 5 | In a rural location, European robins show magnetic compass orientation without screening. **a**, Orientation at the University campus (same data as in Fig. 1a). **b**, Orientation at a rural location (spring 2011, $n = 28$, mean direction $342^\circ \pm 32^\circ$, $r = 0.47$, $P = 0.002$) where the anthropogenic electromagnetic noise was much weaker (blue traces in **c, d**) than at the University (red traces in **c, d**). **c**, Magnetic field intensity. **d**, Electric field intensity.

orientation is not limited to a specific resonance frequency. It is caused by electromagnetic fields covering a much broader frequency range and at a much lower intensity (ca. 1 nT at any single frequency) than suggested previously^{10,11}. Most importantly, broadband anthropogenic electromagnetic noise omnipresent in industrialized environments can lead to disorientation. These results have several important implications.

First, the present results could have significant consequences for migratory bird conservation. Magnetic compass information is sensed by night-migratory songbirds on the ground and in free flight^{17,18}, which mostly takes place at altitudes below 1,000 m (ref. 19). So, if anthropogenic electromagnetic fields prevent migratory songbirds from using their magnetic compass, their chances of surviving the migratory journey might be significantly reduced, in particular during periods of overcast weather when sun and star compass information is unavailable. Night-migratory songbird populations are declining rapidly²⁰, and anthropogenic electromagnetic noise could be a previously neglected contributory factor. Nevertheless, billions of migratory birds do find their way every year. It is therefore pertinent to ask, how localized is the disorienting effect of man-made electromagnetic noise?

We therefore compared the orientation of our robins in the unscreened huts at the University site (Figs 1a and 5a) with their orientation in an unscreened wooden shelter located ca. 7.5 km from the University and ca. 1 km outside the Oldenburg city limit, where the anthropogenic electromagnetic noise was much weaker (Fig. 5c, d) and similar in intensity to the electromagnetic noise remaining inside the grounded aluminium-screened huts (Fig. 1c, d, blue trace). In the rural setting, the birds could orient using their magnetic compass in the absence of screening (Fig. 5b). Thus, the disruptive effect of anthropogenic electromagnetic noise on the birds' orientation capabilities appears to be restricted to urban locations where there is typically a high usage of electronic devices. Therefore, the effect on wild birds is probably also quite localized.

Second, the results presented here are likely to provide key insights into the mechanism either of the magnetic compass sense^{21–29} or of some important process that interferes with the birds' orientation behaviour. The biophysical mechanism that would allow such extraordinarily weak,

broadband electromagnetic noise to affect a biological system is far from clear. The energies involved are tiny compared to the thermal energy, $k_B T$, but the effects might be explained if hyperfine interactions in light-induced radical pairs^{12,21–27} or large clusters of iron-containing particles are involved^{28,29}. It would be truly remarkable if electromagnetic noise at the intensities studied here could be shown to disrupt the operation of a radical pair sensor by modifying its quantum spin dynamics. To be sensitive to such exceedingly weak magnetic fields, the electron spin-decoherence would have to be orders of magnitude slower than is currently thought possible. This intriguing prospect has attracted the attention of quantum physicists eager to learn lessons from nature that might ultimately allow more efficient quantum computers to be designed and constructed³⁰. Furthermore, we cannot rule out that the birds might be affected by the electric component of the electromagnetic noise, a possibility that has not been considered previously.

Last, but not least, using a double-blinded protocol we have documented a clear and reproducible effect on a biological system of anthropogenic electromagnetic fields much weaker than the current ICNIRP guidelines^{1,2}: the reference levels for general public exposure to time-varying magnetic fields in the relevant frequency band are 6,000 nT at 150 kHz decreasing to 180 nT at 5 MHz (refs 1, 2). The disruptive effects we observe cannot be attributed to power lines (16.7 Hz or 50 Hz fields) or to mobile phone signals (GHz frequencies) or to any other fields with frequencies below 2 kHz or above 5 MHz because outside this range the electromagnetic noise was of similar intensity in all conditions (Fig. 4 and Extended Data Fig. 2). Electromagnetic noise in the frequency-band 2 kHz–5 MHz originates primarily from AM radio signals and from electronic equipment running in University buildings, businesses and private houses. The effects of these weak electromagnetic fields generated by everyday human activity, however, are striking: they disrupt the function of an entire sensory system in a higher vertebrate.

METHODS SUMMARY

Essential methodological information needed for a basic understanding of the text has been woven into the main text at the appropriate places. The Methods section contains detailed information on the test subjects, electromagnetic shielding, execution and analysis of behavioural experiments, production and measurement of static fields, generation of electromagnetic noise, measurement of time-dependent electromagnetic fields, and blinding procedures.

Online Content Any additional Methods, Extended Data display items and Source Data are available in the online version of the paper; references unique to these sections appear only in the online paper.

Received 28 January; accepted 28 March 2014.

Published online 7 May 2014.

1. International Commission for Non-Ionizing Radiation Protection. ICNIRP guidelines for limiting exposure to time-varying electric, magnetic, and electromagnetic fields (up to 300 GHz). *Health Phys.* **74**, 494–522 (1998).
2. International Commission for Non-Ionizing Radiation Protection. ICNIRP statement on the “Guidelines for limiting exposure to time-varying electric, magnetic, and electromagnetic fields (up to 300 GHz)”. *Health Phys.* **97**, 257–258 (2009).
3. World Health Organization. Extremely Low Frequency Fields. Environmental Health Criteria Monograph no. 238, http://www.who.int/peh-emf/publications/elf_ehc/en/ (2007).
4. Health Protection Agency. Health Effects from Radiofrequency Electromagnetic Fields http://www.hpa.org.uk/webc/HPAwebFile/HPAweb_C/1317133827077 (2012).
5. The INTERPHONE Study Group. Brain tumour risk in relation to mobile telephone use: results of the INTERPHONE international case-control study. *Int. J. Epidemiol.* **39**, 675–694 (2010).
6. Johansen, C. *et al.* Cellular telephones and cancer—a nationwide cohort study in Denmark. *J. Natl. Cancer Inst.* **93**, 203–207 (2001).

7. Merkel, F. W. & Wiltschko, W. Magnetismus und Richtungsfinden zugunruhiger Rotkehlchen. *Vogelwarte* **23**, 71–77 (1965).
8. Wiltschko, W. & Wiltschko, R. Magnetic compass of European robins. *Science* **176**, 62–64 (1972).
9. Wiltschko, R. & Wiltschko, W. *Magnetic Orientation in Animals* (Springer, 1995).
10. Ritz, T., Thalau, P., Phillips, J. B., Wiltschko, R. & Wiltschko, W. Resonance effects indicate a radical-pair mechanism for avian magnetic compass. *Nature* **429**, 177–180 (2004).
11. Ritz, T. *et al.* Magnetic compass of birds is based on a molecule with optimal directional sensitivity. *Biophys. J.* **96**, 3451–3457 (2009).
12. Zapka, M. *et al.* Visual but not trigeminal mediation of magnetic compass information in a migratory bird. *Nature* **461**, 1274–1277 (2009).
13. Hein, C. M. *et al.* Night-migratory garden warblers can orient with their magnetic compass using the left, the right or both eyes. *J. R. Soc. Interface* **7**, 227–233 (2010).
14. Hein, C. M., Engels, S., Kishkinev, D. & Mouritsen, H. Robins have a magnetic compass in both eyes. *Nature* **471**, E11 (2011).
15. Engels, S., Hein, C. M., Lefeldt, N., Prior, H. & Mouritsen, H. Night-migratory songbirds possess a magnetic compass in both eyes. *PLoS ONE* **7**, e43271 (2012).
16. Swanson, J. & Kheifets, L. Biophysical mechanisms: a component in the weight of evidence for health effects of power-frequency electric and magnetic fields. *Radiat. Res.* **165**, 470–478 (2006).
17. Cochran, W. W., Mouritsen, H. & Wikelski, M. Migrating songbirds recalibrate their magnetic compass daily from twilight cues. *Science* **304**, 405–408 (2004).
18. Chernetsov, N., Kishkinev, D., Kosarev, V. & Bolshakov, C. V. Not all songbirds calibrate their magnetic compass from twilight cues: a telemetry study. *J. Exp. Biol.* **214**, 2540–2543 (2011).
19. Bruderer, B. The study of bird migration by radar part 2: major achievements. *Naturwiss.* **84**, 45–54 (1997).
20. Sanderson, F. J., Donald, P. F., Pain, D. J., Burfield, I. J. & Van Bommel, F. P. Long-term population declines in afro-paleartic migrant birds. *Biol. Conserv.* **131**, 93–105 (2006).
21. Schulten, K., Swenberg, C. E. & Weller, A. A biomagnetic sensory mechanism based on magnetic field modulated coherent electron spin motion. *Z. Phys. Chem.* **111**, 1–5 (1978).
22. Ritz, T., Adem, S. & Schulten, K. A model for photoreceptor-based magnetoreception in birds. *Biophys. J.* **78**, 707–718 (2000).
23. Maeda, K. *et al.* Chemical compass model of avian magnetoreception. *Nature* **453**, 387–390 (2008).
24. Rodgers, C. T. & Hore, P. J. Chemical magnetoreception in birds: the radical pair mechanism. *Proc. Natl. Acad. Sci. USA* **106**, 353–360 (2009).
25. Liedvogel, M. & Mouritsen, H. Cryptochromes—a potential magnetoreceptor: what do we know and what do we want to know? *J. R. Soc. Interface* **7**, 147–162 (2010).
26. Mouritsen, H. & Hore, P. J. The magnetic retina: light-dependent and trigeminal magnetoreception in migratory birds. *Curr. Opin. Neurobiol.* **22**, 343–352 (2012).
27. Solov'yov, I. A., Domratcheva, T. & Schulten, K. Separation of photo-induced radical pair in cryptochrome to a functionally critical distance. *Sci. Rep.* **4**, 3845 (2014).
28. Kirschvink, J. L., Winklhofer, M. & Walker, M. M. Biophysics of magnetic orientation: strengthening the interface between theory and experimental design. *J. R. Soc. Interface* **7** Suppl. 2, S179–S191 (2010).
29. Wu, L. Q. & Dickman, J. D. Neural correlates of a magnetic sense. *Science* **336**, 1054–1057 (2012).
30. Gauger, E. M., Rieper, E., Morton, J. J. L., Benjamin, S. C. & Vedral, V. Sustained quantum coherence and entanglement in the avian compass. *Phys. Rev. Lett.* **106**, 040503 (2011).

Acknowledgements We thank M. Wuschek, Rohde & Schwarz, Bundesnetzagentur, and ETS Lindgren for help with measuring the electromagnetic fields, the workshops at the University of Oldenburg, especially T. Geiger, for building equipment, etc, and a large number of Bachelors, Masters and PhD students for help in conducting the experiments. We are grateful to the following for financial support: Defense Advanced Research Projects Agency (QuBE: N66001-10-1-4061 to P.J.H. and H.M.), VW-Stiftung (Lichtenberg professorship to H.M.), DFG (FOR 701 and MO 1408/2-2 to H.M.), Heinz Neumüller Stiftung (to C.M.H. and S.E.), BMBF (to H.M.), the European Research Council (to P.J.H.) and the EMF Biological Research Trust (to P.J.H.).

Author Contributions S.E. and N.-L.S. contributed equally to this work and are listed alphabetically. H.M. and N.-L.S. designed the study. S.E., N.L., C.M.H., M.Z., A.M. and D.E. performed the experiments. S.E., N.L., C.M.H., M.Z. and H.M. analysed the data. A.K., P.J.H. and N.-L.S. provided physical insight needed to properly produce and measure the electromagnetic fields. N.-L.S. and S.E. were in charge of generating the electromagnetic noise. N.-L.S. measured the electromagnetic fields. H.M., P.J.H., N.-L.S. and S.E. wrote most of the paper. All authors read and commented on the manuscript.

Author Information Reprints and permissions information is available at www.nature.com/reprints. The authors declare no competing financial interests. Readers are welcome to comment on the online version of the paper. Correspondence and requests for materials should be addressed to H.M. (henrik.mouritsen@uni-oldenburg.de).

METHODS

Test subjects. In our study, we tested European robins caught on the campus of the University of Oldenburg, Germany. The birds were housed indoors in individual cages in a windowless room under a light regime simulating the local photoperiod. The tests were performed on the campus of the University of Oldenburg during the spring migratory seasons in 2005 (when we tested 22 birds), 2008 (18 birds) and 2011 (30 birds) and during the autumn migratory seasons in 2010 (24 birds) and 2011 (42 birds). The number of birds caught during the previous migratory seasons and the experimental facilities available for the specific experiment in the given season determined the choice of sample sizes. In addition to these experiments, which were performed specifically for the present study, tests were also conducted with various groups of students in spring 2007¹², spring 2008¹², autumn 2008¹³ (tests with garden warblers, *Sylvia borin*), spring 2009¹², autumn 2009^{14,15}, autumn 2010¹⁵, and spring 2011¹⁵. These additional experiments, done primarily for other studies that have already been published^{12–15}, included tests with control groups which repeatedly confirmed and extended the results presented in Fig. 1, namely that: (a) night-migratory songbirds orient properly using their magnetic compass in the grounded and screened huts in the unchanged geomagnetic field^{12–15}, and (b) they adjust their orientation appropriately when the horizontal component of the static field is rotated by -120° (refs 12–15). Furthermore, in two previous studies^{12,15} we tested groups of European robins in the screened and grounded huts while exposing them to a static field the vertical component of which had been inverted, leaving the horizontal component still pointing to the North. In this field, the polarity of the field lines is unchanged and still points towards magnetic North, but the axis of the static field lines is the same as if the static field had been turned 180° horizontally. Since these robins flipped their orientation ca. 180° (refs 12,15), the birds in the grounded and screened huts were using their standard magnetic inclination compass^{8,9}. All animal procedures were approved by the Animal Care and Use Committees of the Niedersächsisches Landesamt für Verbraucherschutz und Lebensmittelsicherheit (LAVES, Oldenburg, Germany).

Static magnetic fields. Static magnetic fields were produced with double-wrapped, three-dimensional Merritt four-coil systems³¹ with an average coil dimension of 2 m. All experiments were performed within the central space of the coils where the magnetic field homogeneity was better than 99%. Before the beginning of each experiment, the ambient geomagnetic field was measured using a Flux-Gate magnetometer (FVM-400, Meda Inc.) in the centre and at the edges of the experimental volume within which the orientation funnels were placed. Birds were tested in two different static magnetic field conditions: in a magnetic field closely similar to the natural geomagnetic field in Oldenburg (normal magnetic field, NMF) and in a magnetic field of the same strength and inclination as the local geomagnetic field but rotated 120° anticlockwise in the horizontal plane (changed magnetic field, CMF). To produce the CMF condition, the appropriate currents ran through the two subsets of windings per axis of the three-axial, four-coil Merritt system in the same direction. In the NMF condition, the currents that were needed to produce the CMF condition ran through the two subsets of windings but in opposite directions so that no significant changes (that is < 10 nT) to the geomagnetic field were produced by the coils³¹. The actual fields experienced by the birds under the two magnetic field conditions were as follows (mean \pm standard deviation): NMF condition, 48,900 nT \pm 150 nT; inclination, $67.7^\circ \pm 0.6^\circ$; horizontal direction, $360^\circ \pm 0.1^\circ$. CMF condition: 49,000 nT \pm 470 nT; inclination, $68.0^\circ \pm 1.1^\circ$; horizontal direction, $-120^\circ \pm 0.5^\circ$.

Electromagnetic shielding of experimental huts. Most of the experiments were performed inside wooden huts (Extended Data Fig. 1a) placed at the Wechloy (Natural Sciences) Campus of the University of Oldenburg (Extended Data Fig. 1d) in the city of Oldenburg (population ca. 160,000; Extended Data Fig. 1c). Some of the orientation experiments in spring 2011 took place in an unshielded wooden shelter, normally occupied by horses, located in fields ca. 7.5 km from the University and ca. 1 km outside the built-up part of the city of Oldenburg (Extended Data Fig. 1c). An earth barrier in the form of a highway bridge foundation was located between the testing location and the city of Oldenburg.

To attenuate time-dependent electromagnetic fields inside the wooden huts, the four walls (including the door) and the roof were covered with 1-mm-thick aluminium sheets, overlapping by at least 20 mm and bolted together with self-cutting screws every 5–10 cm (Extended Data Fig. 1b). We also tested whether the efficiency of the screens could be improved by adding aluminium sheets on the floor. No improvement was found, probably because negligible electromagnetic noise comes from below. Most of the experiments were therefore performed in huts screened on five sides in which the air-circulation was improved and the humidity variability reduced compared to shielding on six sides.

The aluminium walls of this five-sided Faraday cage were interconnected at all times. In the grounded conditions, this aluminium screening assembly was electrically connected at a single location to a single grounding rod with a depth of 8 m. In the ungrounded conditions, the grounding rod was manually disconnected from the aluminium screening assembly. Disconnection of the grounding removed the

screening effect of the aluminium shields. In fact, the ungrounded aluminium screens acted as an antenna that slightly increased the magnetic field intensity at some frequencies inside the test chambers compared to the unshielded condition (compare Fig. 1c, d with Fig. 2e, f). The disconnection of the grounding during the critical grounding/ungrounding experiments (Fig. 2) was performed by a member of the laboratory who was not involved in the behavioural experiments, and the persons performing and evaluating the experimental results were not aware of the change in conditions until after the completion of the experiments.

All electronic devices were placed outside this cage, disconnected from their protected earths and grounded via the same grounding rod as the Faraday cage. This is necessary because the protected earth from the standard power outlet would act as an antenna and introduce electromagnetic noise into the system. When properly grounded, the shielding attenuated the time-dependent magnetic fields with frequencies up to at least 20 MHz by approximately two orders of magnitude inside the testing chambers. The screening efficiency was estimated by generating electromagnetic noise just outside the chambers while measuring the electromagnetic noise arriving within. The anthropogenic electromagnetic noise observed at the University of Oldenburg is dominated by frequencies below 5 MHz. Higher frequency contributions were mostly at or below the detection limit of our equipment and are therefore not shown in Figs 1–5.

Generation of electromagnetic noise. To produce electromagnetic noise, a passive loop antenna (ETS Lindgren, Model 6511, 20 Hz–5 MHz) was placed vertically under the centre of the central orientation funnel and aligned along the North–South axis (48 cm vertically from the centre of the loop to the central funnel).

Broadband electromagnetic noise in the range 2 kHz–9 MHz was produced by a signal generator (Hewlett Packard, 33120A, 15 MHz Arbitrary Waveform Generator) connected to the antenna using either the maximum output (10 V peak-to-peak (pp)) for the strong noise condition or the minimum output (50 mV pp) for the weak noise condition used as a control (the generated noise with the output set to 50 mV pp was weaker than the measurement limit except for the electric component below 500 kHz, see blue traces in Fig. 3d, e and Extended Data Fig. 2). An alternative to this control would have been to use the ‘silent shorting’ design suggested by Kirschvink *et al.*²⁸. We experimented with this method, but even the shorted condition led to measurably increased electromagnetic fields inside the huts, which is why we chose the control described above.

The band-pass electromagnetic noise (20 kHz–450 kHz and 600 kHz–3 MHz) was produced using a vector signal generator (Rohde & Schwarz, SMBV 100A, 9 kHz–3.2 GHz) connected to the same passive loop antenna.

Measurements of time-dependent electromagnetic fields. The magnetic and electric components of the time-dependent electromagnetic fields were measured separately with different antennas connected to a signal analyser (Rohde & Schwarz, FSV 3 Signal and Spectrum Analyzer 10 Hz–3.6 GHz). All such measurements were performed at a similar time of day as the behavioural experiments, but not while the actual tests were running. This procedure was chosen because we wanted to exclude any possibility that the measurements or measuring equipment could influence in any way the electromagnetic noise fields present while the birds were being tested.

The magnetic component between 10 kHz and 5 MHz was measured with a calibrated passive loop antenna (ETS Lindgren, Model 6511, 20 Hz–5 MHz). The electric component between 10 kHz and 10 MHz was measured with a calibrated active biconical antenna (Schwarzbeck Mess-Electronic, EFS 9218, 9 kHz–300 MHz). The signal analyser was set to ‘max hold’ and a resolution bandwidth of 10 kHz. For each condition we measured the fields for a period of 40 min. The traces shown in Figs 1–5 are based on 5,000 measurement points between 10 kHz and 5 MHz.

For the low-frequency range (5 Hz–32 kHz), we used the EFA-300 system (Narda Safety Solutions). The magnetic component was measured using the calibrated EFA Magnetic Field Probe 100 cm² (EFA-300 system, Narda Safety Solutions). The electric component was measured with the calibrated Narda Electric Field Unit (EFA-300 system, Narda Safety Solutions). For each measurement, the antennas were connected to the EFA-300 hand-held signal analyser, and this signal analyser was also set to ‘max hold’ and the fields were measured for a period of 40 min (Extended Data Fig. 2).

It must be stressed that anthropogenic electromagnetic noise fields are always present but highly variable in their amplitude, phase and frequency spectrum. Two measurements of their intensity and frequency composition will never be identical. Consequently, the measurements shown in Figs 1c, d, 2e, f and 5c, d are representative examples of the noise measured at the approximate time of day when the experiments were performed.

The maximal total magnetic field intensity (more precisely the magnetic flux density, B) in the frequency range between 10 kHz and 5 MHz was calculated using the following equation:

$$B(\Delta f) = \frac{1}{N} \frac{\Delta f}{\Delta f_0} \sum_i B_i(f_i, \Delta f_0)$$

in which $B(\Delta f)$ denotes the total magnetic flux density in the bandwidth of interest, $\Delta f = 5 \text{ MHz} - 10 \text{ kHz} = 4,990 \text{ kHz}$, and $B_i(f_i, \Delta f_0)$ is the magnetic flux density at the N different frequency values f_i (every 1 kHz between 10 kHz and 5 MHz, that is, $N = 4,990$) for a resolution bandwidth Δf_0 , which equals 10 kHz here. Expressed in words, $B(\Delta f) = (\text{the sum of the magnetic field intensity values/no. of values}) \times (\text{frequency range size/resolution bandwidth})$, in our case: $(\text{the sum of the magnetic field intensity values}/4,990) \times (4,990 \text{ kHz}/10 \text{ kHz})$ for the total frequency range from 10 kHz to 5,000 kHz. Extended Data Table 1 lists these values for the different conditions tested.

Behavioural experiments. All birds were tested in so-called Emlen funnels³² lined with scratch-sensitive paper³³, inside wooden huts ($4 \text{ m} \times 4 \text{ m} \times \text{ca. } 3 \text{ m}$, Extended Data Fig. 1a), where no directional cue other than the geomagnetic field was available. In 2005, the experiments took place in these simple wooden huts. From 2007 onwards, the walls and ceilings of the huts were lined with aluminium shields as described above. All electronic equipment was placed outside the hut in a separate wooden annex inside an aluminium box and grounded to minimize the generation of electromagnetic noise by the equipment itself.

One hour ($\pm 10 \text{ min}$) before the experiments started (half an hour before until half an hour after sunset), the birds were placed outdoors in wooden transport cages that allowed them to see parts of the evening sky. This gave the birds the possibility to calibrate their magnetic compass from twilight cues^{17,34}. Immediately thereafter, the birds were placed in modified aluminium Emlen funnels (35 cm diameter, 15 cm high, walls 45° inclined³²), which were coated with thermal paper³³ on which the birds left scratches as they moved. The top of each funnel was covered with a translucent Plexiglas lid that prevented the birds from seeing any landmarks in the hut. The overlap point of the paper was adjusted to one of the cardinal directions (N, S, E or W). This overlap point was changed randomly between huts and nights. This is important because the papers are always evaluated relative to the overlap point by researchers who do not know in which direction it was positioned. Even if someone would intentionally try to ignore the condition-blinding protocols (this is highly unlikely), this procedure adds a second level of blinding, and it becomes impossible for 'wishful thinking' to influence the results in any way, since the persons evaluating the papers cannot know which geographical direction is equivalent to a given direction on the paper. The location of the overlap point is only revealed and taken into consideration after the primary evaluation of the papers has taken place (for procedures see below).

The birds were tested for 1 h under dim white light conditions (2.1 mW m^{-2}) produced by incandescent bulbs (spectrum given in ref. 12). In each hut, nine birds were tested simultaneously. The birds were placed in a randomized funnel position each night and were put into the funnels from different directions, and we observed no systematic differences between the nine funnel positions or between the four huts. A second, and in a few instances a third, round of tests on a given night started 1.5 h ($\pm 10 \text{ min}$) after the first or second round. In most cases, each bird was tested in a different hut in each round but under the same magnetic field condition (NMF or CMF) and if applicable under the same time-dependent electromagnetic noise condition. The results of the different tests can therefore be treated as independent. The mean direction of each bird in each condition was calculated by unit-vector addition of the individual mean directions from the typically 3–15 tests per bird per condition in which the bird was judged to be oriented.

If more than one condition was tested in a given season, the same experimental birds were tested in all conditions. The experimental condition experienced by a given bird was mostly interchanged every second day, and whenever possible, different conditions were run simultaneously in different huts, so that any putative daily variation, for instance induced by the weather³⁵, would be averaged out amongst the experimental groups.

In spring 2008, we decided to test the effect of the grounding of the shielding and performed experiments in two different huts. One of them was grounded (g) and

the other was left ungrounded (u) without the experimenters knowing which one was which. The experimental condition for each bird alternated every other day; half the birds were tested in g-u-g-u conditions while the other half were u-g-u-g as follows: group 1, grounded on days 1 and 2, ungrounded on days 3 and 4, grounded on days 5 and 6, and ungrounded on days 7 and 8; group 2, ungrounded on days 1 and 2, grounded on days 3 and 4, ungrounded on days 5 and 6, and grounded on days 7 and 8. The data from these measurements are presented in Fig. 2 as follows: Fig. 2a: group 1: days 1, 2 and group 2: days 3, 4. Figure 2b: group 2: days 1, 2 and group 1: days 3, 4. Figure 2c: group 1: days 5, 6 and group 2: days 7, 8. Figure 2d: group 2: days 5, 6 and group 1: days 7, 8.

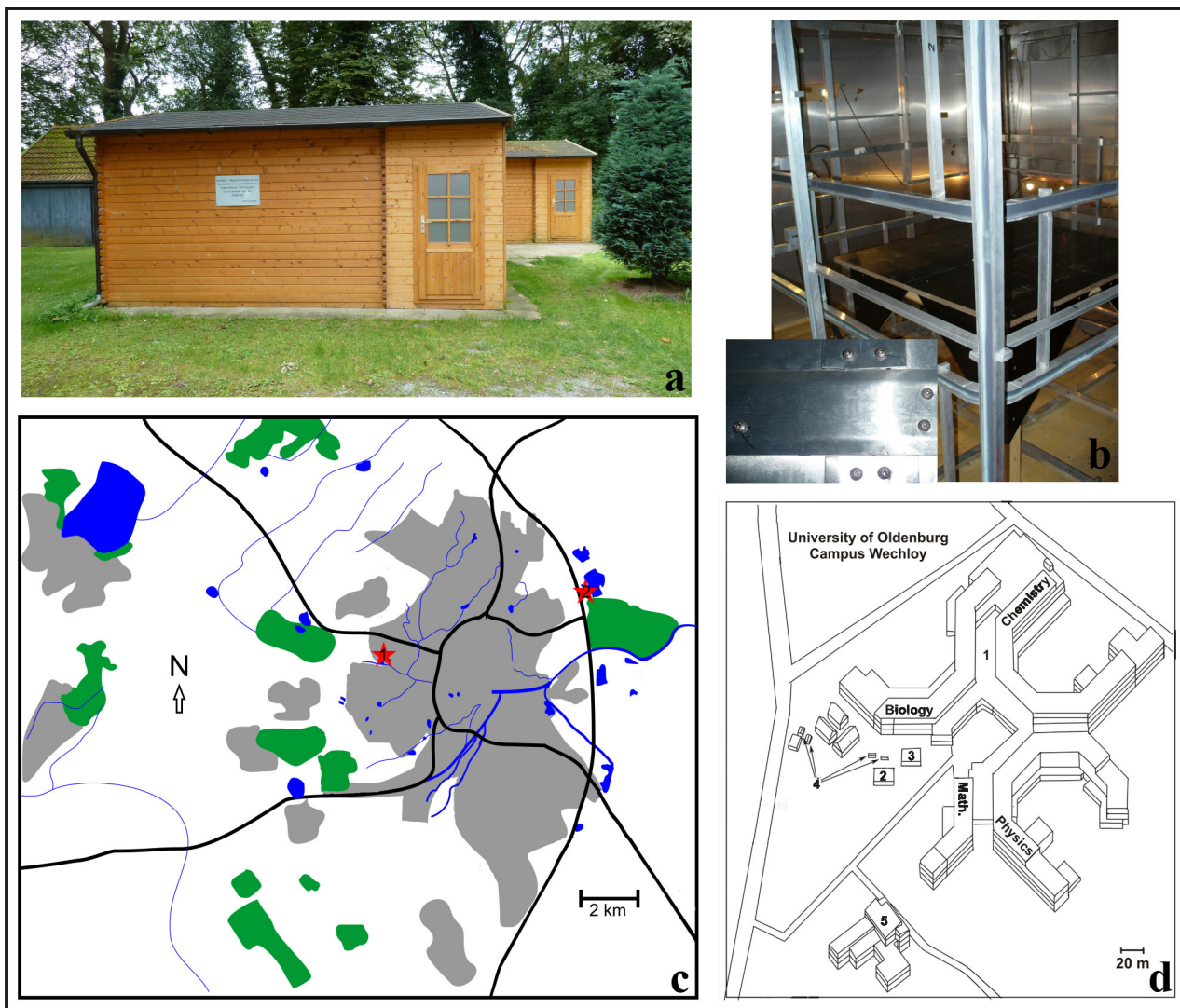
In 2010 and 2011, we performed experiments in which we added broadband electromagnetic noise (for details see above). The direction of the static magnetic field and electromagnetic noise conditions in a given hut were changed regularly; usually different conditions were tested concurrently in different huts on any given night.

At the rural location, 12 European robins were tested simultaneously in a wooden shelter located in a field (Extended Data Fig. 1c). Here, the birds were tested under natural magnetic conditions without a magnetic coil system. Other testing procedures were the same as in the huts on the University campus.

Before we started the experiments in any migratory season, we tested the birds in NMF and CMF conditions with no experimental manipulation for several nights to ensure that they were in migratory mood and to get a control direction.

Orientation data analysis. Independently, two researchers visually determined each bird's mean direction to the nearest 10° from the distribution of the scratches without knowing the direction of the overlap-point of the paper or the magnetic field conditions experienced by the bird. If one of the two researchers considered the scratches to be randomly distributed and the other did not, or if the two independently determined mean directions deviated by more than 30° , a third independent researcher was asked to determine the mean direction. If this third individual determined a mean direction similar to one of the first two, and if the individual with initially differing opinion also agreed with this direction, the mean of the two similar directions was recorded as the orientation result. If the three independent researchers could not agree on a mean direction, the bird's heading was defined as random and excluded from the analyses (7% of all tests). Birds with fewer than the pre-established lower limit of 100 scratches on the paper were considered inactive¹⁵ and were also excluded from the analysis (40% of all tests). The observers performed this screening before they knew the direction of the overlap-point (see above). In this way we can be certain that the person making the decision on whether the bird left more or less than 100 scratches was not influenced by the bird's directional preferences. The average mean heading for each bird was calculated from all its oriented tests recorded under a given experimental condition. On the basis of these individual mean directions, group mean vectors were calculated by summing unit vectors in the mean directions of each individual bird and dividing by the total number of birds tested. The significance of the group mean vector was tested using the Rayleigh test³⁶.

- Kirschvink, J. L. Uniform magnetic fields and double-wrapped coil systems: improved techniques for the design of bioelectromagnetic experiments. *Bioelectromagnetics* **13**, 401–411 (1992).
- Emlen, S. T. & Emlen, J. T. A technique for recording migratory orientation of captive birds. *Auk* **83**, 361–367 (1966).
- Mouritsen, H., Feenders, G., Hegemann, A. & Liedvogel, M. Thermal paper can replace typewriter correction paper in Emlen funnels. *J. Ornithol.* **150**, 713–715 (2009).
- Muheim, R., Phillips, J. B. & Åkesson, S. Polarized light cues underlie compass calibration in migratory songbirds. *Science* **313**, 837–839 (2006).
- Hein, C. M., Zapka, M. & Mouritsen, H. Weather significantly influences the migratory behaviour of night-migratory songbirds tested indoors in orientation cages. *J. Ornithol.* **152**, 27–35 (2011).
- Batschelet, E. *Circular Statistics in Biology* (Academic, 1981).

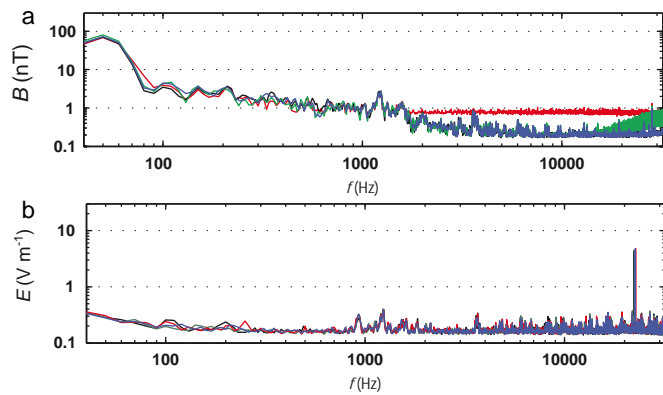


Extended Data Figure 1 | Wooden huts and experimental locations.

a, Photograph of one of the four identical wooden huts used for our experiments. **b**, Photograph from the inside of an experimental hut showing the aluminium screening, parts of the Merritt coil system, and the table on which the funnels were placed. The insert shows the self-cutting screws used to connect the aluminium plates. **c**, Simple map of the city of Oldenburg. Built-up areas are shown in grey and nature-protected areas in green. Black lines denote

highways, blue denotes water. Red stars: '1' indicates the location of the University campus and '2' the rural location used for some of the tests.

d, Map of the University of Oldenburg Wechloy Campus. 1, main University building housing the biology, chemistry, physics and mathematics institutes; 2, botanical greenhouse; 3, iron-free wooden building; 4, the locations of the four wooden huts used for our experiments; 5, 'Next Energy' building.



Extended Data Figure 2 | Electromagnetic noise measurements in the range from 40 Hz to 32 kHz. a, Magnetic field intensity (B). **b,** Electric field intensity (E). The colour coding of the traces corresponds to Fig. 4. Notice that the frequency-axis (f) is logarithmic.

Extended Data Table 1 | The accumulated time-dependent magnetic field intensity summed over all the frequencies in the spectra recorded for each behavioural test condition

	Oldenburg unshielded	Oldenburg grounded shielding	Oldenburg ungrounded shielding	Rural location	10 kHz - 5 MHz strong	10 kHz - 5 MHz weak	20 - 450 kHz bandpass	600 kHz - 3 MHz bandpass
	Fig. 1 and 5 red trace	Fig. 1 and 2 blue trace	Fig. 2 red trace	Fig. 5 blue trace	Fig. 3 and 4 red trace	Fig. 3 and 4 blue trace	Fig. 4 green trace	Fig. 4 black trace
<i>f</i> (kHz)	Accumulated field intensity (nT)							
10 - 5000	1008.10	2.56	827.86	2.60	278.88	3.31	133.09	34.83
100 - 5000	714.17	1.98	705.88	1.74	229.56	2.35	101.11	33.98
20 - 450	855.63	0.38	125.59	0.31	119.30	0.69	128.27	0.71
600 - 3000	81.89	0.87	561.05	0.79	98.81	1.00	1.16	32.48

ARTICLE

Received 6 Apr 2014 | Accepted 19 May 2014 | Published 24 Jun 2014

DOI: 10.1038/ncomms5164

OPEN

A magnetic compass aids monarch butterfly migration

Patrick A. Guerra¹, Robert J. Gegear² & Steven M. Reppert¹

Convincing evidence that migrant monarch butterflies (*Danaus plexippus*) use a magnetic compass to aid their fall migration has been lacking from the spectacular navigational capabilities of this species. Here we use flight simulator studies to show that migrants indeed possess an inclination magnetic compass to help direct their flight equatorward in the fall. The use of this inclination compass is light-dependent utilizing ultraviolet-A/blue light between 380 and 420 nm. Notably, the significance of light <420 nm for inclination compass function was not considered in previous monarch studies. The antennae are important for the inclination compass because they appear to contain light-sensitive magnetosensors. For migratory monarchs, the inclination compass may serve as an important orientation mechanism when directional daylight cues are unavailable and may also augment time-compensated sun compass orientation for appropriate directionality throughout the migration.

¹Department of Neurobiology, University of Massachusetts Medical School, 364 Plantation Street, Worcester, Massachusetts 01605, USA. ²Department of Biology and Biotechnology, Worcester Polytechnic Institute, Gateway Park, 60 Prescott Street, Worcester, Massachusetts 01605, USA. Correspondence and requests for materials should be addressed to S.M.R. (email: Steven.Reppert@umassmed.edu).

During the fall, eastern North American monarch butterflies (*Danaus plexippus*) migrate south from their northern range to overwinter in sites atop the mountains of Michoacán in central Mexico^{1–3}. Monarchs use an antenna-based time-compensated sun compass to navigate during this long journey^{4–6}, in which eye-sensed directional daylight cues (for example, sun azimuthal position) are integrated in the sun compass found in the midbrain central complex area^{7,8} and time compensated by antennal circadian clocks^{9,10}. Curiously, during the absence of directional daylight cues that precludes the use of the time-compensated sun compass (for example, overcast sky conditions), migrants have been observed flying in the expected southern migratory direction during the fall migration¹¹, suggesting that migrants might also use a magnetic compass to help guide directionality.

We now show that migratory monarch butterflies have an inclination magnetic compass that allows them to orient in the proper southern direction during the fall migration. The inclination compass is light dependent, using light in the ultraviolet-A/blue spectral range. Relevant light-sensitive magnetosensors appear to reside in the antennae, and the inclination compass functions at Earth-strength magnetic fields. The inclination compass is an essential orientation mechanism that migrants can use when directional skylight cues are unavailable, and it may also augment time-compensated sun compass orientation.

Results

Migrant monarchs can use a magnetic field for orientation. We performed indoor magnetic compass trials during the 2012 and 2013 fall migration seasons, in which individual monarchs collected from at least three different locations (see Methods) were tested in a flight simulator that was surrounded by a magnetic coil system used to vary the three different magnetic field parameters (horizontal, vertical, and intensity) (Fig. 1a). To facilitate flight in trials, they were conducted under diffuse white light conditions (spectrum: peak at 600 nm, range: 350–800 nm; total irradiance: 7.45×10^{15} photons $s^{-1} cm^{-2}$; Fig. 1b), which also provided migrants with wavelengths of light that are crucial for a functioning magnetic sense in other insects^{12,13}.

Migrants from the 2012 and 2013 migratory seasons that were flown under artificial magnetic field conditions (inclination angle = 45° ; total magnetic field strength = $141 \mu T$) and that flew continuously for 5 min were significantly directional with a mean equatorward orientation (2012: $\alpha = 162^\circ$, $r = 0.707$, $P = 0.0001$, $n = 18$; 2013: $\alpha = 179^\circ$, $r = 0.668$, $P = 0.0001$, $n = 27$). There was no difference in orientation direction between years (Watson's $U^2_{18, 27} = 0.028$, $P > 0.5$), and the pooled orientation bearing was 172° ($r = 0.676$, $P = 0.0001$, $n = 45$) (Fig. 1c). The 5-min flight duration was previously found to be the minimal time required to evaluate directional orientation behaviour in individual butterflies in the flight simulator⁶.

For assessing directionality in individual monarchs, we used a Z -value of ≥ 500 , as in previous publications^{9,10,14,15} (see Methods). Z , which is the critical value of the Rayleigh test, is calculated by the equation: $Z = nr^2$, in which n is the number of observations and r is the magnitude of the mean vector. Previous studies have shown, using reconstructed flight paths, that directional flight was apparent at $Z \geq 500$ and ambiguous at $Z < 500$ (ref. 14); this Z -value parameter helped define the non-directionality of non-migrant, summer butterflies tested in the flight simulator outdoors under sunny skies.¹⁴ Using the Z -value as a measure of directionality, we found that 87% of the 45 monarchs that flew continuously for 5 min exhibited a Z -value of > 500 . Accordingly, these 39 migrants provide a valid representation of

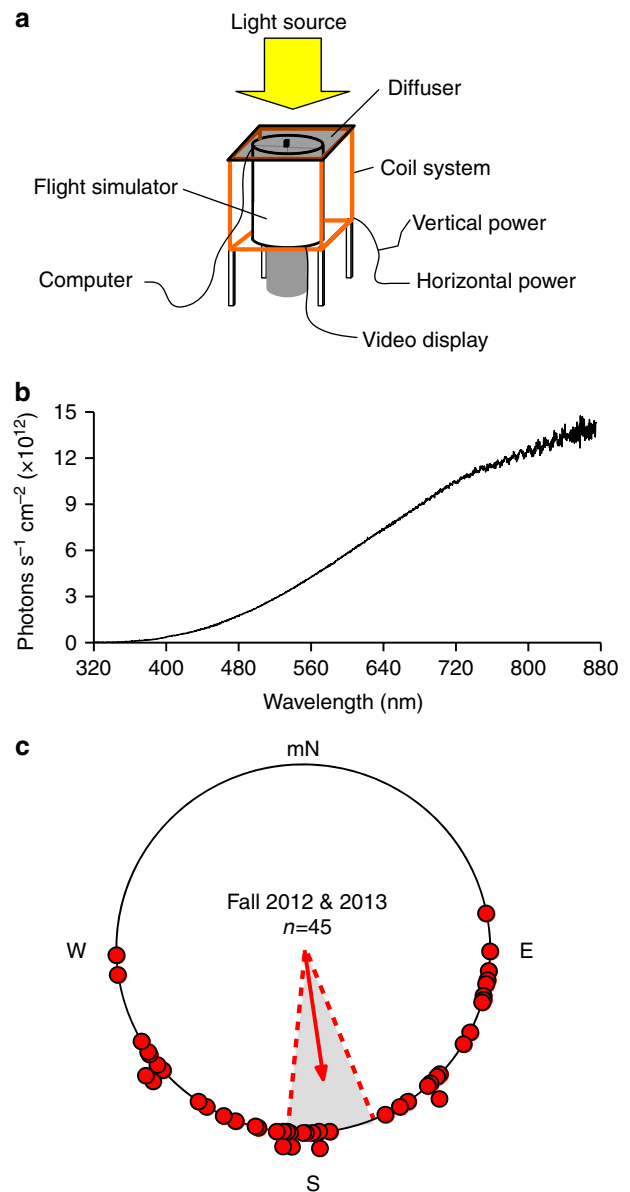


Figure 1 | Fall migrant monarch butterflies can use a magnetic field to orient in the proper southerly fall migratory direction. (a) Flight simulator and coil system used in magnetic compass trials. (b) Irradiance curve of lighting conditions during flight simulator trials. Light measurement was taken inside the flight simulator, with the flight encoder and diffuser in position, at the position of the head of the tethered monarch butterfly during trials. (c) Orientation of individual directional fall monarchs during the fall 2012 ($n = 18$) and 2013 ($n = 27$) migration seasons (red dots; both years pooled: $n = 45$) in a generated field with a 45° inclination angle, at a $141 \mu T$ field intensity. For the circle diagram, arrow indicates mean group orientation, shaded area is 95% confidence interval, mN is magnetic north.

the population of butterflies that flew. They were thus re-flown following the various trial perturbations outlined below with their first flight orientation values used as a control for comparison with subsequent experimental flight studies.

Migrants have an inclination magnetic compass. Most long-distance migratory animals studied to date use the inclination angle component of the Earth's magnetic field to guide their

latitudinal movement in either a poleward or equatorward direction^{16–18}. We examined whether or not monarchs also have an inclination magnetic compass by testing the orientation behaviour of individuals when the vertical component of the field was inverted (-45°). This field manipulation alters the directional information provided by the inclination angle such that individuals would perceive it as a 180° shift^{16,19} and is the acid test for the existence of an inclination compass^{16,19,20}. Eight migrants (initial Z -values: $1,151.0 \pm 134.3$, mean \pm s.e.m.; Fig. 2a, left) re-flew for 5 min a second time under the same magnetic field conditions but with the inverted vertical component. The eight migrants re-flown continued to exhibit Z -values > 500 (980.7 ± 150.1) but displayed a grouped orientation towards magnetic North ($\alpha = 1^\circ$, $r = 0.817$, $P = 0.002$, $n = 8$; Fig. 2a, right) that was opposite (Moore's test: $R' = 1.418$, $P < 0.001$) from their initial group orientation ($\alpha = 175^\circ$, $r = 0.857$, $P = 0.0008$, $n = 8$; Fig. 2a, left) by $\sim 180^\circ$. These results demonstrate that individual fall migrants use the inclination angle of a magnetic field as a directional cue, suggesting that monarchs, like birds and sea turtles^{16–18}, rely on an inclination compass for long-distance navigation.

Some animals use a polar compass for directionality and do not reverse their direction when the vertical component is inverted^{21,22}. To rule out a potential contribution of a polar compass to directionality in migratory monarchs, we re-flew migrants at vertical field parameters mimicking those at the equator in which the inclination is 0° but still at a field strength of $141 \mu\text{T}$; if the monarch's magnetic compass is strictly inclinational, then directionality should be severely compromised with only the horizontal (polar) component present (that is, without a vertical component). The seven migrants that re-flew for 5 min under these conditions (initial Z -values $1,087.4 \pm 308.4$ and group orientation of 146° , $r = 0.717$, $P = 0.021$, Fig. 2b, left) now exhibited a low degree of

directionality, flying in circles, with Z scores < 500 (69.1 ± 30.9) (Fig. 2b, right). Thus, the inclination magnetic compass is the dominant magnetic compass in monarchs, and the low Z scores represent the default state of orientation behaviour without the use of any inclination information.

The inclination compass uses ultraviolet-A/blue light. We next examined both the light sensitivity and spectral requirement of the inclination response. In migratory birds, the inclination compass is light-sensitive and thought to depend on radical pair-based chemical processes mediated by the flavoprotein cryptochrome (CRY)^{16,18,23}. Given the ability of the two types of monarch butterfly CRYs to restore a light-dependent magnetic response in CRY-deficient *Drosophila*^{12,13}, it is likely that monarchs also possess a light-dependent inclination compass. This was examined by using long-wavelength pass filters that transmitted wavelengths of light at > 420 nm or > 380 nm (Fig. 3a). Light intensity through the > 420 nm filter was 6.76×10^{15} photons $\text{s}^{-1} \text{cm}^{-2}$ (91% of full-spectrum irradiance), while light intensity through the > 380 nm filter was 6.82×10^{15} photons $\text{s}^{-1} \text{cm}^{-2}$ (92% of full-spectrum irradiance). These filters were used because the previous light dependence of the monarch CRY proteins for rescuing magnetosensitivity in CRY-deficient *Drosophila* was between 380 and 420 nm (ref. 13). When monarchs were exposed to light using the > 420 nm filter, the five monarchs that flew for 5 min (initial Z values 985.2 ± 150.1 and group orientation of 162° , $r = 0.866$, $P = 0.014$, Fig. 3b, left) each exhibited a low degree of directionality, flying in circles, with Z -values < 500 (9.0 ± 2.6) (Fig. 3b, right); those orientation values were no different from those from migrants without a vertical component ($t_6 = 1.6023$, $P = 0.1602$). When the > 380 nm pass filter was used, allowing

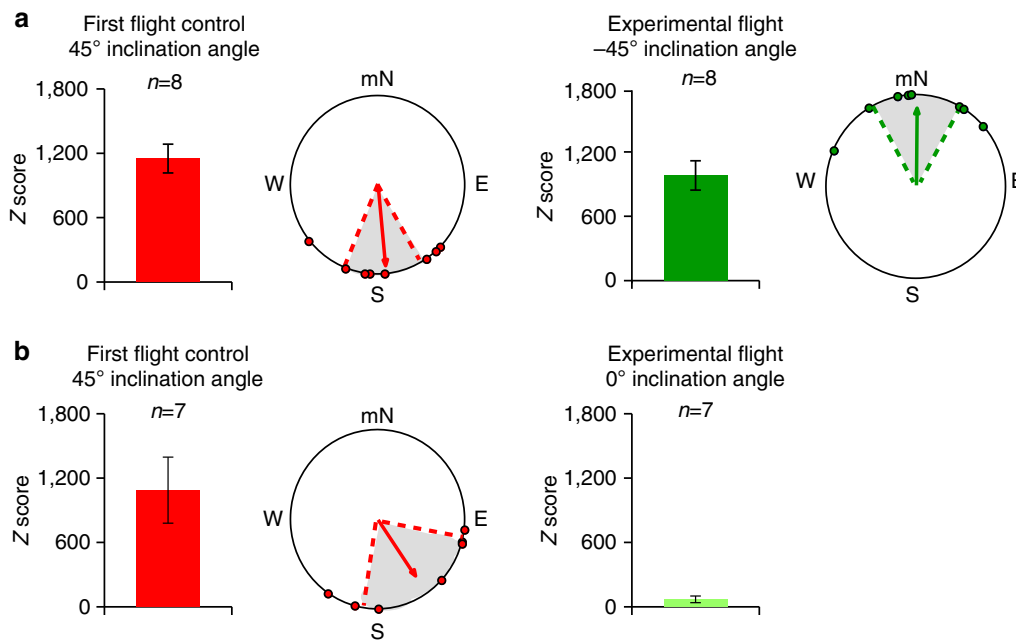


Figure 2 | The inclination magnetic compass of fall migratory monarch butterflies. (a) Fall migrant monarchs that oriented equatorwards during their initial flight (left; red; $n = 8$), shifted their orientation towards magnetic North when tested a second time under similar generated field conditions (right; dark green; $n = 8$), but with the inclination angle reversed (-45°). (b) Fall migrant monarchs that oriented equatorwards during their initial flight (left; red; $n = 7$), each displayed flight with significantly reduced directionality (that is, Z score < 500) when tested a second time under a horizontal field (0° inclination angle) with the same field intensity ($n = 7$). For both **a** and **b**, bar graphs indicate the mean $Z \pm$ s.e.m. score of animals for each group. Circular diagrams are the group orientation behaviour for each group in which each monarch plotted (dot) had a Z score > 500 . For each circular diagram, the arrow indicates mean group orientation, shaded area is 95% confidence interval, and mN is magnetic north.

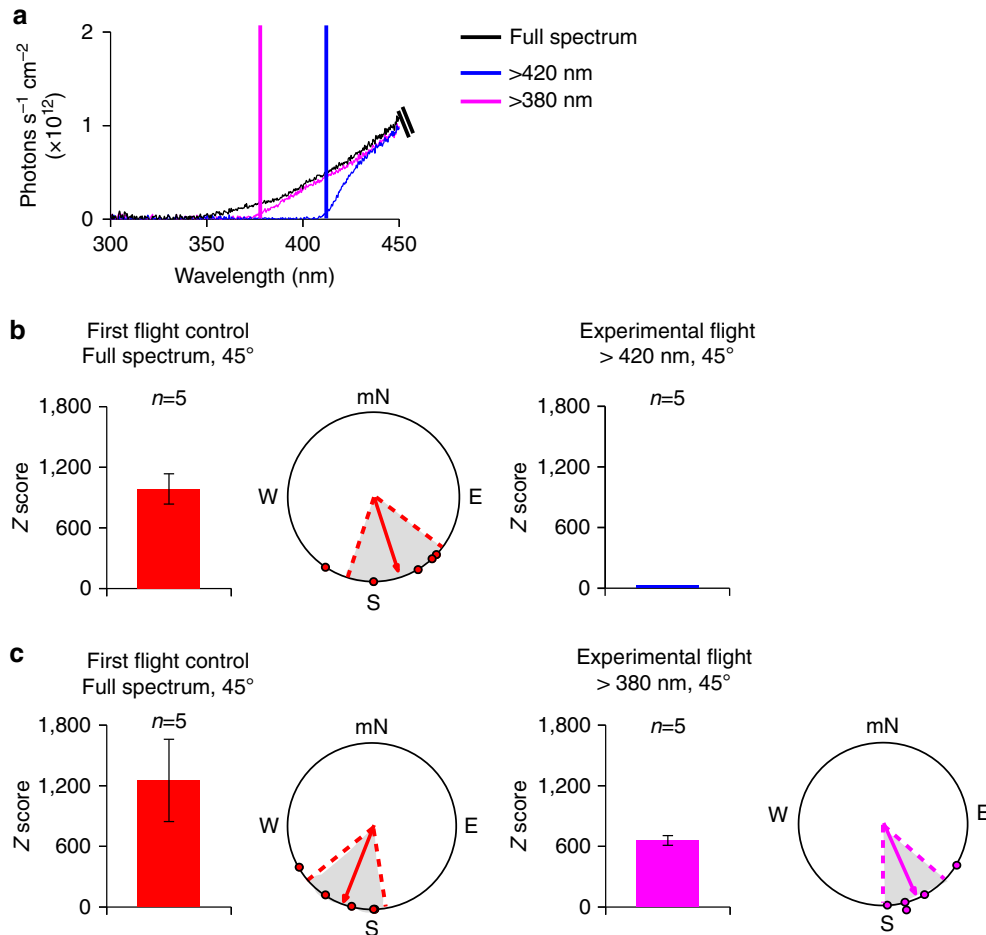


Figure 3 | The inclination magnetic compass uses ultraviolet-A/blue light. (a) Irradiance curves of lighting conditions during flight simulator trials. Black line indicates full spectrum light, blue line denotes filtered light that provided wavelengths of light >420 nm only, and purple line designates filtered light where only wavelengths of light >380 nm were available. (b) Migrants that oriented equatorwards during their first flight when tested under full spectrum lighting conditions (left; red; $n=5$) had significantly less directional flight, that is, $Z < 500$ (right; blue; $n=5$), when tested under light that contained wavelengths >420 nm. (c) In contrast, monarchs that oriented equatorwards under full spectrum light during their initial flight (left; red; $n=5$), maintained similar oriented flight that was equatorwards when tested under lighting conditions that included wavelengths >380 nm (right; purple; $n=5$). For all trials, the inclination angle was 45° and the field intensity was $141 \mu\text{T}$. In both **b** and **c**, bar graphs indicate the mean $Z \pm$ s.e.m. score of animals for each group. Circular diagrams consist of the group orientation behaviour for each group in which each monarch plotted (dot) had a Z score >500 . In each circular diagram, arrow indicates mean group orientation, shaded area is 95% confidence interval, and mN is magnetic north.

the addition of light between 380 nm and 420 nm, the five monarchs that flew for 5 min (initial Z -values $1,252.6 \pm 406.5$ and group orientation of 202° , $r=0.92$, $P=0.006$, Fig. 3c, left) exhibited clear directionality with Z -values >500 (658.1 ± 47.8 and group orientation of 157° , $r=0.946$, $P=0.004$, Fig. 3c, right). Thus, the monarch inclination compass appears to be light dependent with light in the ultraviolet-A/blue light spectral range (380 nm and 420 nm) important for inclination compass function. The >420 nm and >380 nm filters transmitted light intensities that were 91 and 92% of full-spectrum irradiance, respectively, yet each filter gave strikingly different orientation values. Hence, the contribution of decreased irradiance of the filters to the biological responses was negligible. The importance of light in the spectral range of 380–420 nm for compass function in monarchs is consistent with the inclination response being CRY dependent¹³.

The antennae likely contain relevant magnetosensors. We next addressed the location of the magnetosensor. Previous work has

demonstrated that the antennae of migratory monarchs are multimodal sensory organs that play an integral role for proper light-dependent, directional flight^{3,9,10,15}. Accordingly, it is possible that the antennae also house the magnetoreceptors necessary for migratory monarchs to utilize the inclination angle of the Earth's magnetic field. We thus re-tested first fliers under the inverted inclination angle conditions (-45°), but in which re-flown monarchs either had black-painted or clear-painted antennae for the second flight trial. The test condition was evaluated under the inverted inclination angle to rigorously examine the antennae as the potential source of the magnetosensor. Monarchs with black-painted antennae exhibited a low degree of directionality and flew largely in circles during this second flight ($Z = 127.6 \pm 47.6$; $n=5$) (Fig. 4a, right) compared with the directionality of their first flights ($Z = 1,231.3 \pm 181.2$ and group orientation of 146° , $r=0.826$, $P=0.024$; Fig. 4a, left). The orientation values from migrants with black-painted antennae were no different from those from migrants without a vertical component ($t_{10} = 1.0818$, $P=0.3047$). In contrast, monarchs with clear-painted antennae maintained

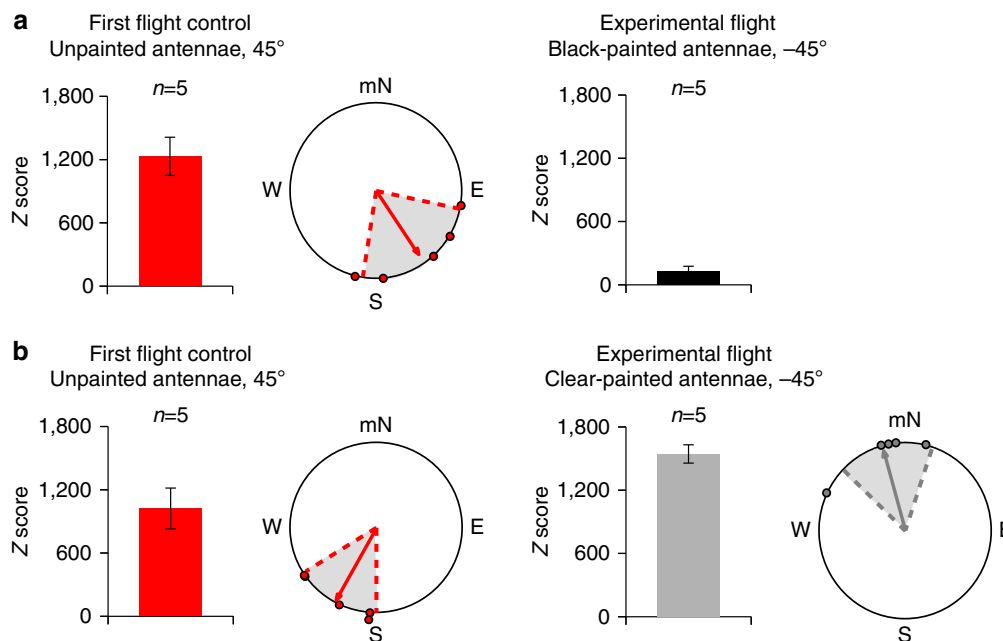


Figure 4 | The light-dependent magnetosensor involves the antennae. (a) Fall migrants that were oriented equatorwards during their initial flight (left; red; $n=5$) had significantly less directional flight (that is, $Z < 500$) when both antennae were painted black during their second flight (right; black; $n=5$). (b) In contrast, fall migrants that were directed towards magnetic South during their initial flight (left; red; $n=5$) shifted towards magnetic North when tested with clear-painted antennae under reversed inclination angle conditions (right; grey; $n=5$). For both **a** and **b**, monarchs (left diagrams; red) were tested in a generated field with a 45° inclination angle and an intensity of $141 \mu\text{T}$. In contrast, monarchs (right diagrams; black for **a** and grey for **b**) were tested in a generated field that had the same intensity, but where the inclination angle was -45° . In both **a** and **b**, each bar graph indicates the mean $Z \pm \text{s.e.m.}$ score of animals for each group. Each circular diagram consists of the group orientation behaviour for each group in which each monarch plotted (dot) had a Z score > 500 . For each circular diagram, the arrow indicates mean group orientation, shaded area is 95% confidence interval, and mN is magnetic north.

Z -values > 500 (clear-painted: $1,543.8 \pm 86.6$, $n=5$ versus unpainted: $1,022.0 \pm 193.6$, $n=5$) and were significantly oriented as a group towards magnetic North ($\alpha = 345^\circ$, $r = 0.9$, $P = 0.009$, $n=5$; Fig. 4b, right) in a direction close to opposite (Moore's test: $R' = 1.332$, $P < 0.001$) from their initial group orientation in the direction of magnetic South ($\alpha = 209^\circ$, $r = 0.92$, $P = 0.006$, $n=5$; Fig. 4b, left). Remarkably, these data are consistent with the hypothesis that fall monarchs use a light-dependent, antenna-based inclination magnetic compass for directionality.

The black paint itself was not the cause of the low degree of directionality (Z -values < 500) because previous outdoor studies of the time-compensated sun compass have shown that monarchs with black-painted antennae are each highly oriented (Z -values > 500), indicating that the sun compass has integrated skylight information (sensed through the eyes) for directionality⁹. However, because of the desynchronized antennal clocks, the result of painting the antennae black, those migrants can no longer orient as a group in the proper flight direction. Intriguingly, without light input to the antennae and directional light cues for retinal processing, the migrants in the present study fly in circles, unable to find any directional cues, as light cues for both the sun compass and inclination compass are absent. In fact, this explains the low degree of directionality and circular orientation patterns that have been observed in another monarch flight simulator study in which individuals were exposed to the $> 420 \text{ nm}$ long-wavelength filter outdoors with only blue sky visible²⁴.

The monarch inclination compass at Earth-strength fields. Although exposure to a strong magnetic field can disorient

migrant monarchs thereby suggesting that monarchs may possess a magnetic sense^{25,26}, and even though animals that use a magnetic field for orientation can orient using a field that is considerably stronger than the Earth's geomagnetic field²⁷, we re-tested first fliers at a field intensity that fell within the range of the Earth's geomagnetic field ($25\text{--}65 \mu\text{T}$) to determine if the inclination compass of migrants also functions at an Earth-strength field intensity. All re-flown migrants had Z scores > 500 (Fig. 5a, right; Fig. 5b). We found that migrants that were oriented equatorward in trials at our stronger field intensity of $141 \mu\text{T}$ ($\alpha = 185^\circ$, $r = 0.681$, $P = 0.033$, $n=7$; Fig. 5a, left) were also similarly oriented equatorward (Moore's test: $R' = 0.474$, $P > 0.5$) when tested in a second flight trial occurring in a magnetic field with a 60° inclination angle, at an Earth-strength field intensity of $57 \mu\text{T}$ ($\alpha = 173^\circ$, $r = 0.869$, $P = 0.002$, $n=7$; Fig. 5a, right). Furthermore, consistent with our results that tested migrants under reversed inclination angle conditions at $141 \mu\text{T}$ (Figs 2a and 4b), migrants that then flew for a third time in trials when tested at $57 \mu\text{T}$ but with a reversed inclination angle (-60°) switched their orientation behaviour towards magnetic North in a direction near opposite of their second (control) flight ($\alpha = 331^\circ$, $r = 0.892$, $P = 0.01$, $n=5$; Fig. 5b, right), in which the inclination angle was 60° . Moreover, the orientations of the second control flight ($57 \mu\text{T}$; 60° inclination angle) and third flight of migrants ($57 \mu\text{T}$; -60° inclination angle) were significantly different from each other (Moore's test: $R' = 1.279$, $P < 0.005$). Taken together, these data demonstrate the ability of migrant monarchs to use an inclination compass to orient in the proper equatorward migratory direction, which includes conditions at an Earth-strength field intensity and at an inclination angle encountered during their journey south. The

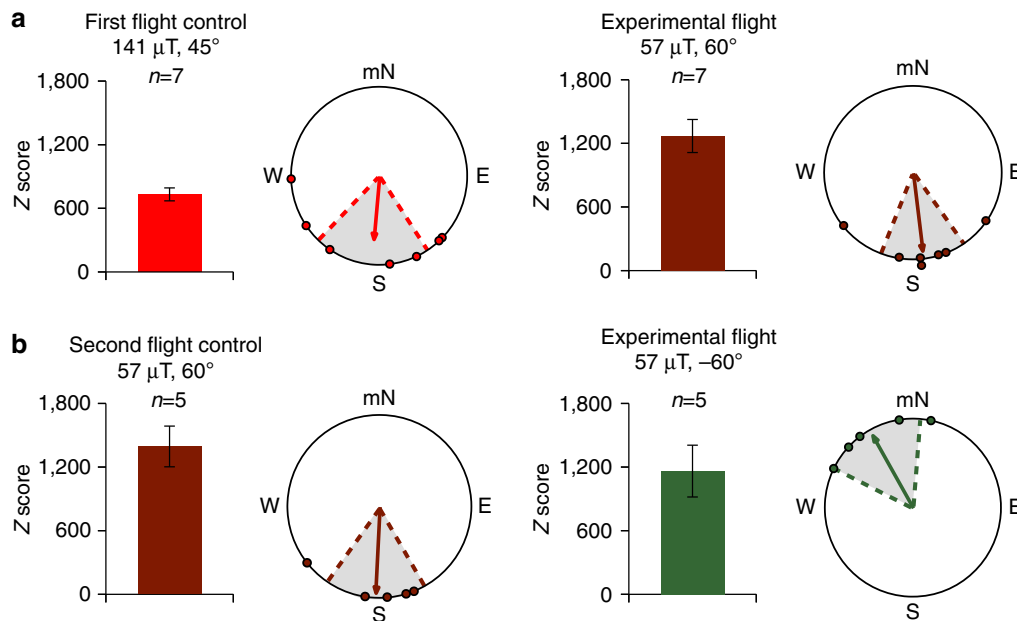


Figure 5 | The inclination compass of monarchs functions at an Earth-strength field intensity. (a) Orientation of individual directional monarchs (left; red; $n = 7$) in a generated field with a 45° inclination angle, at a $141 \mu\text{T}$ field intensity. The orientation of individual directional monarchs (right; maroon; $n = 7$) tested a second time (same monarchs from left circular diagram), but in a generated field with a 60° inclination angle, at a $57 \mu\text{T}$ field intensity. (b) Monarchs that flew towards magnetic South (left; maroon; $n = 5$) in a field with a 60° inclination angle and a $57 \mu\text{T}$ intensity (second flight) reversed their flight orientation to magnetic North (right; green; $n = 5$) in a generated field with a -60° inclination angle at a $57 \mu\text{T}$ field intensity, when tested a third time (same monarchs from left circular diagram). In both **a** and **b**, circular diagrams consist of the group orientation behaviour for each group in which each monarch plotted (dot) had a Z score > 500 . In each circular diagram, the arrow indicates mean group orientation, shaded area is 95% confidence interval, and mN is magnetic north. For both **a** and **b**, bar graphs indicate the mean $Z \pm \text{s.e.m.}$ score of animals for each group.

data support the idea that monarchs can use an inclination compass during their actual fall migration in the wild.

Discussion

As fall migratory monarchs have been observed to maintain a constant southwards flight direction under dense cloud cover conditions¹¹, it has been hypothesized that fall migrants may use geomagnetic cues for directionality, when directional daylight cues are unavailable to them during migration^{3,11}. Previous studies examining the existence of a magnetic compass in migratory monarchs, however, have yielded weak, conflicting results. For example, although work has shown that monarchs can become disoriented when exposed to experimentally generated strong magnetic fields^{25,26}, other work using a flight simulator found that migrants do not fly in an oriented manner when tested using simulated overcast skies, under either artificial or ambient magnetic fields^{5,28}. The defined spectral requirement for the inclination compass discovered in our studies potentially explains why previous flight simulator studies were unable to identify an inclination magnetic compass. In one of those studies²⁸, it is clearly stated that the test lighting conditions (consisting of a milky-white, non-UV-transmitting, translucent Plexiglas lid) excluded UV-A/blue light. Because both flight simulator studies were from the same group, it is likely that the lighting conditions of the other study⁵ also excluded the relevant spectral feature for detecting the use of an inclination compass. Moreover, given that we observed the use of an inclination magnetic compass by individuals that were tested in different years, sampled from at least three different locations, and tested at different magnetic field intensities, strengthens the idea that the spectral requirement is what is necessary for a functioning magnetic sense in monarch butterflies.

To our knowledge, our work is the first demonstration of the use of an inclination magnetic compass by a long-distance migratory insect. Our data suggest that the inclination compass may facilitate the fall migratory journey to the overwintering sites (that is, migrants respond to the sign of the inclination angle and respond by flying equatorward with a positive inclination angle as seen in our results), in a similar and/or concurrent manner as the time-compensated sun compass, or serve as a calibrator or backup mechanism to the sun compass³. Whether or not migrants possess a geomagnetic map sense that allows them to recognize or locate specific locations (for example, overwintering sites) as observed in sea turtles^{29,30} remains to be determined, however. The data also suggest that the antennae may contain the light-sensitive magnetosensors for the light-dependent inclination compass, thereby providing an additional migration-relevant function for the antennae of monarch butterflies. Involvement of the eyes and/or the brain in magnetosensing in migrant butterflies has not been ruled out. Knowledge of the presumed location of the relevant light-sensitive component of the magnetosensor in monarchs opens the way for evaluation of both the molecular and genetic mechanisms of magnetoreception^{31,32} and the involvement of their CRYs^{12,13}. Taken as a whole, our study reveals another fascinating aspect of monarch butterfly migratory behaviour. Greater knowledge of the mechanisms underlying the fall migration may well aid in its preservation, currently threatened by climate change and by the continuing loss of milkweed and overwintering habitats. Another vulnerability to now consider is the potential disruption of the magnetic compass in monarchs by human-induced electromagnetic noise, which can apparently disrupt geomagnetic orientation in a migratory bird³³.

Methods

Animal rearing and housing. In 2012, fall migratory monarch butterflies were captured by Fred Gagnon (between 1 September 2012 and 22 September 2012) near Greenfield, Massachusetts (latitude 42°59'N, longitude 72°60'W). In 2013, fall migratory butterflies were captured by Fred Gagnon (between 1 September 2013 and 28 September 2013; near Greenfield, Massachusetts), Carol Cullar (10 October 2013; near Eagle Pass, Texas [latitude 28°51'N, longitude 100°53'W]), and David Cook (30 October 2013; near St. Marks, Florida [latitude 30°9'N, longitude 84°12'W]). After capture, migrants were housed indoors in glassine envelopes in a Percival incubator under fall-like conditions: a light:dark cycle (LD) set to prevailing light conditions (12 h:12 h LD, 0600–1800 Eastern Standard Time), a constant temperature of 21 °C during the light phase and a constant 12 °C during the dark period, and 70% humidity.

Flight simulator trials and analysis. Monarchs were housed under fall-like conditions for at least 10 days before testing. Monarchs of mixed sex were tethered for flight trials as previously described, and their flight behaviour was assayed with a flight simulator^{9,10,15}. Flight direction was recorded by computer configured to record the direction of flight every 200 ms. Flight simulator trials for both fall 2012 and 2013 were conducted indoors at the University of Massachusetts Medical School (Worcester, Massachusetts: latitude 42°28'N, longitude 71°76'W), between 1100 and 1630 EST. Migrants were held in a non-metallic holding cage positioned within the coil system (see below) for 1 h before testing in the flight simulator, to acclimate them to the generated magnetic field²⁷ and to trial conditions^{9,10,15}.

To facilitate flight during trials, the flight simulator was illuminated from above (Fig. 1a) by diffuse white light (Utilitech 250W no. 0320778; spectrum: peak at 600 nm, range: 350–800 nm; intensity: 7.45×10^{15} photons $s^{-1} cm^{-2}$; Fig. 1b), which also provided migrants with wavelengths of light that are critical for a functioning magnetic sense in other insects^{12,13}. A diffuser was positioned in the light path, directly on top of the opening of the flight simulator⁷ (Fig. 1a). Irradiance measurements (using an Ocean Optics USB 2000 fiber optic spectrophotometer) were taken inside the flight simulator, with the flight encoder and diffuser in position, at the position of the head of the tethered monarch butterfly during trials.

The flight simulator was surrounded by a Helmholtz coil system (Fig. 1a) that was used to control the magnetic field in which an individual butterfly was tested. The coil system consisted of two independent two-coil systems arranged orthogonally, with each coil powered by its own power supply, and constructed in accordance with coil system designs used previously³⁴. One coil was used to control the horizontal component of the magnetic field, and this coil was aligned with the north-south magnetic axis. The second coil was used to control the magnetic field's vertical component³⁴. Magnetic field parameters at the position of the tethered monarch during flight simulator trials (horizontal and vertical field components) were measured using an Applied Physics Systems tri-axial fluxgate magnetometer (model 520A). Using these values, the inclination angle and total field intensity were calculated for each magnetic field condition.

The flight behaviour of monarchs was monitored on a video screen during trials, as well as recorded onto DVD. The behaviour of monarchs during trials was recorded for 82 out of 92 trials (for the 10 unrecorded trials, the DVD recorder malfunctioned, for example, the DVD became full during a trial that prevented the trial from being recorded). Two independent observers, unaware of the flight treatment (for example, first flight control or experimental condition), the magnetic field used during trials, and the antennal condition of migrants (for example, black- or clear-painted antennae), monitored recorded trials and verified the flights of butterflies (for example, flight > 5 min) in the flight simulator. For all conditions, we determined the significance of flight orientation and the mean direction of monarchs tested in the flight simulator using circular statistics (for example, Rayleigh's test for both individual and mean group orientation, Watson U^2 test for unpaired group comparisons, Moore's test for paired group comparisons) in Oriana (Kovach Computing Services).

Z score analysis. Because Z score is sample size dependent, butterflies from each group and under each condition (18 control and treatment groups) that were used in all of the comparisons in our study (12 statistical comparisons) were flown for the same amount of time and therefore any observed differences in Z scores were not simply the result of differences in flight times. There were no differences in the mean flight time values between groups in each of the comparisons that we made in our analyses (all *P*-values for each comparison were non-significant, the Bonferroni corrected $\alpha = 0.0042$ for 12 statistical tests). The following are the flight times in seconds (mean \pm s.e.m., number of animals in each group) for each group used in our comparisons: Fall 2012 first flights: 429.7 ± 23.9 , 18; Fall 2013 first flights: 407.8 ± 20.9 , 27; inclination angle control group: 464.9 ± 41.5 , 8; inclination angle test group: 346.9 ± 24.7 , 8; horizontal field control group: 347.1 ± 19.1 , 7; horizontal field test group: 324.7 ± 9.0 , 7; 420 nm control group: 392.6 ± 56.8 , 5; 420 nm treatment group: 318.24 ± 0.31 , 5; 380 nm control group: 373.64 ± 57.3 , 5; 380 nm treatment group: 351.44 ± 20.7 , 5; black-painted control group: 507.84 ± 57.98 , 5; black-painted treatment group: 343.64 ± 13.2 , 5; clear-painted control group: 426.2 ± 52.52 , 5; clear-painted treatment group: 458.88 ± 58.31 , 5; Earth-strength control group: 396.47 ± 24.48 , 7; Earth-strength treatment group:

505.37 ± 36.39 , 7; Earth-strength inclination control group: 519.96 ± 29.60 , 5; Earth-strength inclination treatment group: 383.64 ± 23.42 , 5.

Testing for magnetic sensitivity in monarchs. To first assay for a magnetic response in migrants, after a 1-h acclimation period to the generated magnetic field (inclination = 45°; total magnetic field strength = 141 μ T), we observed the flight behaviour of individual butterflies in flight simulator trials during fall 2012 and 2013. Only monarchs that flew continuously (> 5 min)^{9,10,15} were considered for analysis, and we found no difference in the flight behaviour of monarchs between years (Watson's $U^2_{18, 27} = 0.028$, $P > 0.5$). Out of the 171 monarchs tested during fall 2012 and 2013, 45 flew > 5 min during their first flight. This 26% success rate of migrants tested indoors in our trials is similar to the success rate of monarchs that flew continuously for 5 min during their first attempt in outdoor flight simulator trials (31% success rate; 34 out of 110 monarchs in fall 2010 (ref. 15)) (Fisher's exact test, $P = 0.4174$), as well as outdoor flight release trials that yielded useable flight data (35% success rate; 23 out of 66 monarchs¹⁵) (Fisher's exact test, $P = 0.2031$). Of these 45 fliers, 39 flew directionally (Z score > 500); this 87% rate of individual directionality was similar to the rate of individual directional fliers previously observed in outdoor flight simulator trials (92%, 46 out of 50 migrants¹⁰) (Fisher's exact test, $P = 0.5095$).

These monarchs that demonstrated significant directional flight behaviour (Z score > 500) during their first flight were then used in our subsequent experiments (see below). Within each experimental group, each monarch was only tested once. To minimize the use of monarchs, some butterflies were tested in more than one treatment group. For each treatment, monarchs were acclimated to trial field conditions for 1 h before testing, and only monarchs that flew > 5 min were used in analysis.

Testing for the use of an inclination compass. To test for the use of an inclination compass, monarchs were then tested a second time under similar generated magnetic field conditions as during their first flight, but where we reversed the inclination angle (–45°) by reversing the vertical component of the field, using our vertical coil system (horizontal component remained unchanged). All re-fliers during this second trial ($n = 8$) that flew for the required 5 min were directional (Z score > 500). To confirm the use of an inclination compass and to rule out the potential use of polarity for directionality, we tested another set of monarchs a second time under field conditions in which the inclination was 0° but still at a field intensity of 141 μ T (that is, a horizontal field with the same total field intensity as that of the first flight control). All re-fliers that flew for the required 5 min ($n = 7$) under this horizontal field exhibited significantly reduced directionality (Z score < 500) in comparison with their first flight.

Testing spectral requirement of the inclination compass. To determine whether a working inclination compass requires the presence of specific wavelengths of light, we re-tested monarchs after their first flight under filtered light conditions. Monarchs were re-tested under first flight magnetic field conditions (inclination angle = 45°; total field intensity = 141 μ T), but where light consisted of wavelengths of either > 420 nm or > 380 nm (long-wavelength filters E420 and E380 from Gentex). For each of these filtered light conditions, we had five monarchs that flew > 5 min. All five monarchs that flew under > 420 nm lighting conditions had significantly reduced directionality (Z scores < 500) relative to the first control flight; in contrast, all five monarchs that flew under > 380 nm lighting conditions had similar directionality (Z scores > 500) as their first control flight.

Locating the putative magnetosensor in monarchs. To determine whether the inclination compass of migrants consists of a light-dependent, antenna-based mechanism, migrants were re-tested after their first flight trial (inclination = 45°; total magnetic field strength = 141 μ T), but where butterflies either had both antennae painted black ($n = 5$) or clear ($n = 6$) during this second trial (field conditions were as during their first flight but with a reversed inclination angle, –45°). Black paint was used to prevent the sensing of light by the antennae, while clear paint was used as a control for the painting process, as clear paint still permits the antennae to receive light^{9,10,15}. Antennal painting has no effect on flight motivation or capability in monarchs^{9,10,15}. During this second flight, 10/11 monarchs flew > 5 min (5 black-painted, 5 clear-painted). Here, all monarchs with black-painted antennae had significantly reduced flight directionality relative to the first control flight (Z score < 500), whereas all monarchs with clear-painted antennae had similar flight directionality as their first flight (Z score > 500).

Inclination compass at Earth-strength magnetic conditions. To determine whether the inclination compass of migrants functions at Earth-strength field intensities, we compared the first flights of monarchs under our stimulus of 141 μ T (45° inclination angle), which is stronger than that of the Earth's geomagnetic field (25–65 μ T), with a second flight using a generated magnetic field with a field intensity (57 μ T) that fell within that of the Earth's. We initially aimed at presenting migrants with a magnetic field that had a field intensity and inclination angle that was consistent with the geographical location of trials, but, due to limitations with the testing room (that is, a slightly higher than ambient horizontal

component), we were unable to do so. Regardless, using our coil system, we were able to produce a magnetic field with an intensity within the range of the Earth's natural field, with an inclination angle (60°) that corresponded to an inclination angle that actual migrating monarchs will encounter during their journey to their overwintering sites (that is, 60° = Waco, Texas; National Oceanic and Atmospheric Administration National Geophysical Data Centre, <http://www.ngdc.noaa.gov/ngdc.html>). We had 7 migrants that flew for >5 min under these Earth-strength field conditions (57 μ T with a 60° inclination angle), and all of them flew directionally (Z score > 500). These seven migrants were then tested a third time, but where the inclination angle (-60°) of the Earth-strength field was reversed during trials using our coil system. Under these conditions, five out of seven migrants (71%) flew >5 min. All five of these fliers flew directionally (Z score > 500).

References

- Brower, L. P. Understanding and misunderstanding the migration of the monarch butterfly (Nymphalidae) in North America: 1857–1995. *J. Lepid. Soc.* **49**, 304–385 (1995).
- Urquhart, F. A. *The Monarch Butterfly* (University of Toronto Press, 1960).
- Reppert, S. M., Gegebar, R. J. & Merlin, C. Navigational mechanisms of migrating monarch butterflies. *Trends Neurosci.* **33**, 399–406 (2010).
- Perez, S. M., Taylor, O. R. & Jander, R. A sun compass in monarch butterflies. *Nature* **397**, 29 (1997).
- Mouritsen, H. & Frost, B. J. Virtual migration in tethered flying monarch butterflies reveals their orientation mechanisms. *Proc. Natl Acad. Sci. USA* **99**, 10162–10166 (2002).
- Froy, O., Gotter, A. L., Casselman, A. L. & Reppert, S. M. Illuminating the circadian clock in monarch butterfly migration. *Science* **300**, 1303–1305 (2003).
- Heinze, S. & Reppert, S. M. Sun compass integration of skylight cues in migratory monarch butterflies. *Neuron* **69**, 345–358 (2011).
- Heinze, S., Florman, J., Asokaraj, S., El Jundi, B. & Reppert, S. M. Anatomical basis of sun compass navigation II: the neuronal composition of the central complex of the monarch butterfly. *J. Comp. Neurol.* **521**, 267–298 (2013).
- Merlin, C., Gegebar, R. J. & Reppert, S. M. Antennal circadian clocks coordinate sun compass orientation in migratory monarch butterflies. *Science* **325**, 1700–1704 (2009).
- Guerra, P. A., Merlin, C., Gegebar, R. J. & Reppert, S. M. Discordant timing between antennae disrupts sun compass orientation in migratory monarch butterflies. *Nat. Commun.* **3**, 958 (2012).
- Schmidt-Koenig, K. Directions of migrating monarch butterflies (*Danaus plexippus*; Danaidae; Lepidoptera) in some parts of the eastern United States. *Behav. Process.* **4**, 73–78 (1979).
- Gegebar, R. J., Casselman, A., Waddell, S. & Reppert, S. M. Cryptochrome mediates light-dependent magnetosensitivity in *Drosophila*. *Nature* **454**, 1014–1018 (2008).
- Gegebar, R. J., Foley, L. E., Casselman, A. & Reppert, S. M. Animal cryptochromes mediate magnetoreception by an unconventional photochemical mechanism. *Nature* **463**, 804–807 (2010).
- Zhu, H., Gegebar, R. J., Casselman, A., Kanginakudru, S. & Reppert, S. M. Defining behavioural and molecular differences between summer and migratory monarch butterflies. *BMC Biol.* **7**, 14 (2009).
- Guerra, P. A. & Reppert, S. M. Coldness triggers northward flight in remigrant monarch butterflies. *Curr. Biol.* **23**, 419–423 (2013).
- Wilttschko, W. & Wilttschko, R. Magnetic orientation and magnetoreception in birds and other animals. *J. Comp. Physiol. A* **191**, 675–693 (2005).
- Lohmann, K. J. Magnetic-field perception. *Nature* **464**, 1140–1142 (2010).
- Phillips, J. B., Jorge, P. E. & Muheim, R. Light-dependent magnetic compass orientation in amphibians and insects: candidate receptors and candidate molecular mechanisms. *J. R. Soc. Interface* **7**, S241–S256 (2010).
- Wilttschko, W. & Wilttschko, R. Magnetic compass of European robins. *Science* **176**, 62–64 (1972).
- Light, P., Salmon, M. & Lohmann, K. J. Geomagnetic orientation of loggerhead sea turtles: evidence for an inclination compass. *J. Exp. Biol.* **182**, 1–10 (1993).
- Quinn, T. P. Evidence for celestial and magnetic compass orientation in lake migrating sockeye salmon fry. *J. Comp. Physiol. A* **137**, 547–552 (1980).
- Marhold, S., Burda, H. & Wilttschko, W. A magnetic polarity compass for direction finding in a subterranean mammal. *Naturwissenschaften* **84**, 421–423 (1997).
- Ritz, T., Adem, S. & Schulten, K. A model for photoreceptor-based magnetoreception in birds. *Biophys. J.* **78**, 707–718 (2000).
- Sauman, I. *et al.* Connecting the navigational clock to sun compass input in monarch butterfly brain. *Neuron* **46**, 457–467 (2005).
- Perez, S. M., Taylor, O. R. & Jander, R. The effect of a strong magnetic field on monarch butterfly (*Danaus plexippus*) migratory behavior. *Naturwissenschaften* **86**, 140–143 (1999).
- Larue, A., Naber, S. & Talmagi, J. Geomagnetic navigation in monarchs and black swallowtails. *Ohio J. Sci.* **106**, 117–123 (2006).
- Wilttschko, W., Stapput, K., Thalau, P. & Wilttschko, R. Avian magnetic compass: fast adjustment to intensities outside the normal functional window. *Naturwissenschaften* **93**, 300–304 (2006).
- Stalleicken, J. *et al.* Do monarch butterflies use polarized skylight for migratory orientation? *J. Exp. Biol.* **208**, 2399–2408 (2005).
- Lohmann, K. J. *et al.* Geomagnetic map used in sea-turtle navigation. *Nature* **428**, 909–910 (2004).
- Putman, N. F., Endres, C. S., Lohmann, C. M. F. & Lohmann, K. J. Longitude perception and bicoordinate magnetic maps in sea turtles. *Curr. Biol.* **21**, 463–466 (2011).
- Zhan, S., Merlin, C., Boore, J. L. & Reppert, S. M. The monarch butterfly genome yields insights into long-distance migration. *Cell* **147**, 1171–1185 (2011).
- Merlin, C., Beaver, L. E., Taylor, O. R., Wolfe, S. A. & Reppert, S. M. Efficient targeted mutagenesis in the monarch butterfly using zing finger nucleases. *Genome Res.* **23**, 169–180 (2013).
- Engels, S. *et al.* Anthropogenic electromagnetic noise disrupts magnetic compass orientation in a migratory bird. *Nature* **509**, 353–356 (2014).
- Lohmann, K. J. & Lohmann, C. M. F. Detection of magnetic inclination angle by sea turtles: A possible mechanism for determining latitude. *J. Exp. Biol.* **194**, 23–32 (1994).

Acknowledgements

We thank Fred Gagnon, Carol Cullar, David Cook and the Aschens for supplying butterflies; and Alison Earley, James Phillips-Portillo, Amit Sinha, Stanley Heinze and Lauren E. Foley for technical and logistical support. This work was supported by United States Air Force Office of Scientific Research (AFOSR) grant FA9550-10-1-0480.

Author contributions

All authors contributed to the experimental design, data analysis and writing the paper. P.A.G. performed all the experiments.

Additional information

Competing financial interests: The authors declare no competing financial interests.

Reprints and permission information is available online at <http://npg.nature.com/reprintsandpermissions/>

How to cite this article: Guerra, P. A. *et al.* A magnetic compass aids monarch butterfly migration. *Nat. Commun.* 5:4164 doi: 10.1038/ncomms5164 (2014).



This work is licensed under a Creative Commons Attribution-NonCommercial-ShareAlike 4.0 International License. The images or other third party material in this article are included in the article's Creative Commons license, unless indicated otherwise in the credit line; if the material is not included under the Creative Commons license, users will need to obtain permission from the license holder to reproduce the material. To view a copy of this license, visit <http://creativecommons.org/licenses/by-nc-sa/4.0/>

SCHEDULE B

Attachment

CALIFORNIA FORM 700 FAIR POLITICAL PRACTICES COMMISSION
Name <u>Christi Creegan</u>

ASSESSOR PARCEL NUMBER OR STREET ADDRESS : 3079 Harrison Avenue

LIST OF SOURCES OF RENTAL INCOME OF \$10,000 OR MORE

Sierra Nevada Media Group

Eagle Protect PBC

